Properties of
Sputter Deposited
Zinc and Zinc Alloy
Coatings

Dissertation

zur Erlangung des Grades

des Doktors der Ingenieurwissenschaften

der Naturwissenschaftlich–Technischen Fakultät III

Chemie, Pharmazie, Bio- und Werkstoffwissenschaften

der Universität des Saarlandes

von

Markus Trampert

Saarbrücken

15.12.2006

Tag des Kolloquiums: 15.12.2006

Dekan: Prof. Dr. K. Hegetschweiler

Vorsitzender   Prof. Dr. R. Busch
1. Berichterstatter: Prof. Dr. J. Breme
2. Berichterstatter: Prof. Dr. W. Arnold

Acknowledgement

Abstract

The intensive use of de-icing salts and the need for weight reduction of cars by use of thinner, high strength steels call for an improved corrosion protection of car body parts. Therefore today's car manufacturing uses steel sheets which are precoated by zinc and thus cathodically protected. The present study examines sputtering as an environmentally friendly alternative coating process which allows the deposition of coatings that can not be realised by currently used hot dipping or electrodeposition processes. Magnetron sputtering and ion beam sputtering deposition experiments delivering pure zinc and zinc alloy coatings have been carried out. Following this, the obtained coatings were examined with regard to their morphologies, chemical composition, crystallographic structures, mechanical properties and corrosion performance. The experiments showed that the morphologies of sputtered zinc films depend very strongly on the sputter parameters. Particularly the relatively low normalised substrate temperature T_s/T_m, i.e. the ratio between the temperature of deposition and the melting point of the deposited metal or alloy, plays an important role in the morphology development. At higher deposition temperatures, the obtained deposits deviated from those predicted by the structure zone models and even consisted of whisker like structures. The zinc alloy coatings condensed in unknown, metastable or even amorphous phases. The obtained films showed properties similar or better than conventionally deposited ones. In particular the alloyed zinc coatings showed promising perspectives due to their significantly better corrosion performances.

Kurzzusammenfassung

Der verstärkte Einsatz von Streusalz und das Ziel einer Gewichtseinsparung in Kraftfahrzeugen durch den Einsatz von dünneren, hochfesten Stählen erfordern einen verbesserten Korrosionsschutz von Karosserieteilen. Daher verwendet die heutige Automobilindustrie zinkbeschichtete und somit kathodisch geschützte Stahlbleche. Die vorliegende Arbeit untersucht Sputtern als umweltfreundlichen Beschichtungsprozess, der die Abscheidung von Schichten ermöglicht, welche nicht durch die derzeit verwendeten Feuerverzinkungs- oder Galvanisierungsprozesse hergestellt werden können. Hierzu wurden Magnetron- und Ionenstrahl-Sputter-Experimente durchgeführt, welche pure Zink- und Zinklegierungsschichten lieferten. Anschließend wurden die erhaltenen Schichten in Hinblick auf ihre Morphologie, chemische Zusammensetzung, kristallographische Strukturen, mechanische Eigenschaften und Korrosionseigenschaften untersucht. Die Beschichtungsexperimente zeigten, daß die Morphologien der gesputterten Zinkschichten sehr stark von den Sputter-Parametern abhängen. Insbesondere die relativ geringe normalisierte Substrattemperatur, d. i. das Verhältnis zwischen Beschichtungstemperatur und dem Schmelzpunkt des abgeschiedenen Metalls oder der Legierung, spielen eine entscheidende Rolle bei der Entwicklung der Schichtmorphologie. Bei höheren Beschichtungstemperaturen weichen die erhaltenen Schichten von den - von den verschiedenen Strukturzonenmodellen vorhergesagten - Strukturen ab und zeigen sogar Whiskerartige Strukturen. Die Zinklegierungsschichten kondensierten in unbekannten, metastabilen oder sogar amorphen Phasen. Die Korrosionseigenschaften der erhaltenen Schichten sind vergleichbar oder sogar besser als die der konventionell beschichteten. Insbesondere die Zinklegierungsschichten zeigten vielversprechende Perspektiven aufgrund ihrer deutlich besseren Korrosionseigenschaften.

Zusammenfassung

Der verstärkte Einsatz von Streusalz und das Ziel einer Gewichtseinsparung in Kraftfahrzeugen durch den Einsatz von dünneren, hochfesten Stählen erfordern einen verbesserten Korrosionsschutz von Karosserieteilen. Daher verwendet die heutige Automobilindustrie zinkbeschichtete und somit kathodisch geschützte Stahlbleche. Die vorliegende Arbeit untersucht Sputtern als umweltfreundlichen Beschichtungsprozess, der die Abscheidung von Schichten ermöglicht, welche nicht durch die derzeit verwendeten Feuerverzinkungs- oder Galvanisierungsprozesse hergestellt werden können. Ein weiterer Vorteil dieser Beschichtungsmethode ist die hohe Umweltverträglichkeit, die sogar strengere Umweltauflagen erfüllt, da sie in geschlossenen Beschichtungskammern ohne das Aufkommen von Abwässern erfolgt. Hierzu wurden Magnetron- und Ionenstrahl-Sputter-Experimente durchgeführt, welche pure Zink- und Zinklegierungsschichten lieferten. Anschließend wurden die erhaltenen Schichten in Hinblick auf ihre Morphologie, chemische Zusammensetzung, kristallographische Strukturen, mechanische Eigenschaften und Korrosionseigenschaften untersucht.

Morphologie und chemische Zusammensetzung: Die Beschichtungsexperimente zeigten, daß die Morphologie der gesputterten Zinkschichten sehr stark von den Sputterparametern abhängen. Als bestimmender Parameter kristallisierte sich die Substrathaltertemperatur heraus. Da Zink ein niedrig schmelzendes Metall mit hohem Dampfdruck ist, weichen die erhaltenen Strukturen von jenen, die durch die bekannten Strukturzonenmodelle für gesputterte Schichten vorhergesagt werden, ab. Abhängig von den anderen Sputterparametern wie Sputterleistung, Sputterart (DC/AC), Beschichtungsrate, rotierender oder statischer Substrathalter, die indirekt die Substrattemperatur beeinflussen, reichen die erhaltenen Morphologien von dichten kompakten Morphologien bis zu offenen, schwammartigen Strukturen. Mit steigender Substrattemperatur wird ein Anstieg der Korngröße und Porosität wahrgenommen. Bei hohen Beschichtungstemperaturen mit normalisierten Substrattemperaturen von $T_s/T_m > 0.5$ wurde sogar das Wachstum von whiskerartigen Strukturen beobachtet. Aufgrund der höheren Energie von gesputterten Teilchen weichen die erhaltenen Zinkbeschichtungen auch von jenen ab, die aus Verdampfungsprozessen erhalten werden. Die Entstehung dieser whiskerartigen Mikrostrukturen bei gesputterten Zink- und niedrig legierten Zinklegierungsschichten scheinen das Ergebnis eines Zusammenspiels von hoher Beschichtungstemperatur, niedrigem Schmelzpunkt des abgeschiedenen Zinks, Restgasen, niedriger Beschichtungsrate und der hohen kinetischen Energie der gesputterten, adsorbierten Atome zu sein.

Das Legieren mit Eisen, Titan, Chrom, Aluminium und Magnesium verändert die Strukturentwicklung der Beschichtungen. Bei höheren Legierungskonzentrationen wird eine Verdichtung mit Tendenz zu geringeren Korn- oder Säulengrößen beobachtet. Für die hoch legierten Zink-Eisen-Proben werden sogar bei erhöhten Substrattemperaturen keine Whisker mehr festgestellt. Die Phasenzusammensetzung vieler Zinklegierungsbeschichtungen, die in dieser Arbeit gesputtert wurden, weichen von denjenigen ab, die gemäß der Gleichgewichtsphasendiagramme erwartet werden. Viele von ihnen sind metastabile Strukturen und bestehen bei gegebener Zusammensetzung aus einphasigen, übersättigten Mischkristallen (Zn-Fe, Zn-Ti), obwohl die jeweiligen Gleichgewichtsphasendiagramme ein Zweiphasen-System und/oder die Bildung von Verbindungen bei dieser Zusammensetzung vorhersagen. Die Zink-Titan-Beschichtungen kondensieren zusätzlich in einer nanokristallinen/amorphen Struktur. Die Abweichung vom Gleichgewichtszustand kann durch die Tatsache erklärt werden, daß Sputtern eine Dampfabschreckungsmethode ist, die fernab vom thermodynamischen Gleichgewicht stattfindet. Die Bildung von metastabilen Strukturen durch Sputtern ist ein komplexes Zusammenspiel von Thermodynamik und Umwandlungskinetik. Viele Faktoren wie die Aktivierungsenergie für Selbstdiffusion, die Beschichtungsrate und die Beschichtungstemperaturen bestimmen die resultierende Struktur.

Die chemische Analyse mit XPS- und Auger-Spektroskopie zeigt, daß die gesputterten Zink- und Zinklegierungsschichten chemisch rein sind. Lediglich auf der Schichtoberfläche wurden Spuren von Kohlenstoff und Sauerstoff gefunden. Genauso wie Hinzulegieren führt auch der Ionenbeschuss sogar

bei erhöhten Temperaturen zu einer Verdichtung der Zink- und niedrig legierten Zinklegierungsschichten. Aufgrund der Ionendosis und des resultierenden Ionen-zu-Atomankunfts-Verhältnisses ist die Beschichtungsrate aufgrund von Resputtern reduziert. Zusätzlich kann eine Einlagerung von Argon in den Film beobachtet werden. Darüber hinaus verändert der Ionenbeschuss die kristallographische Struktur der Beschichtung, da er eine starke Textur in [002]-Richtung und eine Reduktion des Gitterabstandes in c-Richtung verursacht.

Die in Sauerstoff dotierten Argon-Sputtergas-Atmosphären durchgeführten Beschichtungsexperimente waren dazu gedacht, die Abhängigkeit des Auftretens von whiskerartigen Strukturen aufgrund der Sputtergas-Zusammensetzung zu untersuchen. Dabei wurde kein Zusammenhang festgestellt. Das Hinzumischen von Sauerstoff führte nicht zu einem verstärkten Whisker-Wachstum, nur größere Anteile von Zinkoxyden wurden in diesen Beschichtungen gemessen.

Kristallographische Struktur: Die Röntgenbeugungsspektren zeigten, daß die kristallographische Struktur und Zusammensetzung der gesputterten Schichten von mehreren Beschichtungsparametern abhängen: der Beschichtungstemperatur, dem Target-Legierungsgehalt, der Beschichtungsrate, der Sputterart. Entsprechend des Zusammenspiels dieser Parameter reichen die kristallographischen Strukturen und Zusammensetzungen von kristallinen, einphasigen Systemen (z.B. Zn) über kristalline, mehrphasige Systeme (z.B. Zn-Mg) bis zu röntgenamorphen Systemen (z.B. Zn-Ti). Im Gegensatz zur galvanisch beschichteten Referenzprobe mit zufälliger, hexagonaler Struktur zeigen die gesputterten Zinkschichten eine hexagonale Struktur mit Textur in [002]-Richtung. Diese Textur ist für Proben, die bei niedrigen Substrattemperaturen beschichtet wurden, besonders ausgeprägt. Die legierten Zinkbeschichtungen kondensierten in unbekannten metastabilen Phasen, deren Beugungsspektren mit keiner der für Zinklegierungsphasen in der JCPDS-Datenbank oder Literatur angegebenen Kristallstrukturen übereinstimmen. Aus diesem Grund wurden diese Kristallstrukturen, für die eine Abnahme des c/a-Verhältnisses beobachtet wird, versuchsweise simuliert. Beim Glühen wandelten sich alle metastabilen Phasen in bekannte, stabile Phasen um.

Mechanische Eigenschaften: Die Mikrohärtemessungen zeigten, daß die Vickers-Härten der Beschichtung durch die Legierungszusammensetzungen und Substrattemperaturen bestimmt sind. Für alle Zinklegierungsbeschichtungen führte ein Anstieg des Legierungsgehaltes zu einem Anstieg der Härte. Des weiteren wurde für Proben, die bei niedrigen Substrattemperaturen beschichtet wurden, höhere Härten gemessen als für solche, die bei hohen Temperaturen abgeschieden wurden.

Fast alle Beschichtungen zeigten sehr gute Haftung auf den Stahlsubstraten, wodurch sie für Standardumformprozesse und Klebefügungen in der Karrosseriemontage geeignet wären.

Korrosion: Die Gleichgewichts-Elektrodenpotential vs. Zeit-Versuche zeigten, daß das Legieren mit anderen Elementen das Startpotential in Richtung des Gleichgewichts-Elektrodenpotentials des Legierungselementes verschiebt. Das Potential wird negativer für unedlerere Elemente wie Al und Mg, während es für edlerere Fe, Ti und Cr ansteigt. Für alle gesputterten Beschichtungen, ob unlegiert oder legiert, scheint die normalisierte Lebensdauer von der Schichtmorphologie abzuhängen. Der Einfluß der Beschichtungstemperatur und der daraus resultierenden Schichtmorphologie auf die Standzeit kann für fast alle Beschichtungen beobachtet werden. Alle Proben, die bei einer Substrattemperatur von $+8\,°C$ beschichtet wurden, zeigen längere Standzeiten als jene Proben, die bei einer erhöhten, nicht konstanten Temperatur T_{float} im selben Los beschichtet wurden. Die am höchsten legierten Zink-Titan- und Zink-Chrom-Beschichtungen bieten nur für sehr kurze Standzeiten kathodischen Schutz, die offensichtlich kürzer sind als ihre eigentlichen Standzeiten. In diesen Fällen sind die Beschichtungen noch vorhanden. Da sie jedoch an edleren Komponenten wie Titan und Chrom durch Entzinkung angereichert oder durch deren Korrosionsprodukte bedeckt sind, erreichen sie sehr schnell Korrosionspotentiale, die höher als jenes von blankem Stahl sind.

Die **potentialdynamischen** Stromspannungsmessungen zeigten auch, daß das Zulegieren von Zink mit anderen Elementen das Korrosionspotential der legierten Beschichtungen in Richtung des Nor-

malpotentials des jeweiligen Legierungselementes verschiebt. Die Polarisierungsexperimente zeigten, daß Zinkvollmaterial nicht passiviert, wohingegen dünne Schichten auf Stahlsubstraten, ob feuerverzinkt, galvanisch beschichtet oder gesputtert, passivieren. Im Gegensatz zu den unlegierten Zinkschichten zeigen die legierten Zinkschichten ein anderes Passivierungsverhalten. Die höher legierten Schichten haben niedrigere kritische Stromdichten und Polarisationswiderstände, wohingegen die Korrosionsstromdichten mit dem Hinzulegieren nicht signifikant variieren. Die erhöhten Polarisationswiderstände deuten einen verbesserten Korrosionsschutz dieser Beschichtungen an.

Die Salzsprühtests lassen erkennen, daß fast alle gesputterten Schichten so gut oder sehr viel besser als die Referenzbeschichtungen sind. Genau wie in den Tauchprüfungen wurde auch hier der Einfluß der Beschichtungstemperatur und der Morphologie auf die Lebensdauer beobachtet. Alle Proben, die bei einer Substrattemperatur von $+8\,°C$ beschichtet wurden, zeigen längere Standzeiten als jene Proben, die bei einer erhöhten, nicht konstanten Temperatur T_{float} im selben Los beschichtet wurden. Desweiteren wurde eine signiftikante Verbesserung des Korrosionsverhaltens durch Hinzulegieren erzielt. Insbesondere bei den Zink-Chrom- und den Zink-Titan-Schichten wurde die Zeit bis zum Auftreten von Rotrost im Vergleich zur Referenzbeschichtung EZ um das 11fache verlängert. Im Gegensatz zu den anderen Beschichtungen war bei diesen Schichten das Volumen der entstehenden Korrosionsprodukte reduziert und die Proben erhielten ihr metallisches Erscheinungsbild. Diese Ergebnisse verdeutlichen, daß die mit Zinklegierungsschichten beschichteten Stahlbleche auch in Anwendungen verwendet werden könnten, bei denen unlackierte Stahlbleche erforderlich sind. Die anschließenden Röntgenbeugungsmessungen der Proben, die im Salzsprühtest getestet wurden, erklären den guten Korrosionsschutz der legierten Beschichtungen. Die Messungen zeigten, daß es einen Zusammenhang zwischen den gebildeten Korrosionsprodukten, deren Korrosionsschutz und der resultierenden Lebensdauer gibt: Beschichtungen, die Korrosionsprodukte mit höherem Simonkolleite und Zinkcarbonathydroxid-Anteilen liefern, bieten besseren Korrosionsschutz und damit längere Standzeiten.

Der Korrosionstest VDA 621-415 mit zyklisch wechselnder Beanspruchung, der an Zink-Eisen-beschichteten Stahlblechen durchgeführt wurde, zeigte, daß die Zink-Eisen-Filme besseren kathodischen Schutz gewähren als die reine Zink-Referenzschicht EZ. Bei gleicher Schichtdichte ist die Breite der Unterrostungszone um 25 % verringert. Ein Nachteil der Zink-Eisen-Beschichtungen ist jedoch das Auftreten von aus der Schicht stammendem Rotrost, der die Akzeptanz dieser Schichten durch die Kunden und damit der Automobilindustrie gefährdet.

Zusammenfassend lässt sich festhalten, daß Sputtern eine interessante alternative Beschichtungsmethode darstellt. Die erhaltenen Beschichtungen zeigen gleichwertige oder bessere Eigenschaften als die konventionell beschichteten. Insbesondere die Zinklegierungsschichten zeigen erfolgsversprechende Perspektiven aufgrund ihres deutlich verbesserten Korrosionsverhaltens. Allerdings könnten die in heutigen Inline-Beschichtungsprozessen benötigten Beschichtungsraten und die damit verbundene Freisetzung von Kondensationswärme ein Problem für die Schichtmorphologie darstellen. Da Zink ein niedrig schmelzendes Metall mit hohem Dampfdruck ist und sein Schichtwachstum beim Sputterprozess sehr empfindlich auf die Substrattemperatur reagiert, würde ein industrieller Beschichtungsprozess eine ausreichende Kühlung der Stahlbleche im Vakuum erfordern. Dies setzt weitere Entwicklungen für den Bau solcher Beschichtungsanlagen voraus. Weitere Untersuchungen könnten sich mit der Frage beschäftigen, ob das Korrosionsverhalten und andere Schichteigenschaften durch eine Wärmebehandlung der Beschichtung verbessert werden könnte. Die Ergebnisse aus Laborversuchen bezüglich des Korrosionsverhaltens sollten außerdem in Feldversuchen bestätigt werden. Dies würde zusätzlich die Untersuchung von verschiedensten Umwelteinflüssen und anderen korrosionsbestimmenden Faktoren während des Betriebes eines Fahrzeuges erlauben. Letztendlich könnte der Gebrauch von Zinklegierungsbeschichteten Stahlblechen im unlackierten Zustand auch für andere Anwendungen als die der Automobilindustrie ins Auge gefasst werden.

Contents

List of Abbreviations

AES	Auger Electron Spectroscopy
ASS	Amorphous super saturated solid solution
ASTM	American Society of Mechanical Engineers
BSE	Back Scattered Electrons
CCD	Charge Coupled Device
CRT	Cathode Ray Tube
CSS	Crystalline super saturated solution
DC	Direct Current
DIBS	Dual Ion Beam Sputtering
DIN	Deutsches Institut für Normung
EDX	Energy Dispersive X-ray Analysis
EN	European Norm
ESCA	Electron Spectroscopy for Chemical Analysis
EZ	Electro deposited zinc coating
FWHM	Full Width at Half Maximum
GIAB	Grazing Incidence Asymmetric Bragg
IBAD	Ion Beam Assisted Deposition
IBS	Ion Beam Sputtering
ISO	International Organization for Standardization
JCDPS	Joint Commitee on Powder Diffraction Standards
OCP	Open Circuit Potential
PV	Peak to Valley
PVD	Physical Vapour Deposition
RF	Radio Frequency
SCE	Standard Calomel Electrode
SE	Secondary Electrons
SEM	Scanning Electron Microscope
SST	Salt Spray Test
SZM	Structure Zone Model
TF	Texture Fraction
UHV	Ultra High Vacuum
VDA	Verband der Automobilindustrie e.V.
WDX	Wavelength Dispersive X-ray Spectroscopy
XPS	X-ray Photoelektron Spectroscopy
XRD	X-ray Diffraction Analysis
ZF	Galvanealed zinc coating

Chapter 1

Introduction and State of the Art

1.1 Corrosion of Metals

The European standard EN ISO 8044 [1] defines the term corrosion as "physicochemical interaction between a metal and its environment that results in changes in the properties of the metal, and which may lead to significant impairment of the function of the metal, the environment, or the technical system, of which these form a part".

Studies undertaken by several countries including the United States, the United Kingdom, Japan, Australia, Kuwait, Germany, Finland, Sweden, India, and China have shown the economic consequences of metallic corrosion to be very serious. The common finding of these studies was that the annual corrosion costs ranged from approximately 1 to 5 percent of the Gross National Product of each nation. The total costs of corrosion include not only direct costs but also considerable indirect costs. These are estimated to be equal to the direct costs and cover lost time, and thus lost productivity because of outages, delays, failures, and litigation. [2–4]

1.1.1 Electrochemical Corrosion

Although atmospheric air is the most common environment, aqueous solutions and thin aqueous layers are, due to their electrical conductivity, the environments most associated with corrosion problems. The corrosion of metals in aqueous environments is almost always an electrochemical or electrolytic process. If a metal is immersed in an ion containing solution it adopts a potential caused by the charge exchange across the solid/liquid interface. The metal and electrolyte together are electrically neutral, and no measurable external current flows from or to the electrode unless an external voltage is applied. As soon as a second metal/solution system, with a different potential, is connected via an external wire or the metals themselves electrons flow from one system to the other. A self driving galvanic cell is created and one is able to measure a potential difference and a flowing current between the systems. The current flow is driven by the dissolution of the metal in one half cell and the discharge of ions in the other half cell. It is a redox reaction with a cathodic reaction and an anodic reaction which requires electrical contact and a continuous ionic path (i.e. electrolyte) between both half cells. Figure 1.1 shows as an example the schematic of corroding iron. In an ionic conducting phase as an aqueous solution there are three typical anodic oxidation half cell reactions. All of them oxidise a metal atom M in the solid state and transfer it into a charged metallic ion according to Eq. (1.1 - 1.3):
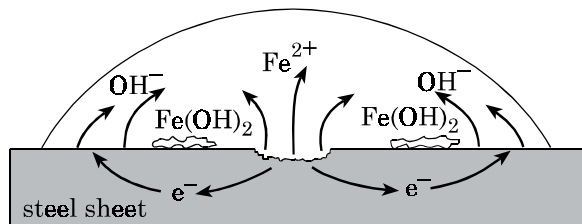
Figure 1.1: Schematic of corroding iron: Creation of an electrochemical cell on the surface

$$M_{(s)} \quad \rightarrow \quad M^{n+}_{(aq)} + ne^-_{(s)} \tag{1.1}$$

$$M_{(s)} + nH_2O_{(aq)} \quad \rightarrow \quad M(OH)_{n(s)} + nH^+_{(aq)} + ne^-_{(s)} \tag{1.2}$$

$$M_{(s)} + nH_2O_{(aq)} \quad \rightarrow \quad MO^{n+}_{n(aq)} + 2nH^-_{(aq)} + ne^-_{(s)} \tag{1.3}$$
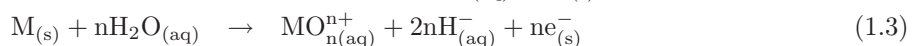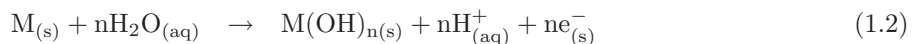
where n describes the number of electrons transferred from the valence electron shell of the metal in each half reaction and also represents the charge of the metallic cation in the first reaction.

In aqueous systems the cathodic reduction reactions involve the reduction of oxygen, protons and water. These reactions which consume electrons are dependent on the pH–value of the media. The following reactions given in Eq. occur frequently:

$$2H^+_{(aq)} + 2e^- \quad \rightarrow \quad H_{2(g)} \quad \text{hydrogen ion reduction in strong acidic media pH} \leq 4 \tag{1.4}$$

$$O_{2(g)} + 4H^+_{(aq)} + 4e^- \quad \rightarrow \quad 2H_2O_{(aq)} \quad \text{reduction of dissolved oxygen in low acidic media} \tag{1.5}$$

$$O_{2(g)} + 2H_2O_{(aq)} + 4e^- \quad \rightarrow \quad 4OH^-_{(aq)} \text{ reduction of dissolved } O_2 \text{ in neutral or alkaline media} \tag{1.6}$$

$$2H_2O_{(aq)} + 2e^- \quad \rightarrow \quad H_{2(g)} + 2OH^-_{(aq)} \quad \text{dissolution of water} \tag{1.7}$$
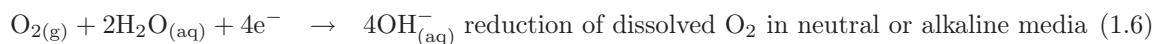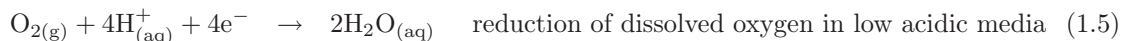
Apart from these reactions also other cathodic reactions are possible, including the reduction of metallic species in solution, e.g. $Fe^{3+} + e^- = Fe^{2+}$.

The driving force for redox reactions of the form $\sum_{ox} \nu_{ox} S_{ox} + ne^- \rightleftharpoons \sum_{red} \nu_{red} S_{red}$ to occur is the change in free energy ΔG given as

$$\Delta G = \Delta G^0 + RT \ln K_a \quad \text{with} \quad K_a = \frac{\prod a^{\nu_{ox}}_{ox} \cdot a^n_{e^-}}{\prod a^{\nu_{red}}_{red}} \tag{1.8}$$

where R is the Rydberg constant, T the absolute temperature and a the activities of the species participating in the reactions.

If an electrochemical cell is created, where both half reactions occur in two separated cells and these cells operate at equilibrium under thermodynamically reversible conditions, the energy dissipated by an infinitesimal passage of charge $(I \rightarrow 0)$ is given as:

$$\Delta G + \Delta W_{electr.} = 0 \tag{1.9}$$

$$\Delta G = -Q \cdot \Delta E = -nF \cdot \Delta E \tag{1.10}$$

$$\Delta G = -nF \cdot [(E_e)_{cathode} - (E_e)_{anode}] \tag{1.11}$$

where $\Delta W_{electr.}$ is the electric energy needed for the transport of the charge Q, ΔE is the potential difference between the equilibrium potentials of the oxidation and reduction reactions, n is the number of electrons per atom of the species involved in the reaction, F the Faraday constant, i.e. the charge of 1 mole of electrons and E_e the equilibrium potentials of the respective reactions. The equilibrium

potentials E_e of each reaction can be determined by the Nernst equation:

$$E_e = E_0 + \frac{RT}{nF} \ln K_a \tag{1.12}$$

The equation shows that the thermodynamic feasibility of the overall reaction is determined by the potential difference ΔE between the equilibrium potentials of the oxidation and reduction reactions. To make the oxidation reaction occur the change in free energy ΔG must be negative. This requirement is fulfilled for

$$(E_e)_{anode} < (E_e)_{cathode} \tag{1.13}$$

where E_0 is the standard potential of the respective reaction. The potential difference ΔE shows the general thermodynamic feasibility of a corrosion reaction, but it gives no information about the oxidation and cathodic reduction rates, which are affected by a variety of factors.

1.1.1.1 Electrochemical Polarisation

The equilibrium potential E_e determined by the Nernst equation describes the thermodynamic equilibrium of the respective anodic or cathodic reaction. At this potential no measurable material conversion takes place. By applying an external current or by coupling with another reaction the potential of the reaction is moved out of equilibrium. Electrochemical testing uses an external power source to apply a voltage (potentiostatic measurement), or current (galvanostatic measurement) to force an imbalance between the cathodic and anodic sites, thus causing electrons to flow and re-establish charge neutrality. The resulting current (or voltage) is measured and plotted versus the voltage (or current) in a so called current–potential or polarisation curve. Figure 1.2 shows an example of an anodic polarisation curve for the oxidation reaction $Me \rightleftharpoons Me^{n+} + ne^-$.
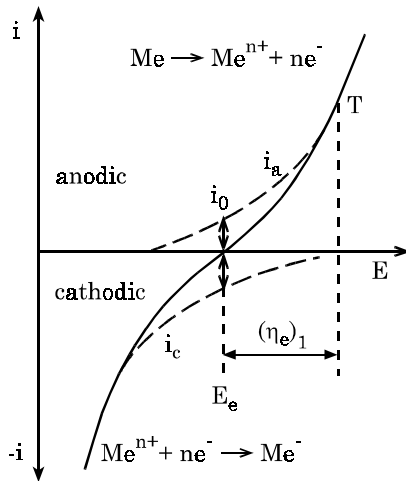
Figure 1.2: Anodic polarisation curve for the metal dissolution reaction $Me \rightleftharpoons Me^{n+} + ne^-$

This polarisation curve follows the Butler-Volmer equation which describes the overall current of the anodic and cathodic reaction.

$$i = i_o \times \left\{ e^{\left(\beta \frac{nF}{RT} \eta \right)} - e^{\left(-(1-\beta) \frac{nF}{RT} \eta \right)} \right\} \tag{1.14}$$

where

i : external current
i_0 : corrosion current at E_e
β : symmetry coefficient ($0 \leq \beta \leq 1$)
η : overpotential

The currents of the anodic reaction (oxidation) are positive, those of the cathodic reaction (reduction) negative. The overpotential η is a measure of how far the reaction is from equilibrium. It is defined as the difference $\eta = E - E_e$ between the applied voltage E and the equilibrium voltage E_e. At equilibrium where $E = E_e$ and $\eta = 0$, no current is measured ($i_a = -i_c = i_0$). The metal dissolution i_a equals the metal cation deposition $-i_c$. If the potential is made more positive, more anodic than E_e, metal dissolution proceeds since $i_a \geq |i_c|$. For potentials lower than E_e metal deposition proceeds since $i_a \leq |i_c|$. Over a small potential range the two reactions oppose each other. However for sufficiently large overpotentials one reaction becomes negligible and the overpotential is in the so called Tafel region. Point T in Fig. 1.2

indicates the begining of the Tafel region for the anodic process where the last term of the Butler-Volmer equation can be neglected and the metal dissolution current density is given by the Tafel equation:

$$i_a = i_0 \, e^{\beta \, \frac{nF}{RT} \, \eta} \tag{1.15}$$

In the same manner as for the anodic reaction the analysis can also be made for a reduction reaction $O + ne^- \rightleftharpoons R$ occurring at the cathode.

1.1.1.1.1   Mixed Potential Theory   A corroding metal can be regarded as an accumulation of cathodic and anodic sites which are electrically connected by the metal itself. A schematic of an electrochemical cell, created on an iron surface has already been shown in Fig. 1.1. On the surface of a freely corroding metal the anodic current, flowing due to the metal dissolution $Me \rightleftharpoons Me^{n+} + ne^-$, must be counterbalanced by a cathodic current created by the reduction reaction $O + ne^- \rightleftharpoons R$. The basis for the mixed potential theory is the idea that the cathodic and anodic reactions take place in fast changing, statistically migrating anodic and cathodic areas on the surface of the corroding metal. Due to this fact a mixed potential, lying in between the anodic and cathodic rest potential, is created on the entire metal surface. The coupling of anodic and cathodic reactions and the resulting polarisation curves for the corrosion in acidic, oxygen free or alternatively neutral, oxygen containing solutions can be seen in Fig. 1.3 and Fig. 1.4. The condition where $i_a + i_c = 0$ is achieved only at an unique potential, i.e. the
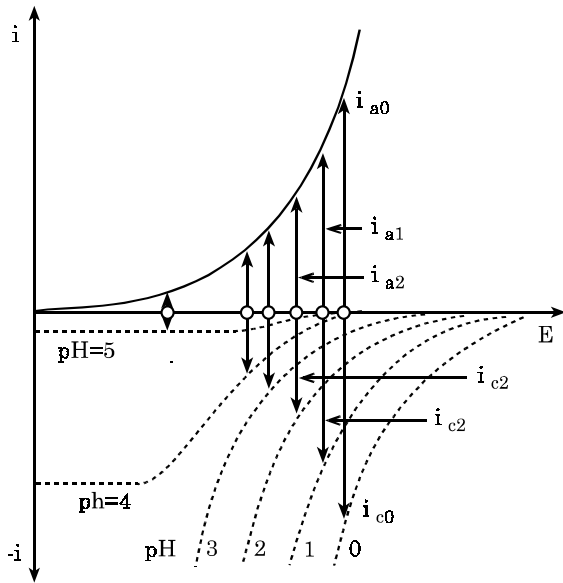
Figure 1.3: Current potential curves for acidic corrosion according to the mixed potential theory [5]
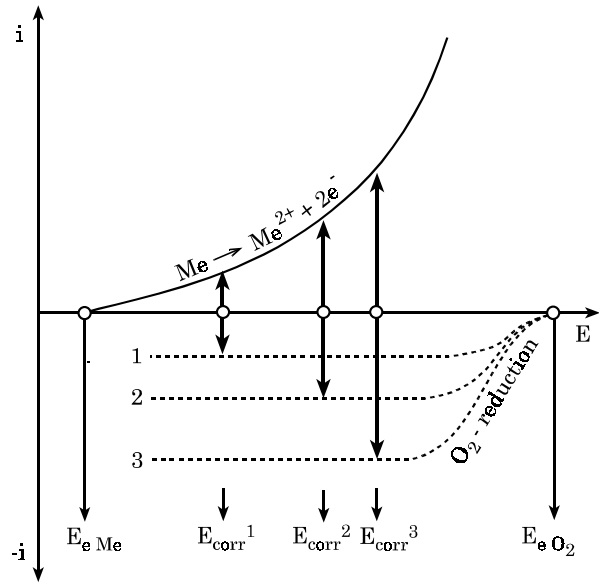
Figure 1.4: Current potential curves for oxygen corrosion according to the mixed potential theory [5]

corrosion potential E_{corr} which must lie between the two equilibrium potentials of the single reactions.

$$(E_e)_a < E_{corr} < (E_e)_c \tag{1.16}$$

The individual reactions on their part are driven by overpotentials such as the anodic activation overpotential $\eta_a^A = E_{corr} - (E_e)_a$ which drives the dissolution of the metal and the cathodic activation overpotential $\eta_c^A = E_{corr} - (E_e)_c$ which drives the cathodic reaction.

1.1.1.1.2   Local Cell Theory   In contrast to the mixed potential theory the idea of the local cell theory is that the anodic and cathodic areas are macroscopically or microscopically fixed at certain positions of the corroding system. The local-cell theory can be explained by contact corrosion. Contact

corrosion occurs if two metals A and C with different corrosion potentials E_{ea} and E_{ec} are immersed in an aqueous solution and are electrically connected. A schematic of a local cell which is created by a steel sheet (iron) with a porous zinc layer on top can be seen in Fig. 1.5. Figure 1.6 shows the polarisation curves of such a local cell. Due to the resistance of the electrolyte no complete potential balance is

Figure 1.5: zinc–iron local cell

Figure 1.6: Current potential curves for a contact corrosion reaction [5]

achieved. Only an approximation of the potentials to the contact corrosion potentials $(E_{corr})_a$ and $(E_{corr})_c$ takes place where the anodic and cathodic currents are equal. The more noble metal C tends to be the preferred cathode, where the reduction of the oxidant, e.g. the evolution of hydrogen, takes place. The less noble metal A on the other hand tends to be the anode. The latter is anodically oxidised, an increased dissolution takes place and the created ions are hydrated with water molecules. As a result the corrosion of the less noble metal is accelerated and the corrosion of the more noble metal is slowed down. Apart from the macroscopic local cell there are a lot of corrosion effects which are caused by microscopic local cells. The reasons for the development of local cells are heterogeneities in the metal, on the metal surface, the liquid phase and those differences which are caused by physical conditions. Examples of such heterogeneities and the corresponding local cells are [5,6]:

- Dissimilar electrode cells: differences in surface composition, presence of alloying elements, enrichment of alloying elements at the grain boundaries, different phases within the metal e.g. ferrite-cementite, porous metal coating e.g. zinc on iron

- Deformation cells: mechanical stresses in metals, cold worked metals, identical metals with different grain sizes

- Grains with different orientations and resulting thereof dissolution rates: single phase materials with random or preferred, textured grain structure

- Concentration cells: different compositions of the attacking media

- Differential aeration cells: differences in oxygen replenishment on the metal surface

- Differences in flow velocity of the corrosive media

- Differential temperature cells: temperature gradients along the length of the corroding surface

The electrochemical cells lead to locally limited zones of attack and thus uneven metal removal on the metal surface. The corrosion rate depends in these cases on the sizes of the cathodic and anodic areas. With decreasing area the length of the ionic path within the electrolyte diminishes, the corrosion current increases and resulting the corrosion rate is raised. This type of non uniform corrosion is called pitting corrosion.

For the development of a galvanic element the electrical conductivity of the aqueous solution is very important. The conductivity is increased by dissolved salts which themselves are not involved in the corrosion reaction. In the same manner the corrosion rate of unalloyed steels in salt solutions is affected by the oxygen content of the solution but not by the salt content itself. Nevertheless many dissolved salts have a strong indirect effect on local corrosion processes, e.g. chloride ions stimulate the dissolution of iron by enrichment at local anodes and hinder the development of protective layers.

1.1.1.2   Passivation

Some metals and alloys show a natural corrosion resistance. They behave in a much more noble fashion than would be expected from their position in the electromotive force series. They resist oxidation. With anodic dissolution these materials create a surface layer of metal oxides, sometimes salts, which are almost without pores, and isolate the material from the environment. All further reactions on the metal surface are hindered, thus no oxidation takes place anymore. The metal is passivated.

In case of a passivating material the shape of the polarisation curve is different from a non passivating material. Figure 1.7 shows the schematic polarisation curve for the anodic process of a passivating metal / metal ion system, which can be divided in two regions: the active and the passive region. The active region starts at the corrosion potential E_{corr}. Here the metal dissolution occurs unimpeded by the presence of surface films. The anodic current i_a should conform to the Tafel equation (Eq. 1.15). At potential E_{pass}, which is close to the equilibrium potential $((E_e)_{M/MO})$ of the metal and one of its oxides/hydroxides, the anodic current deviates from the Tafel relationship. The anode undergoes a so called active–passive transition where i_a drops significantly to the passive value i_{pass}. The thermodynamic requirement for this passivation is $E > (E_e)_{M/MO}$. The maximum current density achieved immediately before transition is called i_{crit}. It can be considered as the current density required to generate a sufficiently high surface concentration of metal cations such that the nucleation and growth of the surface film can proceed. For potentials $E > E_a$ the metal is in the passive region, the current is independent of potential, and the metal dissolution occurs at a constant rate. The subsequent curve shape of the polarisation curve depends on the particular metal and the properties of the created passive layers. For some metals such as Fe and Ni at the break through potential E_{b1} a steep increase of the current density curve occurs (curve 1). On the outside of the oxide film oxygen evolution takes place, requiring that the created film is electronically conductive. This precondition is met since the formed films are very thin (nanometer range) and possess semiconducting or even metallic properties. For some metals such as chromium or chromium containing alloys the increase of the current density (curve 2) occurs already at the break through potential E_{b2}. The created oxide film starts to dissolve oxidatively, generally as a hydrolysed cation in a higher oxidation state, e.g. a passive Cr_2O_3-film on chromium with chromium in the $+3$ state dissolutes to chromate CrO_4^{2-} with chromium in the $+6$ state. This anodic reaction is subject to passivation once again starting at the trans passivation potential E_{tp}. This phenomenon of transpassivity is depicted by curve 2. With further increase of E a new increase of the current density occurs as oxygen evolution takes place. For ion conducting passive layers the passage of charge is hindered and no further electrode reactions take place (curve 3).
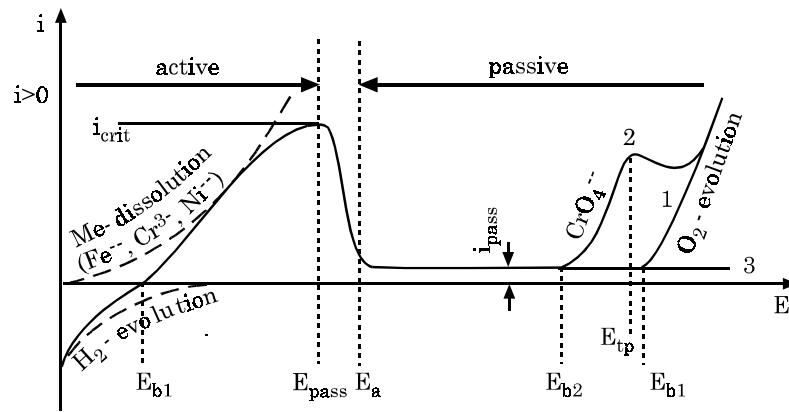
Figure 1.7: Polarisation curve of a passivating metal/metal ion system [5]

1.1.1.3 Types of Corrosion

There are generally five types of corrosion attacks that can be distinguished.

1. **Uniform attack**
   As the name suggests this is the uniform loss of metal with time. It is the idealised form of corrosion which can be explained by the mixed potential theory [5–7].

2. **Non uniform corrosion**
   The mechanisms of the non uniform corrosion can be depicted with the local cell theory and the different types of local cells already described in par. 1.1.1.1.2 above. It usually results from a small anode-large cathode combination and is the major cause of car body corrosion. Based on the local cell types created the following sub types of non uniform corrosion exist [5–8]:

   - Pitting corrosion due to the formation of aeration or concentration cells: different supply of oxidants or specific ions, e.g. chloride
   - Selective corrosion: leaching due to the formation of dissimilar electrode cells, e.g. loss of zinc out of brass (dezincification or parting), spongiosis of cast iron
   - Intergranular corrosion: special case of selective corrosion localised at the grain boundaries of the metal. In this case the grains act as cathodes while the grain boundary is the anode.

3. **Stress corrosion or corrosion fatigue**
   Corrosion phenomenon caused by electrochemical attack in corrosive media and simultaneous mechanical loading, i.e. tensile stresses or vibrations [5–8].

4. **Erosion and cavitation corrosion**
   Erosion corrosion can be found in liquids with high flow velocities. It is the result of simultaneous corrosion and erosion of the corrosive media. Cavitation corrosion is caused by the mechanical impact of imploding gas bubbles generated by a decay of pressure in fast flowing media. The imploding gas bubbles dislodge soft or brittle constituents from the surface [5, 8].

5. **Wear corrosion**
   This type of corrosive attack is caused by the simultaneous effect of abrasion and corrosion [5].

1.1.2 Corrosion of Iron and Zinc

1.1.2.1 Corrosion of Iron

It is an inescapable fact that iron, the major component of steel, in the presence of oxygen and/or water, is thermodynamically unstable with respect to its oxides. The overall reaction is spontaneous. The Gibbs energy of the system is lowered as the reaction proceeds. The free enthalpies of the oxidation reactions for

iron are $\Delta G_{298}^0(\text{Fe}\,/\,\text{FeO}) = -245.1\,\text{kJ/mol}$, $\Delta G_{298}^0(\text{Fe}\,/\,\text{Fe}_2\text{O}_3) = -742.2\,\text{kJ/mol}$ and $\Delta G_{298}^0(\text{Fe}\,/\,\text{Fe}_3\text{O}_4) =$ -1015.5 kJ/mol [9].

The standard potential for the dissolution reaction $\text{Fe}^{2+}_{(\text{aq})} + 2\text{e}^- \rightleftharpoons \text{Fe}_{(\text{s})}$ is –0.44 V_{SHE}, while that of the reaction $\text{Fe}^{3+}_{(\text{aq})} + \text{e}^- \rightleftharpoons \text{Fe}^{2+}_{(\text{aq})}$ is –0.771 V_{SHE} [8]. The standard potential of electrochemical reactions is measured versus a standard hydrogen electrode denoted by the unit V_{SHE}. The arbitrary choosen standard hydrogen electrode is built up by a platinum sheet, which is dipped at 25 °C into a solution with a hydrogen ion activity of one (hydrocloric acid solution $c_{\text{HCl}}= 1.153\,\text{mol/l}$) and contemporary washed around by gaseous hydrogen at a pressure of 101325 Pa.

The corrosion of iron in an aerated, neutral, aqueous sodium chloride solution proceeds by the formation of hydrated oxides. The half cell reactions [10] can be expressed as

$$
\begin{array}{llrcll}
\text{Anodic reactions a1} & & \text{Fe} + 2\text{H}_2\text{O} & \rightarrow & \text{Fe(OH)}_2 + 2\text{H}^+ + 2\text{e}^- & (1.17) \\
\text{a2} & & \text{Fe} + 3\text{H}_2\text{O} & \rightarrow & \text{Fe(OH)}_3 + 3\text{H}^+ + 3\text{e}^- & (1.18)
\end{array}
$$

$$
\begin{array}{llrcll}
\text{Cathodic reactions c1} & & 2\text{H}_2\text{O} + 2\text{e}^- & \rightarrow & 2\text{OH}^- + \text{H}_2 & (1.19) \\
\text{c2} & \text{O}_2 + & 2\text{H}_2\text{O} + 4\text{e}^- & \rightarrow & 4\text{OH}^- & (1.20) \\
\text{c3} & \text{O}_2 + & 2\text{H}^+ + 2\text{e}^- & \rightarrow & \text{H}_2\text{O}_2 & (1.21) \\
\text{c4} & & 2\text{H}^+ + 2\text{e}^- & \rightarrow & \text{H}_2 & (1.22)
\end{array}
$$

$$
\begin{array}{llrcll}
\text{Overall reactions 1} & & \text{Fe} + 2\text{H}_2\text{O} & \rightarrow & \text{Fe(OH)}_2 + \text{H}_2 & (1.23) \\
\text{1'} & 2\text{Fe} + \dfrac{1}{2}\text{O}_2 + & \text{H}_2\text{O} & \rightarrow & \text{Fe(OH)}_2 & (1.24) \\
\text{2} & & 2\text{Fe} + 6\text{H}_2\text{O} & \rightarrow & 2\text{Fe(OH)}_3 + 3\text{H}_2 & (1.25) \\
\text{2'} & 2\text{Fe} + \dfrac{3}{2}\text{O}_2 + & 3\text{H}_2\text{O} & \rightarrow & 2\text{Fe(OH)}_3 & (1.26) \\
\text{Further reaction} & & \text{Fe(OH)}_3 & \rightarrow & \text{FeO(OH)} + \text{H}_2\text{O} & (1.27)
\end{array}
$$

In a metal water system, many different chemical and electrochemical reactions may occur: the dissolution of the metal as a metallic cation or as a complex anion, the change of state of oxidation of the metallic ions, direct oxidation of the metal to an oxide or hydroxide, change of the oxidation state of the oxide, precipitation of ions into oxides or hydroxides, reduction and oxidation of water, etc. The thermodynamic equilibrium conditions of metals in electrochemical reactions, calculated according to the Nernst equilibrium equations, can be graphically displayed in potential-pH equilibrium diagrams according to Pourbaix. The Pourbaix diagram of the iron-water system is displayed in Fig. 1.8.

Line a.) represents the equilibrium for the reaction

$$\text{O}_{2(\text{g})} + 4\text{H}^+_{(\text{aq})} + 4\text{e}^- \rightleftharpoons 2\text{H}_2\text{O}_{(\text{aq})} \tag{1.28}$$

whose equilibrium potential according to the Nernst equation at standard condition is given by

$$E_a = E_a^0 + \frac{0,059}{4} \lg p_{\text{O}_2} \cdot \left[\text{H}^+\right]^4 \tag{1.29}$$

For the prerequisite that $p_{\text{O}_2} = 1$ bar E_a is given as $E_a = 1.228 - 0.059\,\text{pH}$.

In the same manner line b.) indicates the equilibrium for the reaction

$$2\text{H}^+_{(\text{aq})} + 2\text{e}^- \rightleftharpoons \text{H}_2 \tag{1.30}$$

whose equilibrium potential E_b at $p_{\text{H}_2} = 1$ bar is given as $E_b = 0 - 0.059\,\text{pH}$.

Figure 1.9 shows the theoretical conditions of the Pourbaix diagram where iron corrodes, is immune or passivates.
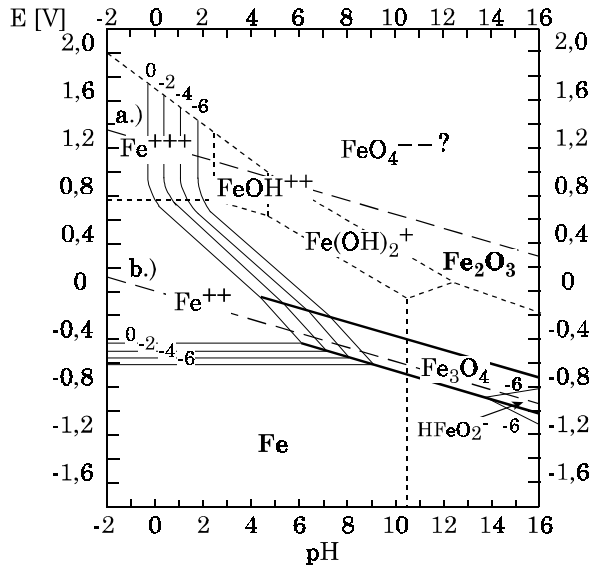
Figure 1.8: Potential-pH equilibrium diagram for the system iron water, at 25 ℃ [11]
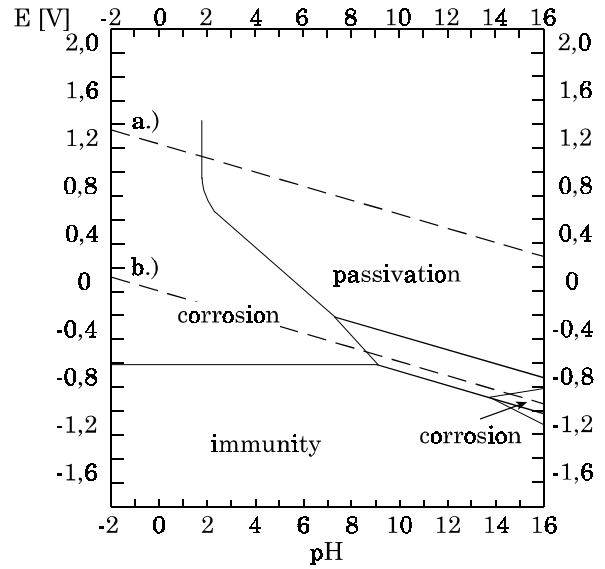
Figure 1.9: Theoretical conditions for corrosion, immunity and passivation of iron, at 25 ℃ [11]

The influence of the H^+ ion concentration, expressed as pH of the electrolyte solution, on the corrosion rate of iron is shown in Fig. 1.10.
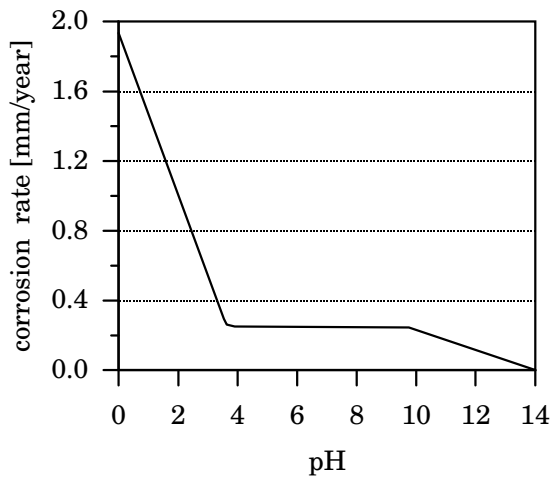
Figure 1.10: Effect of pH value on the corrosion rate of iron [6]

Actually the various oxides and hydroxides of iron form a rather complicated system of compounds. The term rust is a collective term for the mixture of oxide and hydroxides. The compound FeO(OH) exists in three different forms $\alpha-, \beta-, \gamma-$FeO(OH) plus an amorphous form. The red rust which is created by corrosion of iron in humid air consists of $\gamma-$FeO(OH) called lepidocrite. The hydrated oxides can lose water during dry periods and revert to the anhydrous ferrous and ferric oxides. In addition, a layer of magnetite (Fe_3O_4 or $FeO \cdot Fe_2O_3$) often forms between iron oxide (FeO) and haematite (Fe_2O_3). The occurrence of the various oxide species is dependent on pH, oxygen availability, various pollutants, and the composition of the steel.

1.1.2.2 Corrosion of Zinc

In the same manner as iron also zinc is thermodynamically not stable in the presence of oxygen and/or water and is easily oxidised. Its Gibbs free energies are $\Delta G_{298}^0(\text{Zn} / \text{ZnO}) = 318.3\,{}^{\text{kJ}}/_{\text{mol}}$ and $\Delta G_{298}^0(\text{Zn} / \text{ZnO}_2) = 1022.6\,{}^{\text{kJ}}/_{\text{mol}}$. The standard potential for the dissolution reaction of zinc $\text{Zn}_{(aq)}^{2+} + 2e^- \rightleftharpoons \text{Zn}_{(s)}$ is -$0.763\,V_{\text{SHE}}$ [8]. Depending on the pH of the aqueous electrolyte the corrosion of zinc proceeds under evolution of hydrogen or the reduction of oxygen [12]. The occurring reactions are:

$$\text{Anodic reactions a1} \qquad \text{Zn} \quad \rightarrow \quad \text{Zn}^{2+} + 2e^- \tag{1.31}$$

$$\text{Cathodic reactions c1} \qquad 2H^+ + 2e^- \quad \rightarrow \quad H_2 \tag{1.32}$$

$$\text{c2} \qquad O_2 + 4H^+ + 4e^- \quad \rightarrow \quad 2H_2O \tag{1.33}$$

$$\text{Overall reactions} \qquad \text{Zn} + H_2O \quad \rightarrow \quad \text{ZnO} + 2H^+ + 2e^- \tag{1.34}$$

$$\text{Zn} + H_2O \quad \rightarrow \quad \text{ZnO}_2^{2-} + 4H^+ + 2e^- \tag{1.35}$$
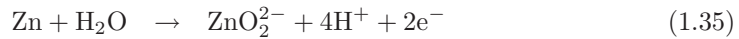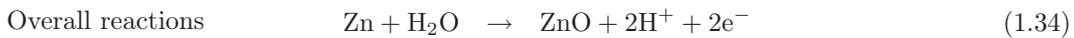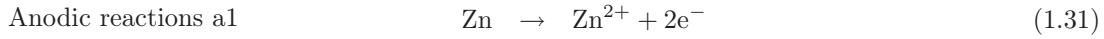
The Pourbaix diagram Fig. 1.11 shows the thermodynamic instability of zinc in water or aqueous solutions [11, 13]. Below line a) zinc tends to dissolve under evolution of hydrogen over the whole pH–
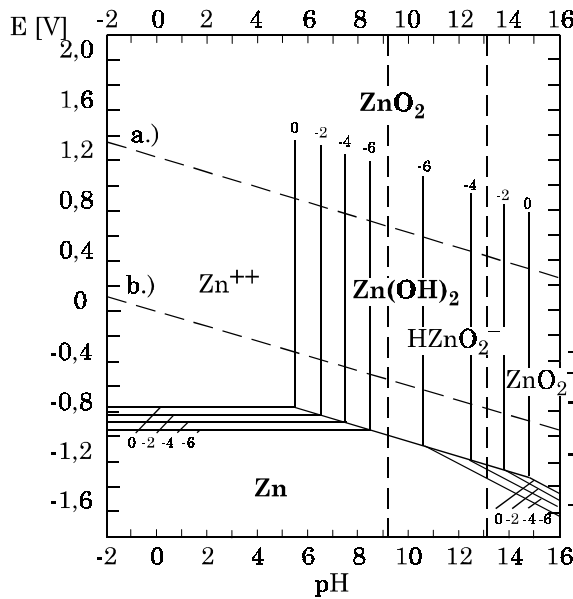
Figure 1.11: Potential-pH equilibrium diagram for the system zinc–water at 25 ℃ after Pourbaix [11]
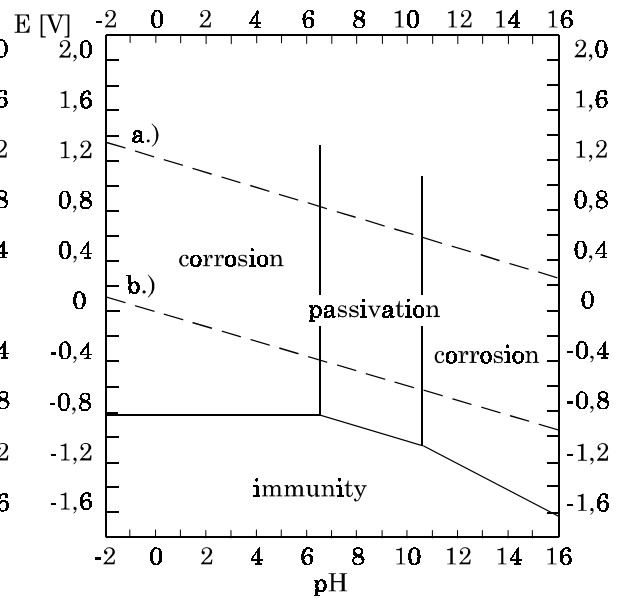
Figure 1.12: Theoretical reaction behaviour of zinc in water [11]

range. In the acidic range Zn^{2+}–ions are produced, in the neutral region the stable Zn(OH)_2 is formed and for alkaline solutions HZnO_2^- or ZnO_2^{2-} ions go in solution. This diagram is valid only in case that these species, with which zinc can form soluble complexes or insoluble compounds, are not present in the solution. Deduced from Fig. 1.11 it is possible to determine the theoretical conditions where zinc corrodes, passivates or is immune. These conditions are shown in Fig. 1.12.

The Pourbaix diagram shows that zinc is an amphoteric material that corrodes in acidic and alkaline solutions. Therefore the H^+ ion concentration has a significant effect on the corrosion rate of zinc. The influence of the H^+ ion concentration of the electrolyte solution expressed as pH is shown in Fig. 1.13.

The good corrosion resistance in aqueous solutions, distinguishing zinc from iron, depends on the initial ability to form a protective layer. Therefore the corrosion in distilled water is much more severe then
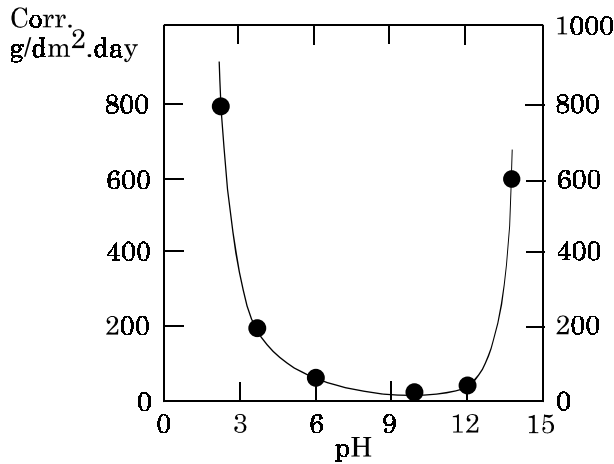
Figure 1.13: Effect of pH value on the corrosion rate of zinc [11]

in solutions containing scale forming salts. With many chemical agents it forms insoluble compounds. The most common compounds found in corrosion products are zinc oxides and hydroxides (ZnO, $\varepsilon-\mathrm{Zn(OH)_2}$), carbonates ($\mathrm{Zn_5(CO_3)_2(OH)_6}$), chlorides ($\mathrm{Zn_5Cl_2(OH)_8 \cdot H_2O}$), sulfates ($\mathrm{Zn_4SO_4(OH)_6 \cdot nH_2O}$ and $\mathrm{ZnSO_4 \cdot nH_2O}$) and chlorosulfates ($\mathrm{NaZn_4Cl(OH)_6SO_4 \cdot 6H_2O}$ and $\mathrm{Zn_4Cl_2(OH)_4SO_4 \cdot 5H_2O}$) [14, 15]. The stability, composition and compactness of these compounds affect the corrosion resistance of zinc in many environments. In a chloride containing solution, different zinc chloride compounds are formed. The type of compound formed varies with the pH of the solution as can be seen in Fig. 1.14.

The stability of pure zinc depends not only on the pH of the solution but also the stability of zinc oxides and zinc hydroxides. In solutions with a pH between approximately 8,5 and 12 zinc can be covered with a hydroxide film which inhibits the further zinc dissolution. The solubility of $\varepsilon-\mathrm{Zn(OH)}$ and the amorphous $\mathrm{Zn(OH)_2}$ which represent respectively the least and the most soluble compounds are shown in Fig. 1.15.
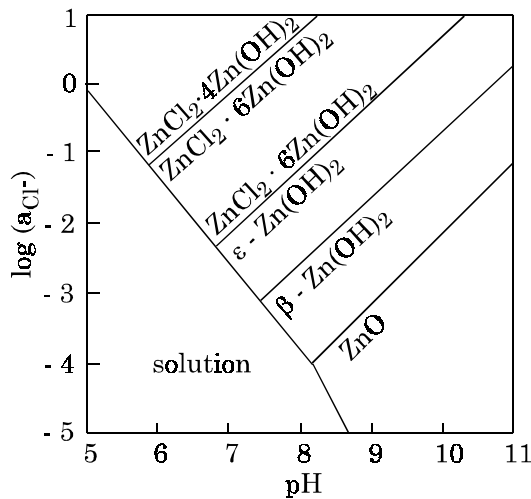
Figure 1.14: Equilibrium diagram for zinc corrosion products in a chloride environment [16]
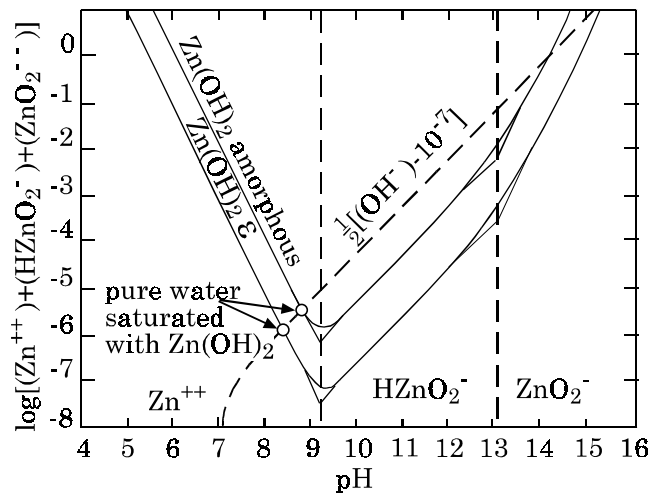
Figure 1.15: Influence of pH on the solubility of zinc hydroxides at 25 ℃ [11, 17]

The presence of the low electrically conducting zinc carbonate, which is formed according to the reaction $5\mathrm{Zn(OH)_2} + 2\mathrm{CO_2} \rightleftharpoons \mathrm{Zn_5(CO_3)_2(OH)_6} + 2\mathrm{H_2O}$, is responsible for the high corrosion resistance of zinc in most atmospheres, with the exception of high sulfur dioxide containing industrial environments. A sequence of formation of the major zinc compounds found in corrosion products formed in four different types of atmospheric environments under sheltered conditions is shown in Fig. 1.16.
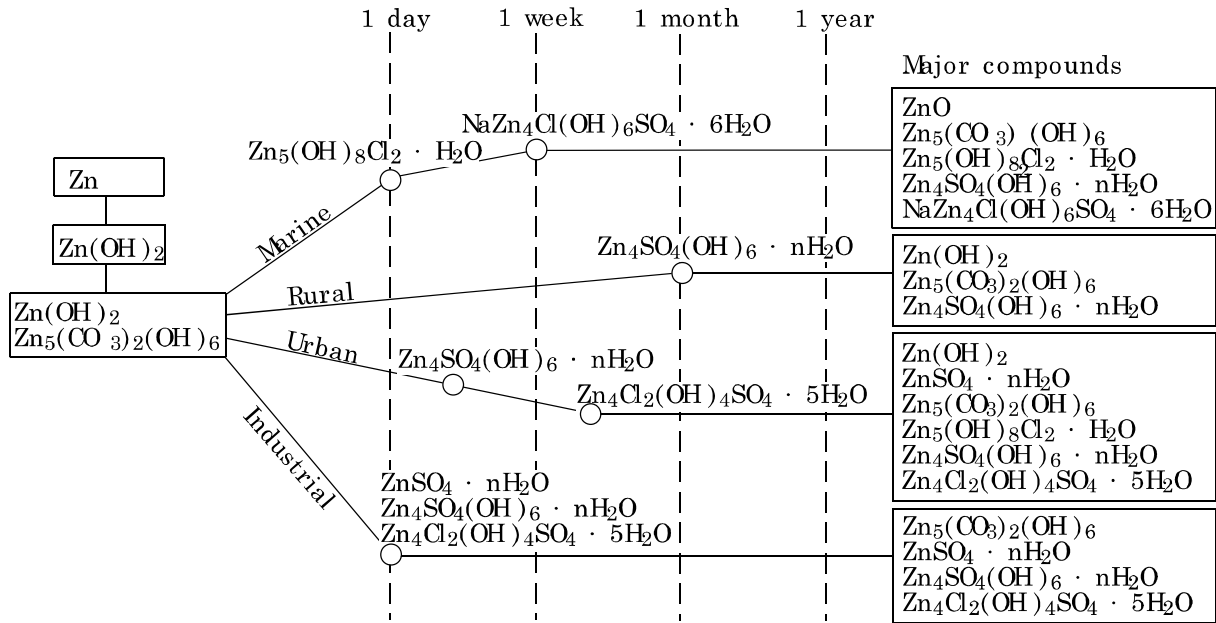
Figure 1.16: Sequence of corrosion products formed in different atmospheric environments [17]

1.1.3 Cathodic Protection of Steel with Zinc

Cathodic protection provides corrosion control by making the structure to be protected the cathode of a corrosion cell. It concerns the intended creation of a local cell. The potential of the structure to be protected is lowered with respect to an auxiliary anode, and usually brought into or near the immunity region as shown in the Pourbaix diagram in Fig. 1.17. In case of cathodic protection of steel with zinc the substrate is cathodically protected by the less noble zinc coating. The zinc anode is sacrificially oxidised and dissolves, whereas the more noble steel acts as cathode for the oxygen reduction. Since cathodic protection is designed to bring a metal into a thermodynamically stable region it is, where it can be applied, by far the most reliable corrosion protection method.

Apart from their respective potentials in the electromotive force series the galvanic corrosion of the system zinc/steel is determined by several factors shown in Fig. 1.18 [18].

On account on its lower position in the electromotive force series than iron (less noble), its small self-corrosion, zinc corrodes by a factor of 5 to 100 times slower than steel, and together with the possibility that its corrosion products refill the injuries of the coating, zinc is the ideal metal to be used as sacrificial anode for the cathodic protection of steel [18, 20]. In case of automotive body panels the cathodic corrosion protection acts at spots where the paint system has been damaged or completely removed due to stone chipping or scratching down to the bare steel or where due to geometry and manufacturing reasons painting is not possible. The sacrificial protection has even a long range effect. Depending on the resistance of the electrolyte it is working over several tenths of millimeters [21]. Figure 1.19 shows schematically the difference in corrosion attack taking place on a phosphated, painted steel sheet and one additionally cathodically protected by zinc coating.

1.2 Corrosion and Corrosion Protection of Automotive Body Parts

Until the late 1950's, corrosion of motor vehicles was a concern limited to marine environments. However, primarily with the increased use of de-icing salts, but also with the acid rain, the occurrence of perforations in automotive body panels rapidly increased from the late 1950's through to the 1970's. In order to improve visual appearance during service and to increase lifetime, from these days on great efforts in improving the corrosion protection of automotive body parts have been made. Additionally, nowadays

Figure 1.17: Regions of cathodic protection of iron with zinc [11]
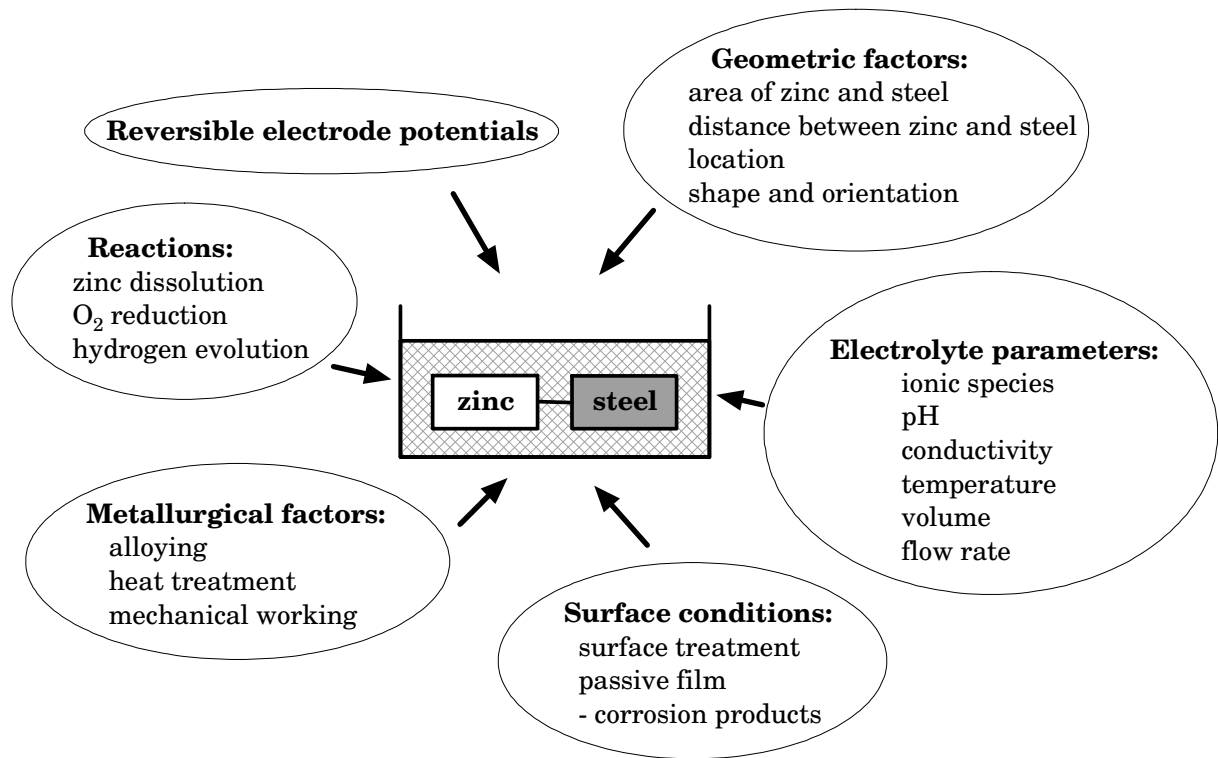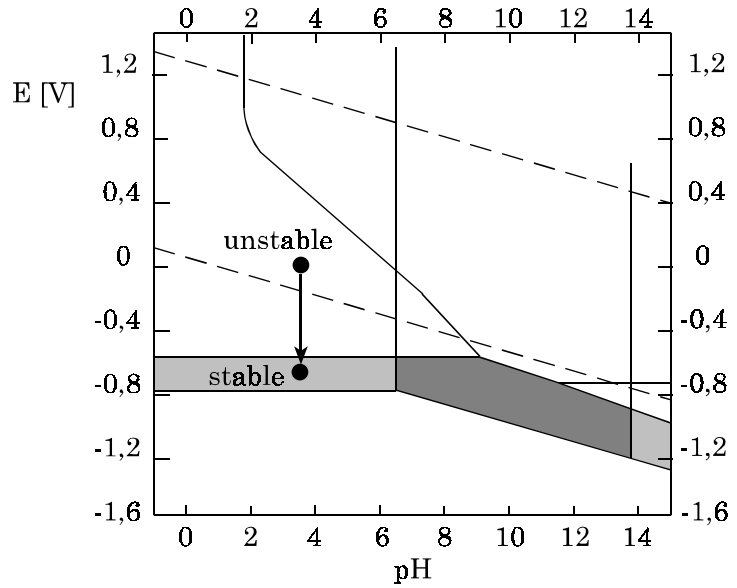
Figure 1.18: Factors involved in the galvanic corrosion of a zinc/steel couple [18]
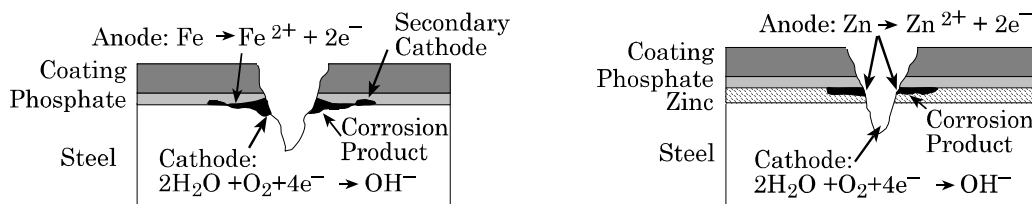
Figure 1.19: Unprotected and cathodic protected steel sheets [19]

there is a strong interest to reduce the body weight to improve the performance of the car, especially its fuel consumption and the resulting carbon dioxide emission [22–26]. Since the body can account for up to a third of the entire vehicle weight, important savings can be achieved by using thin, high strength steel sheets requiring better corrosion protection.

The cost related to corrosion of automobiles in the USA is estimated to be approximately $ 23.4 billion per year. This is divided up into three components: (1) increased manufacturing cost due to corrosion-resistant materials and engineering ($ 2.5 billion), (2) repairs and maintenance necessitated by corrosion ($ 6.5 billion), and (3) corrosion-related depreciation ($ 14.4 billion). An additional cost element that was not calculated is the cost due to reduced safety in automobiles caused by corrosion. While, compared to the 1970's, the cost of corrosion in automobiles has increased substantially in terms of straight dollar figures, it has decreased in relative terms: Considering the nowadays considerably higher quantity of cars as well as the significantly higher average cost of a new vehicle, the percentage of the Gross Domestic Product (GDP) due to motor vehicle corrosion has decreased from 0,37 percent in 1975 to 0.27 percent in 1998 [23]. The challenging objective to make corrosion protection better as well as cheaper has therefore been partially achieved.

1.2.1 Types of Corrosion Occurring with Automotive Body Parts

A motor vehicle, especially the car body is exposed to several forms of corrosion. On the basis of the corrosion mechanisms already presented in 1.1.1.3 and the damages they cause, a distinction between the following corrosion types can be made [6, 19, 23, 27–29]:

- **Perforation corrosion** is the most obvious form of corrosion with painted steel body panels leading to a local perforation of the steel sheet. In case of outer panels this **cosmetic corrosion** with the occurrence of red rust adversely affects the visual appearance of the vehicles and thus lowers their resale value. Regarding the point of origin two sub types can be distinguished: "Outside–In corrosion" takes place on spots where the paint system is damaged i.e. due to stone chipping. "Inside–out corrosion" starts at the inner sections of the car body like hollow spaces and flanges. **Structural corrosion** is an advanced perforation corrosion which impairs the function of the car body. It is critical with safety parts or the frame of the car.

- **Galvanic corrosion** resulting from contact of two dissimilar metals in the presence of an electrolyte.

- **Uniform corrosion** leading to general thinning of the material. Occurs on the entire surface of an exposed car component.

- **Crevice corrosion** and **pitting corrosion** are severe forms of localised attack, leading to several small but potentially deep pits. They occur in tight pockets of stagnant electrolytes containing chlorides and other chemical species that can form at holes, joints or fasteners. **Poultice corrosion** is a specific form of crevice corrosion that occurs under deposits of road debris as e.g. mud.

1.2.2 Corrosion Causes and their Prevention

The various types of corrosion in motor vehicles are caused by several factors such as the design, the manufacturing process, and the operating conditions of the vehicle [6, 23].

1.2.2.1 Design

The design of a vehicle should strive to reduce or avoid dissimilar metal contacts, crevices, stresses, poor drainage, and locations where salt and dirt can build up. Also the choice of materials is very important.

The use of corrosion resistant metals, coated steels, and polymers as well as the choice of primers, paints, and sealers affects the corrosion performance very strongly.

1.2.2.2   Manufacturing Process

Various elements of corrosion protection included in the design phase can be rendered useless if the quality of the manufacturing process is poor. Firstly, the quality of welding determines the presence of crevices where corrosion can occur. Secondly, the surface pretreatment has to be done properly as it ensures good adhesion of the primer and the final coating. Finally, the application of specific coatings, such as chip resistant coatings and body sealants is crucial as those are applied manually and thus are highly dependent on the skills and attention of the worker.

1.2.2.3   Operating Conditions

The corrosivity of the local environment such as acid rain, de-icing salts or marine environments strongly affects the corrosion of vehicles. Additionally personal driving habits and diligent maintenances of the car such as regular washing can have significant effect on the reduction of corrosion.

1.2.3   Corrosion Prevention by Use of Coatings

As already mentioned in section 1.2.2, the automotive industry tries to improve the corrosion performance of vehicle bodies in two ways: designs which consider the problem of corrosion and controlled manufacturing processes providing good quality standards. This section now deals with the use of coatings as one key factor for a corrosion resistant car design and manufacturing. Based on their different protection mechanisms coatings can be split up into several types [30–33]. Types applied with manufacturing of car bodies are:

- **Galvanic coatings** as e.g. zinc coatings, which protect steel due to cathodic protection as explained in section 1.1.3.

- **Barrier coatings** which physically separate the steel from the environment. They normally are inert or electrochemically not active. If they get damaged or permeable no protection is given anymore.

Due to their different protection mechanisms for the construction of corrosion resistant vehicle bodies a multilayer coating system is used, whose overall corrosion protection may be greater than the sum of its individual layers.

1.2.3.1   Galvanic Zinc Coatings, Precoated Steel

A classification of metallic precoated steel sheets arises from the production processes of the metal coatings. Zinc coated (galvanised) steel is nowadays produced by hot dipping and electrolytic deposition. In contrast to piece goods which are coated in a batch process, coiled steel sheets used for automotive bodies are continuously hot dipped and electrodeposited.

1.2.3.1.1   Continuous Hot-Dipped Zinc Coatings   Continuous hot dipping processes such as the Sendzimir (SZ) and Cook-Norteman (CN) processes are multiple stage processes with successive cleaning, coating and postcoating steps [34]. Initially the sheet undergoes a precleaning treatment to remove rolling oils, loose soils, surface carbon and iron fines from the cold rolled strip. This measure enhances the coating adherence and prevents the contamination of the metal bath. Modern lines utilise an alkali brush system and electrolytic cleaning stage with a direct fired reducing treatment for this purpose. Following this,

the sheet enters the Sendzimir Mill cleaning section. In this section a reducing N_2 / H_2 atmosphere of 500–760 °C reduces residual organic contaminants and surface oxides. After cleaning the sheet is annealed above the recrystallisation temperature. Leaving the furnace the strip passes a gas jet which cools it to 460 °C. Subsequently the clean, annealed steel is immersed in a bath of molten zinc. The immersion time has to be set in such a way that a sufficient wetting and reaction of the melt with the steel surface is achieved. On emerging from the melt bath the coated sheet pulls excess coating metal out of the melt. To obtain smooth coatings with desired thicknesses the sheet has to be wiped. Most sheet coating lines use a gas wiping technique for this purpose, where a jet of steam, air or nitrogen is directed against the emerging sheet. Following this, the sheet reaches the cooling tower where it is cooled down. In case of production of galvanealed coatings (zinc-iron alloy) the cooling tower is replaced by a furnace where the yet not solidified coatings get annealed at about 500 °C.

The continuous hot dipping process can be used to produce various metallic coatings such as:

- Pure zinc (galvanised) coatings

- Galvaneal coatings. With theses coatings an annealing step leads to diffusion of iron from the substrate into the zinc deposit. The result is a multiphase zinc-iron alloy with 8–12 % iron content. Galvaneal coatings have good weldability and paintability [35, 36].

- Galfan coatings with Zn+5 wt.% Al content. Due to their eutectic structure Galfan coatings have outstanding ductility coupled with an excellent corrosion resistance [37, 38].

- Galvalume coating with Zn+55 wt.% Al content. These films display a complex, dendritic, binary alloy structure of aluminium rich and zinc rich regions and about 1.6 % silicon [39, 40].

Figure 1.20 shows the equilibrium phase diagrams of zinc–iron and zinc-aluminium. The zinc–iron phase diagram shows at room temperature the occurrence of a variety of intermetallic phases as the ζ-$FeZn_{13}$, δ-$FeZn_{10}$, Γ_1 and Γ_2 phases and a very limited solubility of $\sim$0.001 at.% Fe in zinc [41]. Since the Galvaneal coating is essentially a diffusion coating where iron diffuses from the substrate into the zinc layer it owns a multilayered structure with a gradient in iron concentration. Along the diffusion path from the steel substrate to the coating top three layers with different compositions and structures can be observed. The first layer at the substrate coating interface consists of Γ_1 and Γ_2 phases followed by a layer made of δ-phase. The top layer is a mixture of ζ- and δ-phases. The overall composition of the Galvaneal coating is about 8–12 at.% iron. Further information on Galvaneal coatings can be found in [36, 43–63].

The zinc–aluminium system is a eutectic system involving a monotectoid reaction and a miscibility gap in the solid state. The maximum solubility of Al in (Zn) is 2.8$\pm$ 0.2 at.% (97.2 at.% Zn) at the eutectic temperature, decreasing to 1.6 at.% (98.4 at.% Zn) at 277 °C and 0.07 (99.93 at.% Zn) at 20 °C [42]. The fcc (Al) solid solution has an extended homogeneity range, interrupted at lower temperatures by a miscibility gap. The fcc (Al) solid solution is denoted as αAl or α'Al on the Al-rich and Zn-rich sides of the miscibility gap, respectively. At 277 °a monotectoid reaction of α, α' and Zn occurs. The Galfan coatings with 5 wt.% Al own nearly the composition of the eutectic reaction occurring at 6 wt.% (11.3 at.%) Al and 381°C.

The continuous hot dipping process allows the coating of welded coils with speeds of up to 200 $^m/_{min}$ [35, 64]. A disadvantage of the hot dipped coatings is their rough surface. For their use in outer body parts the dipped strips have to pass high precision finishing rolls delivering smooth surface textures. See also [35, 65–67]

1.2.3.1.2 Electrodeposited Zinc Coatings During electrodeposition the cold rolled, annealed and dressed steel strip passes the production steps of cleaning and then electrolytic cells as well as chemical passivation. A pretreatment step similar to the one applied with hot dip galvanising cleans the strip surface and activates the electrolytic galvanisation by electrolytic pickling. Following this, the strip
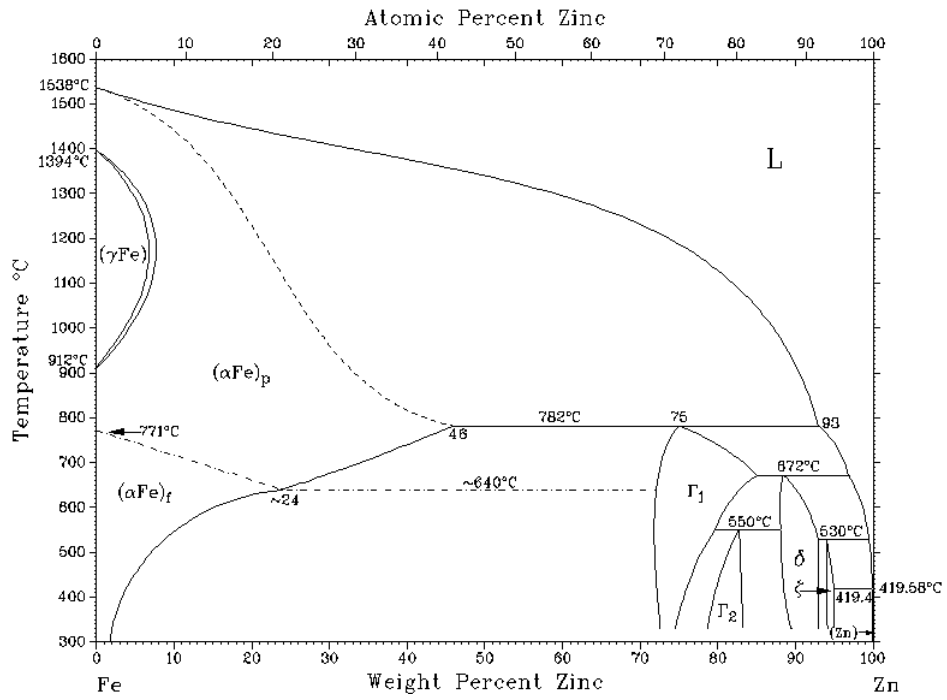
Figure 1.20: Equilibrium phase diagram of zinc–iron [41]
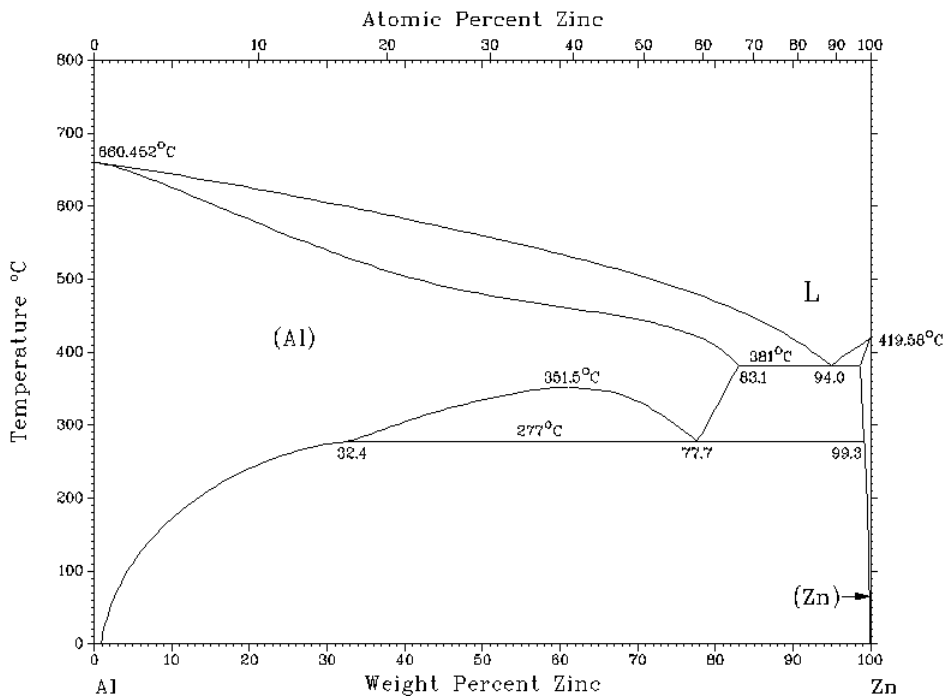
Figure 1.21: Equilibrium phase diagram of zinc–aluminium [42]

passes a series of electrolytic cells in which a electrolyte is flowing between the strip and anodes. By applying an electric current between the anodes and the strip, metal ions from the solution form a coating on the strip. Electrolyte baths used today are either chloride or sulfate based baths since these are more environmentally friendly than the earlier used cyanide baths [67, 68]. The deposits consist of pure hexagonal zinc crystals with either predominant pyramidal or basalplane orientations. The obtained surfaces are smoother than those derived by hot dipping and are therefore suitable also for outer body panel applications.

Electrochemical deposition delivers coatings with compositions, some not achievable by hot dipping, as well as good surface qualities and good formability. The electrolytic process is used to deposit zinc-, zinc–nickel– [69–71], zinc–iron– [72, 73], zinc-chromium– [74] zinc–manganese– [75] and zinc–cobalt– coatings (experimental) [76]. The obtained coatings have higher chemical purity and show higher thickness uniformities in longitudinal and transversal direction than those achieved with hot dipped coatings. As electrolytic galvanisation is not associated with heating of the steel strip it allows also the coating of bake hardening steels, which would loose their bake hardenability with heating.

A disadvantage of the electrolytic process is the cost, as this is higher than for the the hot dipping process. The costs are caused by high consumption of electric energy especially with thicker coatings ($>7.5\,\mu$m) and the waste disposal of sewage and sludges. With increasing awareness for toxic wastes and possible implementations of more strict legislations the costs for waste management will even increase. Ultimately electroplating could be even banned as has already happened with chrome plating in some regions of California [77].

The manufacturing of both coating processes is completed by eventually post treatments, where additional organic or inorganic materials are deposited onto the strip. These post treatments deliver temporary corrosion protection during shipping, lower the working costs during forming and assembly of the car and increase the corrosion protection in joints and flanges during service of the vehicle. Examples for post treatment materials are: corrosion protection oils, corrosion protection oils with additional deep drawing aids (prelubes) and dry lubricants [78, 79]. In the precoated and pretreated state the coiled steel strip is sent to the car manufacturer where it is cut and formed to body parts.

1.2.4 Precoating by Sputter Deposition

Possible alternative processes to the above mentioned ones are the physical vapour deposition (PVD) techniques such as sputtering and evaporation. These techniques allow the deposition of coatings which can not be realised by hot dipping or electrodeposition. The spectrum of coatings, deposited by PVD, ranges from more or less all metals and alloys up to inorganic compounds. Even metastable and non stoichiometric compounds as well as gradient-systems or multilayers can be realised. A further point to be emphasised is the high environmental sustainability of these processes. Since PVD depositions occur in closed chambers and these depositions do not generate polluted waste waters, strict environmental regulations can be fulfilled.

Therefore PVD techniques are becoming more and more important for thin film deposition on large area substrates. While evaporation techniques initially dominated this market, sputter deposition enjoyed a steady growth in market shares within the last 15 years. This development took place although the sputter deposition rates of $100\,\mathrm{nm/s}$ are one magnitude lower than those of thermal evaporation techniques $1000\,\mathrm{nm/sec}$ [80, 81]. Some reasons for the increasing use of sputtering as deposition technique are:

- High thickness uniformity (Δd$\leq$2 %) for coating width $\geq$3 m
- High stability of the deposition rate and layer properties for operation longer than 100 h
- Good adhesion

- Denser structures than evaporated coatings due to the higher energy of the sputtered particles [82, 83]

- Good reproducibility of layer properties from day to day and month to month

- Ability to deposit all kinds of materials including high melting point metals, metal alloys and compounds with precise control of the film composition

- Ability to deposit metal oxides, nitrides, carbides etc. with precise control of the layer stoichiometry

Nowadays sputtering is used for the deposition of metal films on architectural glass, the deposition of "window films" (metal oxide, metal, metal-oxide) which act as optical filters, anti reflex films, transparent conductive top electrodes (ITO) and the deposition of copper on flexible circuits [84]. Nisshin steel works, Japan was one of the first who applied the process on a bigger scale and runs an in-line dry coating process which sputter coats stainless steel with Chromium or Al_xO_y since 1987 [85].

Chapter 2

Methods and Materials

2.1 Sputter Deposition

2.1.1 Principles of Sputtering

Sputter deposition can be defined as the ejection of particles from a solid surface due to the impingement of energetic ions or neutrals and the subsequent condensation of these ejected particles on the desired substrate. It is inherently a vacuum process which results from the momentum exchange initiated at the target surface by incident particles. The angles and energies of the ejected particles are statistically distributed. Possible momentum exchange processes between incident ions and target atoms are depicted in Fig. 2.1. Here M_i and v_i are the mass and velocity of the incident ion and M_t and v_t are the mass and velocity of the target atoms. The quotation mark denotes the velocities of the species after collision. The kinetic energy transferred from an ion which collides with an atom at rest can be calculated from

$$\varepsilon = \frac{E_t}{E_i} = \frac{4M_i M_t}{(M_i + M_t)^2} \cos^2 \theta_i \tag{2.1}$$

where θ denotes the incident angle. To eject an atom from the target the energy transferred must be higher than the threshold energy, usually of the order of a few tens of eV. The incident ion's energies which are most important for thin film processing are in the so called direct knock–on regime, that is 50–1000 eV. In this energy range a considerable amount of target atoms are ejected due to primary recoils [86–96].
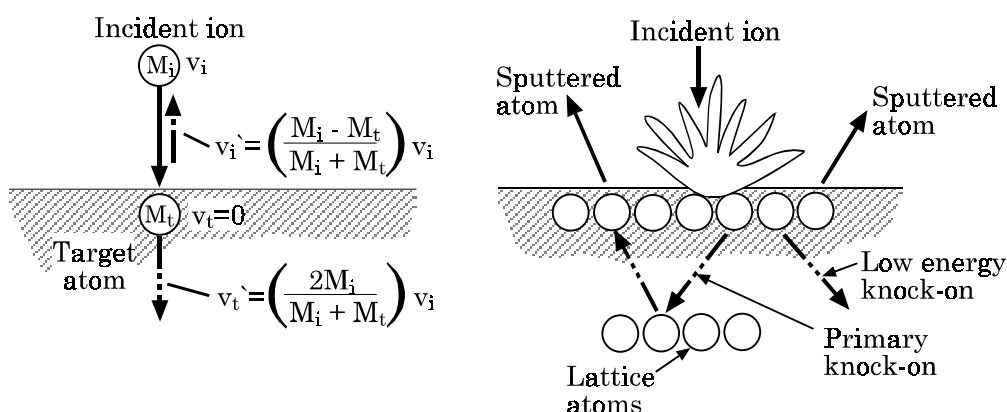
Figure 2.1: Schematic diagrams of the momentum exchange processes occurring during sputtering [88]

The sputter process can be quantified by the total sputter yield Y, i.e. the average number of ejected atoms per incident ion. The current collision cascade model developed by Sigmund [86,87] approximates

the sputter yield as

$$Y(E_i, \Theta_i) = \frac{K_{it}}{U_0} S_n \left(\frac{E_i}{E_{it}} \right) f(\theta_i) \tag{2.2}$$

where U_0 is the surface binding energy (in [eV]), usually given as the heat of sublimation of the target material, $S_n (E_i/E_{it})$ is the reduced nuclear stopping cross section ($\epsilon = E_i/E_{it}$ = reduced energy), and E_{it} and K_{it} are scaling constants dependent on the initial target and projectile species. The sputter yield depends strongly on the type and structure of the target material, the ion species, their energy and their angle of incidence. The yield is less influenced by the temperature of the target, and the ionisation state of the impinging ions. It tends to be greatest when the mass of the bombarding particles is of the same order of magnitude or higher than that of the target material. Particles ejected by a sputter event have kinetic energies in the range of several eV. These energies are considerably higher than those of thermally ejected atoms stemming from an evaporation process. For example the average ejection energy of Ge atoms sputtered by Ar ions of 1.5 keV is approximately 15 eV. Thermally evaporated Ge atoms only have an average energy of 0.1 eV [88]. The spatial distribution of the ejected particles is a cosine–like function of the angle Θ between the target normal and the ejection direction of the particles (see Fig. 2.2).
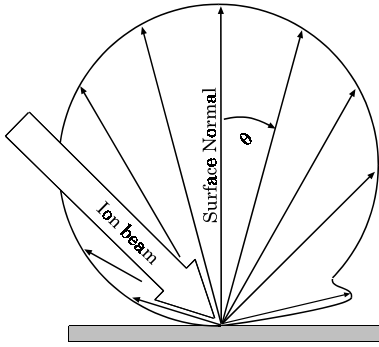
Figure 2.2: Spatial distribution of the sputter yield [97]

The fact that the target material is evaporated by a physical momentum–exchange process rather than a thermal or chemical process makes the sputter process very versatile. More or less every substance can be sputtered. All sputter devices are based on ion generation by low pressure glow discharge. Regarding the ion generation, their acceleration and direction a variety of sputter techniques with different geometries are in use. The sputter techniques used in this work are magnetron sputtering, ion beam sputtering and ion beam assisted sputter deposition.

2.1.2   Magnetron Sputtering

Magnetron sputtering is a variant of the conventional dc or rf-diode plasma based sputter deposition technique. A schematic diagram of a planar magnetron sputter unit as used in this work is depicted in Fig. 2.3. It consists of a chamber with a diode which is pumped to vacuum base pressure prior to operation. In dc-mode a negative potential of several hundred volts is applied to the target. Subsequently a process gas enabling the ignition of the glow discharge is fed into the chamber. Some of the process gas atoms get ionised by natural cosmic radiation. As result of the electric field the formed ions are accelerated towards the target and sputter its surface. As secondary effect the impinging ions create secondary electrons, which cause further ionisation of the sputter gas. In case of the planar magnetron device the ionisation efficiency of the glow discharge is enhanced by superimposing a magnetic field parallel to the target and perpendicular to the electric field. This is achieved by placing permanent magnet bars above the target surface, which create an electron trap beneath the target surface. Due to the $E \times B$ drift the trapped electrons circulate in cycloids over the target surface, which increases their dwell time and path in the sputter gas and thus augments the ionisation probability. The magnetron configuration lowers the chamber pressure needed for the ignition of the plasma, increases the deposition rates and

reduces the thermal loading of the substrates by secondary electrons. The lowered pressure additionally decreases the numbers of collisions of the sputtered particles and hence increases their kinetic impact energy on the substrate. The electron density and thus the generated ion density is highest where the magnetic field is parallel to the target surface. The highest sputter yield occurs right below this region, leading to an erosion track on the target following the shape of the magnetic field. [98]
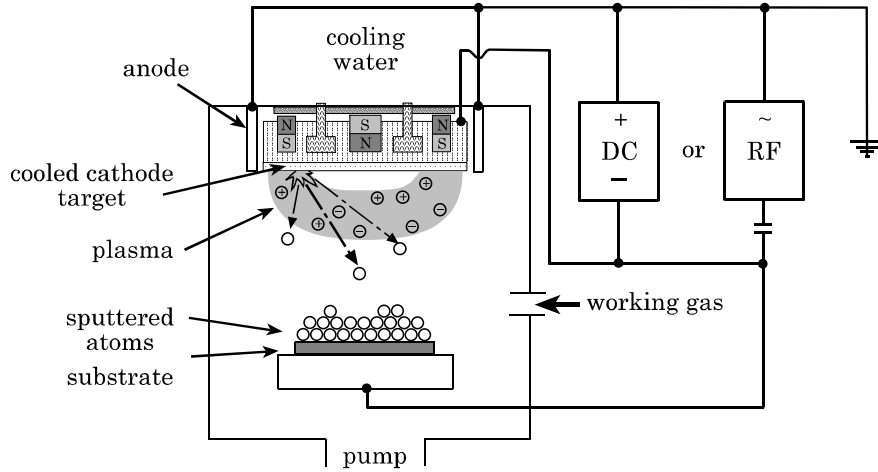
Figure 2.3: Schematic diagram of the magnetron sputter unit MRC 8667 A

Figure 2.4: Photograph of MRC 8667 A
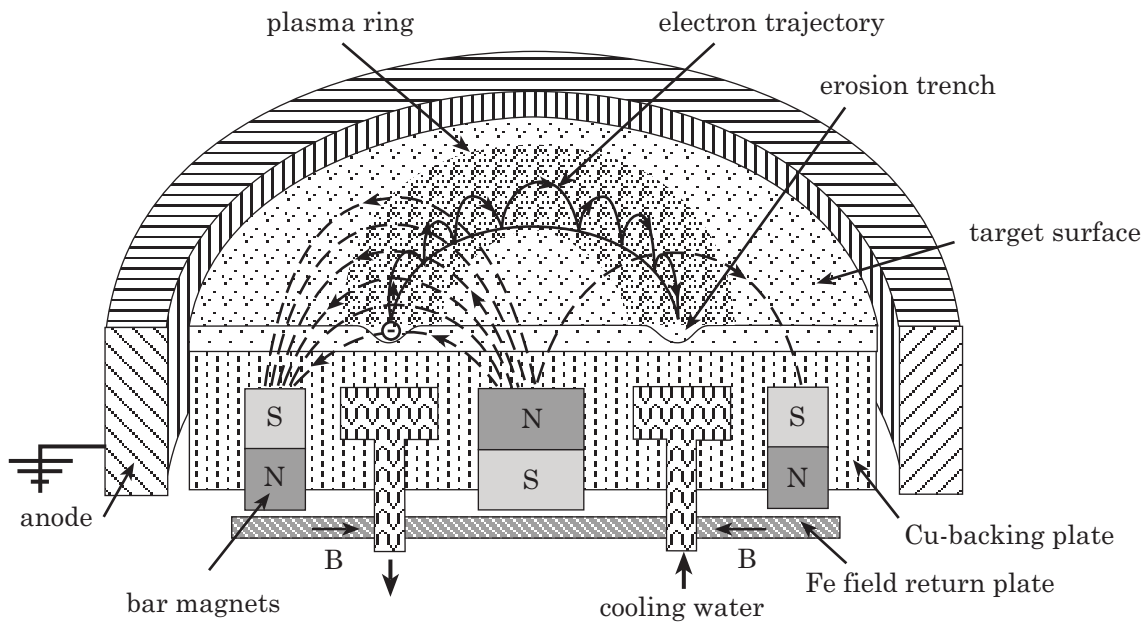
Figure 2.5: Principle of magnetron sputtering

The magnetron unit used in this work is a planar magnetron sputter unit, MRC 8667 A, manufactured by Materials Research Company (MRC), Orangeburg, USA (see Fig. 2.4). In this system three water cooled cathode targets can be mounted simultaneously allowing the deposition of multilayered coatings as well as the codeposition of different materials. For details on the targets used in this work see sec. 2.2.3.3. The deposition unit can be operated in direct current (DC) mode and radio frequency (RF) mode, which allows sputtering of non conductive materials. The DC power is delivered by an MDX 5k Magnetron Drive (0–5 kW, 0–1000 V), Advanced Energy Inc., Wliton, USA. The RF power is supplied by a 1.5 kW generator

(MRC) rated at the internationally allocated industry frequency of 13.56 MHz. During deposition the substrate holder can be biased by 2 to 10 % of the RF target voltage to enhance film density and adhesion by ion plating. The substrate holder placed 70 mm distant from the target, can be rotated (max. rev. 6 $^1/_{min}$) and is water cooled. The pumping system consists of a pre–vacuum rotary pump, Duo 30A, Pfeiffer Vacuum Technology AG, Asslar, Germany and a final–vacuum cryo pump, Cryo Torr 10, CTI Cryogenics, Waltham, USA. As working gas argon for chromatographic use (Alphagaz 2, Air Liquide) with a purity of 99.9999 % was used. The Argon flow was maintained by a Multi Gas Controller 647 A and a flow meter 1259 BX, MKS Instruments, Methuen, USA.

2.1.3 Ion Beam Sputtering

2.1.3.1 Principle of Ion Beam Sputtering

As the title suggests, ion beam sputtering (IBS) is a sputter deposition technique using an ion beam as sputtering source. The system consists of a vacuum chamber containing the sputter target and the substrate, and a separate ion gun, which generates and accelerates ions into a beam. The sputter gun is directed towards the target and produces energetic ions. These ions sputter target atoms on to an adjacent substrate where they condense to form the desired film. Since the glow discharge needed for the generation of ions is confined within a separate gun there is no undesired interaction between the plasma and the substrate. This fact distinguishes IBS from other plasma based sputtering techniques, in which the substrate is immersed in the plasma. IBS allows to operate at much lower background pressures the vicinity of the target and the substrate. The result are increased free-mean paths of the accelerated ions and sputtered atoms, leading to reduced energy losses and sharp energy distributions of these particles. In other sputter deposition systems broad energy ranges for these particles prevail. The main advantage of the IBS process, i.e. of the use of an ion gun, is that the intensity, the energy and the angle of incidence of the bombarding ions can be varied independently over a wide range of well defined conditions. A disadvantage is its low deposition rate.

2.1.3.2 Ion Beam Assisted Deposition by Dual Ion Beam Sputtering

Ion beam assisted deposition (IBAD) is a combined process in which a film formed on a substrate is bombarded simultaneously with a directed beam of energetic ions. The adatoms forming the film might stem from an evaporation or sputter process. The simultaneous ion bombardment adds a component to the film or modifies it in a number of characteristics such as: improved adhesion, nucleation density, control of residual stresses and orientation, grain size, lattice expansions and contractions, morphology, and optical properties [87, 99–102]. The IBAD process is characterised by the bombarding ion energy E_i, the ion to atom arrival rate ratio I_f/A_f, the angle of incidence of the assisting ions θ_i (versus the surface normal) and the type of the assisting ions (different masses). The advantage of the IBAD process over other ion assisted deposition processes is that these parameters can be controlled precisely and independently of each other. In the presented work ion beam assisted depositions have been performed by dual ion beam sputtering. The term dual ion beam sputtering (DIBS) describes an IBAD process in which the film forming adatoms are provided by ion beam sputtering and the ion assistance is given by a second ion gun.

2.1.3.3 Dual Ion Beam Sputtering Unit

In this work IBS and DIBS experiments were carried out with a dual ion beam sputtering unit, of which the schematic is given in Fig. 2.6. It was developed at the Joint Research Centre of the European Commission, Ispra, Italy for depositions at high vacuum conditions and is equipped with two Kaufman ion sources, whose working principle will be presented in the following paragraph 2.1.3.4. The axis of the sputter gun

forms an angle of 60 ° to the target normal in order to optimise the sputter yield. The assisting gun is also inclined at 60 °. Both guns are situated at a distance of approximately 130 mm from the target and substrate holder. The targets, described in sec. 2.2.3.3 are mounted on a water cooled target holder which is at a distance of 150 mm from the substrate holder. The pumping system consists of a Turbo Molecular Pump TMP 1100 C, Leybold Heraeus, Köln, Germany with a pumping speed of $1000 \, l/\mathrm{sec}$, backed up by a rotary pump D25B (Leybold Heraeus) with a pumping speed of $25 \, \mathrm{m^3/h}$. The chamber pressure is monitored with a Total Pressure Controller TPG 300, Balzers, Balzers, Liechtenstein, which uses a thermotron for pressures ranging from atmospheric pressure down to $1 \cdot 10^{-1}$ Pa and a Penning ionisation gauge for the pressure range down to $1 \cdot 10^{-7}$ Pa. The Argon process gas (Alphagaz 1, Air Liquide) with a purity of 99.9 % is introduced directly into each ion gun. The gas flow and therefore chamber pressures are varied via two Mass Flow Meters 1259C, MKS Instruments, Methuen, USA controlled by a Multi Gas Controller 147 from MKS Instruments. The chamber base pressure is $< 5 \cdot 10^{-5}$ Pa. Before commencing the deposition experiments the chamber is evacuated to a pressure of $< 2 \cdot 10^{-4}$ Pa.

To investigate the growth behaviour and the resulting morphology of the coatings over a wide range of substrate temperatures a substrate holder which can be cooled and heated was built. Cooling to temperatures between -80 ℃ and $+20$ ℃ is achieved by attaching a cryostat Thermo Haake, Karlsruhe, Germany which pumps cooled ethanol into the substrate holder. To heat the substrates up to $+200$ ℃ hot silicon oil is supplied by a heating bath circulator MD, Julabo, Seelbach, Germany. To reach temperatures above $+200$ ℃ two electrical heating resistance cartridges are inserted. The temperature of the substrate holder is measured by a Chromel/Alumel thermo couple.
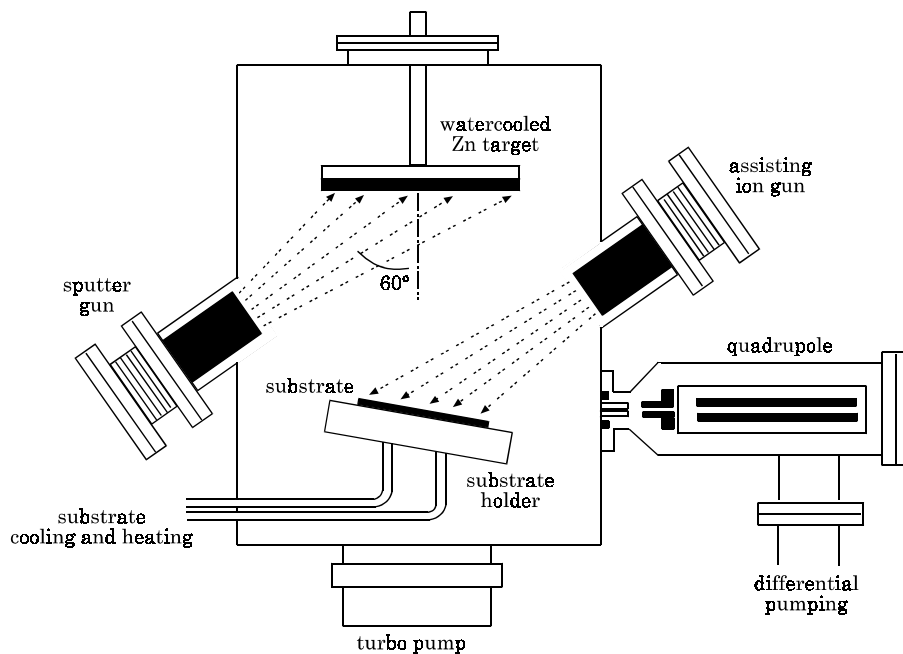
Figure 2.6: Schematic of a Dual Ion Beam Deposition unit

2.1.3.4 Kaufman Ion Sources

Both ion sources used in the DIBS unit are Kaufman type ion sources with a beam diameter of 30 mm produced by Commonwealth Scientific Corporation, Alexandria, USA. This type of ion source was first developed by Harold Kaufman at NASA as a propulsion system for space applications. Figure 2.7 shows a cutaway sketch of a Kaufman ion source, whereas Fig. 2.8 depicts a schematic diagram of the ion source and its electrical circuits [97].
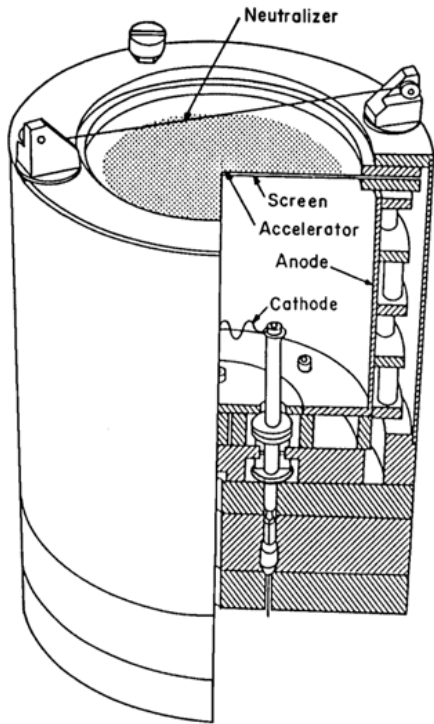
Figure 2.7: Cutaway sketch of a Kaufman ion source [97]
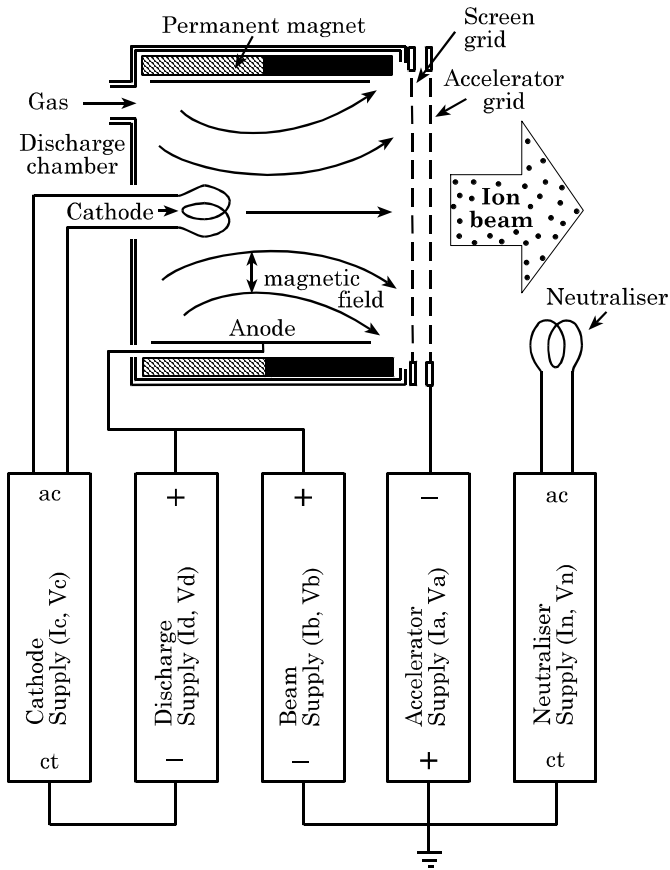
Figure 2.8: Schematic diagram of a Kaufman ion source and its electrical circuits [97]

For the operation of the ion gun the working gas (in this work Ar is used) is directly introduced into the discharge chamber. The neutral gas atoms are struck by energetic thermal electrons and emitted from the heated cathode filament. A fraction of the neutral gas atoms gets ionised and ignites the glow discharge. To increase the ionisation efficiency the effective electron path in the chamber has to be lengthened. Therefore a magnetic field parallel to the axis of the cylinder is generated by permanent magnets around the chamber forcing the electrons to move in cycloids. The ions formed are then either neutralised by recombination with electrons of the plasma or by striking the walls of the discharge chamber. Alternatively they can be attracted to the negative potential of the accelerator grid in the ion optics. Ions that approach the ion optics, consisting of the screen grid and accelerator grid, are extracted from the discharge chamber and get accelerated into the ion beam. The apertures of the two grids, made of molybdenum, are aligned in a way that the extracted ions do not strike and erode the acceleration grid. The standard ion optic configuration consists of two flat grids extracting a collimated beam. These grids can be replaced by concave or convex grids to focus or defocus the ion beam. To balance the positive charge of the beam ions, which would disrupt the beam due to their mutual repulsion, a neutraliser filament is used. The neutraliser filament adds thermal electrons to the beam so that each small beam volume has nearly equal numbers of positively and negatively charged particles. Under normal operation conditions the recombination of the ions and electrons is negligible. To prevent a back streaming of the neutralising electrons into the discharge chamber the neutraliser filament is set to a higher potential than the accelerator grid. The energy E_i (measured in [eV]) of the ions extracted into the beam equals the potential difference ground–anode potential V_b multiplied by the charge of the ion. Each of the ion guns is driven by a power supply ID 2500, Commonwealth Scientific Corporation, which supplies a beam voltage of $100-1500$ V and a beam current of $2-60$ mA.

2.1.3.5   Ion to Atom Arrival Rate Ratio

To quantify the effect of the assisting ion beam on a deposition it is necessary to determine the ion to atom arrival rate ratio I_f/A_f, which is the ratio of the number of bombarding ions to the number of condensing adatoms per area and time. In an IBAD process both parameters can be varied independently. The adatom flux A_f arriving at the surface can be calculated from the expression,

$$A_f = \frac{D_r N_A \rho}{M} \cos(\theta_A) \qquad \text{with} \qquad D_r = \frac{d}{t}$$

where D_r is the deposition rate, N_A is Avogadro's number, ρ the mass density of the film, M the atomic weight of the depositing species and θ_A the incident angle of the adatoms measured versus the surface normal. The deposition rate D_r can be calculated from the measured film thickness d and the deposition time t. The ion flux I_f is obtained from

$$I_f = \frac{I_p}{e \cdot A_p} \cos(\theta_i)$$

where I_p is the ion current measured at the probe area A_p, e is the charge on each ion (usually $1 =$ elementary charge) and θ_i is the incident angle of the assisting ions.

For the measurement of the ion current density a two dimensional current probe array was placed on the substrate holder. The array consists of 8×8 electrodes, each with a probe area A_p of 5 mm $\times$ 5 mm, separated by lines with a width of 0.6 mm. The array is connected to a multichannel analyser controlled by a personal computer running a LabVIEW® program, written by the author within this work. A screen shot of the LabVIEW® program is shown in Fig. 2.9. The measuring system sequentially applies a bias voltage of -30 V to the electrode to be measured, while setting the others to ground potential. The program measures the ion current I_p at the respective electrode, stores the data, and advances to the next electrode. After measuring all probes it visualises the spatial ion current distribution of the
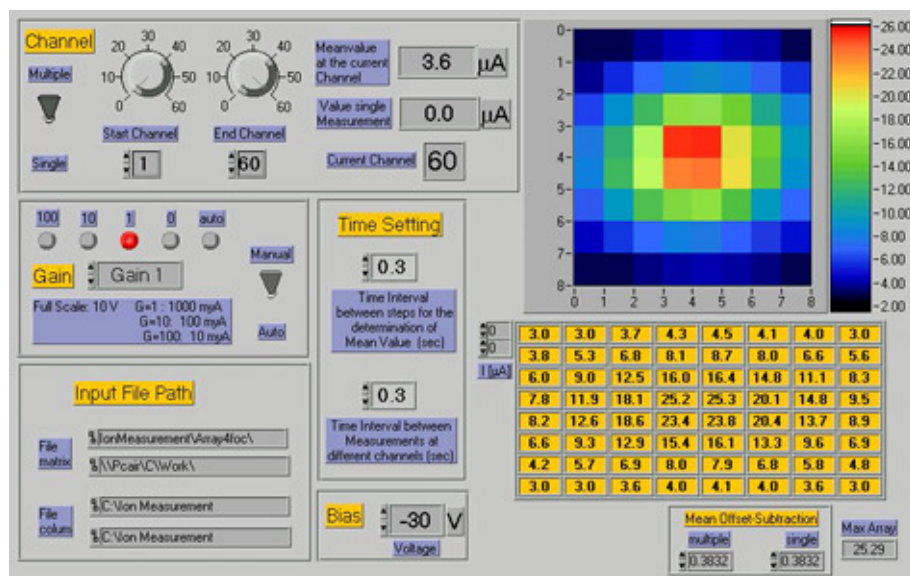
Figure 2.9: Screen shot LabVIEW program

entire array. The measurements disregard multiple ionisation, the emission of secondary electrons, and the charge exchange between the ions. In this way the program allows a determination of the ion current densities as a function of the substrate positions and following the calculations of the respective ion to atom arrival ratios as described above.

2.1.3.6 Process Gas Analysis by Quadrupole Mass Spectrometry

To investigate the influence of gas contaminations on the growth behaviour and thus on the resulting morphologies of zinc coatings, depositions in oxygen doped argon atmospheres were carried out. For this purpose very small flows of oxygen were introduced into the chamber by a precision valve. To monitor and control the gas composition during the depositions a sputter process monitor SPM 125, Balzers, Liechtenstein based on a quadrupole mass analyser has been connected to the chamber. The analyser, working under UHV conditions, is separated by a diaphragm from the deposition chamber and is differentially pumped by a turbo molecular pump TCP 040, Balzers Pfeiffer. This setup allows the measurement of the chamber atmosphere even at elevated pressures (up to $1\,Pa$) which occur at usual sputter depositions. The gas to be measured is ionised by a dual filament ion source directly immersed in the process environment. To increase the sensibility and dynamic range of the measurements the quadrupole is equipped with a secondary electron multiplier (SEM). The analyser is able to measure particles with specific masses m/e up to a value of 100, where m is the mass of the particle and e its charge. The quadrupole is operated by a control unit QMI 422, Balzers in connection with the computer program Quadstar 422, Balzers running on a personal computer. The program controls the data acquisition from the quadrupole and visualises the measured data [103].

2.2 Materials and Sample Preparation

2.2.1 Substrate Materials

For the sputter experiments polished silicon wafers and mild steel sheets were used as substrates. The p-type, boron doped silicon wafers, made by Mateck, Jülich, Germany had a thickness of $0.635\,mm$ and a diameter of 2". The polished silicon wafers with a surface roughness $R_a < 1\,nm$ have been used for the morphology investigations on the coating fracture crossections and hardness measurements, as their

smooth surface allows a better observation of the "pure" coating morphologies. Even when the silicon wafers and steel sheets are different substrate materials, for the deposited films no differences in growth and morphology have been observed. Especially the phenomenon of epitaxy has not been observed, as it is revealed by the XRD measurements, which deliver the same crystal structures and orientations for films deposited on silicon wafers or steel sheets.

Since steel sheets are the construction material of the car body they were used for the analysis of the surface morphology and the technological evaluation of the coatings (roughness, adhesion, formability, electrochemistry and corrosion testing). As steel substrates an unalloyed mild steel (material No 1.0338, brandname Solstamp) delivered by Sollac, Florange, France was chosen. The 1.0338 grade is a cold rolled steel, widely used in the automotive industry for bending and drawing applications. The mechanical properties and the chemical composition of the steel measured by Sollac within the joint re search project are given in Tab. 2.1.

	Material.No	YS[MPa]	UTS[MPa]	A_{80} [%]	d [mm]	R_a [μm]
data sheet	1.0338	140-210	270-350	$\geq$38	0.7-2	-
measured data		154	296	44	0.9	1,64

	C [%]	Mn [%]	P [%]	S [%]	N [ppm]	Si [%]	Al [%]	Ti [%]
data sheet	<0.08	<0,4	<0.03	<0.025	-	<0.1	>0.02	-
measured data	0.003	0.116	0.008	-	25	0.021	0.043	0.115

Table 2.1: Mechanical properties and chemical composition of the steel substrates

2.2.2 Reference Samples

As reference samples electrodeposited zinc coatings EZ 100/100 and galvanealed coatings ZF 140 RB on cold rolled steel sheets were used. The double side EZ coated 1.0338 grade steel sheets, tradename Solcar, were supplied by Sollac, Florange, France. The designation EZ 100/100 indicates the coating thicknesses per side measured in [μm] multiplied by ten. The galvanealed coatings ZF 140 RB applied on both sides of 1.0350 grade steel sheets were delivered by Thyssen Stahl Service Center, Leverkusen, Germany. With this coating the designation ZF 140 RB indicates the total coating mass of 140 $^{g}/_{m^2}$ for both sides of the zinc iron alloyed coating (R) with improved surface (B). The properties of the references are given in Tab. 2.2. The values for the EZ sample were measured by Sollac within the joint research project, the details for the Galvaneal sample were taken from the Thyssen delivery program.

Sample name	Material No.	coating		A_{80} [%]	d_{sub} [mm]	designation	d_{coat} [μm]	mass $^{g}/_{m^2}$
		YS [MPa]	UTS [MPa]					
EZ	1.0338	154	296	44	0.9	EZ 100/100	9.7	70 per side
Galvaneal	1.0350	140–300	270–420	26	1	ZF 140 RB	10	70 per side

Table 2.2: Properties of reference samples

2.2.2.1 Morphology of Reference Samples

2.2.2.1.1 Electroplated Zinc Coating On examination by eye the electrogalvanised reference coating EZ has a bright grey, matt appearance. The SEM–images in Fig. 2.10 show the cryo fracture cross-sections of the coating. The film has a compact, dense structure without voids, but a rough surface. Its thickness is 9 μm. Single grains have random orientations and different sizes, ranging from 0.5 to 5 μm.
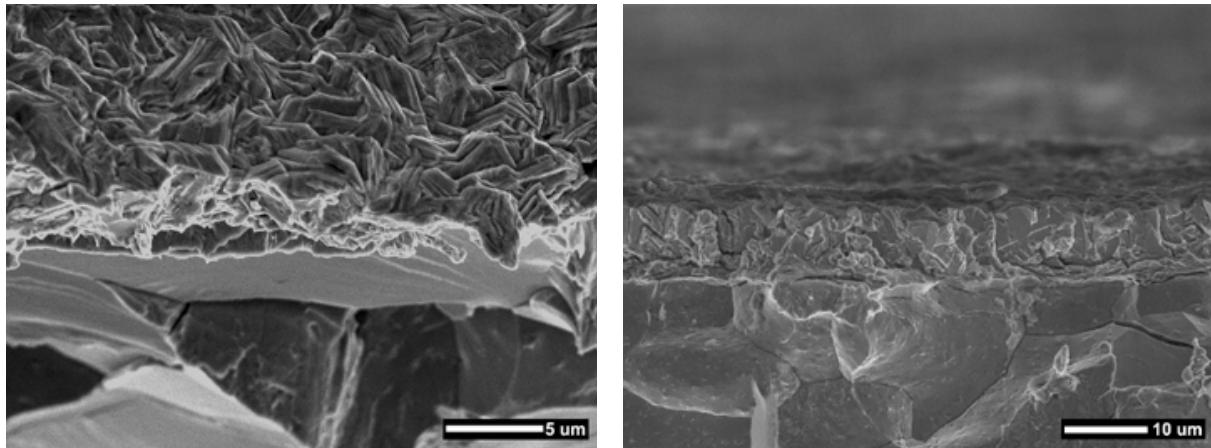
Figure 2.10: Cross-sections of an electrogalvanised zinc coating EZ

2.2.2.1.2   Galvanealed Coating   On examination by eye the $9.6\,\mu$m thick Galvaneal coating has, in contrast to the electroplated zinc coating EZ, a dull, grey appearance. The SEM–image in Fig. 2.11 shows its cryo fractured cross-section. The film has a compact, dense structure consisting of randomly oriented, polygonally crystallites with grain sizes of 0.85 to $7\,\mu$m.
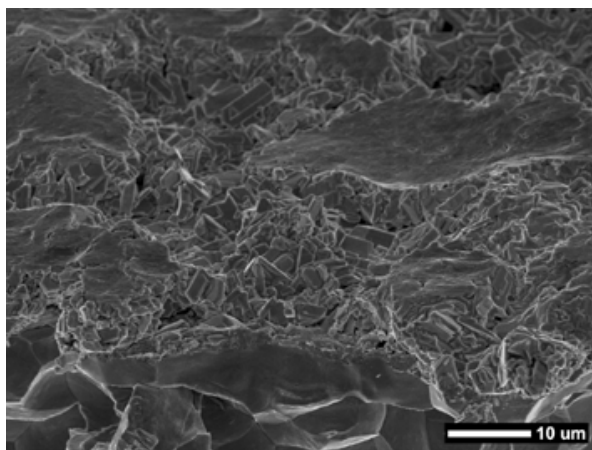
Figure 2.11: Morphology of a Galvaneal coating

2.2.3   Coating Materials

Table 2.3 shows the thermal-, electrochemical-, structural- and mass properties of pure zinc and the alloying elements of the zinc alloy coatings.

2.2.3.1   The Influence of Vapour Pressure

The vapour pressures of the substances used as coating materials were calculated according to Alcock et al. [109]. The following graph 2.12 depicts the vapour pressures of these materials in the temperature range from 298 K up to their melting point or 1000 K respectively. The graph shows that the vapour pressures of the coating materials vary over several decades in the temperature range from 213 K to 473 K. Especially the elements magnesium and zinc have a very high vapour pressure. Due to this fact, especially at higher deposition temperatures, a certain rate of reevaporation from these elements is to be expected.

element	T_m [K]	T_b [K]	$Me \rightleftharpoons$ $Me^{x+} + x \cdot e^-$ [V vs. SHE]	atomic radius r_0 [pm]	bond length a_0 [pm]	crystalline structure	atomic weight [amu]	density at 20°C [g/cm³]
Zn	692.73	1179	-0.763	135	266	hdp	65.38	7.140
Fe	1809	3158	-0.440	140	248	bcc*	55.847	7.873
Ti	1939	3631	-1.63	140	290	hdp*	47.88	4.506
Cr	2130	2952	-0.91	140	250	bcc	51.996	7.140
Al	933.52	2740	-1.66	125	286	fcc	26.98	2.699
Mg	923	1366	-2.37	150	320	hdp	24.305	1.738
source:	[104]	[104]	[105]	[106]	[107]	[108]	[108]	[108]

* modification at room temperature

Table 2.3: Material properties of the coating materials [104, 105, 108]
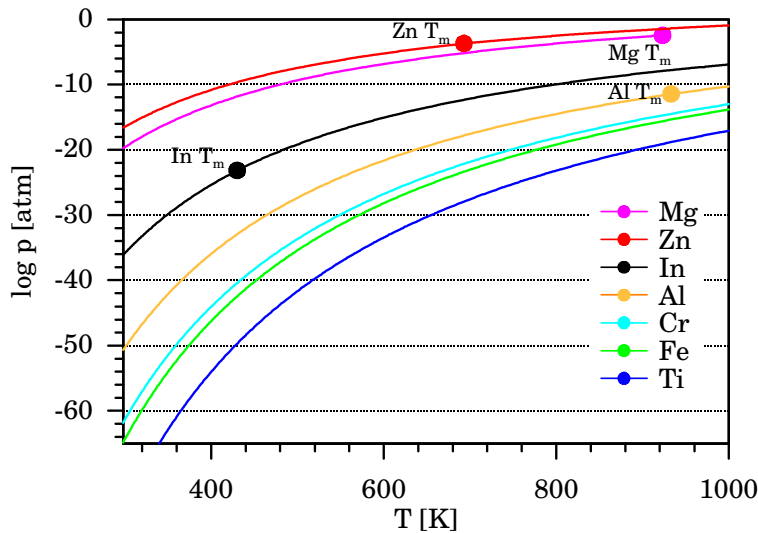
Figure 2.12: Vapour pressures of coating materials

2.2.3.2   Equilibrium Phase Diagrams

Figures 2.13 to 2.15 present the equilibrium phase diagrams of the zinc titanium, zinc chromium and zinc magnesium. The phase diagrams of zinc-iron and zinc aluminium have been already shown in section 1.2.3.1.1. Since sputtering is a non equilibrium process with energies one magnitude higher than energies occurring in thermal processes, the deposited phases can deviate strongly from stable equilibrium phases. The significantly reduced diffusion occurring at low substrate temperatures, and the tendency for surface diffusion to dominate over bulk diffusion at any temperature, creates unusual and in some cases unique phase constitutions in sputtered coatings [110]. They often consist of metastable phases or are even amorphous. Due to this fact the equilibrium phase diagrams should only be used for general orientation.

2.2.3.3   Target Materials

As zinc alloys (apart from the Zn-Al alloy) were not commercially available as target materials these alloys were deposited from mosaic targets. The basis for the mosaic targets used in the IBS, DIBS and magnetron depositions were pure zinc targets with a purity of 99.99 %. On these zinc targets screws or plates of the alloying elements (purity 99.9 %) were mounted. By varying the surface area fractions (numbers of screws or plates) it was possible to change the compositions of the deposited alloys. A photograph of a mosaic magnetron target is shown in Fig. 2.16. An exception from the mosaic target depositions were the magnetron sputtered zinc-aluminium films which have been deposited from an alloy target with a composition of Zn+2.7 at.% Al. The purity of the Zn-Al target is 99.99 %.
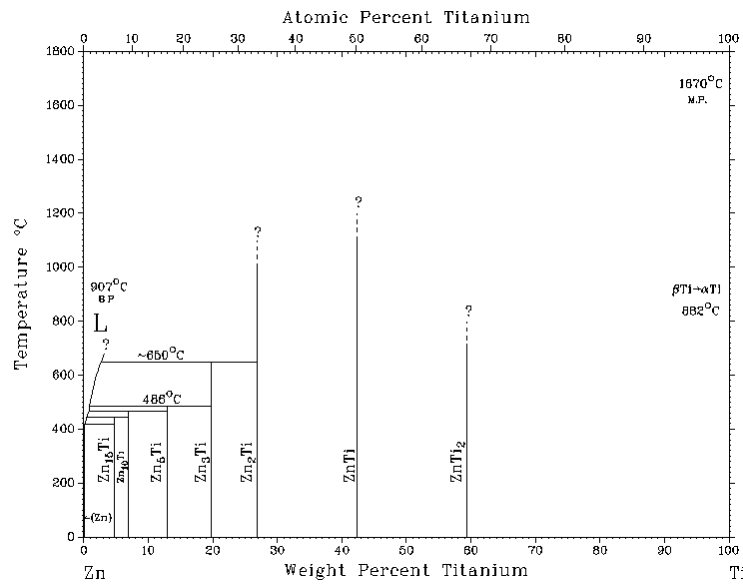
Figure 2.13: **Zinc–titanium** phase diagram [42]
The experimental determination of the zinc–titanium phase diagram is rather difficult as the melting point of Ti is at 1670 °C and the boiling point of zinc at 1atm amounts to 907 °C. Therefore only some parts of the phase diagram are known. The solubility of Ti in (Zn) has been estimated to be 0.0006 at.% Ti at 300 °C by metallographic examination. In the equilibrium state the deposited coatings with a composition of up to 15 at.% titanium could consist of the intermetallic phases $Zn_{15}Ti$, $Zn_{10}Ti$, Zn_5Ti and Zn_3Ti.
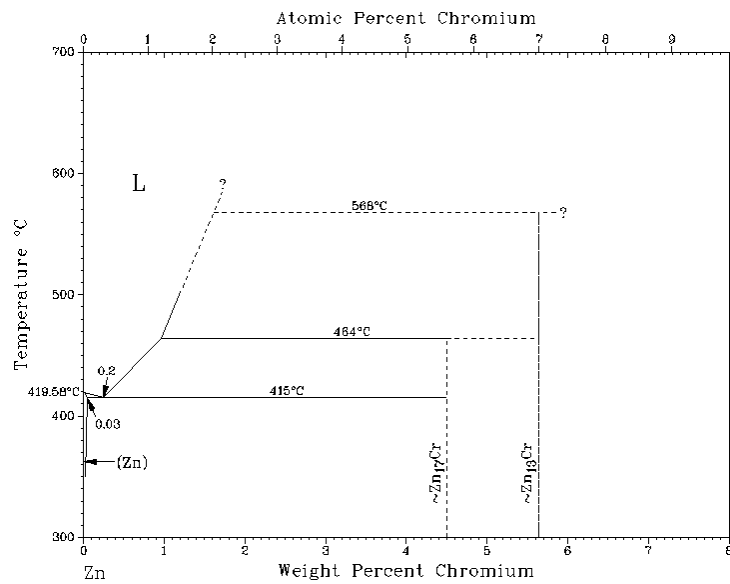
Figure 2.14: **Zinc–Chromium** phase diagram [42]
This equilibrium phase diagram is not further investigated than to a content of 8 at.% chromium. The assessed maximum solid solubility of Cr in (Zn) is 0.04 at.% Cr at the eutectic temperature of 415 °C. At 500 °C, a solubility of 1.5 at.% Cr in liquid Zn has been reported. The system shows the existence of two intermetallic phases: $Zn_{17}Cr$ and $Zn_{13}Cr$ which could be observed in the deposited coatings.
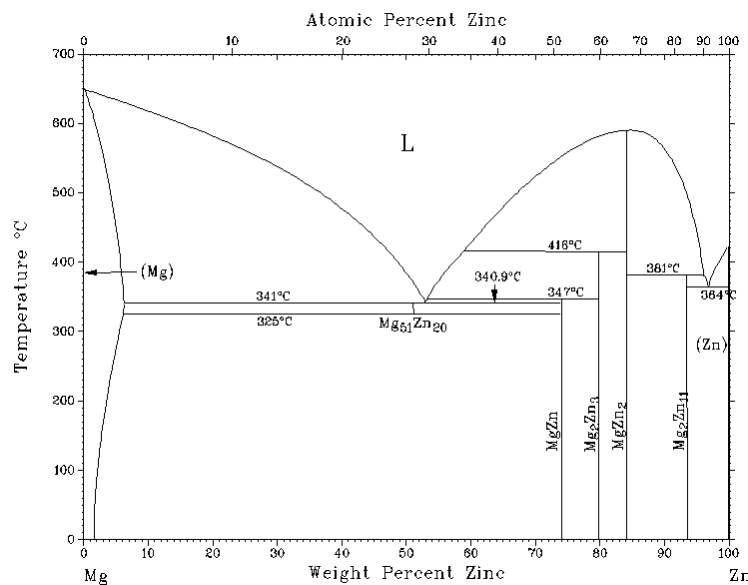
Figure 2.15: **Zinc–Magnesium** phase diagram [111]
This equilibrium phase diagram shows the presence of various eutectoid, peritectic and eutectic reactions. At room temperature the four intermetallic phases Mg_2Zn_{11}, $MgZn_2$, Mg_2Zn_3 and $MgZn$ can be observed. The coatings deposited up to an alloy content of 15 at.% magnesium could consist of the intermetallic Mg_2Zn_{11}- and $MgZn_2$- phases.

Figure 2.16:
Mosaic target of the magnetron deposition unit with visible erosion track

2.2.4 Deposition

2.2.4.1 Substrate Pretreatment

Steel Substrates

The steel sheet substrates were delivered in an oiled state to prevent corrosion during shipping and storage. Due to this reason the sheets had to be carefully cleaned in a two-stage cleaning process before deposition: one chemical cleaning step outside the deposition chamber and a second sputter etching step inside the deposition chamber.

The chemical cleaning was done with a 5 % alkaline cleaning solution in an ultrasonic bath at 60 °C for 3 minutes. When testing different cleaning solutions the strong alkaline cleaner (Hakupur 50/380, Kluthe, pH=12) showed the best cleaning results and therefore the best adhesion of the deposited coatings. After rinsing with water the samples were cleaned for 2 min in an ultrasonic bath with deionised water at 60 °C. Subsequently the steel sheets were rinsed with isopropanol and dried with a blast of nitrogen. After drying, the samples were quickly mounted in the magnetron deposition chamber, the chamber was closed and pumped to the base pressure of $3 \cdot 10^{-5}$ Pa. Just before deposition the samples have been sputter etched for 10 min at a sputter power of 1 kW / 700 V. This plasma pretreatment removes a 5 to 20 nm thick toplayer of ironoxides and other surface impurities originating from production [81, 112].

Silicon Substrates

The silicon wafers were cut to the required sample size and cleaned in an ultrasonic bath with isopropanol. Following this, the samples were dried with a blast of nitrogen and instantly placed in the deposition units. After closure the chambers were pumped to their respective base pressure. With the magnetron sputter experiments the plasma cleaning step was performed similar to the one applied to the steel substrates. With the experiments in the DIBS unit the silicon wafers were sputter etched for 10 min by the assisting ion gun (beam voltage = 500 V, beam current = 10 mA) just before deposition.

2.2.4.2 Mounting

The optical appearance of the first depositions with the magnetron sputter unit showed, that the morphology of sputtered zinc coatings depends very strongly on the substrate temperature. Interestingly, samples with the same pretreatment from the same batch showed completely different morphologies: some of the samples had a metallic, shiny appearance while others were dull and grey. This observation led to the consideration that the samples must have had different thermal histories in the sputter process where a

variety of heating processes lead to an increase of substrate temperature during deposition [113, 114]. In general, the heat is provided by

- kinetic energy of electrons and ions from the plasma (does not hold for IBS samples)

- potential energy of electrons and ions from the plasma (does not hold for IBS samples)

- kinetic (≈ 4 to $20\,\text{eV}$ per atom) and potential (heat of condensation) energy (≈ 1 to $9\,\text{eV}$ per atom) of the sputtered species from the target

- reflected highly energetic neutrals from the target, mostly argon

- radiation from the plasma (≈ 1–$9\,{}^{\text{eV}}\!/_{\text{atom}}$) (does not hold for IBS samples)

It was considered that the metallic shining samples had by chance a good thermal contact with the water cooled substrate holder. The dull grey samples were microscopically lying on spikes of the rough surface, thereby not allowing a sufficient heat transfer away from the substrate.

As a result of these observations in further magnetron depositions one set of samples was glued with a heat conductive paste onto the watercooled substrate holder, while a second set was loosely lying on the substrate holder. In this way it was possible to deposit two types of samples in one batch: one cold type of samples with good heat transfer and a temperature close to that of the substrateholder ($T_s = +8\,°C$) and one warm type of samples with a floating temperature ($T_s = T_{\text{float}}$) depending on the heat influx and draining.

To grow films under extremely different thermal conditions and to simulate the worst case of thermal coupling to the cooled substrate holder a further setup was tested. In this setup one cold set of samples was glued with heat conducting paste onto the cooled substrate holder as described above, while the second set of substrates was laid onto an inox steel mesh. The steel mesh isolated the samples almost completely from the substrate holder. Their substrate temperature is denoted as $T_s = T_{\text{isolated}} = T_{\text{iso}}$.

In order to be able to deposit samples at defined substrate temperatures additional experiments were carried out with the IBS unit. Since a good heat transfer from the substrate holder is imperative for depositions at defined substrate temperatures the heat conducting glue was used here, too. The substrate temperatures were varied between $-60\,°C$ and $+200\,°C$.

2.2.4.3 Sample Nomenclature

Magnetron sputtered zinc coatings

Sample nomenclature is set up in the way that the first letter Z indicates the base material zinc which is common for all sputtered samples. For the magnetron sputtered pure zinc coatings this letter Z is followed by a second letter A to I in ascending order, which describe different sets of deposition parameters. The last digit written as subscript indicates the deposition temperature of the respective sample. (Tab. 2.4)

Z	[A–I]	$_8$ or $_{\text{float}}$ or $_{\text{iso}}$
base material zinc	set of sputter parameters	substrate temperature T_s $+8\,°C$, T_{float} or T_{iso}

e.g. ZB_{float}

Table 2.4: Sample nomenclature for magnetron sputtered zinc coatings

Magnetron sputtered zinc alloy coatings

In case of the alloyed coatings the initial letter Z is followed by the chemical symbol Xx of the respective alloying elements iron (Fe), titanium (Ti), chromium (Cr), aluminium (Al) or magnesium (Mg). The

number Y on third position indicates the rounded, average atomic percentage, of the alloying element of the two sample batches processed in the same deposition run. Some of the sample names optionally include also the foreseen purpose of the sample (characterisation by XPS or VDA testing). All optional parameters are given in brackets in tables 2.5 and 2.8.

Z	Xx	Y	($_8$ or $_{float}$ or $_{iso}$)	(int, XPS or VDA)
base material zinc	alloying elements Fe, Ti, Cr, Al and Mg	rounded, average amount of alloying of samples ZXx_8 and ZXx_{float} [at. %]	substrate temperature T_s +8 °C , T_{float} , T_{int} or T_{iso}	purpose

e.g. $ZFe13_{float}$

Table 2.5: Sample nomenclature for magnetron sputtered zinc alloy coatings

Ion beam sputtered coatings

To distinguish between magnetron and ion beam sputtered coatings the ion beam sputtered films are marked with the letters IB. The additionally ion assisted depositions are marked with the final letter A and a number (1 or 2) giving a qualitative description of the ion to atom arrival ratio in ascending order. (Tab. 2.6)

Z	(Fe)	IB	(Y)	(x)	(A)
base material zinc	alloying element Fe	ion beam sputtered	rounded, average amount of alloying [at. %]	substrate temperature T_s in °C	ion assisted deposition

e.g. ZIB_{+80}

Table 2.6: Sample nomenclature for ion beam sputtered coatings

2.2.4.4 Deposition Parameters Magnetron Sputtered Samples

At the beginning of the study different sets of sputter parameters were tested. Different sputter modes, DC and RF, as well as sputter powers in the range of 400 W to 1000 W were applied at different gas flows. The substrate holder was set at ground potential or biased with -50 V to -290 V. The influence of the substrate holder rotation on substrate heating and deposition rate was investigated. By changing the deposition time also the coating thickness was varied.

Magnetron Sputtered Zinc Coatings

Tab. 2.7 gives an overview of the different magnetron sputtered pure zinc coatings and their deposition parameters.

The different sets of parameters lead to very different results. As the deposition parameters of the ZC deposition delivered the best results for pure zinc coatings, these parameters have been further applied with all zinc alloy depositions, in order to separate the influence of alloying on coating morphologies and properties, without changing the deposition parameters.

Sample	Sputter Power [W]	Mode	Bias [V]	Ar flow [sccm]	p [Pa]	Substrate temperature T_s	Time [min]	Substrate holder
ZA	400	RF	50	137	0.05	+8℃ , T_{float}	40	static
ZB	400	RF	50	137	0.11	+8℃ , T_{float}	240	rotating
ZC	**600**	**DC**	**-**	**137**	**0.11**	**+8℃ , T_{float}**	**240**	**rotating**
ZD	800	RF	150	137	0.08	+8℃ , T_{float}	12	static
ZE	1000	RF	100	137	0.15	+8℃	240	rotating
ZF	600	RF	-	137	0.08	+8℃ , T_{iso}	15	static
ZG	600	RF	290	137	0.11	T_{iso}	65	static
ZH	600	RF	290	137	0.93	+8℃ , T_{float}	180	rotating
ZI	1000	RF	50	137	0.13	+8℃	240	rotating

Table 2.7: Deposition parameters for magnetron sputtered zinc coatings.

Magnetron Sputtered Zinc, -Iron, -Titanium, -Aluminium, -Chromium and Magnesium Coatings

Sample	Sputter power [W]	Mode	Ar flow [sccm]	p [Pa]	No. Fe screws	Substrate temperature T_s	Time [min]	Substrate holder
ZFe 3	600	DC	137	0.11	14	+8℃ , T_{float}	240	rotating
ZFe 3$_{int}$	600	DC	137	0.09	14	T_{int}	10×24 +P	rotating
ZFe 7	600	DC	137	0.11	36	+8℃ , T_{float}	240	rotating
ZFe 13	600	DC	137	0.11	59	+8℃ , T_{float}	240	rotating
ZFe 13_XPS	600	DC	137	0.08	59	+8℃	15	static
ZFe 13_VDA1	600	DC	137	0.08	59	T_{int}	5×24 +P	rotating
ZFe 13_VDA2	600	DC	137	0.08	59	T_{int}	8×24 +P	rotating
ZFe 13_VDA3	600	DC	137	0.08	59	T_{int}	10×24 +P	rotating

Table 2.8: Deposition parameters for magnetron sputtered zinc iron coatings.

With the zinc iron coatings additionally, "interval depositions" were made, where the entire deposition time was split in deposition cycles of 24 min with breaks of 10 min (=P). All other deposition parameters were kept the same. This procedure lead to an intermittent cooling of the samples in the deposition breaks and an intermediate deposition temperature T_{int} lying in between T_{float} and T_8. With coating ZFe 13_XPS, which has been also used for adhesion tests where the influence of interlayers on the coating adhesion have been studied, an titanium interlayer has been additionally deposited between the steel substrate and the zinc iron coating.

Sample	Sputter power [W]	Mode	Ar flow [sccm]	p [Pa]	No. Fe screws	Substrate temperature T_s	Time [min]	Substrate holder
ZTi 2	600	DC	137	0.11	9	+8℃ , T_{float}	240	rotating
ZTi 5	600	DC	137	0.11	22	+8℃ , T_{float}	240	rotating
ZTi 9	600	DC	137	0.11	32	+8℃ , T_{float}	240	rotating
ZTi 10	1000	RF	137	0.11	36	+8℃ , T_{float}	240	rotating

Table 2.9: Deposition parameters for magnetron sputtered zinc titanium coatings.

Sample	Sputter power [W]	Mode	Bias [V]	Ar flow [sccm]	p [Pa]	target	Substrate temperature T_s	Time [min]	Substrate holder
ZAl 4	600	DC	-290	137	0.08	2.7 at.% Al	+8 °C , T_{iso}	3×35+P	static
ZAl 2	600	DC	—	137	0.11	2.7 at.% Al	+8 °C , T_{float}	240	rotating

Table 2.10: Deposition parameters for magnetron sputtered zinc aluminium coatings.

Sample	Sputter power [W]	Mode	Ar flow [sccm]	p [Pa]	No. Cr screws	Substrate temperature T_s	Time [min]	Substrate holder
ZCr 3	600	DC	137	0.11	6	+8 °C , T_{float}	240	rotating
ZCr 11	600	DC	137	0.11	17	+8 °C , T_{float}	240	rotating

Table 2.11: Deposition parameters for magnetron sputtered zinc chromium coatings.

Sample	Sputter power [W]	Mode	Ar flow [sccm]	p [Pa]	No. Mg screws	Substrate temperature T_s	Time [min]	Substrate holder
ZMg 2	600	DC	137	0.11	9	+8 °C , T_{float}	240	rotating
ZMg 15	600	DC	137	0.11	18	+8 °C , T_{float}	240	rotating

Table 2.12: Deposition parameters for magnetron sputtered zinc magnesium coatings.

2.2.4.5   Deposition Parameters Ion Beam Sputtered Samples

Pure Zinc Coatings

The ion beam depositions were performed at a sputter gun beam voltage of 1500 V and an ion beam current of 30 mA. The gas flow into the sputter gun was set to 5 sccm delivering a working gas pressure of about $2 \cdot 10^{-2}$ Pa. The deposition time was set to 60 min. (Tab. 2.13)

Common parameters:	ion energy: 1500 eV, beam current: 30 mA, argon flow: 5 sccm, p=0.02 Pa, substrate holder: static, deposition rate: 4.4 Å/sec, t: 60 min						
sample	T_s [°C]	sample	T_s [°C]	sample	T_s [°C]	sample	T_s [°C]
ZIB_{-60}	-60	ZIB_0	0	ZIB_{+60}	+60	ZIB_{+120}	+120
ZIB_{-40}	-40	ZIB_{+20}	+20	ZIB_{+80}	+80	ZIB_{+140}	+140
ZIB_{-20}	-20	ZIB_{+40}	+40	ZIB_{+100}	+100	ZIB_{+160}	+160

Table 2.13: Deposition parameters for ion beam sputtered zinc coatings

To study the influence of the oxygen content in the sputter atmosphere on the development of whisker like structures, deposition experiments in oxygen "doped" sputter gas atmospheres have been performed. For this purpose very small flows of oxygen were added by a precision valve to the argon flow. With these flow parameters oxygen contents of 0.005 % to 7 % in the chamber atmosphere were realised. The gas composition was controlled by the quadrupole mass spectrometer. As substrate temperature $T_s =$ +70 °C was chosen since this temperature is little below the whisker growth threshold temperature of +75 °C. (Tab. 2.14)

Zinc iron coatings were performed according to Tab. 2.15. All samples were sputtered for 60 min with an ion energy of 1500 eV, a beam current of 30 mA and a substrate temperature $T_s =$ +150 °C. The gas flow into the sputter gun was set to 5 sccm delivering a working gas pressure of about $2 \cdot 10^{-2}$ Pa. The alloying content was altered by varying the number of iron screws in the mosaic target.

In IBAD experiments (section 2.1.3.2) the parameters of the sputter gun were kept identical to those of the unassisted deposition experiments described above. The assisting gun was either collimated,

Common parameters:	ion energy: 1500 eV, beam current: 30 mA, argon flow: 5 sccm, p=0.02 Pa, substrate holder: static, deposition rate: 4.4 Å/sec, t: 60 min	
sample	T$_s$ [℃]	sputter atmosphere [% O$_2$]
ZIB O1	70	0.05
ZIB O2	70	0.08
ZIB O3	70	1.4
ZIB O4	70	7

Table 2.14: Deposition parameters of ion beam sputtered zinc coatings in oxygen "doped" atmospheres

Common parameters:	ion energy: 1500 eV, beam current: 30 mA, argon flow: 5 sccm, p=0.02 Pa, substrate holder: static, t: 60 min				
Sample	ZFeIB 1	ZFeIB 2	ZFeIB 3	ZFeIB 4	ZFeIB 5
Number of Fe screws	6	10	13	15	17

Table 2.15: Deposition parameters of ion beam sputtered zinc iron coatings

what delivers spatially homogeneous ion beam current densities or focused giving a non uniform density distribution. The ion beam currents were varied between 2 and 8 mA, while the accelerating voltages were changed from 100 to 500 V. The argon flow into the assisting ion gun was set to 5 sccm. This resulted in a chamber pressure twice as high as the one of the unassisted depositions. The following Tab. 2.16 gives the deposition parameters of the ion assisted depositions.

Common parameters:	Sputter gun: ion energy: 1500 eV, beam current: 30 mA, argon flow: 5 sccm, Assisting gun: argon flow: 5sccm, p=0.04 Pa, substrate holder: static, t: 60 min						
				Assisting gun			
sample	T$_s$ [℃]	No. Fe screws	ion beam	ion energy [V]	current [mA]	ion current density [$\mu A/cm^2$]	
ZIB A1	25	—	collimated	300	2	18	
ZIB A1	25	—	collimated	300	4	35	
ZFeIB A1	150	6	focused	300	2	not uniform	

Table 2.16: Deposition parameters of ion beam sputtered and ion assisted coatings

2.3   Characterization

2.3.1   Morphology, Scanning Electron Microscopy SEM

To study the morphology of the coatings, fracture cross sections of the films deposited on silicon wafers and steel sheets were analysed by scanning electron microscopy. In case of the brittle silicon wafers the cross sections were prepared by breaking the wafers with wire cutting pliers. The breaking of the ductile steel sheets was done by making a slit in the back side of the samples, cooling the sample in liquid nitrogen and subsequent breaking of the cooled samples.

In a scanning electron microscope (SEM) a fine focused electron beam is scanned across the surface of the specimen. The irradiation of the sample with primary electrons leads to the emission of secondary electrons, backscattered electrons, auger electrons, x–rays and in some materials cathodoluminescence radiation. These radiations are measured by detectors and sent as an intensity modulating signal to a synchronously scanned cathode ray tube (CRT) or digital imaging system. The magnification of the SEM is given as the ratio of the image area displayed at the screen to the area scanned by the electron beam. The schematic of a SEM is depicted in Fig. 2.17. The scanning electron microscopes used here are a conventional SEM, 5400, Jeol Ltd., Tokyo, Japan and variable pressure SEM, 435 VP, LEO Elektronenmikroskopie GmbH, Oberkochen, Germany. The Jeol microscope is equipped with a lanthane hexaboride filament while the LEO instrument uses an tungsten filament for electron emission. Both

instruments have secondary electron (SEs)-, backscattered electron (BSEs)- and x–ray detectors, Link
Pentafet, Oxford Instruments Analytical, High Wycombe, UK. For analysis of the samples presented
within this study the electron beam accelerating voltages were varied between 5 and 15 kV. The obtained
images were digitally saved on a personal computer running the Oxford ISIS software and provided with
micron bars created with a calibrated reference sample.
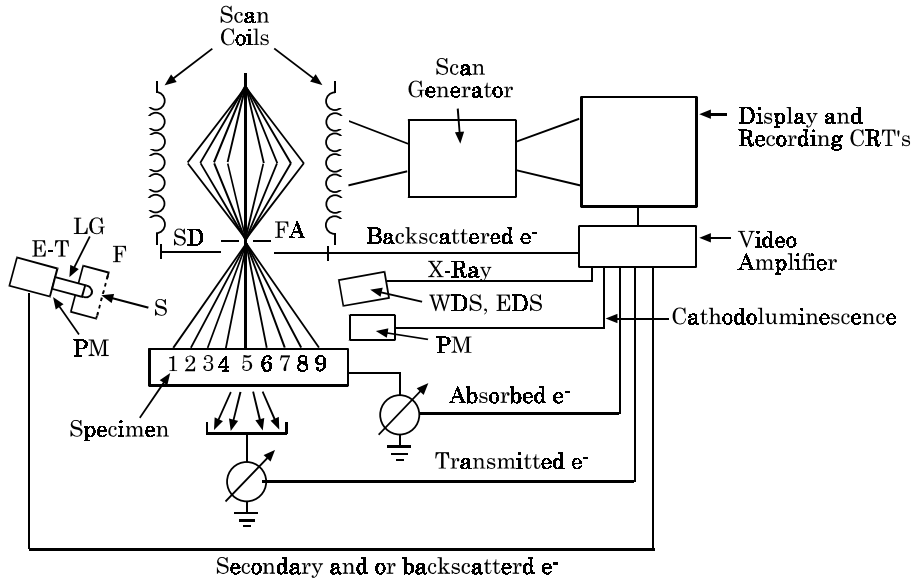
Figure 2.17: Schematic scanning electron microscope [115]

2.3.2   Topography, Scanning White Light Interferometry

To obtain information about the surface topographies of the coated steel sheets scanning white light
interferometry measurements were performed at the Universität des Saarlandes in Saarbrücken, Germany.
The instrument was a scanning white light interferometry microscope, New View 200, Zygo Corporation,
Middlefield, USA, whose working principle is shown in Fig. 2.18. Light from a white light source is
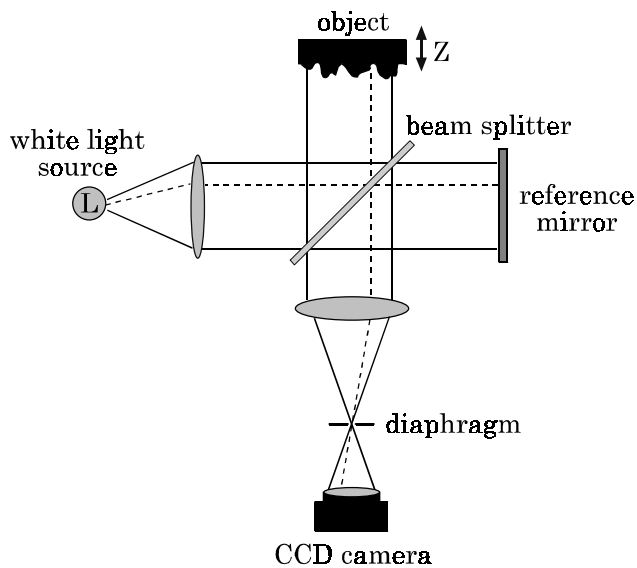
Figure 2.18: Working principle of a white light
interferometer [116]

collimated by a lens and passed to a beam splitter. One beam is sent to the sample to be measured, the

other to an internal reference mirror. After reflection, the beams recombine inside the interferometer, undergo constructive and destructive interference and produce a light and dark fringe pattern, which are imaged by the optics of a CCD–camera. By moving the sample with an piezo actuator to a different vertical position a different interference pattern is obtained since the path of the sample beam has been changed. By scanning the vertical axis, taking multiple interference patterns a three-dimensional interferogram of the surface is obtained. The interferogram gets transformed by the frequency domain analysis program MetroPro, Zygo which delivers quantitative two- and three dimensional graphs of the measured topography and quantitative surface roughness details. As roughness details the standardised surface roughness average R_a [μm] and the non-standardised peak to valley value PV are measured. The spatial resolution of the instrument is limited by the wavelength of the light. With the lenses used the spatial resolution is about $0.5\,\mu$m and the depth resolution about $0.5\,$nm. The measurements for this study were made at 40 fold magnification measuring a rectangular sample area of $313\,\mu$m $\times$ $231\,\mu$m.

Surface characteristics of workpieces are defined by the geometrical product specifications given in standard EN ISO 4287:1997 [117]. One surface characteristic is the R_a value calculated from a measured roughness profile. It is defined as the arithmetic average of the absolute values of the ordinate values $Z(x)$ within the single gauge distance l_m .

$$R_a = \frac{1}{l_m} \int_0^{l_m} |Z(x)|\, \mathrm{d}x \tag{2.3}$$

The R_a value equals the height of a rectangle, whose length is the total gauge length l_m and whose surface equals the sum of all surfaces included between the roughness profile and the middle line [118], see Fig. 2.19.
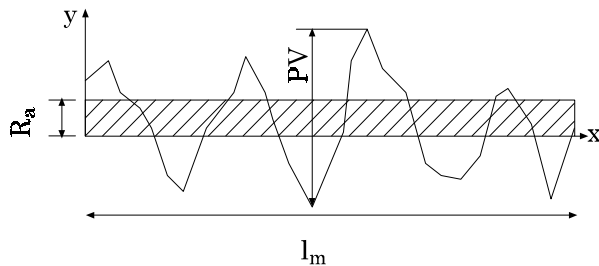
Figure 2.19: Determination of the surface roughness average R_a and PV

2.3.3 Roughness, Laser Profilometry

To measure the roughness of the coatings a laserprofilometer, RM 600 3–D/C, Rodenstock Präzisionsoptik GmbH, München, Germany is used. The system is based on a non–contact optical distance sensor which uses a dynamically focused infrared laser to measure the surface texture. The focal point of the laser on the surface is approximately $2\,\mu$m. During a line scan across the surface the vertical displacements of the objective lens needed to refocus the laser are inductively measured. These lens displacements are proportional to the vertical displacements of the topography. The system has a horizontal resolution of $1\,\mu$m and a vertical resolution of $0.01\,\mu$m. The contactless optical measurement has the advantage that it can be used also on delicate surfaces where a contact stylus of a traditional profilometer might cause damage to the surface. The profilometer is controlled by a computer program which analyses and displays the data according EN ISO 4287 [117]. For this study the average surface roughness R_a was measured.

2.3.4 Topography, Contact Angle Measurement

In addition to the topography measurements there was the idea to make the effect of the different topographies macroscopically visible. A material property which depends, apart from the surface chemistry,

also on the surface topography of a material is its wettability. The wettability of a solid material which is surrounded by a gaseous and a liquid phase depends on the ratio between the free surface energies liquid/gas γ_{LV}, solid/gas γ_{SV} and the free interfacial energy solid/liquid γ_{SL}. The energetic equilibrium state of a liquid droplet on a flat solid surface is described by Young's equation,

$$\gamma_{LV} \cos\theta = f_k(\gamma_{SV} - \gamma_{SL}) \qquad (2.4)$$

Where θ is the so called contact angle subtended at the triple line between the (flat) solid surface and the tangent plane to the liquid/vapour interface [119, 120]. In this case the Young's equation is modified for the correction of surface roughness by a factor f_k. Knowing the surface energies γ_{LV} and γ_{SL}, the surface energy γ_{SV} can be determined by measuring the contact angle θ. The wettability of a surface has an influence on its paintability (important for the use of the zinc coated steel sheet) or its property to be self cleaning (Lotus–effect) [121].
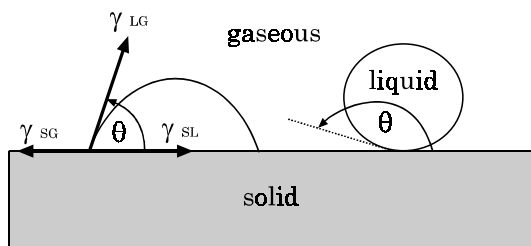
Figure 2.20: Contact angle

The contact angle measurements were performed with a contact angle meter, Digidrop, GBX, Romans sur Isère, France based on the sessile drop method. With this method a droplet ($10\,\mu$l) of a liquid, (in these experiments deionised water was used), is placed from a micro pipette onto the sample. The droplet wets the illuminated surface (cold light source) and is horizontally photographed by a CCD–camera with a macro lens. The photograph is digitally stored and displayed on a personal computer running the Digidrop software (GBX). The software allows the image analysis of the photographs for the determination of the droplet shape and the resulting measurement of the contact angle.

2.3.5 Mechanical Testing

2.3.5.1 Microhardness

To determine the hardness of the thin films and the base material, indentations with a microhardness tester FM-700, Future-Tech Corporation, Tokyo, Japan have been made. The microhardness tester performs a Vickers indentation test, where a diamond pyramid in the form of a square-based pyramid with an angle of 136° between faces is perpendicularly pressed into the surface of the material being tested. After removal of the load the diagonals d_1 and d_2 of the resulting indentation are measured, and the hardness number is calculated. The Vickers hardness number (HV), given in Eq. 2.5, is the ratio of the load applied to the indenter to the surface area of the indentation. In this equation 0.102 is a factor which adopts the applied load given in Newton according to the ISO standard to the formerly used load unit kgf (kilo gram force = kilopond), F is the applied load in Newton, d is the arithmetic mean of the two diagonals (d_1, d_2) in mm and $\Theta=136°$ is the angle between opposite faces of the indenter. The term microhardness usually refers to indentation hardness tests made with forces in the range of 0.098 to 1.96 N. For the indentations made in this study a load of 0.245 N (weight 25 g) has been applied for 15 s.

$$HV = \frac{0.102 \times F \times 2 \times \sin\left(\frac{\Theta}{2}\right)}{d^2} \qquad (2.5)$$

$$= 0.102 \times 1.854 \times \frac{F}{d^2} \qquad (2.6)$$
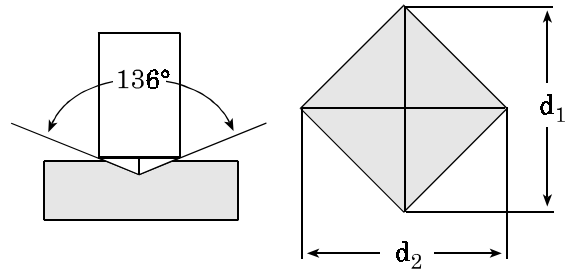
Figure 2.21: Vickers diamond pyramid

2.3.5.2 Coating Adhesion

In their application on steel sheets for automotive body parts coatings have to have very good adhesion and formability. They have to resist all machining and forming processes of the body parts without loss of adhesion. Since zinc coatings are very ductile and soft the widely used scratch test method for the determination of thin film adhesion can not be applied. A different test method must be used. In the future the automotive industry aims to use adhesive bondings as joining method to a much larger extent, as in today's aerospace industry. Due to this reason in this work two adhesion tests based on adhesive bondings were used [122].

Pull–Off Test To test the adhesion strength in normal direction of the coatings, pull–off tests similar to DIN EN 582 [123] were performed. The setup of the test is shown in Fig. 2.22. In preparation for the test a sand blasted steel stamp (A=480 mm^2) with a connector to a tensile test machine was vertically glued onto the coated side of a steel sheet. The adhesive used was a two component epoxy adhesive, Endfest 300, UHU®, Bühl, Germany with a maximum tensile strength of 30 MPa. To obtain this strength the adhesive bondings were cured at 180℃ for 20 min. The pull off test was performed with an electromechanical tensile test machine, RM 100, Schenk Trebel, Germany by loading the samples up to the failure of the adhesive bondings. Following this, the fractures were examined for their type of failure, see Fig. 2.23.
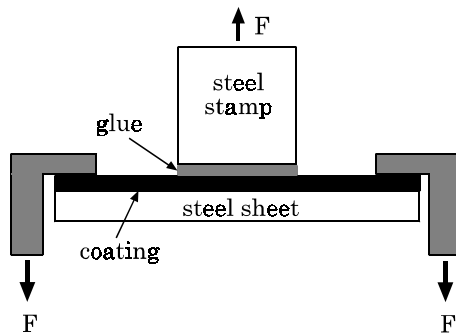
Figure 2.22: Pull–off test

Shear Test To test the adhesion strength in a direction parallel to the coatings, shear test similar to ASTM D 1002 [124] were applied. The specimens were single lap joints, comprising two steel sheet stripes (25 mm × 50 mm), horizontally glued on the coated sides with an overlap of 25 mm × 25 mm. As adhesive also here the two component epoxy Endfest 300 with the oven curing procedure was used. The cured samples were clamped to the jaws of the tensile test machine and pulled in tension up to the failure of the joining. Also here two types of joining failures could be observed: the cohesive fracture of the epoxy adhesive or the adhesive failure of the coating. [125]
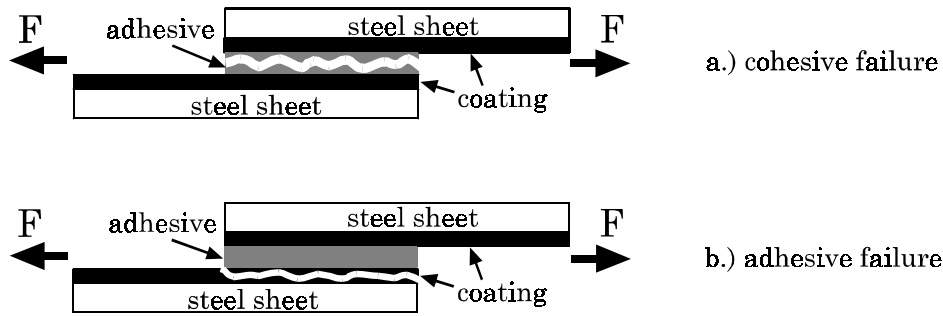
Figure 2.23: Fracture modes

Bending and Clinching Test   The aim of the bending and clinching tests was to check the adhesion of the samples under mechanical deformation. By bending the substrate–coating system stresses emerged in the coating, which might lead to failure of adhesion or crack generation.

In the bending tests coated steel stripes were bent around cylinders with outer diameters of 5 mm and 10 mm. The coated sides were facing outwards. In this way tensile stresses were created in the coatings. Subsequently the samples were embedded in an epoxy resin embedding mass, ground and metallographically polished. Finally, the specimens were examined with an optical microscope for delaminations and cracks.

In the clinching tests coated steel stripes, facing their coated sides outwards, were clinched by 180°. This resulted in very high tensile stresses in the coated outsides. Following the clinched areas were examined with a magnifying glass (Mag. 75 ×) for cracks and visible changes of the coatings.

2.3.6   Chemical Analysis

2.3.6.1   Electron Spectroscopy Methods

The basis for the identification of elements by Auger electron spectroscopy (AES), energy dispersive x-ray analysis EDX or x–ray photo electron spectroscopy (XPS) is atomic core electron spectroscopy whose principle is the following: If an atom is exposed to energetic radiation (electrons, ions, photons) there is a certain probability that an electron is released from an atomic shell and the atom is ionised. This process requires the energy of the incoming radiation to be higher than the binding energy of the electron. If the ionisation is due to the release of one of the electrons in the inner shells, the atom is in an excited, instable state. This state can be terminated by filling the vacancy with one of the outer shell electrons. With this transition an energy corresponding to that of the binding energy difference between the two shells is released. This energy is either emitted as characteristic x–ray radiation or transfered to a second electron in the electron shell, on its part emitted as an Auger- or photoelectron. Figure 2.24 depicts a schematic of possible electron transitions.

2.3.6.1.1   Energy Dispersive X–ray Analysis EDX   In the case of EDX (or EDS) [127, 128] the sample is irradiated by an electron beam. The electron radiation excites the atom and creates the electron vacancy in an inner shell. An electron from an outer shell fills the vacancy and emits an x-ray. The energy difference of the electron shells involved in the process determines the energy (wavelength) of the x–rays generated. If the transition occurs between the L and the K shell an K_α x–ray is emitted. Its energy $E_{K_{\alpha_1}}$ is given by

$$E_{K_{\alpha_1}} = E_K - E_{L_1} = \frac{hc}{\lambda_{K_{\alpha_1}}} \tag{2.7}$$

where E_K and E_{L_1} are the binding energies of the electrons in the K respectively L_1 shell, h Planck's constant, c the speed of light and $\lambda_{K_{\alpha_1}}$ the wavelength of the emitted photon. Other electron transitions
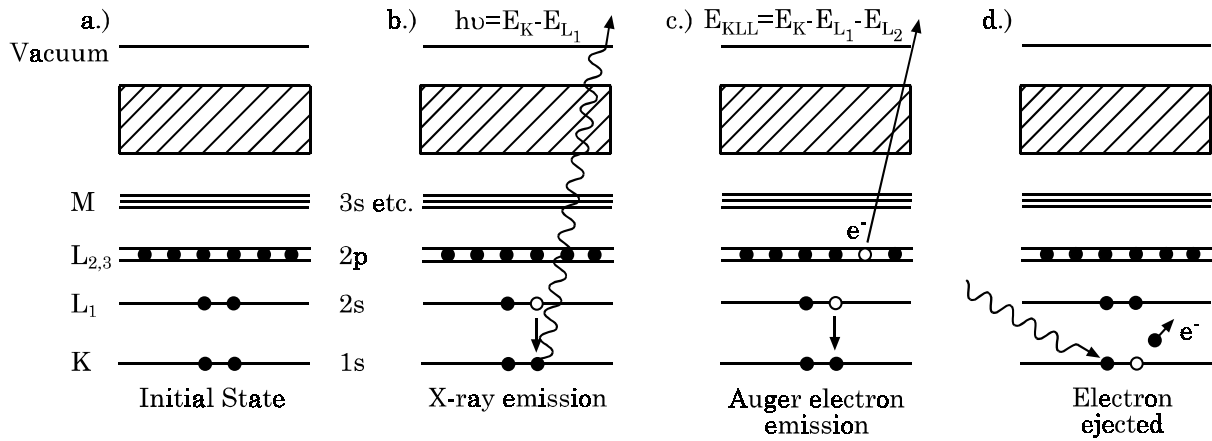
Figure 2.24: Schematic of electron transitions [126]

and resulting photons are: K_β x–rays stemming from $M \rightarrow K$ transitions and L_α x–rays stemming from $M \rightarrow L$ transitions. As every atom of the periodic table has its unique set of K, L, M shells also the emitted x–rays are characteristic for this particular element. This property can be used to identify elements by x-ray spectroscopy, where two types of spectrometers are in use: an energy dispersive spectrometer (EDX) and a wavelength dispersive spectrometer (WDX).

The spectrometers used in this study were energy dispersive spectrometers of Link Pentafet, Oxford, England which are part of the scanning electron microscopes described in section 2.3.1 on page 37. The spectrometers are based on Si(Li) semiconductor detectors. Before measuring, the detectors were calibrated with silicon or tungsten standards. With the EDX measurements the accelerating voltages of the SEM were set to 15 kV. Even at this relatively low electron energy the penetration depth of the electrons into the sample is several microns. In case of thin coated samples also the underlying substrate material gets irradiated and is visible in the spectrum. Since the detector window is made of beryllium the radiation of light elements ($Z \geq 11$) is strongly absorbed and therefore difficult to detect. Additionally, the radiation is absorbed by the sample itself. Due to this reason EDX is rather suitable for the detection and quantitative analysis of heavier elements.

2.3.6.1.2 Auger Electron Spectroscopy AES The Auger process [127, 129, 130] can be described as a series of events: First, primary radiation (electrons or photons) ionises the core level of the atom (e.g. the K shell) and creates a hole in the shell. This hole is filled by an electron from an outer shell whose excess energy is not channelled into the creation of a photon but is spent in ejecting an electron from a third level (e.g. L_2). The ejected electron is known as an Auger electron. Thus, in the end the radiated atom even contains two holes. The ejected Auger electron has an energy given by

$$E_{KL_1L_{2,3}} = E_K - E_{L_1} - E_{L_{2,3}} - \Phi = E_K - E_{L_{2,3}} - E_{L_1} - \Phi \qquad (2.8)$$

where E_K, E_{L_1} and $E_{L_{2,3}}$ are the binding energies of the electrons in the K, L_1 respectively $L_{2,3}$ shell and Φ the work function of the spectrometer. The equations show that the electrons have energies unique to each atom but some transitions like $KL_1L_{2,3}$ and $KL_{2,3}L_1$ can not be distinguished. For the intense lines in the Auger spectrum which are interesting for material analysis by AES the possibility of the energy release as Auger electron has a probability of 0.1 to 1. Due to this high ionisation probability, most often electron radiation is used as ionisation source for AES as analysis method. But even with this process the ratio of emitted Auger–electrons to incoming primary electrons is 10^{-4}. On the way from the ionised atoms to the surface the Auger electrons lose energy due to inelastic recoils with their neighbour atoms. Only electrons that reach the surface without loss of energy can be emitted and detected as Auger

electrons. Electrons with energy losses contribute to the background spectrum or do not even leave the surface. These aspects show that AES is a real surface analysis technique, sensitive only to some tens of nanometers of the surface. When measuring an energy spectrum (0 to 2 keV) the occurrence of Auger electron peaks allows the identification of all present elements, with exception of hydrogen and helium.

The AES measurements for this work were done with a Scanning Auger Multiprobe PHI 600, Perkin-Elmer Physical Electronics, Eden Prairie, USA at ST Microelectronics in Milan, Italy. When sputter etching the surface with an argon ion beam, the instrument can generate a depth profile of thinner samples. Since the investigated coatings had thicknesses of about 4–8 μm it would have been very time consuming to sputter etch the entire coating to obtain a depth profile. For this reason the depth profiles were made by line scans along a polished cross section of the samples. The spectrometer was operated at an accelerating voltage of 10 kV, a beam current of 10 nA and a beam diameter of 0.2 nm.

2.3.6.1.3   X–ray Photoelectron Spectroscopy XPS   X–ray photo electron spectroscopy [127,131, 132] is based on photo electron emission, the release of a core electron after its interaction with a soft x–ray photon (1–5 keV). Also known as electron spectroscopy for chemical analysis (ESCA) it is primarily used to determine the chemical environment of a known element in a given material. The measuring principle determining the kinetic energy E_{kin} of the emitted photo electron is based on the following equation

$$E_{kin} = h\upsilon - E_B - \Phi_{spec}$$

where $h\upsilon$ is the energy of the impinging photon, E_B the electron binding energy and Φ_{spec} the constant work function of the spectrometer. If the photon energy is known and the spectrometer work function is predetermined, the measurement of the kinetic energy delivers the desired binding energy of the electrons. As the binding energy is characteristic for each element and its chemical bonding it can be used as a fingerprint to identify the element and gives information about its environment. In comparison to AES, XPS has an important advantage since x–rays are less prone to damage surfaces than electrons. Like AES, XPS is a very surface sensitive analysis method.

The instrument used was a Nanoscan 50®, Riber-Cameca, France equipped with an x–ray source with exchangeable anodes: an aluminium anode (Al K_α = 1486.6 eV) or a magnesium anode (Mg K_α = 1253.6 eV). The energetic resolution of the system is about 0.5 eV. With a duoplasmatron ion gun, which can be focused, the surface of the sample can be cleaned from contaminations or eroded to create a depth profile. By taking a depth profile by ion beam etching, it is has to be taken into account that due to preferential sputtering a concentration shift can be observed.

2.3.7   X–Ray Diffraction Analysis XRD

X–ray diffraction represents the classical method for determining the crystalline structure of solid materials. It gives information about the lattice parameters and the type of unit cell. This information allows the identification of phases present, the determination of single crystal orientation, the preferred orientation of polycrystals, average crystallites sizes, or the measurement of defects and stresses in polycrystals. X–ray diffraction is based on Bragg's law

$$n\,\lambda = 2\,d_{hkl}\,\sin\Theta \tag{2.9}$$

where n is the order of reflection, λ the wavelength of the incoming x-rays, d_{hkl} the inter planar spacing for the planes (hkl) and Θ the Bragg angle.

The geometrical setup normally employed for the determination of the crystalline microstructure of materials is the conventional $\theta-2\theta$ (or Bragg-Brentano) geometry, shown in Fig. 2.25. With this geometry the incident beam impinges the sample surface under an angle θ versus the surface. The diffracted beam

is subsequently measured at an angle tilted by 2θ versus the incident beam. Depending on the material the penetration depth of x–rays is several microns to several hundred microns. For the analysis of thin films or modified surfaces this fact can be disadvantageous. The scattering from the underlying substrate may interfere or completely mask the signal from the film or the near surface regions. Due to this reason the glancing angle geometry was developed for the investigation of coatings and modified surface layers [133–135]. The schematic of this geometry, also referred to as GIAB (Grazing Incidence Asymmetric Bragg) geometry, is shown in Fig. 2.26. In this setup the angle of incidence ϕ of the impinging beam is very small (0.5–5°) and not varied during a scan. Only the detector is moved to the angle 2θ.
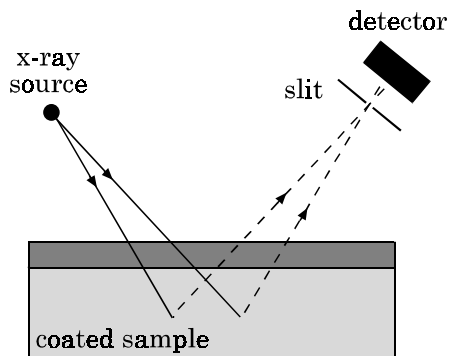
Figure 2.25: Bragg–Brentano geometry
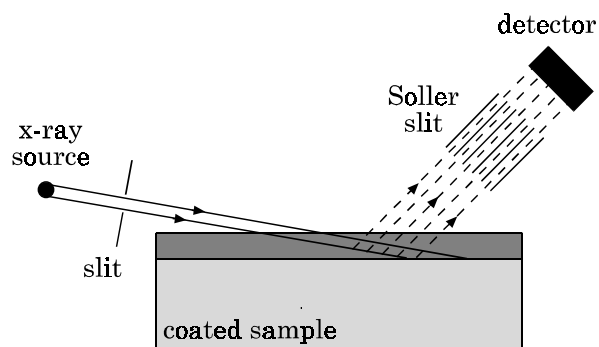
Figure 2.26: GIAB Grazing Incidence Asymmetric Bragg geometry

A difference between both geometries exists in the orientation of the respective crystal planes which contribute to diffraction. In case of the Bragg–Brentano geometry these are the planes parallel to the surface, see Fig. 2.27. The GIAB geometry on the other hand measures planes which are tilted at $\theta - \phi$ with respect to the surface, being ϕ the angle of incidence.
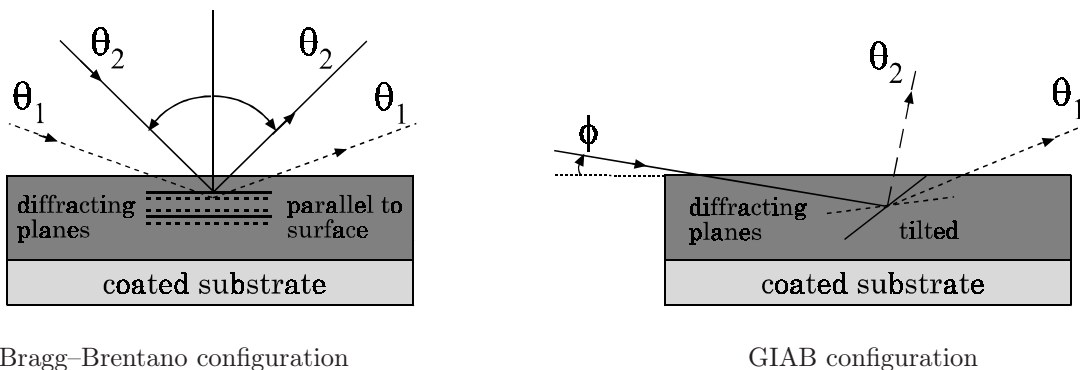
Bragg–Brentano configuration

GIAB configuration

Figure 2.27: Orientation of the lattice planes contributing to diffraction

The XRD instrument used here was constructed at the Joint Research Centre for the specific demands related to the investigation of thin films. It can be used for measurements in Bragg–Brentano and GIAB geometry and is described in detail in [136, 137]. The x–ray beam is delivered by an x–ray tube, Siemens, Germany with static copper anode. The tube was operated at an accelerating voltage of 35 kV and an emission current of 30 mA. The outcoming polychromatic x-ray beam is sent to two crossed slits, which adapt the incoming beam size to the geometry of the specimen. The diffracted beam passes a Soller–slit for angular resolution, and is detected by a solid state detector. The wavelength of the measured Cu–K$_\alpha$ radiation is the weighted average of the K$_{\alpha 1}$($\lambda = 0.1540562$ nm) and K$_{\alpha 2}$($\lambda = 0.1544390$ nm) which equals $\lambda = 0.15418$ nm. A channel–analyser filters the Cu–K$_\alpha$ radiation out of the amplified detector signal. The filtered signal is finally measured and stored via a data acquisition card on a personal computer running a LabVIEW® program. This program additionally controls the stepper motors for positioning

the sample- and detector stage. In the experiments made for this work a 2θ range of 10–90° was scanned in steps of 0.2°. Depending on the intensity measured the measuring period per step was varied between 5 and 15 sec. The instruments angular resolution is about 0.15°.

For the identification of the phases the measured x–ray spectra were compared with reference data from the JCDPS (Joint Committee on Powder Diffraction Standards) database [138]. For the determination of unknown phases which are not included in the database, literature simulations for x–ray spectra from calculated unit cells were done. For this purpose the simulation software Carine was used [139].

2.3.8 Corrosion Testing

2.3.8.1 Electrochemical Corrosion Testing

The electrochemical measurements were performed in an electrochemical standard cell, EG&G, Princeton, USA with a two or three electrode configuration as shown in Fig. 2.28. Mounting of the specimen has been carried out in a way that only the coated surfaces of the steel sheets have been exposed to the saline solution via a window with a Teflon® sealing. The working electrode area was $1\,cm^2$. A standard calomel electrode (SCE), connected to the working electrode (specimen) via a Haber–Luggin capillary tube, was used as reference electrode. The measurements were performed with a potentiostat 272, EG&G, which is controlled by a personal computer running the SoftCorr® III Corrosion Measurement software, EG&G.

The test solutions were acetate buffered sodium chloride solutions with different concentrations. The current potential measurements were made in 3.5 wt.% solutions. For the potential time measurements 5 wt.% solutions were used, making these measurements comparable to salt spray tests. As corrosion is strongly influenced by the pH of the solutions, which may drop due to dissolving of CO_2 from air, the pH had to be kept constant. This was achieved by buffering the solution by adding 72.5 g of sodium acetate to 1 l of the solution and adjusting the pH to 6.8 by adding acetic acid. Phosphate- and borate buffers usually used in this pH–range were not applicable as they react with zinc to form zinc phosphates or -borates.
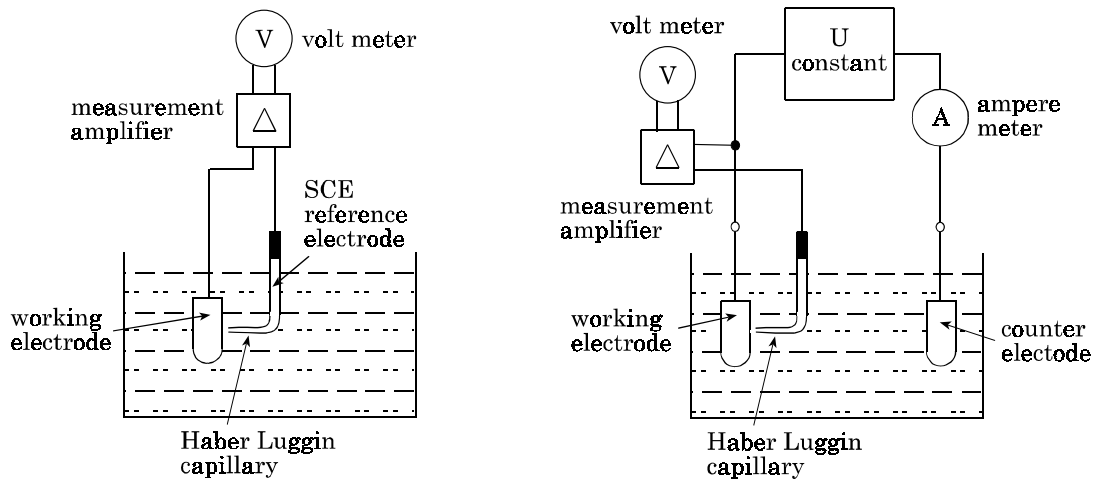
Figure 2.28: Electrochemical cells in two and three electrodes configuration according to DIN 50918 [140]

2.3.8.1.1 Current Density / Potential Measurements With the current density/potential measurements a potential E, measured against a reference electrode, is applied to the working electrode. This potential moves the specimen away from its equilibrium potential also referred as open circuit potential (OCP). The current I flowing in response between the working electrode and the platinum counter electrode tries to reestablish the electrochemical equilibrium in the system. It is recorded as a function of

the potential. By sequential scanning of a potential range, a so called current density/potential plot is obtained.

For the experiments made here the respective scan was started after an initial delay of 90 min. The delay was set in a way that the electrochemical cell system was able to condition a constant OCP value as a reference point for the scan range to be measured, without the occurrence of distinct chemical reactions influencing the measurements [141]. The scan range was set from OCP-200 mV to 0 mV, scanned in potential steps of 0.5 mV at a scan rate of 0.05 $^{mV}/_{sec}$. To establish stable conditions in the electrochemical system the current was measured after a delay time of 10 sec after applying the respective potential.

2.3.8.1.2   Open Circuit Potential / Immersion Time Measurements   The open circuit potential/ immersion time measurements are performed with a two electrodes setup. In this measurement the potentiostat records the change in equilibrium potential E (working electrode/reference electrode; OCP) versus time. The respective experiment was stopped when the OCP reached a stable value close to the potential of the blank steel substrate at about -720 mV vs. SCE.

2.3.8.2   Accelerated Corrosion Testing

Accelerated corrosion tests such as salt spray tests (ASTM B 117–73, DIN 50021–SS) or the VDA 621-415 test allow the assessment of the corrosion performance of coated metal substrates and a prediction of their long term performance in service. In these tests the samples are subjected to regulated environments within a chamber. During the test one or more of the relevant environmental variables can be changed and/or varied cyclically to accelerate the corrosion of the specimen. As the tests create an artificial environment that exaggerates the conditions occurring in service, the test period is extremely short. Correspondingly, the tests deliver only comparative values for the corrosion property one tries to determine.

2.3.8.2.1   Salt Spray Testing DIN 50021   The salt spray tests according to standard DIN 50021–SS "Sprühnebelprüfungen mit verschiedenen Natriumchlorid-Lösungen" [142] were performed at Zeuna Stärker, Augsburg, Germany. The system was a salt spray cabinet SC 1000, Weiss Umwelttechnik, Reiskirchen-Lindenstruth, Germany with a volume of 950 l. During the test at a cabinet temperature of $35 \pm 2\,°C$ the samples are exposed to a continuous spray of an aqueous 5 ± 0.5 wt.% sodium chloride solution. The standard requires that the pH of the collected spray must be in the pH–range of 6.5 to 7.2 (at $23 \pm 2\,°C$). The amount of the spray has to be adjusted in the way that in a period of 16 h in a collecting vessel with an horizontally oriented collecting surface of 80 cm^2 an average volume of 1.5 ± 0.5 $^{ml}/_h$ is collected. During the test the samples are exposed to ambient atmosphere with an global average concentration of approximately 350 ppm CO_2 [143].

In the tests performed for this study five samples of the same coating type, each having an area of 50 mm $\times$ 50 mm, were glued with a neoprene glue onto an acrylic glass support. In this way five sample gave one sample set. The uncoated edges of the samples were masked with a two component car paint to prevent rust at these spots. The acrylic glass supports were mounted on acrylic glass racks in the salt spray cabinet, in the way that the face of the specimens to be tested were inclined at 60–75 ° to the horizontal. The setup in the saltspray cabinet can be seen in Fig. 2.29. The chamber was opened in intervals of 8 and 16 h for inspection of the samples. As a failure criterion the occurring of red rust, visible by eye, on at least three specimens per set was defined.

2.3.8.2.2   Cyclic Corrosion Testing VDA 621-415   Since salt spray test results (e.g. DIN 50021–SS, ASTM B117) of painted and galvanised steel sheets are surprisingly inferior to those of simply painted steel, the car- and steel industry developed new cyclic corrosion tests which provide a more reliable evaluation of the corrosion resistance of coated car body steel sheets [24, 144].
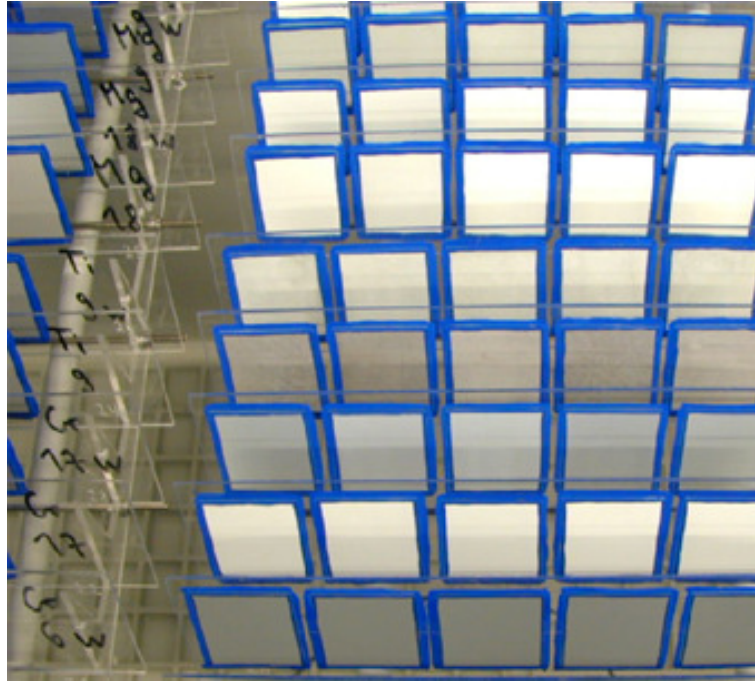
Figure 2.29: Saltspray cabinet with sample racks

The cyclic corrosion test which was applied in this work is the VDA 621–415: "Prüfung des Korrosionsschutzes von Kraftfahrzeuglackierungen bei zyklisch wechselnder Beanspruchung" of the German "Verband der Automobilindustrie e.V." [145]. The test was performed within the BRITE-EURAM project "PVD alternatives to conventional zinc coatings" by BMW, Munich, Germany. The test serves to assess the corrosion protection of car paints in an accelerated laboratory test generating the corrosion processes and corrosion effects quite similar to those occurring in service. The test especially tests the spread of blistering at an injured paint system.

For this purpose the zinc and zinc alloy coated samples were painted with a varnish system, generally used in the car production at BMW. Following this, the painted specimens were scribed down to the blank metal with a hardened graver. The obtained scribe had a width of 0.5 mm. Subsequently, the samples were mounted in the test chamber inclined at 60–75 ° to the horizontal with the scribe mark running perpendicular from the top to the bottom. The test duration was set to 10 cycles (10 weeks), one cycle comprising

1 day	=	24 h salt spray test according DIN 50021–SS
		(35℃, 100 % humidity)
4 days	=	4 cycles condenswater-cycle climate according to DIN 50017–KFW
		(Each cycle: 8 h at 40℃, 100% humidity;16 h at 20℃, 50 % humidity)
2 days	=	48 h at roomtemperature according DIN 50014
		(18 to 28℃, 50 % humidity)

After test stop the samples were rinsed with water and dried with compressed air. They were evaluated according to visible changes. As evaluation parameter the VDA tests measure the average spread of blistering U_d. For this purpose the spread width is measured at different points of the scribe mark and their arithmetic average is calculated. The spread of blistering U_d is given as $U_d = \frac{d - d_0}{2}$, where d is the average width of the blistered zone and d_0 the width of the original scribe mark.

Chapter 3

Results and Discussion

3.1 Morphology Evolution

3.1.1 Deposition Temperature Dependency

3.1.1.1 Magnetron Sputtered Zinc Coatings

Depending on the sputter parameters and the mounting of the substrates on the substrate holder, the magnetron sputtered zinc coatings show a huge variety of different morphologies. They range from an open, sponge like morphology, to a porous grainy morphology or a dense compact columnar structure. Table 3.1 gives the coating thicknesses of the samples whose morphologies are presented from Fig. 3.1 to Fig. 3.11.

Sample	ZA	ZB	ZC	ZD	ZE	ZF	ZG
T_{float}	15.5	7.8	4.9	2.5	—	—	—
$T_s = +8\,°C$	3.4	3.7	6.3	2.5	20	—	—
T_{iso}	—	—	—	—	—	17.5	26

Table 3.1: Coating thicknesses [μm] of magnetron sputtered zinc coatings.

Figures 3.1 and 3.2 show the cross-sections of the samples ZA_{float} and ZA_8. Coating ZA_{float} has an open, porous, sponge like structure and consists of a network of small dendrites. Due to this reason the film is very rough and a general, uniform surface is missing. The actual thickness of 15.5 μm was determined by averaging "hills and valleys". In contrast to sample ZA_{float} sample ZA_8 deposited in the same batch, shows a compact, dense, columnar structure, which forms a relatively smooth surface. The column diameter is about 0.2–0.8 μm. A big difference between these coatings can be noted with their thicknesses. With a thickness of 3.4 μm coating ZA_8 is approximately a factor of five thinner than ZA_{float} (15.5 μm).

The film growth of ZB_{float}, shown in Fig. 3.3, starts with a fine grainy structure. With increasing film thickness the small crystallites transform to round, bud like grains with polygonal surfaces and very different grainsizes. The structure is very porous and has a rough surface. Coating ZB_8 shown in Fig. 3.4 has a dense, columnar structure. With this specimen a transformation in the growth behaviour can be seen after $\approx 1/6$ of its final thickness. At this point the fine, columnar structure growing from the substrate-film interface changes to bigger columns. The column diameter is about 0.2–1.4 μm. The formed surface is quite smooth.

Coating ZC_{float}, shown in Fig. 3.7 and 3.9, has a typical columnar structure, corresponding to the Zone II type described in the structure zone models of Thornton [146] and Messier et al. [147]. With increasing coating thickness the columns are growing in diameter and get separated by voids. The grain

size is about 0.55–4.2 μm. Sample ZC$_8$, shown in Fig. 3.8 and 3.10, also belongs to the Zone II type. The coating is denser packed and presents less voids. The columns are easier to distinguish and do not change their diameter significantly with increasing coating thickness. The grain size is 0.095–1.650 μm. The surface of the film is quite smooth. As the deposition parameters of the ZC-samples (t$_{dep}$ =240 min at 600 W (DC) and rotating substrate holder) provided the best results of all pure zinc deposition experiments, these parameters were chosen for all the following zinc alloy depositions.

Sample ZD$_{float}$, shown in Fig. 3.5, has an open, worm like structure. The coating consists of completely separated grains, which form a non uniform surface. The column diameter is about 0.25–0.65 μm. In contrast to this sample coating, ZD$_8$ has a dense, compact, columnar microstructure. Its surface is quite smooth and the column diameter is about 0.15–0.65 μm.

Figure 3.11 shows the cross-section of sample ZE$_8$, with a large coating thickness of 20 μm. Also this film has a dense structure with very fine columns with column diameters of 0.82 μm and a very smooth surface.

Figure 3.12 displays the detailed cross-section of sample ZF$_{iso}$, which was deposited on an inox steel–mesh, which thermally isolated the substrate from the cooled substrate holder. The coating has a sponge like structure with a network of small dendrites.

A similar structure can be observed with sample ZG$_{iso}$, given in Fig. 3.13. Figure 3.14 gives a detailed view of ZG$_{iso}$, where flower like agglomerates of very small grains create interesting three dimensional structures.

3.1.1.2   Ion Beam Sputtered Zinc Coatings

The obtained thicknesses of the pure zinc films deposited in the temperature range of -60 ℃ up to +160 ℃ are given in Tab. 3.2.

sample	d [μm]	sample	d [μm]	sample	d [μm]	sample	d [μm]
ZIB$_{-60}$	1.6	ZIB$_0$	1.4	ZIB$_{+60}$	2.1	ZIB$_{+120}$	6.2
ZIB$_{-40}$	1.8	ZIB$_{+20}$	1.6	ZIB$_{+80}$	1.9	ZIB$_{+140}$	7
ZIB$_{-20}$	1.9	ZIB$_{+40}$	2.1	ZIB$_{+100}$	2.4	ZIB$_{+160}$	5.5

Table 3.2: Thicknesses of ion beam sputtered zinc coatings

The major fact observed with the ion beam sputtered pure zinc samples is the strong dependence of the coating morphology on the substrate temperature T$_s$. The change in morphology with deposition temperature is macroscopically already visible by eye. The appearance of the samples changes from a silver, metallic appearance for the coolest sample deposited at -60 ℃, to a bright, matt, grey for samples deposited at +40 ℃, to a dark, matt grey for the warm deposited samples with T$_s$ = +100 ℃. The SEM images in Fig. 3.15 to 3.26 on pages 54 and 55, show the cross-sections of ion beam sputtered pure zinc coatings. The coating deposited at the lowest deposition temperature T$_s$ = -60 ℃= 0.31 T$_m$ shows a dense, very compact columnar structure. The single columns are very fine, with an average column diameter of about 0.1–0.2 μm. The surface of the coating is very smooth and only at very few points outgrowing nodular flaws can be observed. With increasing substrate temperature the surface gets rougher and more separate grains protrude from the main surface. Additionally, an increase in column diameter can be noted. At a substrate temperature of T$_s$ = 0 ℃= 0.39 T$_m$ a flat surface is not visible anymore. The tops of the relatively large diameter columns (0.2–0.35 μm), generate a much rougher surface. With increasing temperature this trend proceeds and the grains become more and more separated, see Fig. 3.20. With further increase in temperature the columnar structure completely disappears and the growing crystals build an open, worm like structure. Beyond a transition temperature of about T$_s$ = +75 ℃= 0.5 T$_m$ the appearance of long whiskers or whisker like structures can be observed, see Fig. 3.22. Generally the term "whisker" is reserved for long thin and straight single crystals with
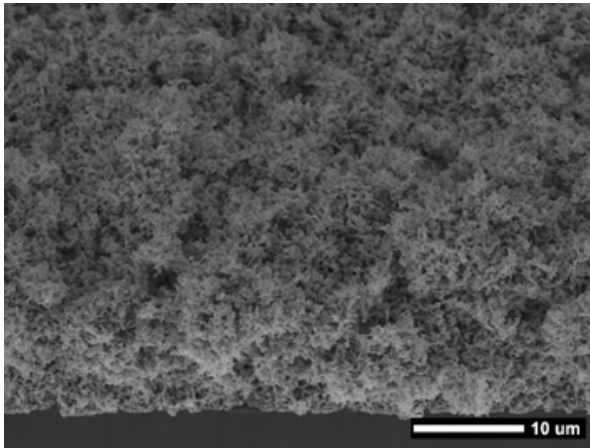
Figure 3.1: Coating ZA_{float} deposited at sputter power 400 W (RF), 50 V Bias, $T_s = T_{float}$ and static substrate holder
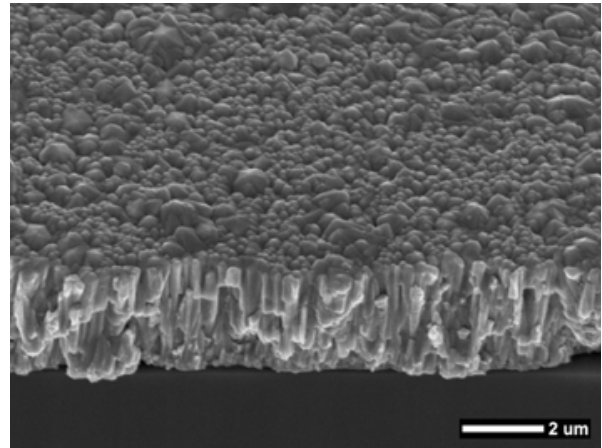
Figure 3.2: Coating ZA_8 deposited at sputter power 400 W (RF), 50 V Bias, $T_s = +8$ ℃ and static substrate holder
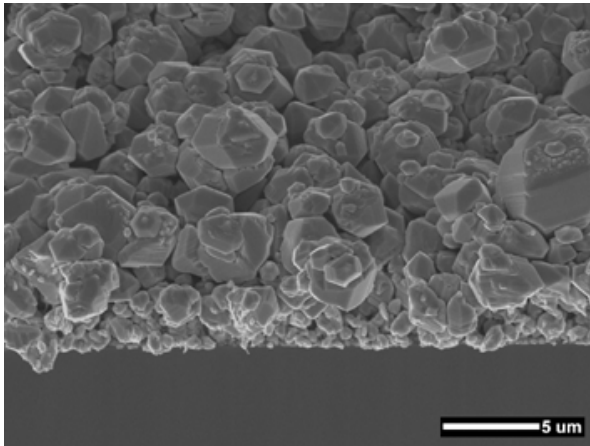
Figure 3.3: Coating ZB_{float} deposited at sputter power 400 W (RF), 50 V Bias and $T_s = T_{float}$
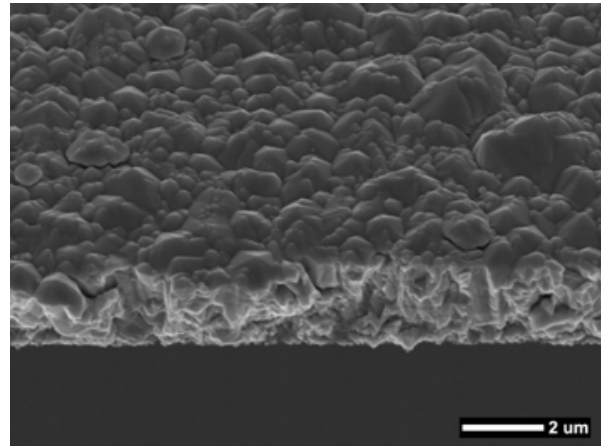
Figure 3.4: Coating ZB_8 deposited at sputter power 400 W (RF), 50 V Bias and $T_s = +8$ ℃
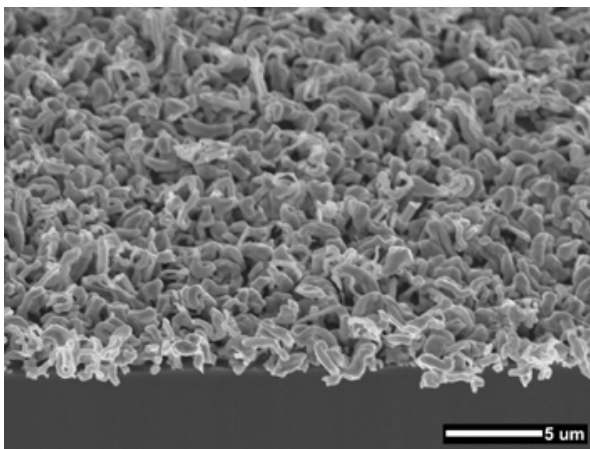
Figure 3.5: Coating ZD_{float} deposited at sputter power 800 W (RF), 150 V Bias, $T_s = T_{float}$ and static substrate holder
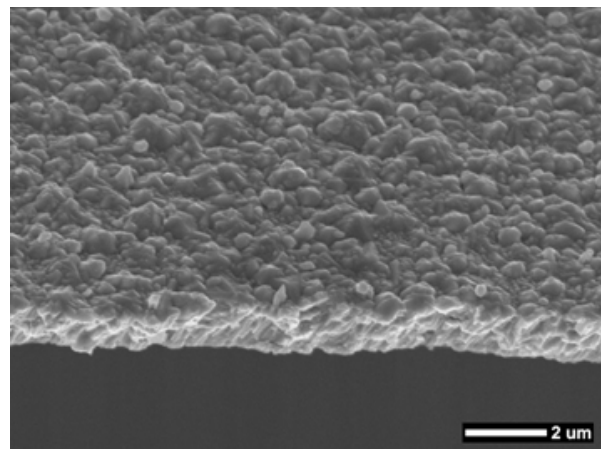
Figure 3.6: Coating ZD_8 deposited at sputter power 800 W (RF), 150 V Bias, $T_s = +8$ ℃ and static substrate holder
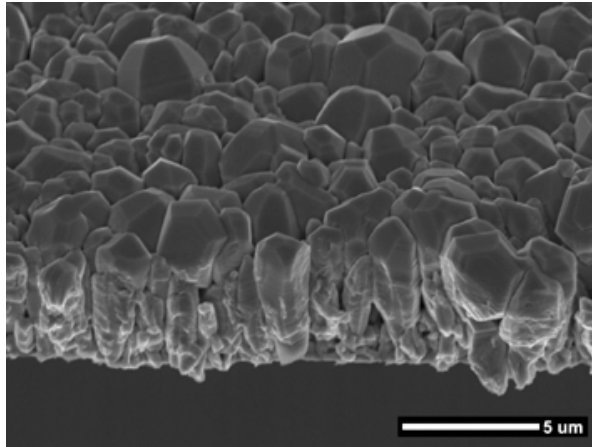
Figure 3.7: Coating ZC$_{float}$ deposited at sputter power 600 W (DC) and T$_s$ = T$_{float}$
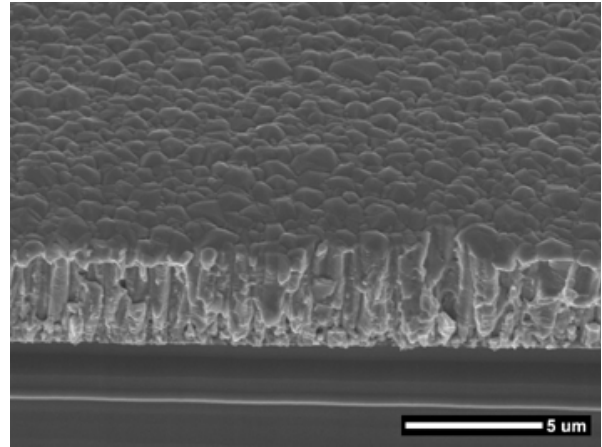
Figure 3.8: Coating ZC$_8$ deposited at sputter power 600 W (DC) and T$_s$ = +8 ℃
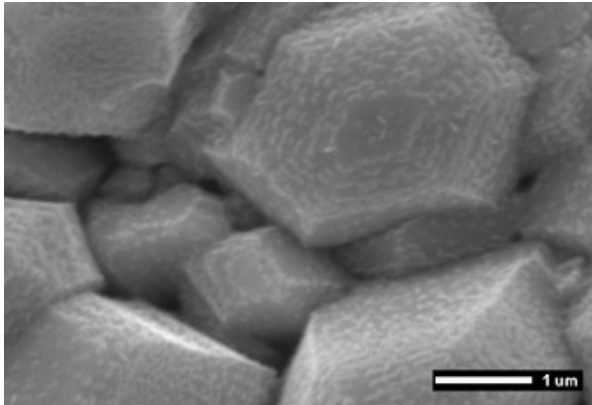
Figure 3.9: Detailed view ZC$_{float}$ on steel, Mag: 20k
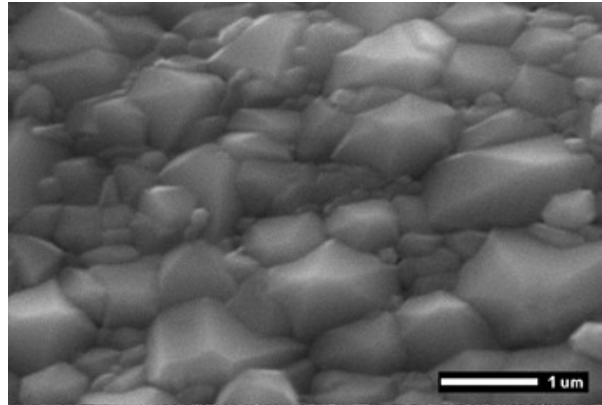
Figure 3.10: Detailed view ZC$_8$ on steel, Mag: 20k
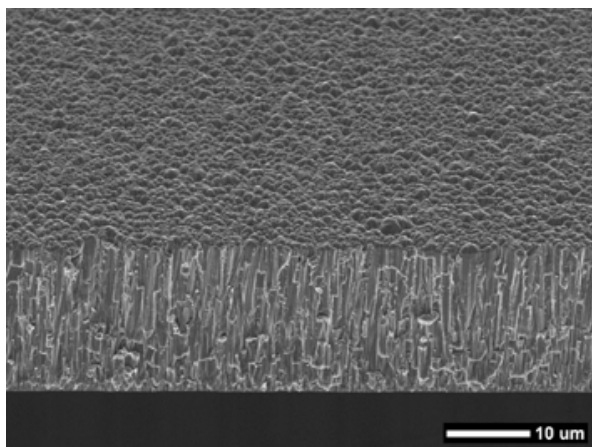
Figure 3.11: Coating ZE$_8$ deposited at sputter power 1000 W (RF), 100 V Bias and T$_s$ = +8 ℃
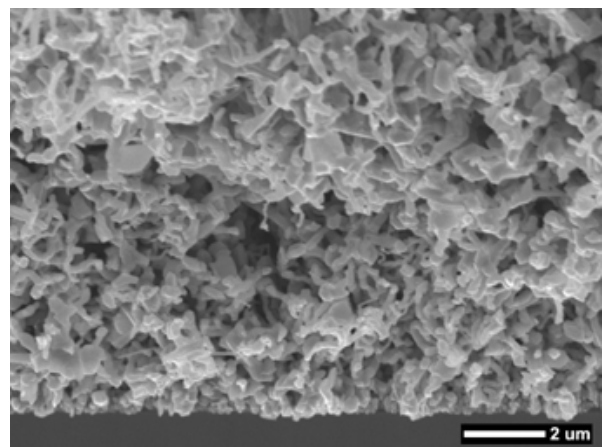
Figure 3.12: Detailed view on the sponge like network of small dendrites of coating ZF$_{iso}$ deposited at sputter power 600 W (RF), T$_s$ = T$_{iso}$ and static substrate holder
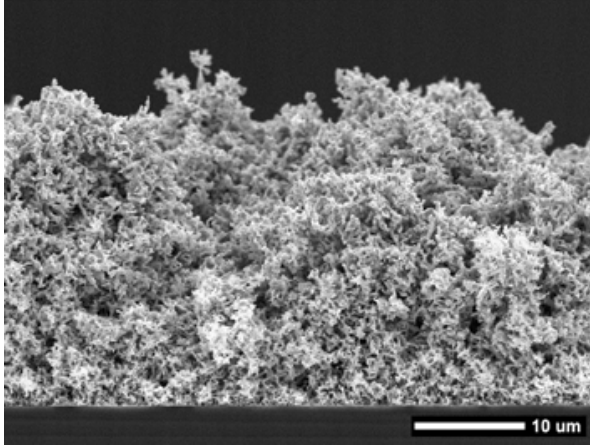
Figure 3.13: Coating ZG_{iso} deposited at sputter power 600 W (RF), 290 V Bias, $T_s = T_{iso}$ and static substrate holder
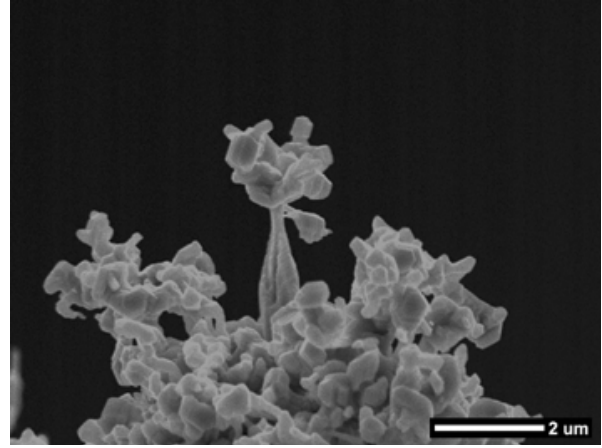
Figure 3.14: Detailed view of a coating ZG_{iso}

uniform cross-section along their length [148, 149]. With further increase of the substrate temperature to $T_s = +100\,°C = 0.54\,T_m$ the coating becomes more open and woolen like with a pronounced growth of whisker like structures, which create a three dimensional network. This growth behaviour is also observed at a substrate temperature of $T_s = +160\,°C = 0.62\,T_m$.

3.1.2 Influence of Alloying

3.1.2.1 Zinc Iron

3.1.2.1.1 Magnetron Sputtered Zinc Iron The zinc iron coatings ZFe 3, ZFe 7 and ZFe 13 have been deposited with the deposition parameters given in Tab. 2.8. They differ only in the alloyed iron content, changed by the number of iron screws screwed in the zinc–iron mosaic target. Table 3.3 gives the thicknesses, grain sizes and chemical compositions of the magnetron sputtered zinc alloy coatings measured by EDX.

Sample	Thickness [μm]		Grainsize [nm]		Composition [at.%]	
	T_{float}	$T_s = +8\,°C$	T_{float}	$T_s = +8\,°C$	T_{float}	$T_s = +8\,°C$
ZFe 3	8.3	6.9	50–580	60–870	2.7	3.3
ZFe 7	6.5	6.2	100–450	100–330	6.8	6.5
ZFe 13	6.6	6	50–1000	50–180	13.2	13.6

Table 3.3: Coating thicknesses and compositions of magnetron sputtered zinc iron coatings.

Figures 3.27 to 3.38 show the respective cross-sections and surfaces of ZFe 3_{float} to ZFe 13_8 with iron contents varying from 2.7 to 13.6 at.% Fe. The first sample ZFe 3_{float} (Fig. 3.27) with an alloy content of 2.7 at.% Fe has a grainy, cauliflower like structure. Small grains with a grain size of 50–580 nm build up agglomerates generating a porous structure with a surface that is nevertheless not too rough. Sample ZFe 3_8 (Fig. 3.28) with an iron content of 3.3 at.% Fe has a compact, dense structure, with a grain size of 60–870 nm.

Sample ZFe 7_{float} (Fig. 3.31) with a higher iron content of 6.8 at.% Fe exhibits a compact, dense columnar structure. The grain size is about 100–450 nm. The cool deposited sample ZFe 7_8 (Fig. 3.32) from the same batch with an iron content of 6.5 at.% Fe has the same columnar structure at decreased grain size of 100–330 nm.

Sample ZFe 13_{float} (Fig. 3.35) with an iron content of 13.2 at.% Fe has a compact columnar structure. At the coating base a dense, compact, uniform region without visible grains is observed. After $1/9$ of the final coating thickness this uniform structure changes to a columnar growth with a grain size
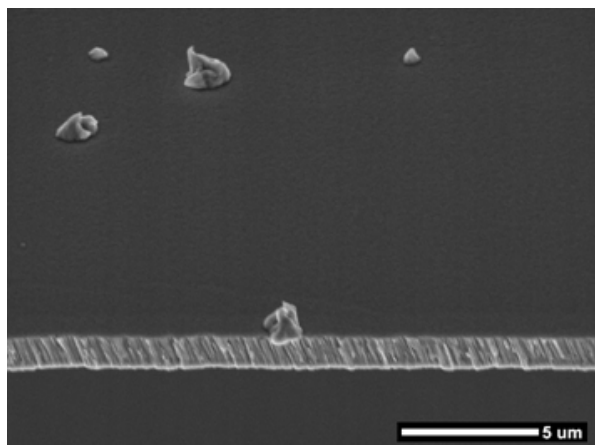
Figure 3.15: Ion beam sputtered zinc coating, $T_s = -60$ ℃
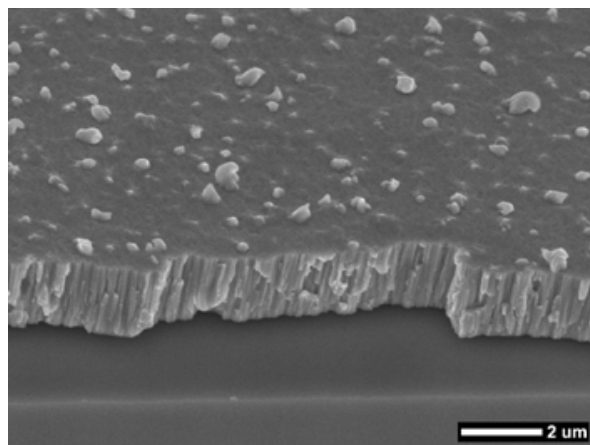
Figure 3.16: Ion beam sputtered zinc coating, $T_s = -40$ ℃
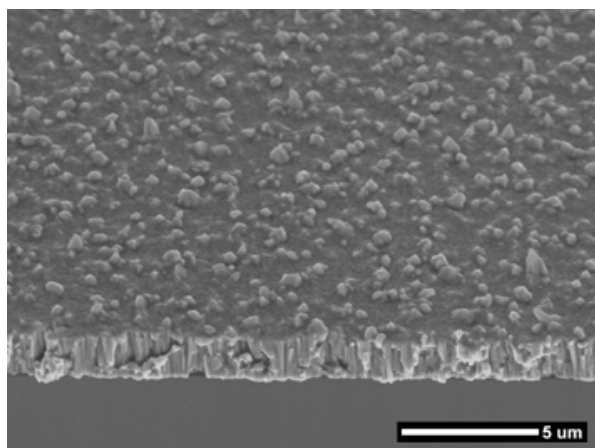
Figure 3.17: Ion beam sputtered zinc coating, $T_s = -20$ ℃
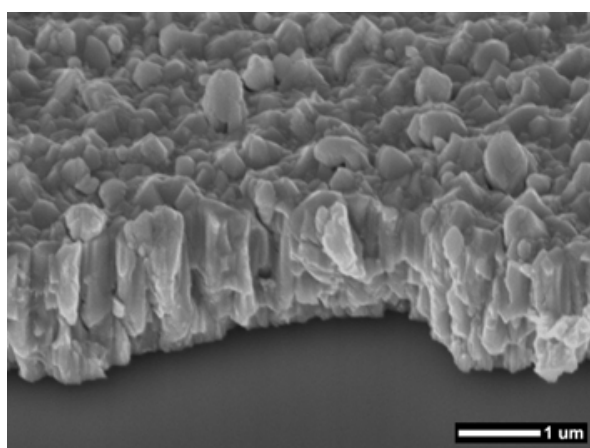
Figure 3.18: Ion beam sputtered zinc coating, $T_s = 0$ ℃
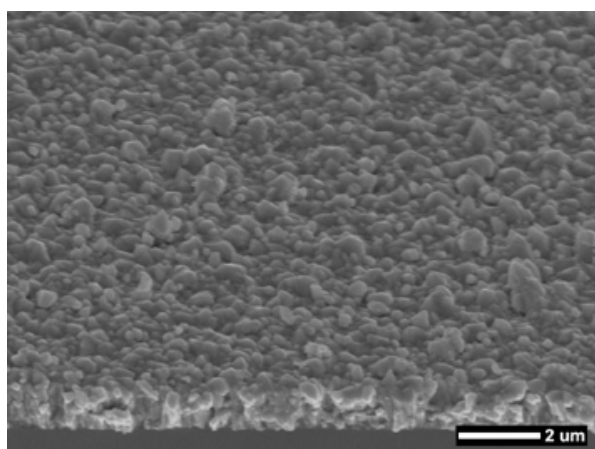
Figure 3.19: Ion beam sputtered zinc coating, $T_s = +20$ ℃
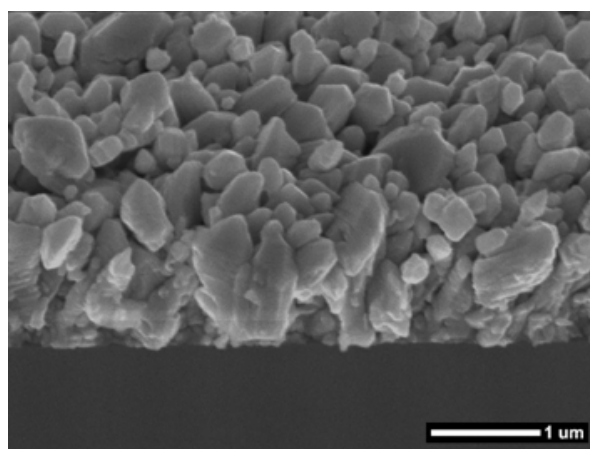
Figure 3.20: Ion beam sputtered zinc coating, $T_s = +40$ ℃
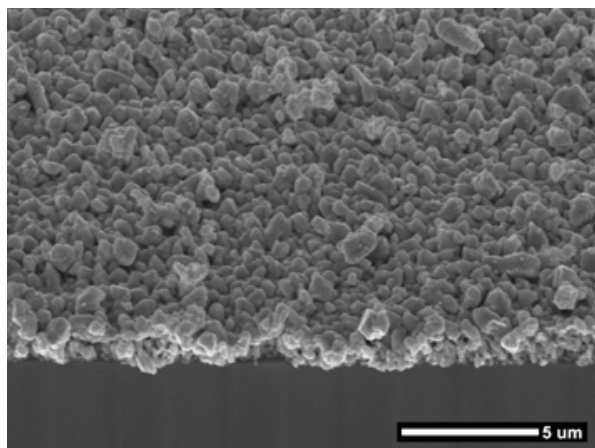
Figure 3.21: Ion beam sputtered zinc coating, $T_s = +60$ ℃
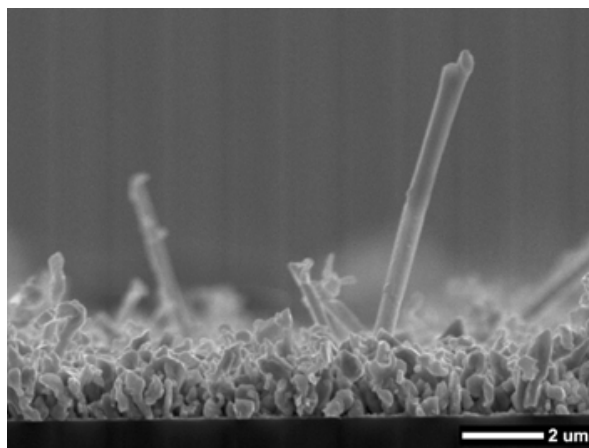
Figure 3.22: Ion beam sputtered zinc coating, $T_s = +80$ ℃
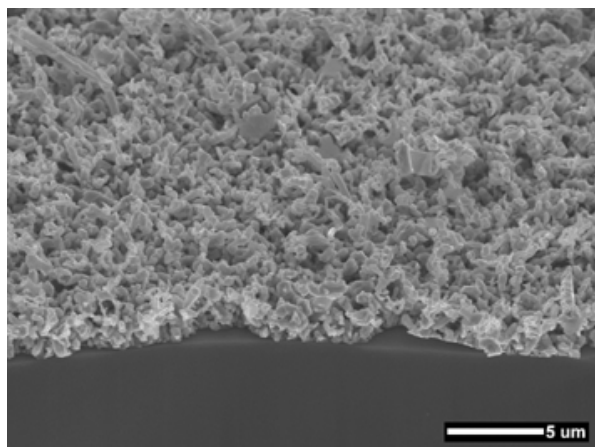
Figure 3.23: Ion beam sputtered zinc coating, $T_s = +100$ ℃
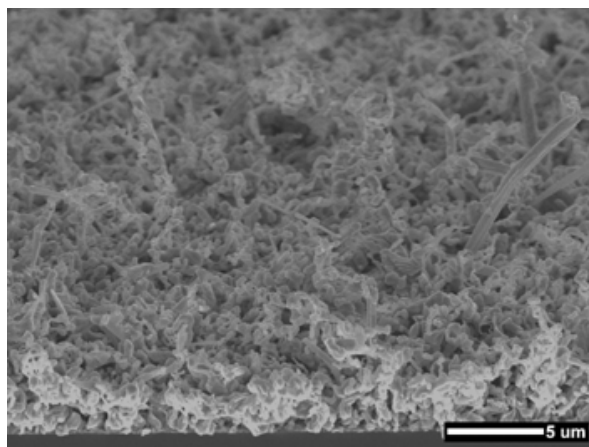
Figure 3.24: Ion beam sputtered zinc coating, $T_s = +120$ ℃
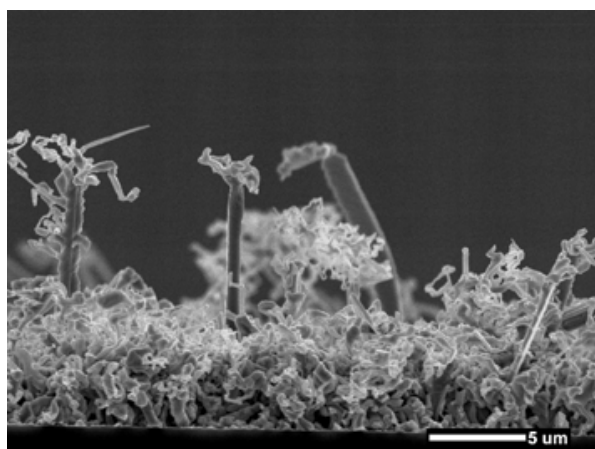
Figure 3.25: Ion beam sputtered zinc coating, $T_s = +140$ ℃
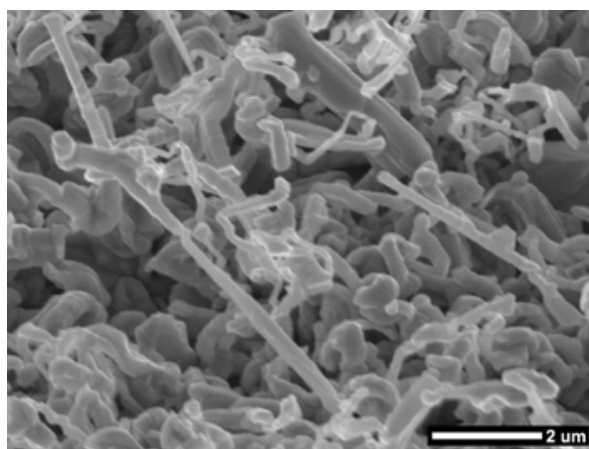
Figure 3.26: Ion beam sputtered zinc coating, $T_s = +160$ ℃

of 50–1000 nm. Also the film growth of the highest alloyed coating ZFe 13$_8$ (Fig. 3.36) with an alloy content of 13.6 at.% Fe, starts at the substrate interface with a compact, dense structure without visible grains. Following this, the structure changes immediately to a compact columnar structure, whose column diameter increases continuously with increasing coating thickness. The created surface with grains ranging from 50–180 nm is very smooth.

3.1.2.1.2 Ion Beam Sputtered Zinc Iron Coatings The SEM images in Fig. 3.39 to 3.43 show the influence of the iron alloying content on the morphology of ion beam sputtered zinc iron coatings. All samples were sputtered for 60 min with an ion energy of 1500 eV, a beam current of 30 mA and a substrate temperature T_s = +150 °C. The alloying content was altered by varying the number of iron screws in the mosaic target according to Tab. 3.4, which additionally displays the reached film compositions and thicknesses.

Sample	ZFeIB 1	ZFeIB 2	ZFeIB 3	ZFeIB 4	ZFeIB 5
Number of Fe screws	6	10	13	15	17
Composition [at.%]	2.6	4.7	7.8	11.5	14.5
Thickness [μm]	4	3.3	2.3	0.7	0.9

Table 3.4: Coating thicknesses and compositions of ion beam sputtered zinc iron coatings

The low alloyed coating ZFeIB 1 (2.6 at.% Fe, Fig. 3.39) has an open, worm like structure with separated grains and rough surface. The same growth behaviour occurs for ZFeIB 2 (Fig. 3.40) at an iron content of 4.7 at.% iron. With increasing iron content of 7.8 at.% Fe (ZFeIB 3, Fig. 3.41) a thin, coherent, columnar film grows, covering the whole substrate. At many spots the film is interrupted by outgrowing worm like crystallites, which appeared already at the lower alloying contents. With further increase of alloying to 11.5 at.% Fe (ZFeIB 4, Fig. 3.42) the number of outgrowing crystallites is strongly reduced. At the highest iron content of 14.5 at.% iron (ZFeIB 5, Fig. 3.43) the outgrowing crystallites disappeared completely. The film finally consists only of fine columns, which generate a very even surface. This change in morphology by variation of the alloying content is also visible by eye. The low alloyed coatings have a dull, dark grey appearance which changes with increasing alloy content to dull, bright grey and then to the shiny, silver, metallic appearance of ZFeIB 5.

3.1.2.2 Zinc Titanium

The depositions of the zinc titanium coatings ZTi 1 to ZTi 10 have been performed with the deposition parameters given in Tab. 2.9. Like the zinc iron depositions also here the alloying content of the mosaic target has been altered by varying the number of added titanium plates. Figures 3.44 to 3.59 present the SEM cross-sections and surfaces of these samples.

Sample	Number of Ti plates	Thickness [μm]		Grainsize [nm]		Composition [at.%]	
		T_{float}	T_s = +8 °C	T_{float}	T_s = +8 °C	T_{float}	T_s = +8 °C
ZTi 1	9	5.6	8.5	45–550	110–570	1.2	1.7
ZTi 5	22	5.4	4.9	170–930	170–1350	5	5.5
ZTi 9	32	4.6	3.6	150–2350	550–2300	9.8	9.4
ZTi 10	36	8	5.9	650–4500	570–2600	7.7	11.1

Table 3.5: Coating thicknesses and compositions of magnetron sputtered zinc titanium coatings.

The lowest alloyed sample ZTi 1$_{float}$ (Fig. 3.44) with an alloying content of 1.2 at.% Ti consists of fine grained agglomerates which generate an open, porous structure. The grainsize of the agglomerating grains is 45–550 nm. Coating ZTi 1$_8$ (Fig. 3.45) with a titanium content of 1.7 at.% has a similar morphology at a grain size of 110–570 nm.
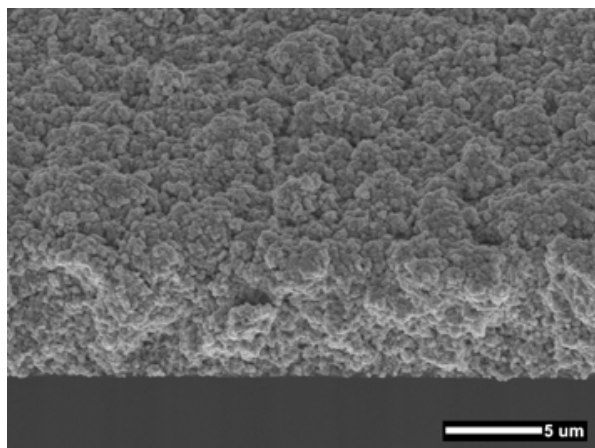
Figure 3.27: Zinc iron coating $ZFe\,3_{float}$ with 2.7 at.% Fe
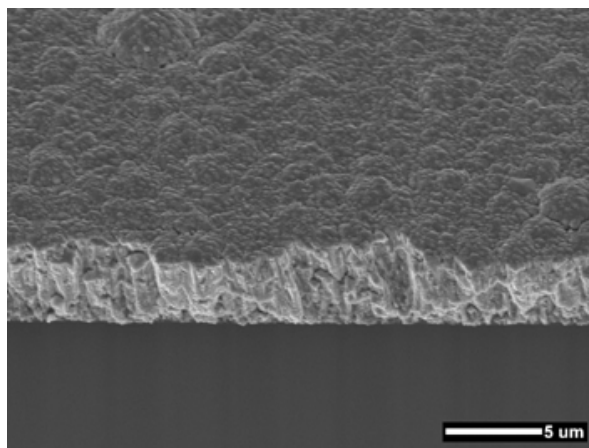
Figure 3.28: Zinc iron coating $ZFe\,3_8$ with 3.3 at.% Fe
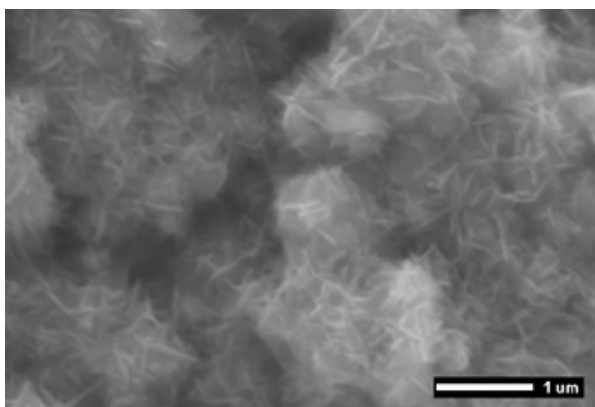
Figure 3.29: Detailed view $ZFe\,3_{float}$ on steel, Mag: 20k
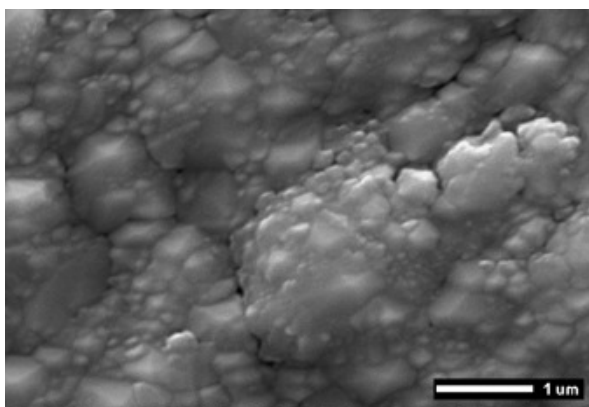
Figure 3.30: Detailed view $ZFe\,3_8$ on steel, Mag: 20k
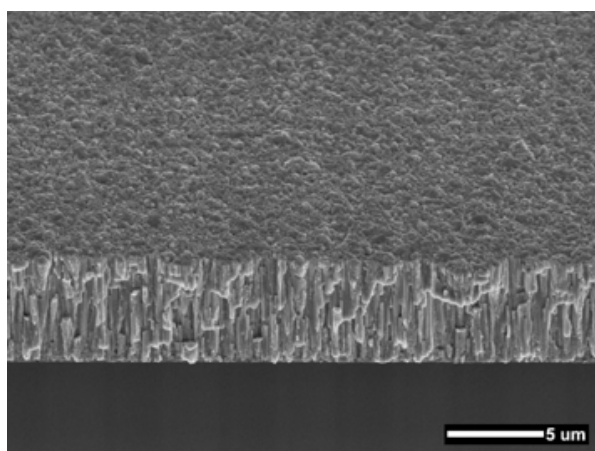
Figure 3.31: Zinc iron coating $ZFe\,7_{float}$ with 6.8 at.% Fe
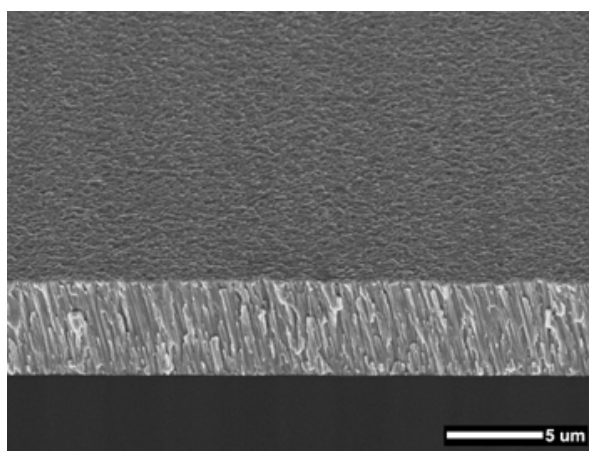
Figure 3.32: Zinc iron coating $ZFe\,7_8$ with 6.5 at.% Fe
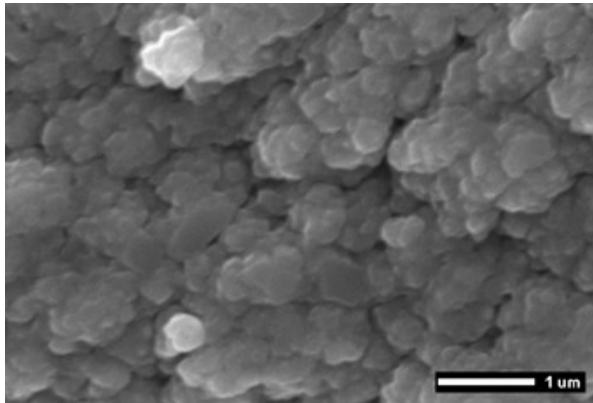
Figure 3.33: Detailed view ZFe 7$_{\text{float}}$ on steel, Mag: 20k
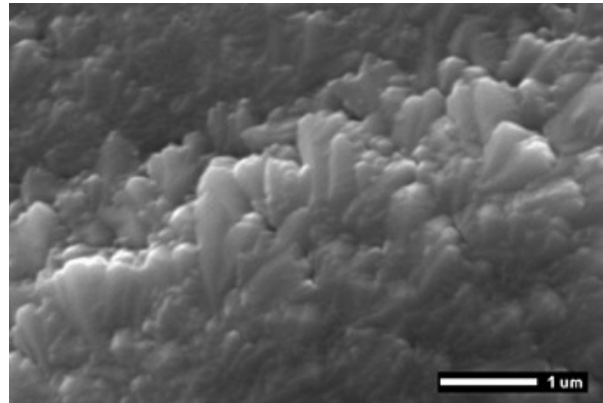
Figure 3.34: Zinc iron coating ZFe 7$_8$ on steel, Mag: 20k
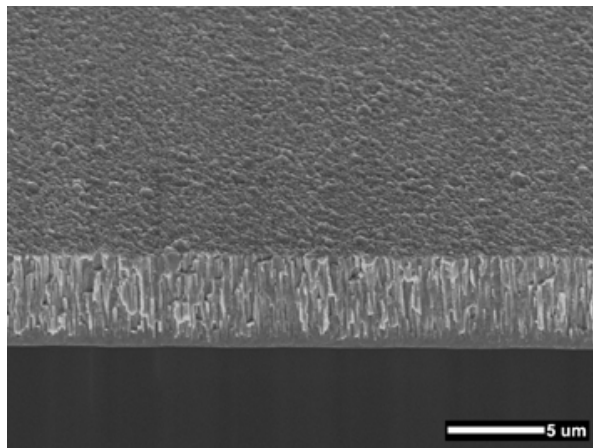
Figure 3.35: Zinc iron coating ZFe 13$_{\text{float}}$ with 13.2 at.% Fe
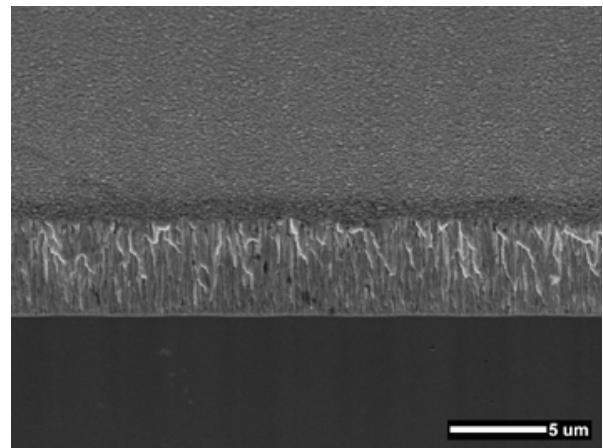
Figure 3.36: Zinc iron coating ZFe 13$_8$ with 13.6 at.% Fe
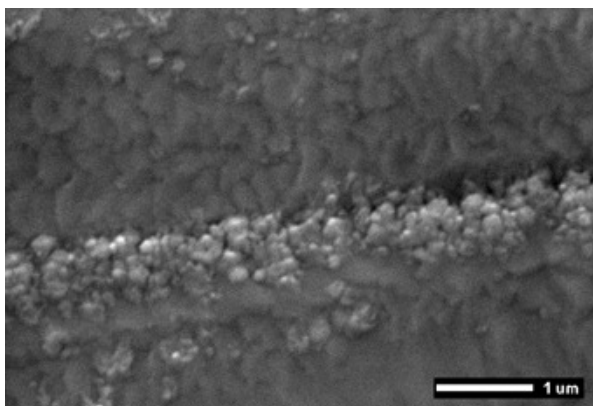
Figure 3.37: Detailed view ZFe 13$_{\text{float}}$ on steel, Mag: 20k
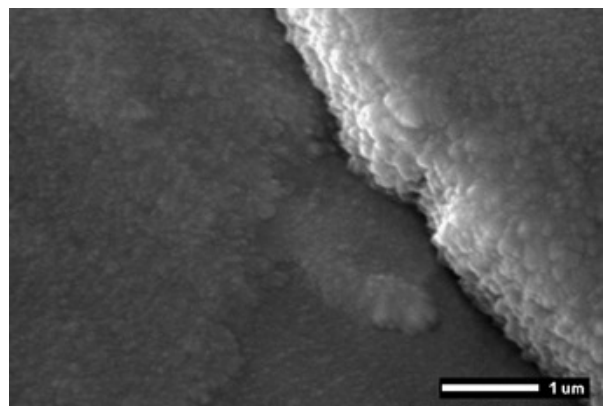
Figure 3.38: Detailed view ZFe 13$_8$ on steel, Mag: 20k
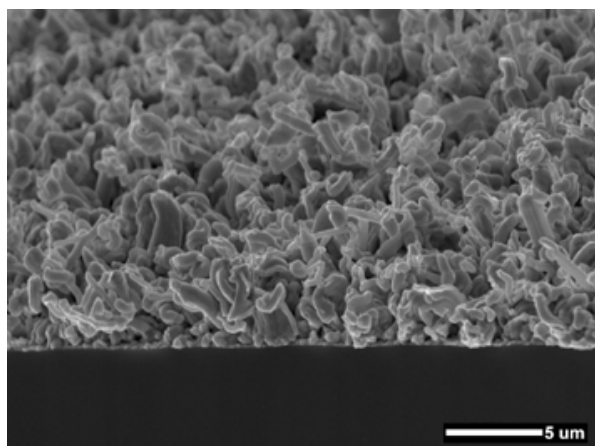
Figure 3.39: Zinc iron coating ZFeIB 1 alloyed with 2.6 at.% iron
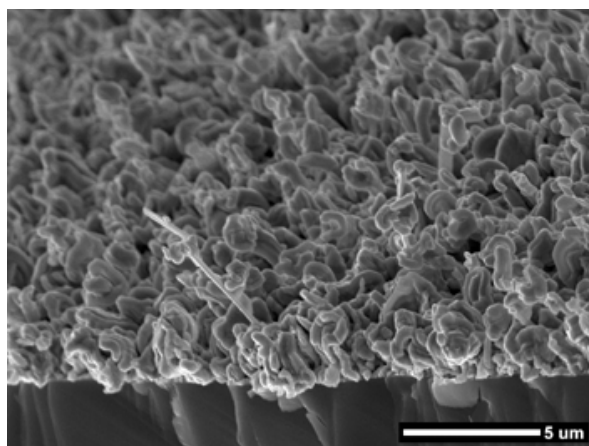
Figure 3.40: Zinc iron coating ZFeIB 2 alloyed with 4.7 at.% iron
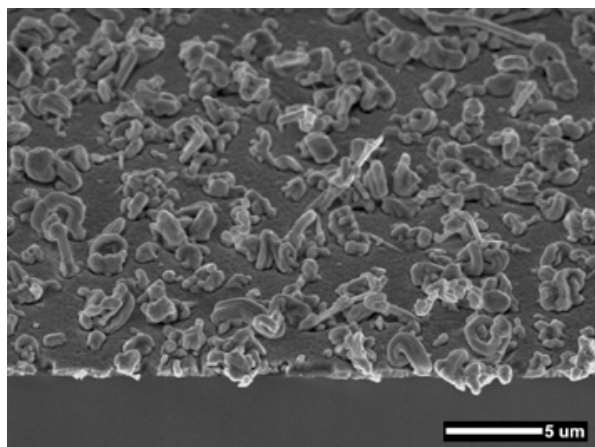
Figure 3.41: Zinc iron coating ZFeIB 3 alloyed with 7.8 at.% iron
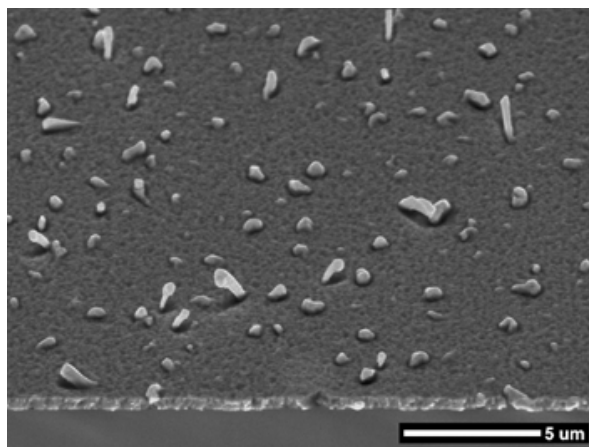
Figure 3.42: Zinc iron coating ZFeIB 4 alloyed with 11.5 at.% iron
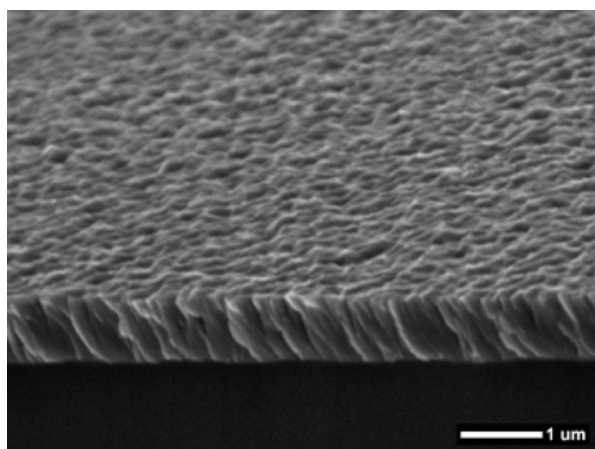
Figure 3.43: Zinc iron coating ZFeIB 5 alloyed with 14.5 at.% iron

With coating ZTi 5$_{\text{float}}$ (Fig. 3.48) alloyed with 5 at.% Ti, at the coating base, dent like columns are visible. At about the half of the thickness a grainy structure of agglomerates develops, exhibiting a cauliflower like appearance. Also sample ZTi 5$_8$ (Fig. 3.49) with an alloy content of 5.5 at.% shows this type of morphology.

The higher alloyed coating ZTi 9$_{\text{float}}$ (9.6 at.% Ti, Fig. 3.52) starts to grow in a compact dense structure, where no single grains can be distinguished. In the middle of the thickness the morphology changes. From here on, round grains grow out of the film surface. Coating ZTi 9$_8$ (Fig. 3.53), from the same batch, with a titanium content of 9.4 at.% reveals a compact, dense structure over the entire thickness. Apart from very few flaws the evolving surface is very smooth.

The deposition with the highest titanium content of the target, where the sputter mode has been changed to RF mode, results for coating ZTi 10$_{\text{float}}$ (Fig. 3.56) in a lowered titanium content of 7.7 at.%. The structure is compact and dense. Looking at the surface, smooth round grains can be noticed. These grains have diameters of 650–4500 nm. Sample ZTi 10$_8$ (Fig. 3.57) has a compact, dense structure with grains ranging in size from 570–2600 nm. The obtained surface is the smoothest one of all deposited zinc- and zinc alloy coatings.

3.1.2.3   Zinc Aluminium

The deposition details of the zinc aluminium coatings ZAl 4 and ZAl 2 are given in Tab. 2.10. The thicknesses and compositions of the coatings obtained by EDX are listed in Tab. 3.6. Figures 3.60 to 3.65 show the morphologies of these coatings.

Sample	Thickness [μm]		Composition [at.%]	
		T_s=+8 °C		T_s=+8 °C
ZAl 4	T_{iso}: 23	2.6	T_{iso}: 3.9	4.5
ZAl 2	T_{float}: 9.7	6.9	T_{float}: 2.2	2.6

Table 3.6: Coating thicknesses and compositions of magnetron sputtered zinc aluminium coatings.

With samples ZAl 4 there was the idea to grow two films under extremely different thermal conditions. One part of the samples was glued with heat conducting paste onto the water cooled substrate holder which allowed a deposition at T_s=+8 °C. The second part was placed onto an inox steel mesh, which nearly completely isolated the samples thermally from the substrate holder. The substrate holder was not rotating in this experiment. The thermally isolated deposited coating ZAl 4$_{\text{iso}}$ (Fig. 3.60) has an open, sponge like structure. The entire coating consists of a network of small dendrites, which do not create a real surface. Its thickness is 23 μm. The cooled coating ZAl 4$_8$ (Fig. 3.61) has a columnar structure whose surface is interrupted at several points by outgrowing nodular grains. With 2.6 μm its thickness is about a factor of ten smaller than the one of ZAl 4$_{\text{iso}}$.

The film growth of sample ZAl 2$_{\text{float}}$ (Fig. 3.62) starts with a dense, grainy structure. After about 1/3 of the final thickness the morphology changes to porous, grainy agglomerates with a grain size of 25–680 nm, generating a cauliflower like surface. The grainsize of 25–500 nm of ZAl 2$_8$ (Fig. 3.63) is comparable to that of ZAl 2$_{\text{float}}$. Also here the upper part of the coating becomes more porous, but in this case it is still more dense than the structure of ZAl 2$_{\text{float}}$.

3.1.2.4   Zinc Chromium

The zinc chromium coatings ZCr 3 and ZCr 11 have been deposited with the deposition parameters given in Tab. 2.11. The obtained coating thicknesses, grainsizes and compositions measured by EDX are given in Tab. 3.7 below. Figures 3.66 to 3.73 show the cross-sections and surfaces of these films. Coating ZCr 3$_{\text{float}}$ (Fig. 3.66) with the lowest alloying content of 2.9 at.% Cr shows a column like structure. The single columns, which have a grainy appearance, are difficult to distinguish since their contours are not
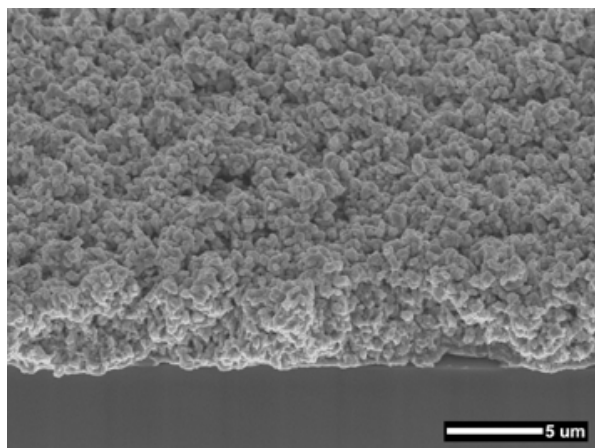
Figure 3.44: Zinc titanium coating ZTi 1$_{\text{float}}$ with 1.2 at.% Ti
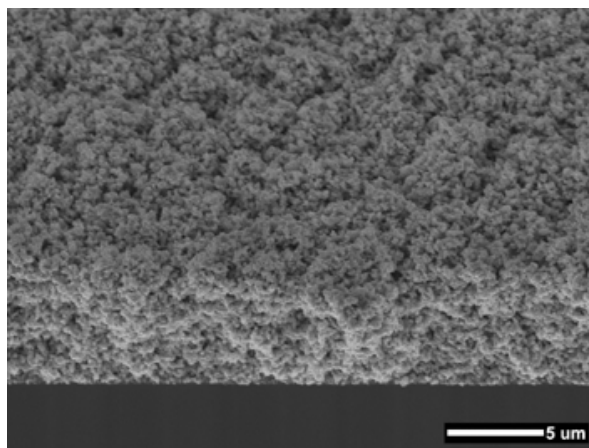
Figure 3.45: Zinc titanium coating ZTi 1$_8$ with 1.7 at.% Ti
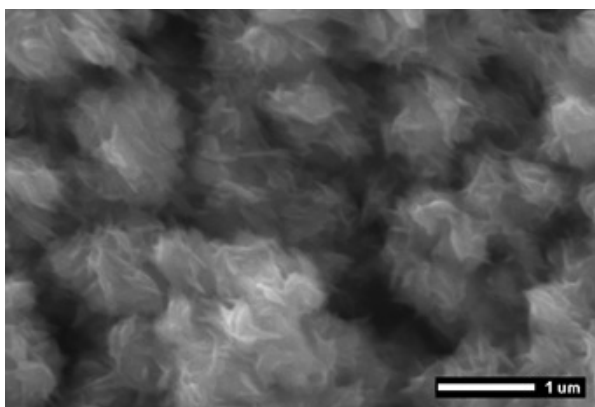
Figure 3.46: Detailed view ZTi 1$_{\text{float}}$ on steel, Mag: 20k
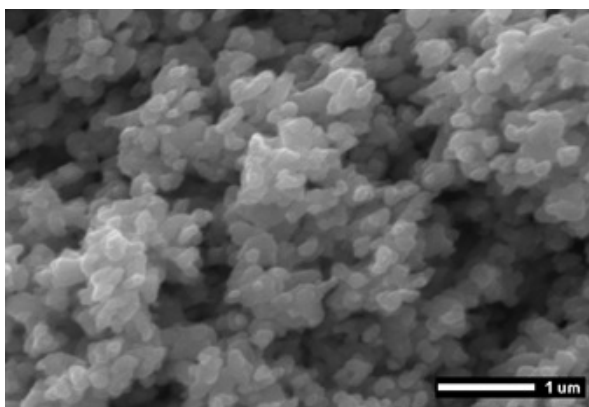
Figure 3.47: Detailed view coating ZTi 1$_8$ on steel, Mag: 20k
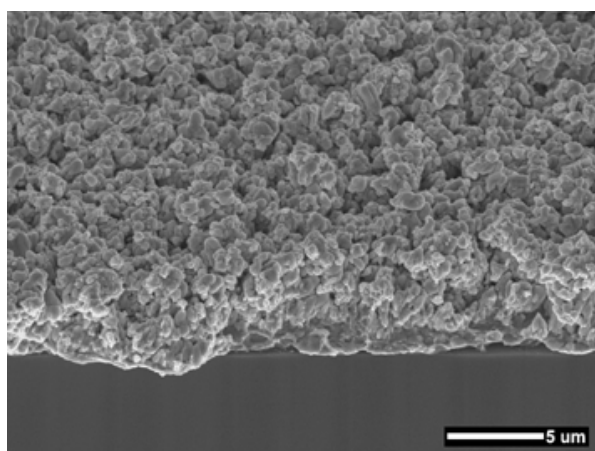
Figure 3.48: Zinc titanium coating ZTi 5$_{\text{float}}$ with 5 at.% Ti
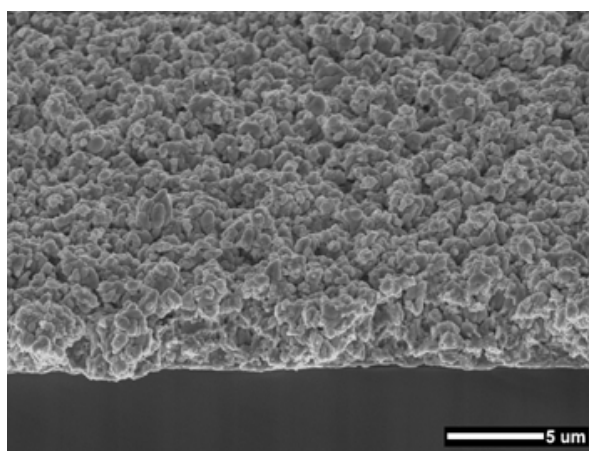
Figure 3.49: Zinc titanium coating ZTi 5$_8$ with 5.5 at.% Ti
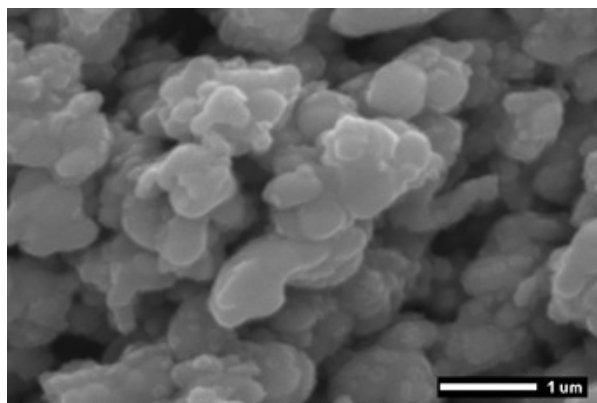
Figure 3.50: Detailed view ZTi 5$_\text{float}$ on steel, Mag: 20k
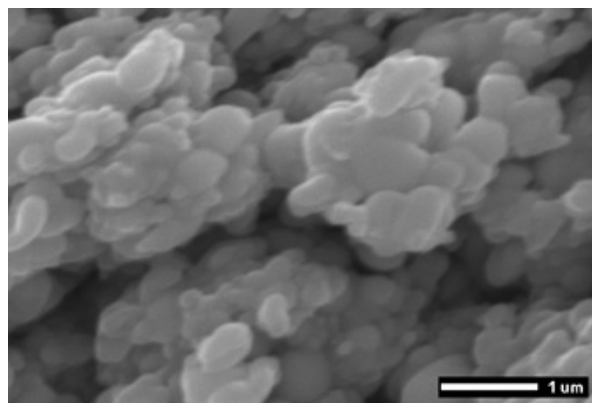
Figure 3.51: Detailed view ZTi 5$_8$ on steel, Mag: 20k
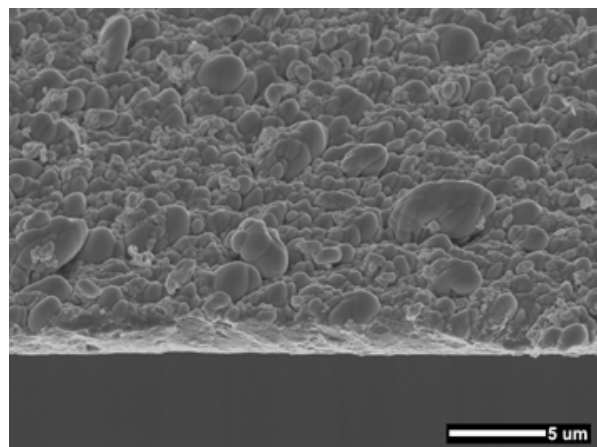
Figure 3.52: Zinc titanium coating ZTi 9$_\text{float}$ with 9.6 at.% Ti
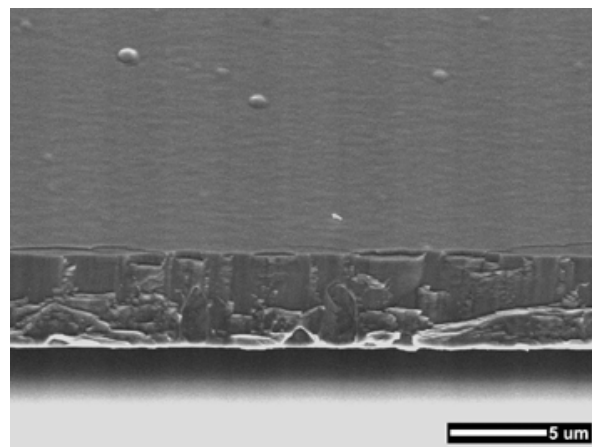
Figure 3.53: Zinc titanium coating ZTi 9$_8$ with 9.4 at.% Ti
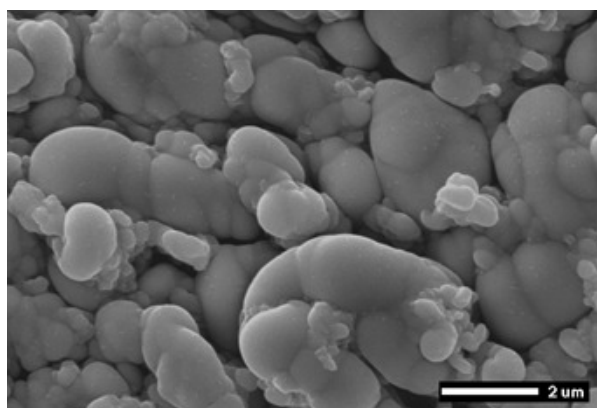
Figure 3.54: Detailed view ZTi 9$_\text{float}$ on steel, Mag: 10k
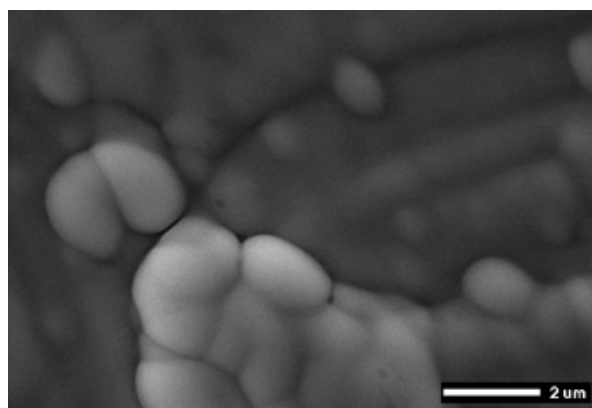
Figure 3.55: Detailed view ZTi 9$_8$ on steel, Mag: 10k
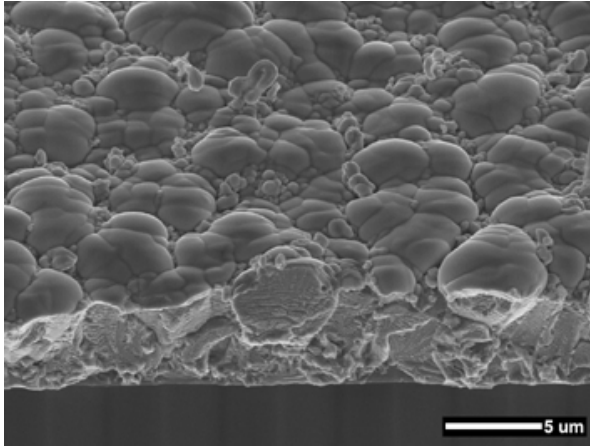
Figure 3.56: Zinc titanium coating ZTi 10_{float} with 7.7 at.% Ti
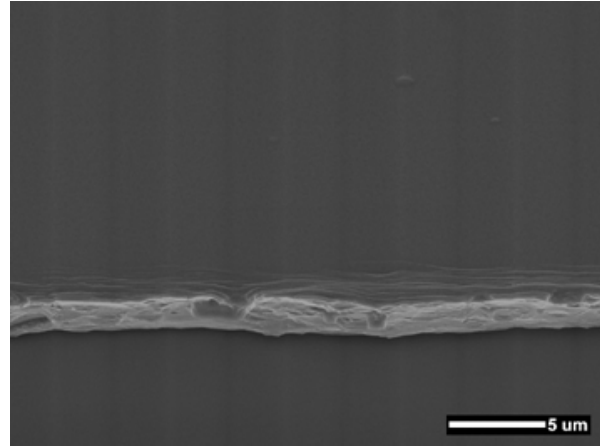
Figure 3.57: Zinc titanium coating ZTi 10_8 with 11.1 at.% Ti
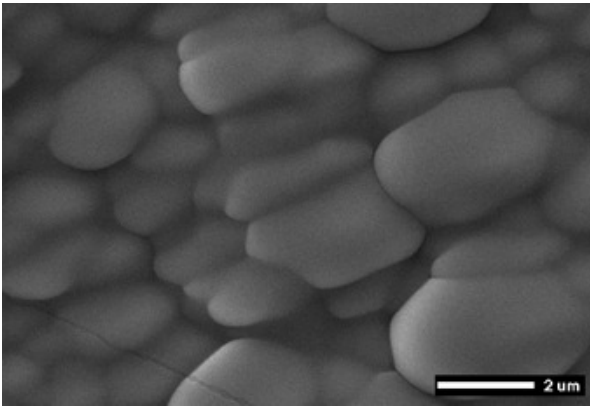
Figure 3.58: Detailed view ZTi 10_{float} on steel, Mag: 10k
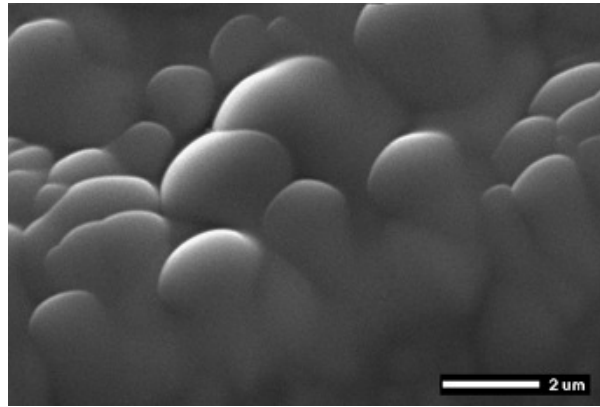
Figure 3.59: Detailed view ZTi 10_8 on steel, Mag: 10k

Sample	Thickness [μm]		Grainsize [nm]		Composition [at.%]	
	T_{float}	T_s=+8 °C	T_{float}	T_s=+8 °C	T_{float}	T_s=+8 °C
ZCr 3	7.7	7.2	210–1750	85–770	2.9	3.1
ZCr 11	6	6.2	120–3150	55–200	10.3	12.8

Table 3.7: Coating thicknesses and compositions of magnetron sputtered zinc chromium coatings.

well defined. The grain size ranges from 210–1750 nm. The resulting surface is relatively flat. Sample ZCr 3_8 (Fig. 3.67), with an alloy content of 3.1 at.% Cr, has a clear columnar structure with fine grains ranging from 85 to 770 nm, which results in a smooth surface.

The higher alloyed coating ZCr 11_{float} (Fig. 3.70) with an alloy content of 10.3 at.% Cr has a clear columnar structure with thin columns, which are easy to distinguish. Their grain size is 120–3150 nm. The columnar structure with fine grains is also found with coating ZCr 11_8 (Fig. 3.71) with 12.8 at.% Cr content. However with 55-200 nm the grains size is much lower than that of ZCr 11_{float}.

3.1.2.5 Zinc Magnesium

The zinc magnesium coatings ZMg 2 and ZMg 15 have been deposited with the sputter parameters given in Tab. 2.12. The resulting coating thicknesses, grainsizes and compositions measured by EDX are listed in Tab. 3.8. The cross-sections and surfaces of these coatings are shown in Fig. 3.74 to 3.81. The first zinc magnesium coating ZMg 2_{float} (Fig. 3.74) with 2.5 at.% Mg has an open, porous, grainy, sponge like structure built of agglomerates of very fine grains. Their grainsizes are 100–210 nm. The resulting surface is rough. Sample ZMg 2_8 (Fig. 3.75) with an alloy content of 2.1 at.% Mg has a compact, grain
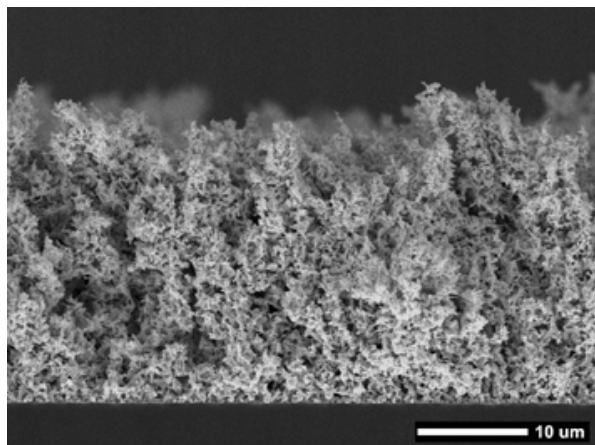
Figure 3.60: Zinc aluminium coating $ZAl4_{iso}$ with 3.9 at.% Al deposited at $T_s = T_{iso}$
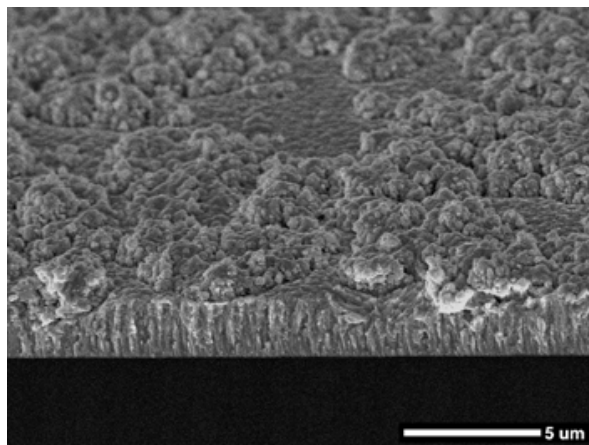
Figure 3.61: Zinc aluminium coating with $ZAl4_8$ with 4.5 at.% Al
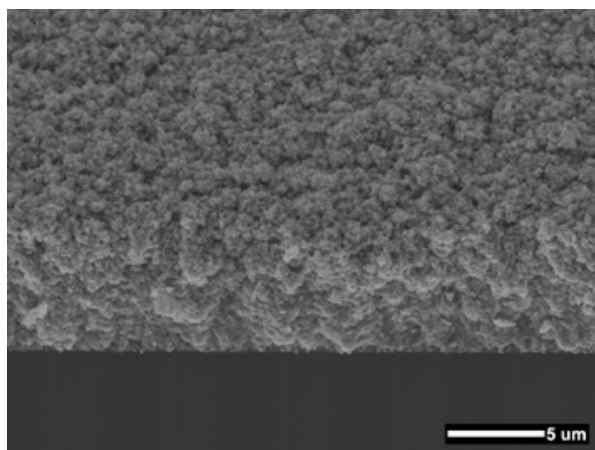
Figure 3.62: Zinc aluminium coating $ZAl2_{float}$ with 2.2 at.% Al
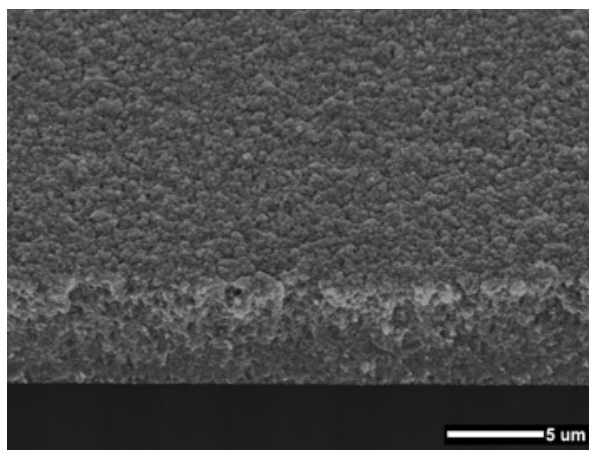
Figure 3.63: Zinc aluminium coating $ZAl2_8$ with 2.6 at.% Al
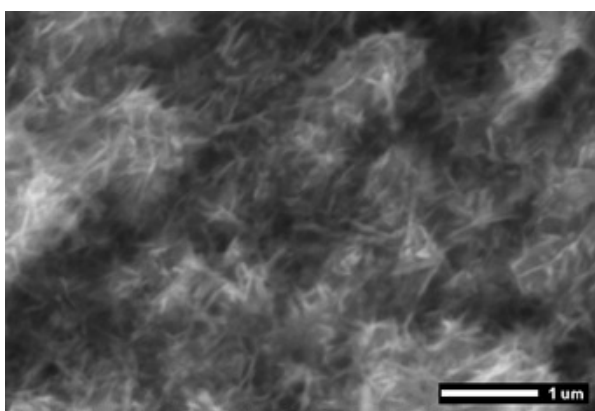
Figure 3.64: Detailed view $ZAl2_{float}$ on steel, Mag: 20k
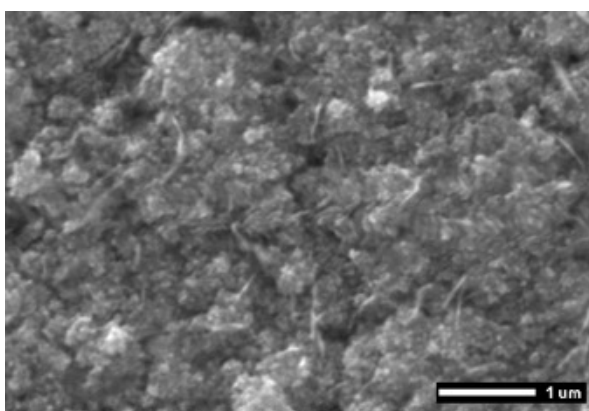
Figure 3.65: Detailed view $ZAl2_8$ on steel, Mag: 20k
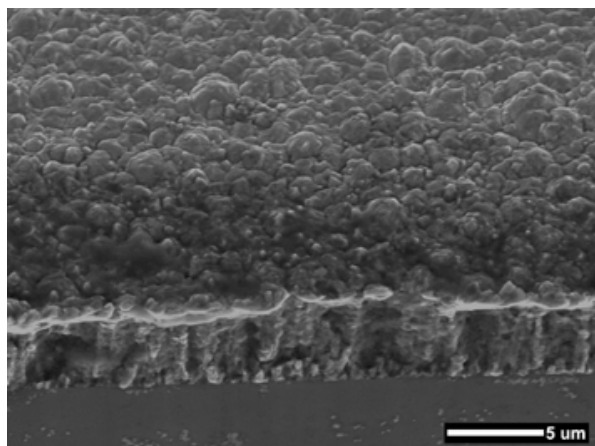
Figure 3.66: Zinc chromium coating ZCr 3$_{\text{float}}$ with 2.9 at.% Cr
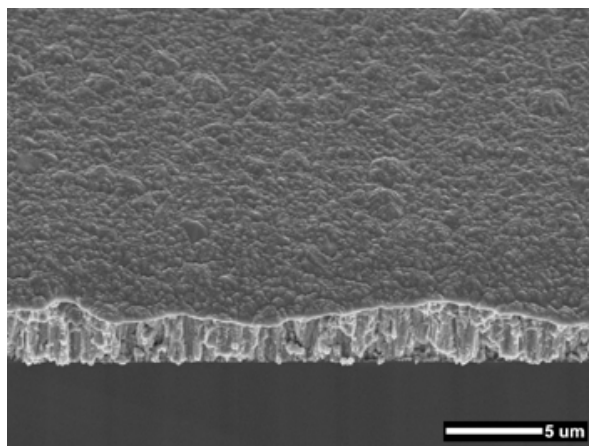
Figure 3.67: Zinc chromium coating ZCr 3$_8$ with 3.1 at.% Cr
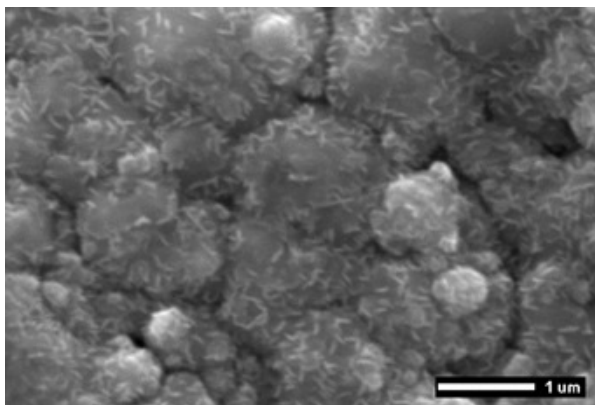
Figure 3.68: Detailed view ZCr 3$_{\text{float}}$ on steel, Mag: 20k
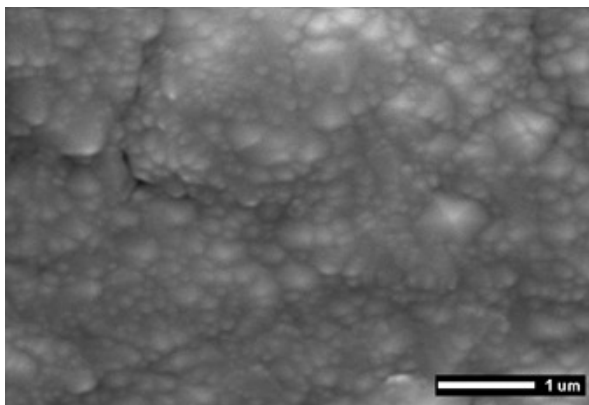
Figure 3.69: Detailed view ZCr 3$_8$ on steel, Mag: 20k
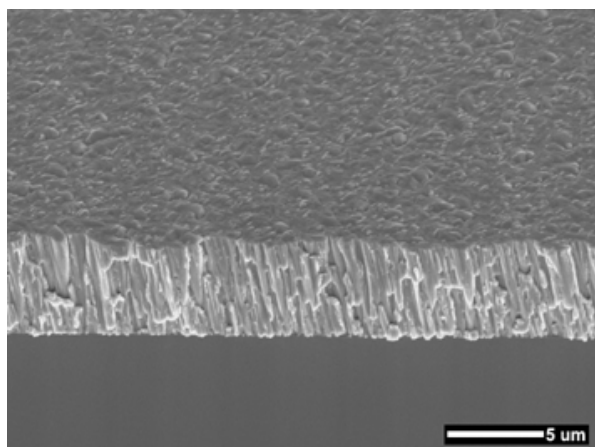
Figure 3.70: Zinc chromium coating ZCr 11$_{\text{float}}$ with 10.3 at.% Cr
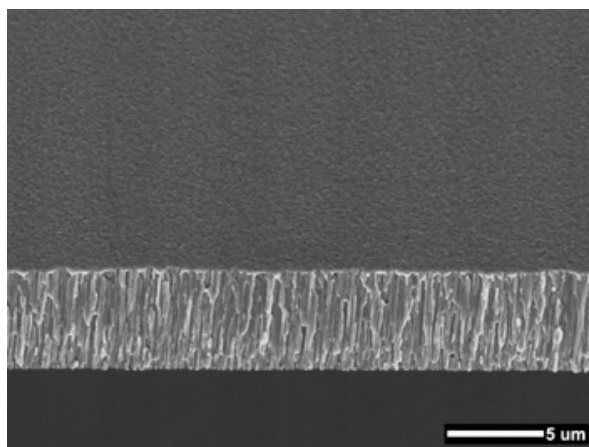
Figure 3.71: Zinc chromium coating ZCr 11$_8$ with 12.8 at.% Cr
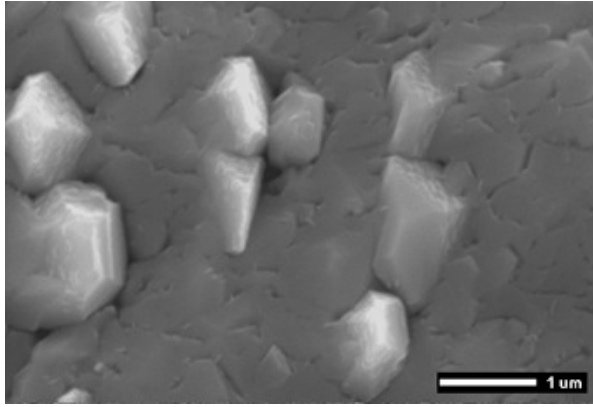
Figure 3.72: Detailed view ZCr 11_float on steel, Mag: 20k
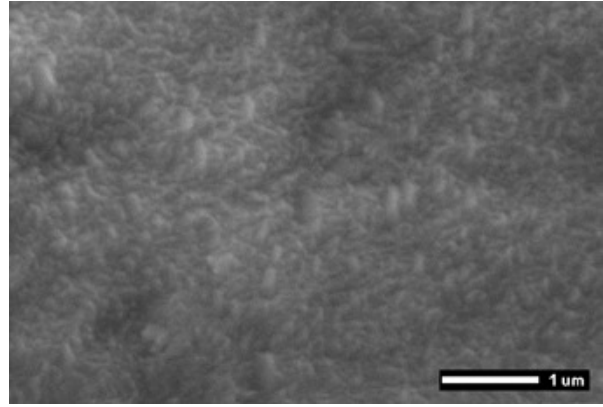
Figure 3.73: Detailed view ZCr 11_8 on steel, Mag: 20k

Sample	Thickness [μm]		Grainsize [nm]		Composition [at.%]	
	T_{float}	$T_s = +8\,°C$	T_{float}	$T_s = +8\,°C$	T_{float}	$T_s = +8\,°C$
ZMg 2	15.3	7.9	100–210	100–450	2.5	2.1
ZMg 15	9.9	9.2	75–2000	200–660	16	13.9

Table 3.8: Coating thicknesses and compositions of magnetron sputtered zinc magnesium coatings.

like structure whose grains with a size of 100–450 nm are difficult to distinguish. The created surface is smooth.

Coating ZMg 15_float (Fig. 3.78) with an magnesium content of 16 at.% Mg shows when examined by eye a very interesting effect. Depending on the direction of observation this sample changes its appearance. In one direction it appears metallic and bright. When tilted by 90 degrees, it looks dull and dark. This macroscopic impression is shown in Fig. 3.82. The examination of the coating cross-section with the SEM on the microscopic scale, presented in Fig. 3.78, explains the reason for this macroscopic behaviour: At the substrate interface the film has a compact dense structure without visible grains. At approximately half of its final thickness this structure changes completely to a structure of big, asparagus head like grains. In the SEM image these grains are tilted. For an observer who changes his viewing angle the different scattering of light, which is caused by the tilted grains, is noted as altered colour impression. The asparagus head like grains have a diameter of 75–2000 nm. The sample ZMg 15_8 (Fig. 3.79) with a magnesium content of 13.6 at.% has a compact dense structure with fibrous texture. The surface is covered by small heads of grains with a grain size of 200–660 nm, which create a smooth surface.

3.1.3 Structure Variations due to Ion Assistance

3.1.3.1 Ion Assisted Zinc Coatings

Figures 3.83 and 3.84 show the cross-sections of ion beam sputtered and assisted zinc coatings ZIB A1 and ZIB A2. These films were deposited with the same sputter parameters than those of the non assisted ZIB depositions already presented in section 3.1.1.2. The substrate temperature was set to 25 °C. Additionally, these films were assisted by defocused argon ion beams with ion energies of 300 eV and spatially homogeneous ion beam current densities. Coating ZIB A1 assisted by an ion current density of 18 $\mu A/cm^2$ (I/A = 0.0384) shows an open, porous structure with clearly distinct grains. The structure resulting in a rough surface is similar to the structure of the non assisted coatings deposited at the same substrate temperature. The crystallites of the 1 μm thick film are randomly oriented as confirmed later by the XRD measurements described in section 3.3.1.3.

Coating ZIB A2 deposited with a higher ion current density of 35 $\mu A/cm^2$ (I/A = 0.0768) has a more
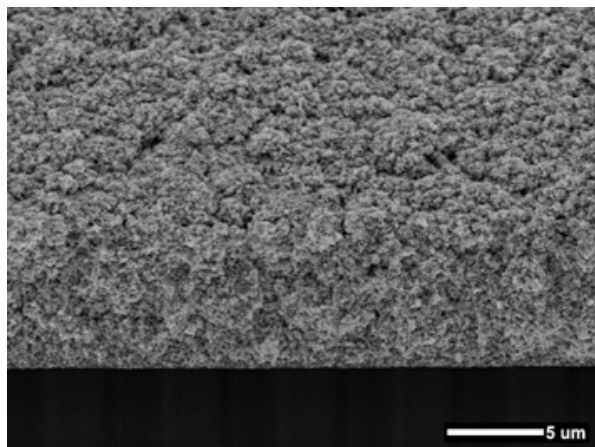
Figure 3.74: Zinc magnesium coating $ZMg\,2_{float}$ with $2.5\,at.\%\ Mg$
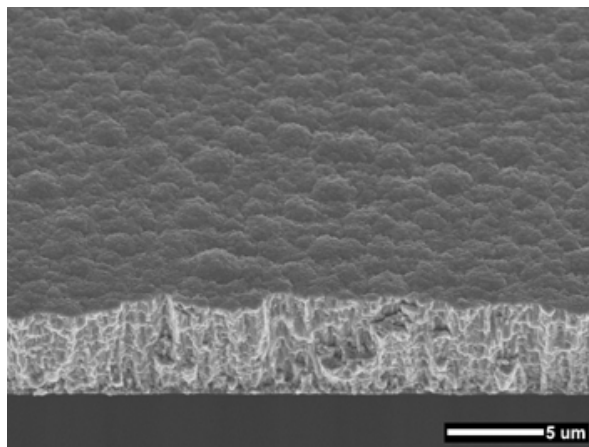
Figure 3.75: Zinc magnesium coating $ZMg\,2_8$ with $2.1\,at.\%\ Mg$
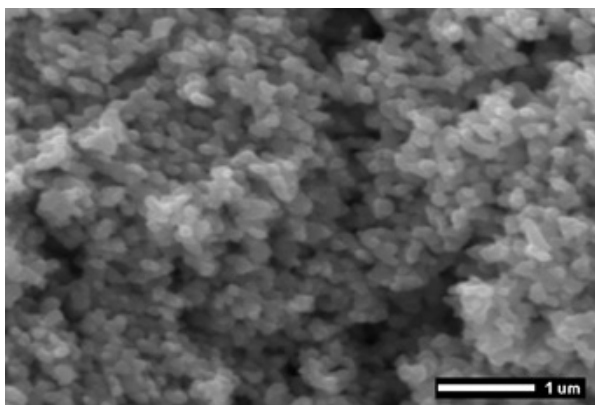
Figure 3.76: Detailed view $ZMg\,2_{float}$ on steel, Mag: 20k
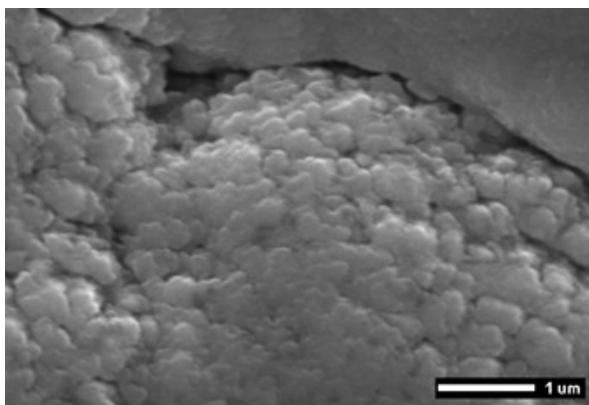
Figure 3.77: Detailed view $ZMg\,2_8$ on steel, Mag: 20k
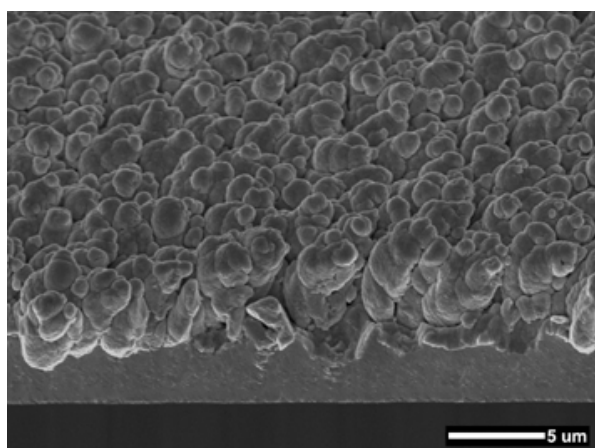
Figure 3.78: Zinc magnesium coating $ZMg\,15_{float}$ with $16\,at.\%\ Mg$. The grains are tilted to the right.
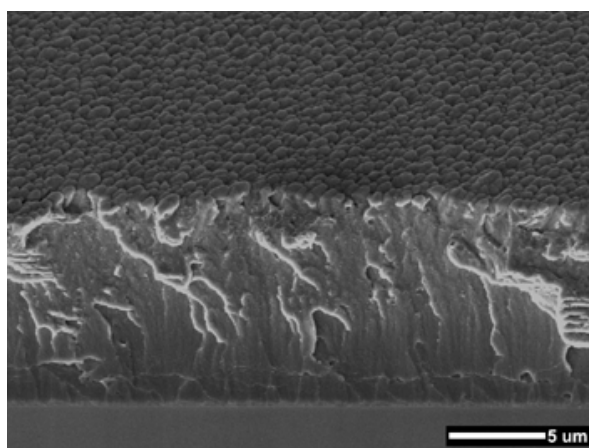
Figure 3.79: Zinc magnesium coating $ZMg\,15_8$ with $13.6\,at.\%\ Mg$
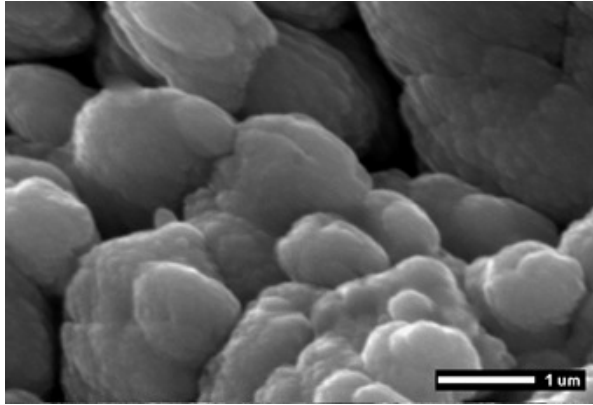
Figure 3.80: Detailed view $ZMg\,15_{float}$ on steel, Mag: 20k
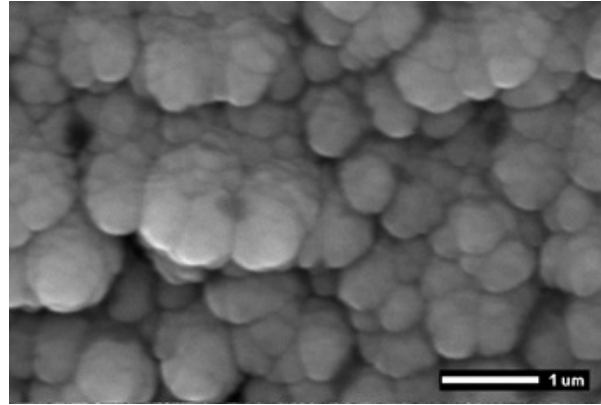
Figure 3.81: Detailed view $ZMg\,15_8$ on steel, Mag: 20k
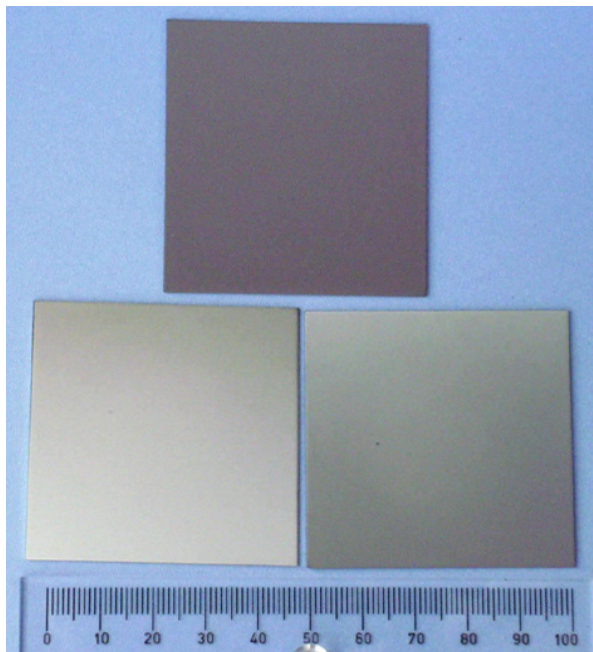
Figure 3.82: Macroscopic appearance of $ZMg\,15_{float}$ and $ZMg\,15_8$. The lower row shows on the left a steel sheet coated with $ZMg\,15_{float}$ and on the right hand side a sheet covered by $ZMg\,15_8$. The diverse colour impressions of the sheets are generated by the different morphologies of the applied coatings. The single sheet in the first row is another $ZMg\,15_{float}$ coated steel sheet. The orientation of the sample is rotated by 90 degrees with respect to the sheet below. Due to the tilted grains the scattering of light is different for different viewing angles and one observes varying colour impressions.

compact and dense structure. The single grains are difficult to distinguish and due to resputtering and dense packing its thickness is reduced to $0.5\,\mu$m. The generally smooth surface is interspersed with small voids. At some spots additionally outgrowing crystallites can be seen.

3.1.3.2 Ion Assisted Zinc Iron Coatings

Figure 3.85 shows the ion current density distribution of a focused argon ion beam of 300 eV ion energy and 2 mA beam current, measured with the 2D–array at the substrate position. The measurement demonstrates that the current density increases towards the focus point of the beam. Figure 3.86 shows the macroscopic appearance of the low alloyed zinc iron coating ZFeIB A1 deposited on a silicon wafer, assisted by an ion beam as described above. For this experiment all further deposition parameters corresponded to those used for the non assisted ZFeIB 1 depositions. The photograph shows that the dull, grey appearance of the outer areas changes to a milky grey, then to a shiny, metallic, silver appearance in the focus point of the beam. To investigate the sample also microscopically it was broken along the indicated, yellow line. The following SEM cross-sections in Fig. 3.87 to Fig. 3.90 are taken step by step along the edge of break, indicated by the arrow, from the circumference towards the focus point. Figure 3.87 shows the low irradiated morphology of the sample at the first observation point 3 mm distant from the outer edge of the wafer. The coating consists of single, worm like grains which form an irregular,
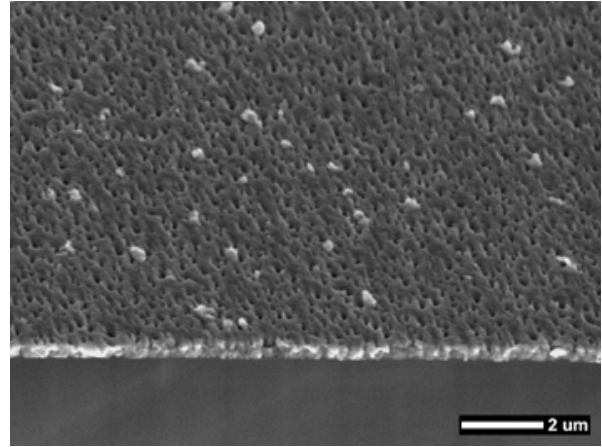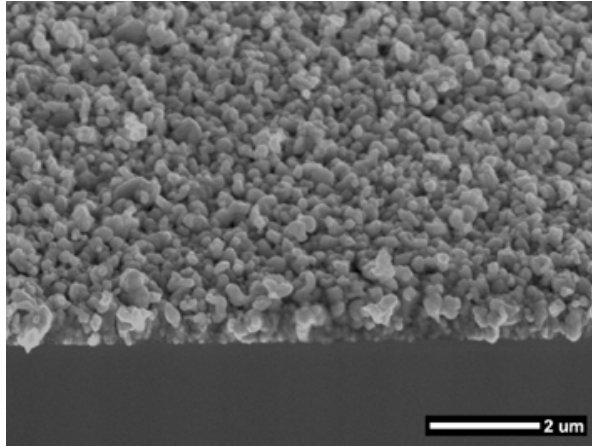
Figure 3.83: Ion beam sputtered zinc coating ZIB A1 deposited at $T_s = +25\,°C$ and assisting argon ion beam of $18\,\mu A/cm^2$ ion current density

Figure 3.84: Ion beam sputtered zinc coating ZIB A2 deposited at $T_s = +25\,°C$ and assisting argon ion beam of $35\,\mu A/cm^2$ ion current density

rough surface. With increasing beam intensity, 15 mm distant from the edge, the growth of a coherent film in between the separated, worm like grains can be observed. With further increasing ion current density this trend proceeds and the worm like grains disappear more and more. Close to the focus point, 25 mm distant from the edge, the grains almost completely disappeared. Only very few and very small ones remained and the surface is smooth and uniform. As already seen with the deposition of ZIB A2, also this experiment reveals the thinning of the coating due to resputtering and dense packing of the film by the assisting beam.

3.1.4 Influence of Gas Atmosphere

To study the influence of the oxygen content in the sputter atmosphere on the development of whisker like structures, deposition experiments in oxygen "doped" sputter gas atmospheres have been performed. Figure 3.91 shows the mass spectrum of an oxygen "doped" gas atmosphere used for deposition runs. The spectrum shows clearly the main argon peaks at 20 and 40 m/Q. Additionally, residual gas components such as nitrogen, water, hydrogen chloride and impurities from the pump oil are detected. For some components multiple peaks are observed in the mass spectrum as they belong to different atomic mass to charge ratios of the respective specie e.g. nitrogen can be detected as single charged molecule, double charged molecule or single ionised atom with the specific atomic mass. Other species deliver multiple peaks as they are present as isotopes with different atomic masses, e.g argon has two isotopes with 40 and 36 amu. The oxygen peak at 32 m/Q corresponds to an oxygen contribution of 0.08 % in the sputter atmosphere. Apart from the substrate temperature all further deposition parameters were the same as those used for the ZIB depositions. As substrate temperature $T_s = +70\,°C$ was chosen since this temperature is little below the whisker growth threshold temperature of $+75\,°C$. Table 3.9 gives the oxygen contents of the sputter gas atmospheres measured with the quadrupole mass spectrometer and the oxygen contents of the coatings measured by EDX respectively. The EDX results hereby give

	oxygen content		
sample	sputter atmosphere [%]	coating [at.%]	thickness [μm]
ZIB O1	0.05	9.4	0.84
ZIB O2	0.08	15.1	0.93
ZIB O3	1.4	26.3	0.77
ZIB O4	7	54.4	0.63

Table 3.9: Samples sputtered in argon/oxygen atmosphere

a rather qualitative statement, since for light elements like oxygen (amu=16) the results are not very precise. The measurements show that a steady increase in oxygen content in the sputter atmosphere
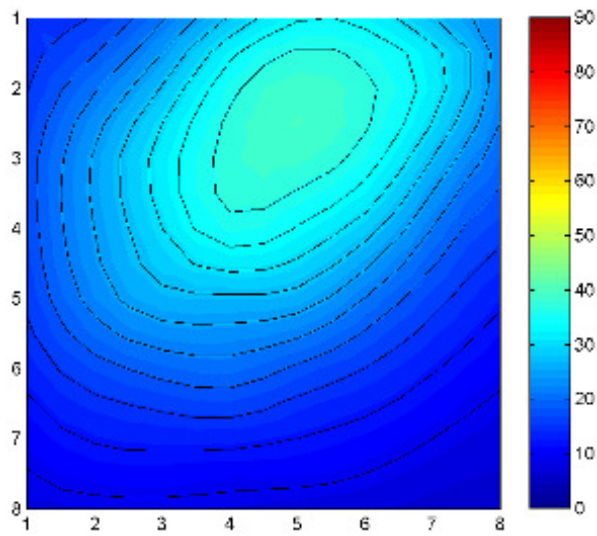
Figure 3.85: Measurement of the ion current density distribution with the 2D–array for a 300 eV, 2 mA ion beam
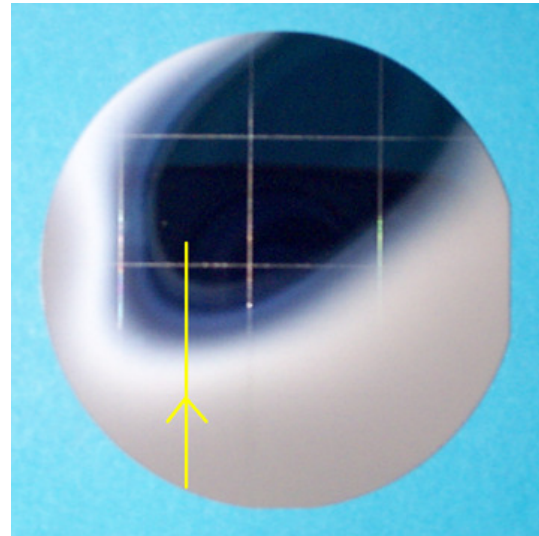
Figure 3.86: "Fingerprint" of the ion beam, macroscopically visible with the coating morphology of ZFeIB A1
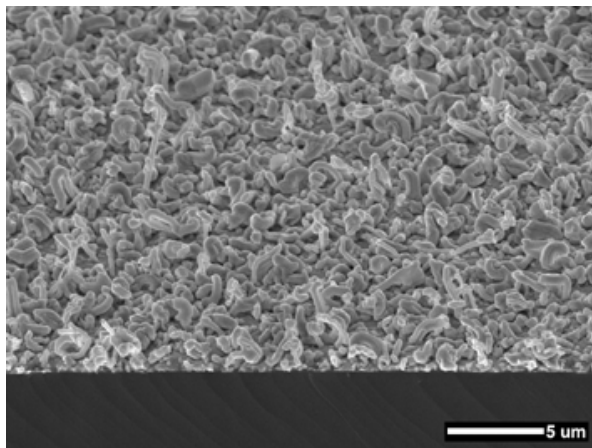
Figure 3.87: ZFeIB A1 cross-section in 3 mm distance
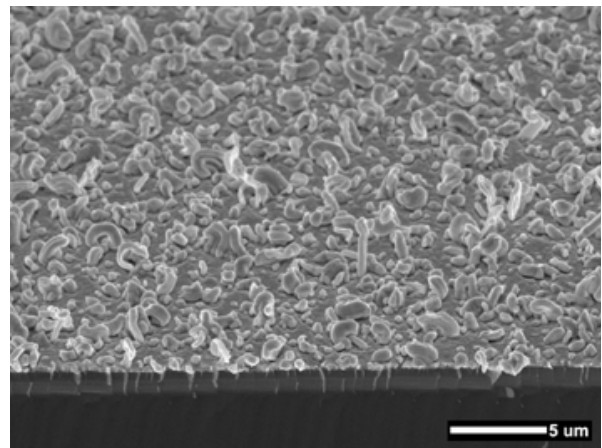
Figure 3.88: ZFeIB A1 cross-section in 15 mm distance
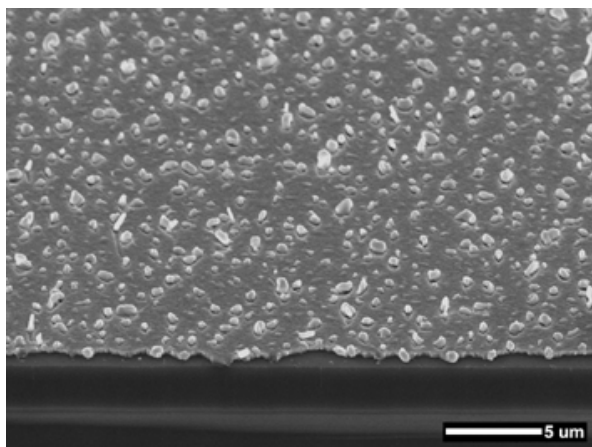
Figure 3.89: ZFeIB A1 cross-section in 20 mm distance
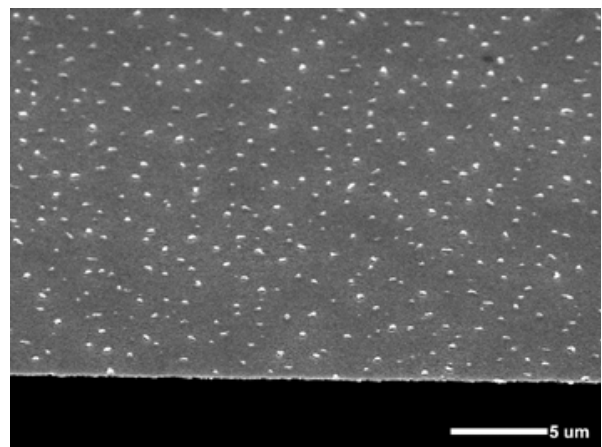
Figure 3.90: ZFeIB A1 cross-section in 25 mm distance
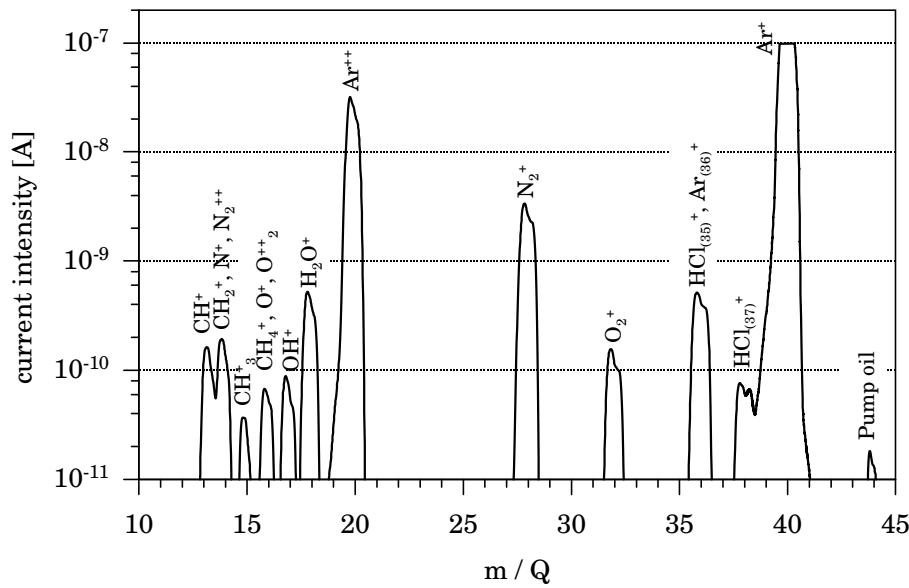
Figure 3.91: Masspectrum of the quadrupole gasanalyser at an oxygen content of 0.08 % in the sputter atmosphere

results also in an increased oxygen content of the coating. The sample deposited in a gas atmosphere with 7 % oxygen content even delivers films with closely stoichiometric ZnO composition. This result is later confirmed by the XRD results in section 3.3.1.3. Figure 3.92 shows the cross section of the zinc coating, sputtered in "pure" argon atmosphere. It shows an open, worm like structure of single grains with a rough surface. A similar structure can be observed with the coating ZIB O2 sputtered in a 0.08 % oxygen "doped" atmosphere. The next sample ZIB O3, shown in Fig. 3.94, sputtered with an increased oxygen content of 1.4 %, has a different morphology. Its column like structure is compact and dense. No single grains and grain boundaries can be noticed. The surface is smoother and slightly cauliflower like. The last Fig. 3.95 shows the smooth and compact, but very thin zinc oxide coating ZIB O4 deposited in an argon/oxygen atmosphere with 7 % oxygen content.

3.1.5 Roughness Measurements

3.1.5.1 Coatings on Silicon Wafers

The graphs in Fig. 3.96 and 3.97 display the results of the roughness measurements made with the laserprofilometer.

Figure 3.96 plots the R_a values of ion beam sputtered zinc coatings deposited on polished silicon wafers versus the substrate temperature T_s of the respective deposition run. The graph shows clearly that there is a strong correlation between deposition temperatures and the obtained coating morphologies, which are quantified here as surface roughnesses. The measured R_a values comply with the qualitative observations already made by the SEM images.

Figure 3.97 plots the R_a values of the magnetron sputtered zinc and zinc alloy coatings deposited on polished silicon wafers. The measurements of the zinc–aluminium coatings ZAl 2 and the lowest alloyed zinc titanium coating ZTi 1$_{float}$, were not possible as the laser has not found its focus point on the non reflective surfaces of these samples. Corresponding with the results of the ion beam sputtered samples also with these coatings independent of their alloying content all samples deposited at higher substrate temperatures T_{float} reveal also higher roughnesses than those deposited at $T_s = +8$ °C. For the influence of alloying no clear trend can be observed. In case of the zinc–iron and zinc–chromium coatings with increasing alloying content the roughness decreases. For the zinc–titanium and zinc magnesium–coatings the opposite behaviour is observed. It has to be noticed that a correlation between the measured surface roughnesses given as R_a-values and the observed grain sizes can not be established as the observed grain structures are too small to be resolved by the profilometer laser with a spot size of $2\,\mu$m. Due to this
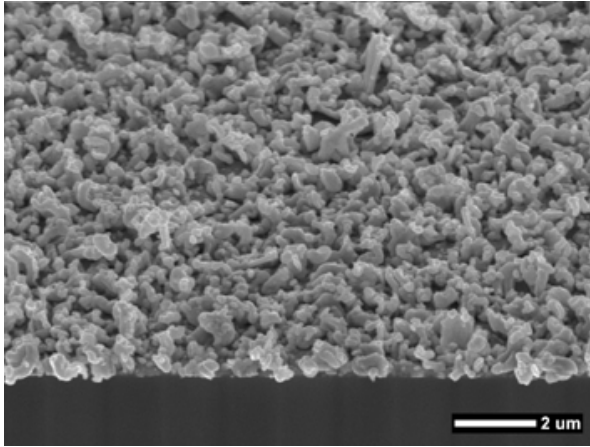
Figure 3.92: Ion beam sputtered zinc coating deposited at $T_s = +70\,°C$ and pure argon atmosphere
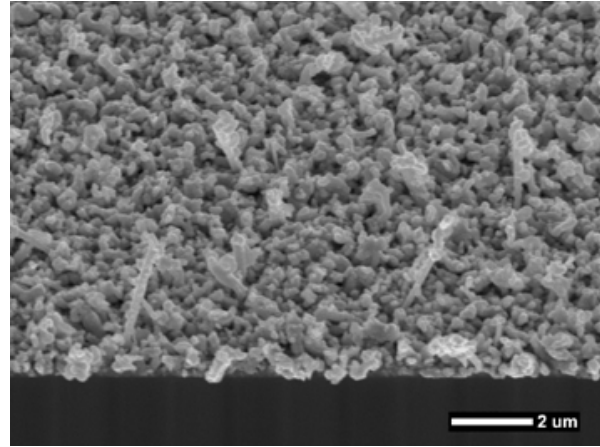
Figure 3.93: Ion beam sputtered zinc coating ZIB O2 deposited at $T_s = +70\,°C$ and 0.08 % oxygen content in the sputter atmosphere
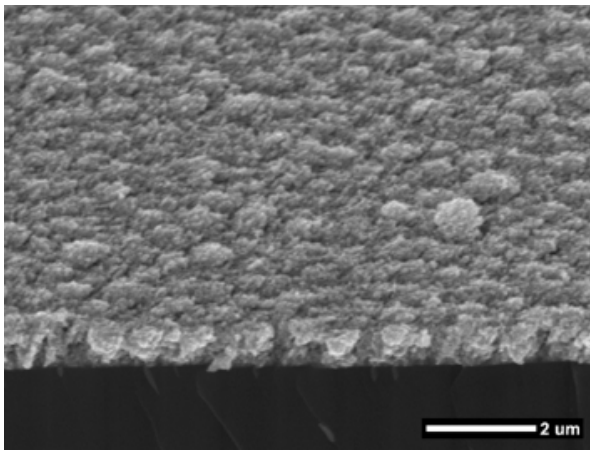
Figure 3.94: Ion beam sputtered zinc/zinc oxide coating ZIB O3 deposited at $T_s = +70\,°C$ and 1.4 % oxygen content in the sputter atmosphere
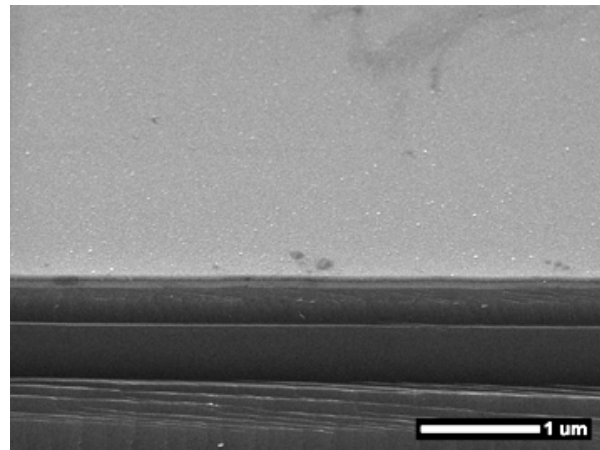
Figure 3.95: Ion beam sputtered zinc oxide coating ZIB O4 deposited at $T_s = +70\,°C$ and 7 % oxygen content in the sputter atmosphere

reason the roughness parameters R_a do not provide evidence for the real micro- or nanoscaled grain structures and their corresponding surfaces.

3.1.5.2 Coatings on Steel Sheets

Figure 3.98 shows the three dimensional roughness profile of a steel sheet coated with the zinc iron coating ZFe 7_8, taken by white light interferometer. The given topography map displays a measured surface area of $0.31\,\text{mm} \times 0.24\,\text{mm}$. In order to compare the topography map with the appearance of the sample, the SEM cross-section of the respective sample is given additionally in Fig. 3.100.

Figure 3.99 and 3.101 show the two dimensional topography mappings of ZFe 7_8 and the electrodeposited reference EZ. These 2D mappings are the basis for the calculation of the peak to valley values and R_a values of the coatings. It has to be noted that the colour coded Z-scale is not equal for both mappings. For each measurement the measured PV range (Z-scale) is adapted to the colour scale range of the interferometer software. The PV value of ZFe 7_8 is $9.108\,\mu\text{m}$, which is about $6\,\mu\text{m}$ lower than the peak to valley value of the EZ reference with a PV value of $15.584\,\mu\text{m}$. The PV value of ZFe 7_8 is also lower than the PV value of the blank steel substrate with $PV = 14.204\,\mu\text{m}$.

Figure 3.102 shows as an example the roughness profile of the EZ coating, which has been extracted along the black line indicated in the 2D mapping. These kinds of roughness profiles are used for the
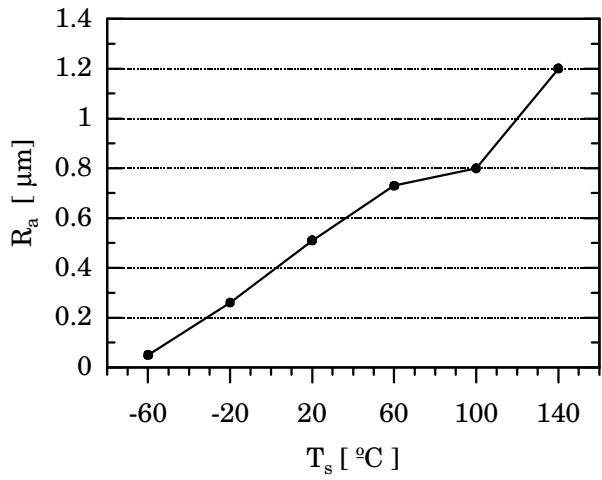
Figure 3.96: Roughness of ion beam sputtered zinc coatings on silicon wafers given as R_a value versus substrate temperature T_s
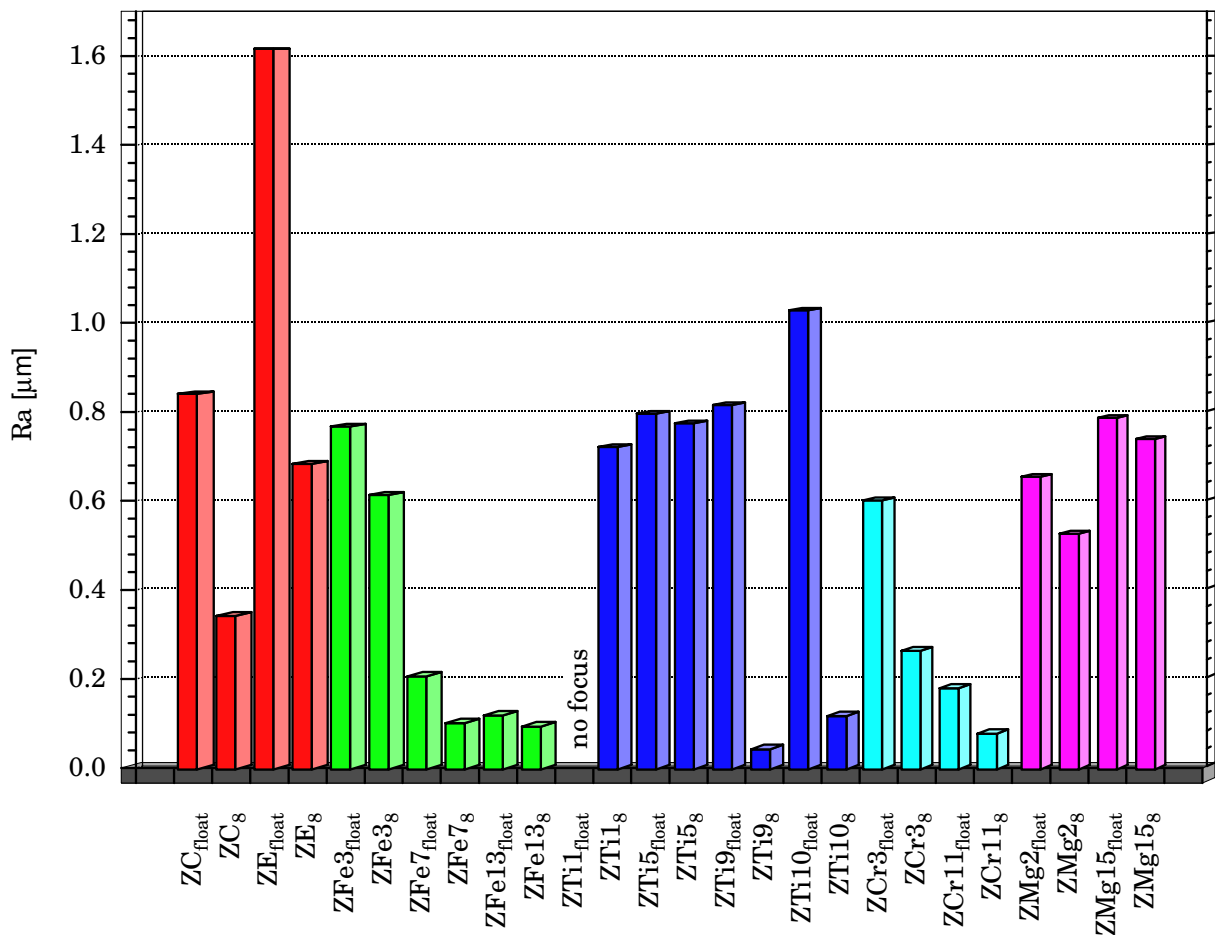
Figure 3.97: Roughness of magnetron sputtered zinc coatings on silicon wafers given as R_a value

calculation of the R_a value of all samples. An overview of the obtained R_a values is given in Fig. 3.103. The R_a values range from about $1.315\,\mu m$ for the smoothest coating ZFe 7_{float} to $2.193\,\mu m$ for the roughest coating ZCr 3_8. The R_a value of about $1.64\,\mu m$ measured with this technique for a blank steel sheet complies with corresponding measurements done with a stylus profilometer.

Combining the laserprofilometer measurements on silicon wafers and the white light interferometer measurements on steel sheets it can be noted that no dependence between the measured R_a values of the coated steel sheets and the different coating compositions or deposition conditions can be found. The roughnesses of the coated steel sheets are mainly determined by the roughnesses of the blank steel sheets. It should to be noted that a certain roughness of coated steel sheets is even obligatory for good paintability. A correlation between the measured sheet roughnesses, i.e. the corresponding surface for corrosion attack, and the corrosion properties of the respective samples discussed in section 3.5 has not be found.

3.1.6 Wettability

The results of contact angle measurements carried out for ion beam sputtered zinc coatings with different surface roughnesses R_a are shown in Fig. 3.104. The contact angle of the settled water droplets on the sample surfaces rises with increasing surface roughness R_a. All these samples are pure zinc coatings with a stable and homogeneous surface chemistry. They did not change their polarity with deposition temperature, as it happens with various compounds. As a result the wetting behaviour is only a function of the surface roughnesses of the films.

The smooth, specular surface of sample ZIB_{-60} deposited at -60℃ wets quite well as can be seen in the photograph of the droplet in Fig. 3.105. It has a contact angle of 102 °. The sample ZIB_{+140} with an open woolen like microstructure is not wetting as can be seen in Fig. 3.106. It has a contact angle of 145 °. For this sample it was even very difficult to deposit a water droplet from the micropipette. The contact area between the droplet and coating is limited to the spikes of the coating. This reduces the spreading of water and causes the droplets to form spherical beads. The coating exhibits a super hydrophobic behaviour.

The contact angle measurements reflect the morphological observations already made by eye, scanning electron microscopy and laserprofilometry very well.

3.1.7 Discussion of Parameters Influencing the Morphology

3.1.7.1 The Significance of the Normalised Deposition Temperature

The performed sputter experiments indicated that the substrate temperature T_s is an important deposition parameter. This fact can be understood by looking at the different film formation and growth phenomena which are based on temperature dependent physical or chemical processes such as: nucleation, adatom mobility (surface diffusion, bulk diffusion), coalescence, grain boundary mobility, recrystallisation.

Like solidification from liquid state also the transition from gaseous to the crystalline state is initiated by nucleation, which occurs as soon as a sufficient number of particles meets due to statistic deviations of particle concentration or -speed. Nucleation can be homogeneous if particles of the same species meet or heterogeneous if these particles are taken up by a different species. However, this process does not occur until the total system deviates from thermodynamic equilibrium, the system is in a supersaturated and supercooled state. In contrast to equilibrium, where very small interactions between the particles occur, in this state nuclei are formed and dissolved constantly. Once a critical nucleus size, which decreases with increasing supersaturation, is reached the nucleus is stable and viable.

Movchan and Demchishin [150] were the first who categorised microstructures, observed in evaporated
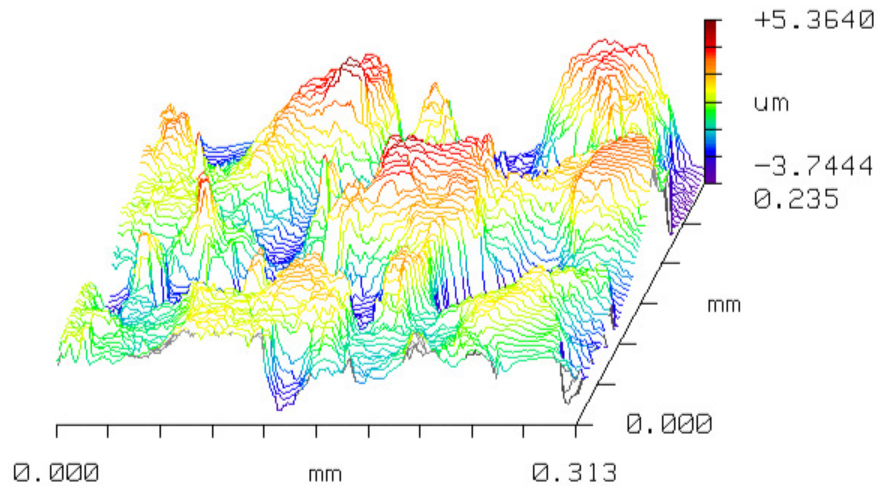
Figure 3.98: Three dimensional roughness profile of a steel sheet coated with zinc iron coating ZFe 7_8
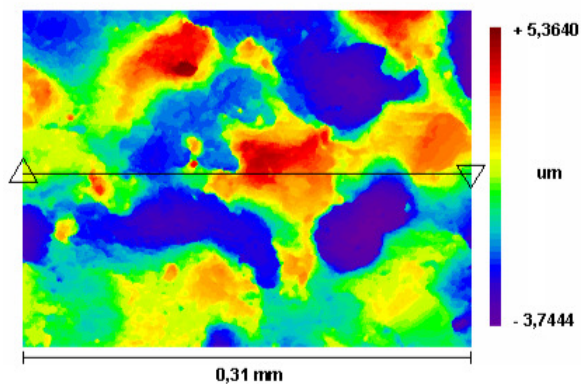
Figure 3.99: Two dimensional roughness map of a steel sheet coated with zinc iron coating ZFe 7_8
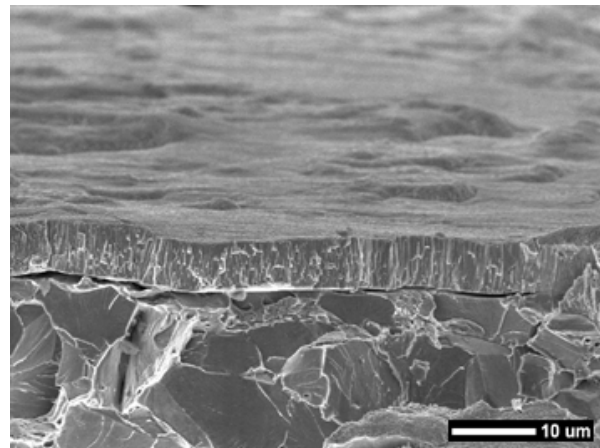
Figure 3.100: SEM cross-section of the zinc iron ZFe 7_8 coated steel sheet
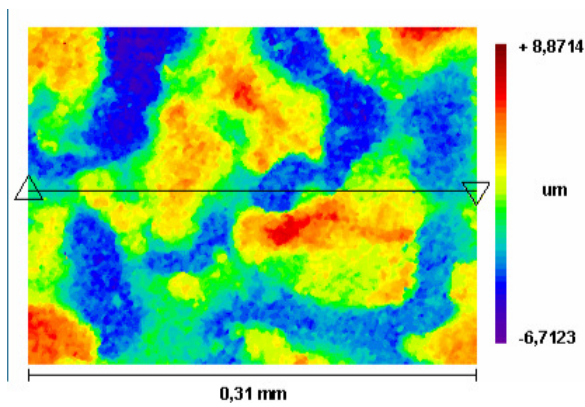
Figure 3.101: Two dimensional roughness map of the electro galvanised EZ reference sheet
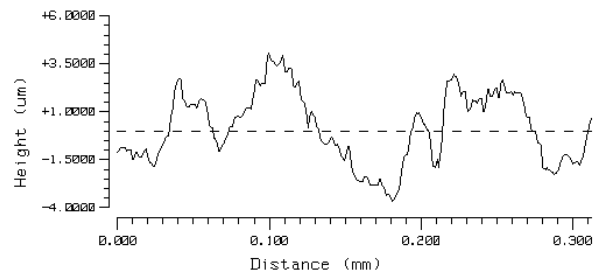
Figure 3.102: Roughness profile of the electro galvanised EZ reference sheet
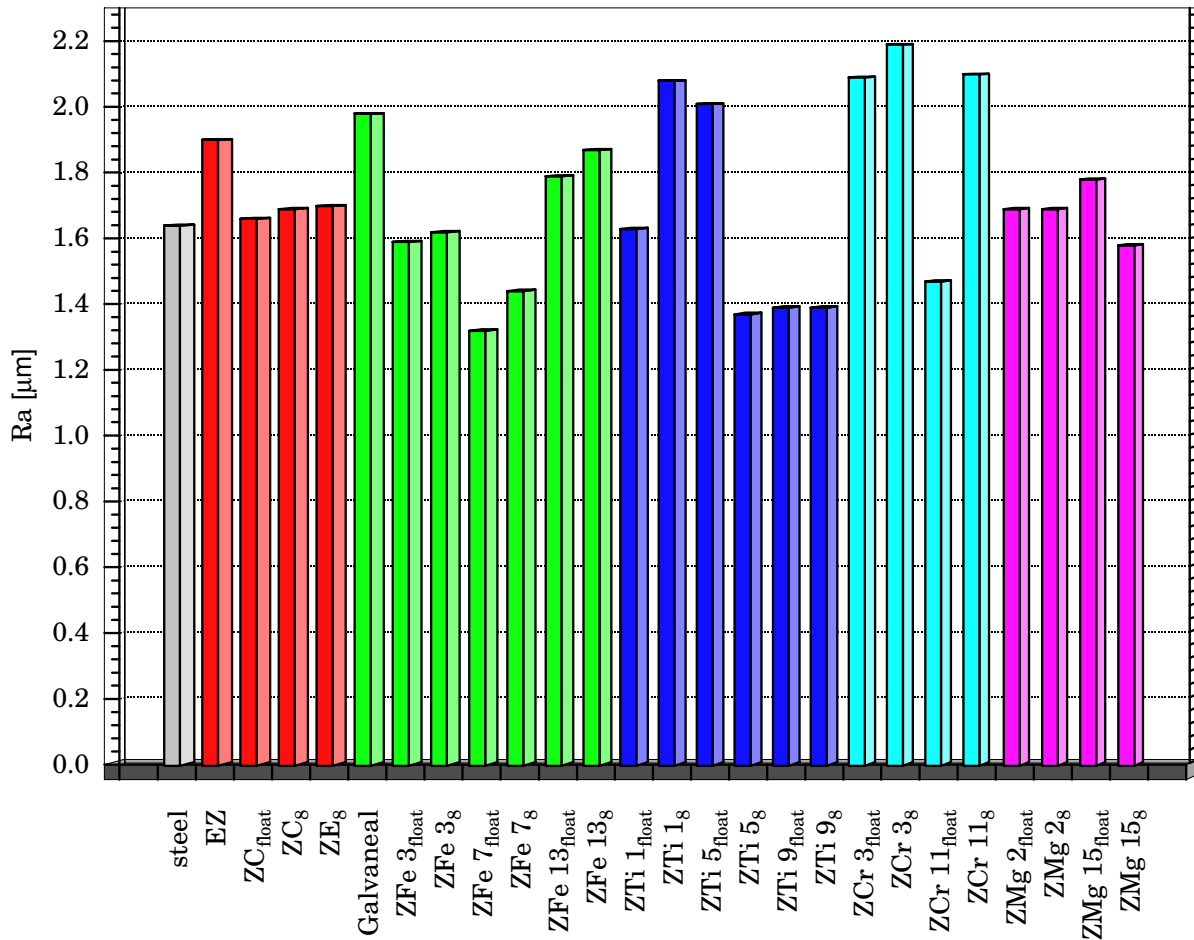
Figure 3.103: Roughnesses of zinc and zinc alloy coated steel sheets, given as R_a–values

films, in a structure zone model (SZM). Their SZM illustrates the general morphological features of a film as a function of the normalised growth temperature T_s/T_m.

The later developed SZM's of Thornton [146], Messier et al. [147], Craig and Harding [151], Grovenor et al. [152], Fountzoulas and Nowak [153] and Barna and Adamik [154–157] include additional process parameters altering the growth phenomena and thus the resulting film structures. As important process parameters for the development of thin film morphologies these authors include: the substrate temperature T_s, the melting point T_m of the deposited material, the substrate material and its roughness, the energy and direction of the vapour flux, the energy and direction of eventually bombarding particles, the presence of other species (intentionally added or process contaminations), possible oxidation and corrosion phenomena, etc.

Figure 3.107 shows the Thornton structure zone diagram which schematically displays the microstructures of magnetron sputtered films as a function of the normalised substrate temperature T_s/T_m and argon pressure. The blue line in Fig. 3.107 indicates the structures theoretically expected for a zinc film ($T_m = 693$ K) sputtered at different argon pressures at a substrate temperature of $T_s = +100$ °C (373 K).

The influence of substrate temperature on the morphology of the ion beam sputtered zinc samples ZIB has been presented in section 3.1.1.2. For the temperature range from -60 °C to +60 °C the obtained microstructures can be categorised according the Thornton diagram. Coating ZIB_{-60} with a T_s/T_m of 0.3 can be classified as Zone T type. At this temperature a large supercooling for the depositing adatoms exist which leads to the creation of a multitude of nuclei. As result a fine grained columnar structure grows. With increasing T_s the obtained structures change to Zone 2 or Zone 3 types. But in the case
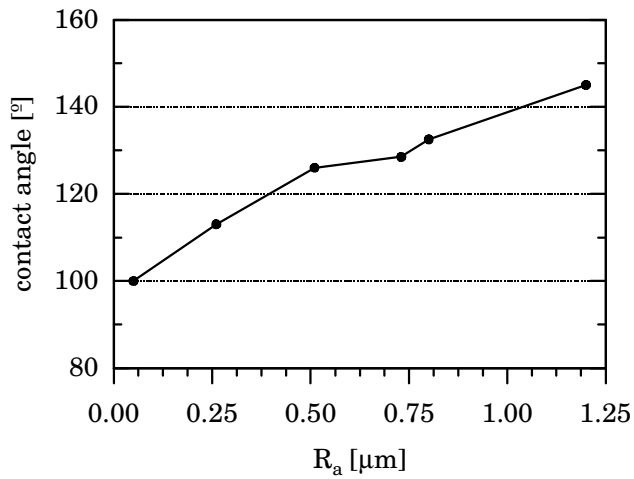
Figure 3.104: Contact angle versus surface roughness given as R_a value
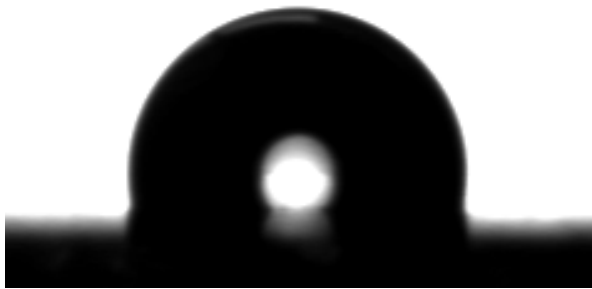
Figure 3.105: Water drop settled on coating ZIB_{-60} deposited at $T_s = -60$ ℃
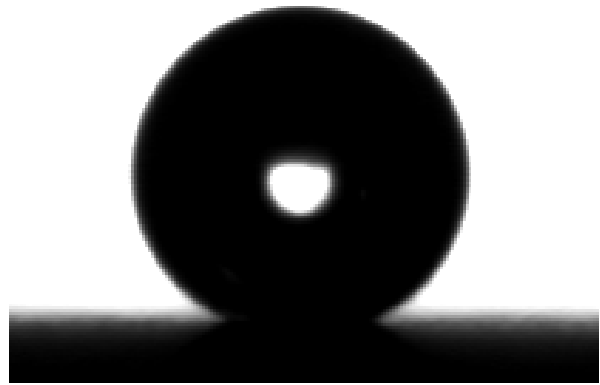
Figure 3.106: Water drop settled on coating ZIB_{+140} deposited at $T_s = +140$ ℃
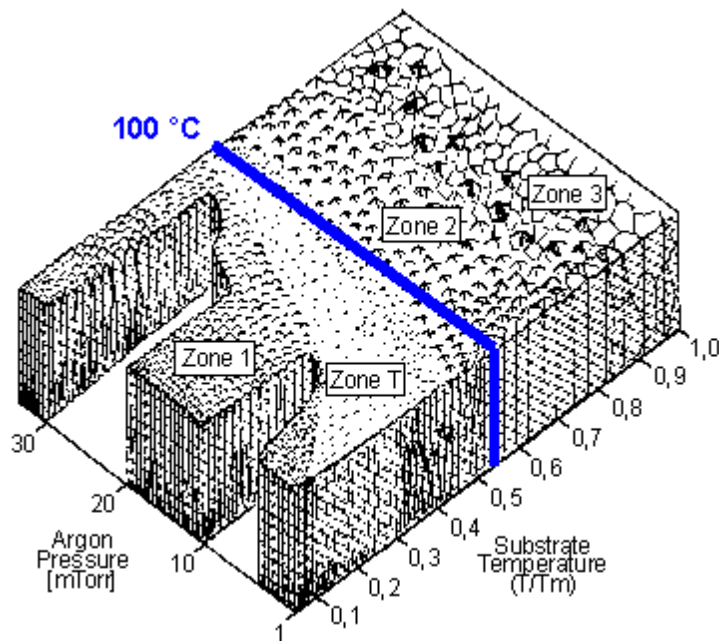
Figure 3.107: Thornton structure zone diagram

of zinc depositions some of the microstructures of these zones have already been obtained at normalised substrate temperatures much lower than those predicted by the Thornton diagram. Due to an increased surface mobility, grain boundary migration and a possible recrystallisation film ZIB_{60} has a "coarse", grained structure. With further increased substrate temperature the microstructures deviate from those types predicted by the structure zone model. At temperatures of $T_s \geq +70\,°C$, where T_s/T_m is above 0.5, the growth of whiskers or whisker like structures can be observed. This structure type does not occur in any of the structure zone models mentioned above. The Thornton model expects a Zone 2 type structure for this temperature range.

The influence of T_s on the morphology is also observed with the magnetron deposited films, especially by comparison of the samples, deposited in the same batch, but mounted with unequal heat transfer to the substrate holder, e.g ZA_{float} versus ZA_8. Sample ZA_8 has a columnar structure which can be classified as Zone 2 type according Thornton. Coating ZA_{float} on the other hand crystallised in a three dimensional sponge like structure, which is not expected by the different SZM's. Apart from the substrate temperature, which depends on the heat influx and cooling efficiency, all other deposition parameters were the same for these experiments. The samples passed the same precleaning steps, they were evacuated to the same base pressure, they were cleaned by the same dose of ion bombardment from the plasma and during deposition they received the same flux of coating material and other bombarding energetic particles. The only difference was their thermal history. As already shown in section 2.1.1 with sputtering a significant rise of the substrate temperature occurs, due to a variety of heating processes. Even the precleaning step by ion bombardment rises the substrate temperature. For the glued samples and their ensured heat flux to the substrate holder a substrate temperature close to that of the substrate holder can be assumed. In the case of the "floating" magnetron deposited samples ($T_s = T_{float}$) the substrate temperature rises during the deposition, especially in case of an assisting ion bombardment [158–160]. These facts hold also for the ion beam sputtered samples.

In comparison to other elements zinc has quite a low heat capacity, see Tab. 3.10. Therefore the rise in temperature, caused by the different heating processes should be more pronounced as would happen for other elements.

material	Zn	Fe	Ti	Al	Cr	Mg
$c_p[10^6\,\mathrm{J/deg\cdot mol}]$ at 100 °C	3,75	9,25	3,94	4,62	3,69	3,83

Table 3.10: Heat capacity of used coating materials. The values given are calculated according to [161]

All magnetron sputtered samples deposited at $T_s = +8\,°C$ have morphologies which can be classified as Zone T or Zone 2 types of the Thornton diagram. These samples have a more or less pronounced columnar structure and vary only in their column size. The samples deposited at $T_s = T_{float}$ on the other hand vary much more. Their morphologies range from a coarse, columnar structure seen with sample ZC_{float} (Fig. 3.7), to an increased grain growth observed with the budlike grains of sample ZB_{float} (Fig. 3.3), to worm like growth of sample ZD_{float} (Fig. 3.5), and to the sponge and woolen like structure of ZA_{float} (Fig. 3.1).

The structures of these films depend indirectly also on further process parameters which influence the substrate temperatures. One parameter is the substrate holder rotation and the resulting deposition rate [162]. In the case of a static substrate holder there is a steady flux of coating material and bombarding energetic particles to the substrates and therefore also a steady release of heat of condensation. In the case of a rotating substrate holder the samples pass the target only periodically every 10 seconds. The heat flux is interrupted and during the depositionless pauses the substrates can dissipate their heat. The different thermal loading can be very well noticed by comparison of the samples ZA and ZB.

This influence of thermal loading is furthermore visible by comparison of continuously and interval deposited samples. With the interval deposition experiments the total deposition time of 240 min was split into single deposition runs of 20 min, interrupted by pauses of 10 min. The microstructures obtained

by these experiments, with deposition parameters equal to those of the continuous experiments, lie in between the microstructures of samples continuously sputtered at $T_s = +8$ °C and $T_s = T_{float}$.

For many coating materials (Ti, Cr, Fe, Cu, Mo, Al etc.) the developed SZM's correspond very well to the experimental results. However, none of the SZM's describes for any of the deposited materials the occurrence of whiskers or whisker like structures at high normalised growth temperatures T_s/T_m. In the case of the sputtered zinc coatings the low melting point of zinc ($T_m = 693$ K) seems to influence the growth behaviour of the films very strongly. For most of the depositions zinc can be categorised as a low melting point material as its normalised substrate temperature T_s/T_m is > 0.5. Thornton reported that: "Structural similarity scaling with T/T_m was not observed for all materials. Although each basic structural region was observed in most cases, transition points varied, possibly because of alloy influences and the fact that surface mobilities, heats of condensation, and vapour pressures do not vary linearly with melting point. Departures were greatest for low melting point materials, probably because the adatom kinetic energy and heat of condensation made low values of T/T_m on the condensate surface difficult to achieve for such materials." [146]

To check the influence of the low melting point and thus resulting high normalised growth temperatures, ion beam sputter depositions with a second low melting point material have been performed. As a coating material indium with a comparatively even lower melting point of $T_m = 429.6$ K was chosen. Indium has a very low vapour pressure and a very selective sensitivity to oxygen. The absorption of residual gases, in the case of indium especially the absorption of oxygen, has an important effect on the surface tension of the particles and therefore an influence on the crystallisation and coalescence [163]. The obtained films grown at substrate temperatures of +30 °C, +80 °C and +140 °C, with sputter parameters identical to those of the ZIB coatings, can be seen in Fig. 3.108 to 3.111. First one notices that the created microstructures do not form continuous films. All films consist of single grains which have not coalesced and whose grain densities change with different T_s. Similar results have been obtained by Musil et al. [162] who investigated the surface morphology of sputter deposited In, InSn(90/10), Sn and Cr films. The microstructure obtained at $T_s = +30$ °C where $T_s/T_m = 0.7$, shown in Fig. 3.108, is comparable to the one of sample ZD$_{float}$. Also here worm like grains are built. A difference to the zinc film exists in the grain density, which is much higher for the zinc films. With the latter the entire substrate surface is covered with a continuous film whose grain size is much smaller.

By increasing the substrate temperature to $T_s = +80$ °C , where $T_s/T_m = 0.82$, an agglomeration of grains, forming bigger islands, can be observed. With further increase of the substrate temperature to +140 °C , where $T_s/T_m = 0.96$, these islands disappear. The substrate surface is now densely covered with very small, spherical grains. It is very probable that the spherical shape of the grains results from liquid indium droplets which have been formed during film condensation. Additionally, in some places bigger polygonal, pyramid like grains can be seen. Also these grains could be evidence for crystallisation via liquid phase [159]. However in the case of indium depositions at high substrate temperatures, even for those close to melting point, no whisker growth has been observed.

3.1.7.2 Vapour Pressure

Apart from its low melting point another property distinguishes zinc from many other coating materials: its high vapour pressure. As already seen in section 2.2.3.1 the vapour pressure of zinc is about 4 to 6 magnitudes higher than the vapour pressures of other materials investigated for the development of the SZM's. It is also higher than that of indium examined before. Due to this reason for zinc a high rate of re-evaporation can be expected at high T_s. Besides other effects the re-evaporation of adatoms and their repeated condensation at cooler parts of the coating could thus lead to the observed morphologies.

Neirynck, Samaey and Van Pouke [159], studied the dependence of the evaporation rate on the re-evaporation temperature of zinc. For this purpose they vapour deposited zinc at different deposition rates
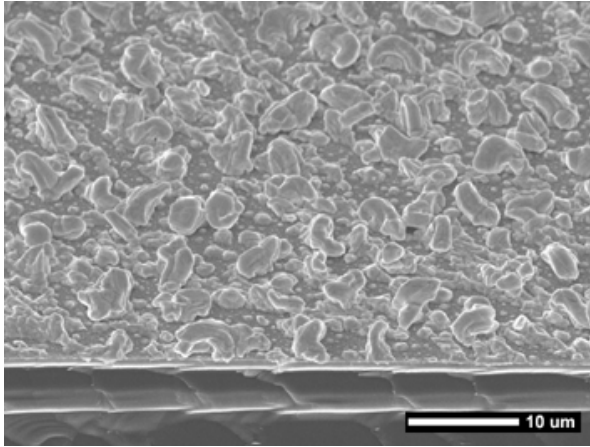
Figure 3.108: Ion beam sputtered indium coating deposited at substrate temperature $T_s = +30$ ℃
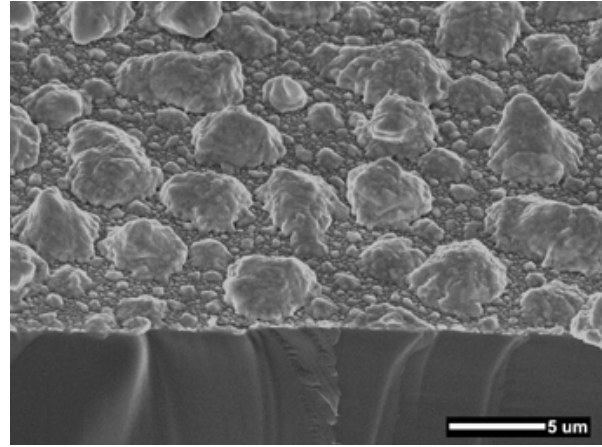
Figure 3.109: Ion beam sputtered indium coating deposited at substrate temperature $T_s = +80$ ℃
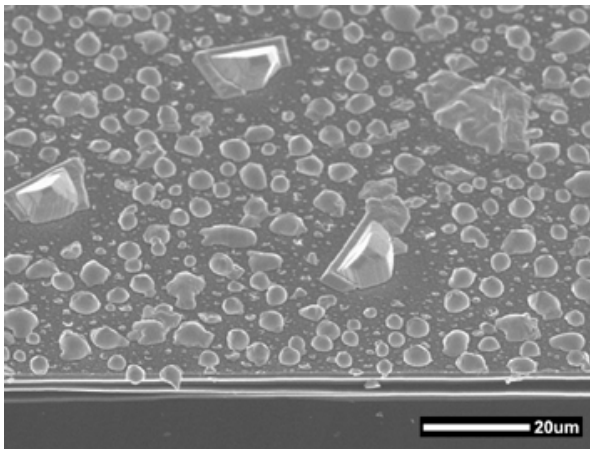
Figure 3.110: Ion beam sputtered indium coating deposited at substrate temperature $T_s = +140$ ℃
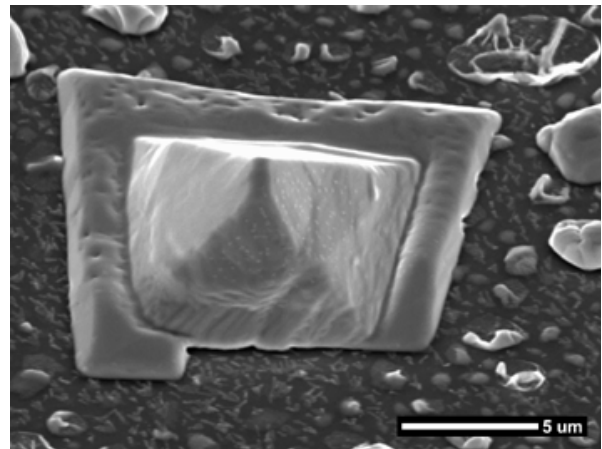
Figure 3.111: Detailed view of ion beam sputtered indium coating deposited at substrate temperature $T_s = +140$ ℃

and determined the maximum substrate temperatures where coatings have been formed. This is termed the "re-evaporation temperature". Their results are listed in Tab. 3.11. The re-evaporation temperatures

evaporation rate [Å/sec]	re-evaporation temperature ℃
400	270
1000	280
2000	320
50000	400

Table 3.11: Influence of the evaporation rates on the re-evaporation temperatures of zinc according [159]

strongly rise with increasing deposition rates. They also investigated the morphologies of the coatings deposited in the temperature range from +50 ℃ to +250 ℃. Even with the depositions made at +250 ℃, corresponding to a normalised growth temperature $T_s/T_m = 0.75$, they do not report the occurrence of whiskers. Depositions made by other evaporation processes such as thermal and electron-gun evaporation or arc evaporation, performed by project partners in the framework of the Brite EURAM project "PVD alternatives to conventional zinc coatings", also did not result in whisker like microstructures.

3.1.7.3 Comparison of Sputtering and Evaporation

A general difference between the evaporation and the sputter process exists in their growth environments [110]. These environments, which could cause different film growths, will be explained subsequently.

Sputtering is inherently associated with the presence of a working gas. Due to this reason only at low working gas pressures sputtered atoms reach the substrate without collision in contrast to the method of evaporation. In case of low pressures, the substrate is additionally bombarded by a flux of energetic working gas atoms. These atoms are ions which have been neutralised and reflected at the target surface. With additional biasing of the substrate holder the substrates can even be subjected to an ion bombardment from the plasma.

In case of evaporation methods the vapour sources are generally point sources. With the different target geometries of sputter units sputtered atoms approach the substrates from a much wider range of directions.

Another difference between these deposition techniques is the type of electromagnetic radiation present. The radiation of a molten evaporation source is in the IR-range, while that of a plasma is in the UV-range.

Further differences between evaporation and sputter processes exist in their nucleation densities, which are higher for sputtered films. Under UHV conditions, if well degassed substrates are used, the nucleation density of sputtered films is solely determined by the substrate temperature [163].

The thermal energies of evaporated atoms are about $0.1\,eV$. They are determined by the temperature of the evaporant source. The average energies of sputtered atoms however are in the range of 10–$40\,eV$. The influence of the different deposition environments on the growth of copper whiskers on tungsten have been studied by Grung [148, 164], who performed sputter experiments in a low pressure mercury triode plasma. In his setup a tungsten wire was partially made the anode and therefore heated by bombarding electrons to a temperature of about $500\,°C$. During the slow deposition ($12\,h$, deposition rate $2 \times 10^{13}\,atoms/cm^2$) the normalised substrate temperature was 0.56. This T_s/T_m value is in the same range as that of zinc depositions made at $T_s = +100\,°C$. The SEM images of the coated tungsten wires showed that the Cu atoms agglomerated into islands, on some of which whiskers grew. The interesting fact was that these Cu whiskers were not observed when the Cu was deposited by evaporation under otherwise identical conditions. Additionally in deposition runs that were so long that even very low flux gas scattered Cu atoms formed Cu islands at the far side of the cylindrical substrate (i.e. out of the line of sight from the target), the whiskers were totally missing. Grung stated that it is most likely the higher kinetic energy of sputtered atoms compared to evaporated atoms which plays an important role in the growth of whiskers.

3.1.7.4   Alloying Elements

The alloying elements can influence the development of the coatings morphologies in two ways. First they form solid solutions with zinc (Zn-Al) or in case of systems with limited solubilities (Zn-Fe, Zn-Ti, Zn-Mg, Zn-Cr) they create intermetallic phases or their metastable preliminary stages. These intermetallic phases on their part can act as catalysts for heterogeneous nucleation. With heterogeneous nucleation the extrinsic phase, in this case the intermetallic phase, provides a new interface which lowers the interface enthalpy and therefore the activation energy for nucleation in comparison to homogeneous nucleation. This results in an increased number of growing grains leading to a grain refinement of the resulting structures. A further discussion on intermetallic phases will be given in section 3.2.

A second way alloying elements influence the coating morphologies, especially for those elements with high reactivity to oxygen, is the effect of grain refinement due to oxide formation. In this case the alloyed reactive elements form oxides which act as catalysts for heterogeneous nucleation leading to the same results described above.

A very similar effect of grain refinement due to segregation and repeated nucleation will be discussed in detail in the following subsection 3.1.7.5 dealing with the influence of the gas atmosphere on the morphology evolution.

The trend to a refined grain size due to alloying, especially the size reductions of the smallest grains independent of their resulting morphologies, see tab. 3.12, might be observed with mostly all alloyed coatings apart from the zinc-titanium alloys. SEM images obtained at higher magnifications (20k), shown in 3.1.2, give indications for the presence of nanoscaled substructures within the observed grains. A determination of the real grainsizes, especially on the smaller scale, was not possible as the limited resolution/magnification of the electron microscope used, did not allow the detection of possibly low nano scaled grain and sub grain structures.

Grainsize [nm]				Grainsize [nm]		
	T_{float}	+8 °C			T_{float}	+8 °C
ZC	550–4200	95–1650		ZAl 2	25–680	25–500
ZFe 3	50–580	60–870		ZCr 3	210–1750	85–770
ZFe 7	100–450	100–330		ZCr 11	120–3150	55–200
ZFe 13	50–1000	50–180		ZMg 2	100–210	100–450
ZTi 1	45–550	110–570		ZMg 15	75–2000	200-660
ZTi 5	170–930	170–1350				
ZTi 9	150–2350	550–2300				
ZTi 10	650–4500	570–2600				

Table 3.12: Grainsizes of the magnetron sputtered zinc alloy coatings.

Regarding the intended use of the coatings as protective films, alloying of zinc with the above described reactive metals which form dense, protective oxide layers could enhance the corrosion protection. Zinc titanium and zinc chromium could probably serve as examples, as shown by the performances of these coatings in section 3.5.2.

3.1.7.5 Gas Atmosphere

An important factor for the deposition of thin films is the gas atmosphere in the deposition chamber, which reacts with the vapourised atoms or molecules and the already condensed particles. In most circumstances this reaction is not intended and is a matter of an unavoidable codeposition of impurities such as residual gases and vapours, e.g. oxygen, water vapour, hydrocarbons etc. In the case of reactive sputtering on the other hand, this reaction is intentionally used to deposit films consisting of compounds, e.g. sputtering of boron in nitrogen atmospheres, creating boron nitride films. In any case, the intentionally added doping elements, additives or other component materials as well as the process impurities, have to be treated as active species, which influence the film formation very strongly. In the following, only the role of impurities will be discussed.

During deposition, impurities condense together with the desired film species on the growing surface and participate in the elementary atomic structure building processes in every stage of the film growth. The effects of codeposited impurities become important when the concentrations of the impurities at the given temperature exceed the solubility limit in the main component. Under these conditions a process induced segregation of the impurities during the growth and coalescence of the crystals takes place. The impurity species accumulate at some spots of the growing crystal surfaces and create a new phase there: either a phase of the impurity species themselves or a compound of the coating material and the impurities. Depending on its self-diffusion the accumulated phase forms three dimensional segregates or two dimensional layers which cover bigger and bigger surface fractions of the growing crystals. This phase of impurities hinders the following incorporation of adatoms. The growth of the crystals is altered or even blocked and the condensation proceeds by repeated nucleation. The resulting structure consists of rounded crystals with decreased grain sizes. The grains are separated by grain boundaries which form broad and deep grooves on the film surface [165, 166]. Apart from the crystalline shape and size also the development of textures can be controlled by impurities.

In the case of indium depositions, the absorption of oxygen alters the developing film structure: it has an important effect on the surface energy of the interface which for its part influences the crystallisation and coalescence of the particles [163]. This results in an increase of the melting and crystallisation temperatures of the individual droplets and the disappearance of a regular crystalline structure. Since the segregated contamination layers hinder the liquid like coalescence and the accompanying recrystallisation, the interfaces between adjacent crystallites are easily stabilised and a film with random orientation and small grain size grows.

The effect of compound formation, segregation and repeated nucleation might be observed for the low alloyed zinc titanium, zinc chromium and zinc aluminium coatings. Since these alloying elements are very reactive to oxygen, see their heats of formation in tab. 3.13, the surface of these alloys could be covered very easily by an oxide layer. As consequence further condensation should proceed by repeated nucleation resulting in a fine grained but porous structure. However, the presence of these oxide layers has not been measured either by EDX or X-ray diffraction due to the very low fractions of these compounds on the entire coating volumes. Probably the very low grainsizes of 25 nm observed with ZAl 2 have been obtained by this mechanism.

Metal oxides	ZnO	Fe_2O_3	Ti_2O_3	TiO_2	Cr_2O_3	Al_2O_3	MgO_2	MgO
ΔH_{298} [kJ/mol]	348.34	824.8	1519.39	944.12	1130.44	1674.72	623	601.64

Table 3.13: Heats of formation for the various metal oxides at 298 K [161]

The growth of crystals becomes even more complicated when the surface chemical interaction of the codeposited species with the growing crystal surfaces is different for various crystallographic planes. Such a system, which has been analysed in detail by Barna et al. [154, 167], is the aluminium-oxygen system. Their experiments showed that oxygen species can penetrate into the topmost layer of the crystal lattice on the (001) and (110) faces while they are situated on the surface of (111) faces. As a consequence the crystal segregates the oxygen species on the (111) faces which become covered by an impurity layer, whereas the (001) and (110) faces incorporate the oxygen species and remain uncontaminated. This anisotropy in segregation leads to a different growth topography and a truncation of edges on the various crystal faces. Only the (111) faces develop curved bunches of growth steps with pinning sites. The segregation of oxygen in the grain boundary area develops broad and deep grain boundary grooves, which become decorated with grains formed by repeated nucleation on the surface covered by the oxide layer. Furthermore, a selective truncation of the growing Al crystals at the edges between (111) faces is observed. Edges formed by (111) and (100) faces are not truncated.

Apart from these observations, the texture formation of Al films is also influenced by the codeposition of oxygen. The different segregation behaviour alters the texture from <111> for pure Al films to a mixed <111> and <100> texture in case of an oxygen codeposition. In other deposition experiments with Al and Al-20 wt.% Sn films the segregation of oxygen and tin induced a lamellar growth of the Al (111) crystal faces [168, 169]. With increasing oxygen content the oxygen doped Al films changed their structure from columnar to nanocrystalline and finally to amorphous [170]. Due to their reduced grainsize these films showed, accordingly to the Hall-Petch relationship [171, 172], a remarkable increase in hardness.

Bergauer et al. [173] who deposited AlSn (20 wt.% Sn) coatings for application as lubricating coatings on the surface of gliding bearings, made an interesting observation, which is also caused by segregation. They observed the appearance of tin whiskers or whisker like structures, quite similar to those found in the zinc depositions made with this study. The system AlSn is an immiscible binary alloy with a solid solubility of Sn in Al below 0.02 at.%. As a consequence the AlSn20 films show a heterogeneous structure, which is characterised by a continuous aluminium matrix with embedded μm-sized tin grains. As very important process parameter for the development of whisker-like structures they found the oxygen content of the sputter gas. In the range of 0.005 % up to 0.02 % oxygen content the films showed

a uniform and fairly smooth surface. With increasing oxygen content (0.05–0.15 %) on the film surface numerous whiskers like structures with different shapes and dimensions appeared in between the well shaped crystals. The whiskers showed a well defined head, terminated by Al crystal facets and a stem with an irregular surface. At 0.15 % oxygen content the whisker density exceeded $350\,1/\mathrm{mm}^2$. Above an oxygen content of 0.5–1 % the whisker formation ceased again. Apart from the oxygen content, the substrate temperature also played an important role for the development of whisker like structures in these deposition experiments. At an oxygen content of 0.15 % the development of whiskers was promoted by increasing the substrate temperature and peaked at 160 °C. The growth mechanisms of the whiskers are still not fully understood, but as possible explanations Bergauer et al. propose a combination of the following effects:

- Initially grown, thin, single crystal tin whiskers, developed by internal stresses during the film deposition, form the core of the observed whiskers

- Continuous deposition of material (Al and Sn) from the gas phase onto the surface of the whisker

- Enhanced surface diffusion of adatoms due to oxygen contamination of the growing Al surface leads to an additional material transport towards the base and the stem of a whisker

These observations made by Bergauer et al. lead to the idea to study the influence of the oxygen content of the sputter gas on the deposition of zinc films. The results of the deposition experiments presented in section 3.1.4, show a different behaviour for the zinc coatings. The codeposition of oxygen, even at much higher concentrations than those used by Bergauer et al., does not promote the growth of whiskers. The added oxygen rather smoothens the coating surfaces until at higher concentrations zinc oxide films are formed. A possible explanation for the different behaviour of the aluminium-tin and zinc coatings could be their different affinity and reactivity to oxygen. Zinc does not readily absorb oxygen, carbon or nitrogen [153] and it is not very reactive to oxygen as can be seen with the heat of formation ΔH_{298} for ZnO at 298K which is $348.34\,\mathrm{kJ/mol}$ [161]. Aluminium on the other hand is much more reactive. The heat of formation ΔH_{298} for Al_2O_3 is $1674.72\,\mathrm{kJ/mol}$ [161].

3.1.7.6 Deposition rate

Apart from the deposition environment, the deposition rate also seems to influence the deposition of zinc coatings. All non ion assisted zinc deposition experiments made in this study showed at higher deposition temperatures the occurrence of whiskers. These observations, made with the ion beam deposited coatings and the magnetron sputtered coatings, are in contrast to the observations of Musil et al. [174]. Even at high deposition temperatures of $T_s = +120$ °C this group, which magnetron sputtered zinc coatings with and without ion assistance, did not observed the occurrence of whiskers. This fact could be explained by the higher deposition rate of about $30\,\mu\mathrm{m/h}$ with their experiments. The ion beam sputtered coatings made here have been deposited at about $1.5\text{-}2\,\mu\mathrm{m/h}$ and the magnetron sputtered ones at $1\text{-}14\,\mu\mathrm{m/h}$.

In a second work on sputter deposited low melting point, metallic thin films Musil et al. [162] showed the influence of the deposition rate on the crystallisation of In/Sn(90/10) films. They found that films deposited at higher deposition rates have a greater tendency for crystallisation.

A dependence of the whisker growth on the deposition rate was also noted by Bergauer et al. [173], with their deposition of AlSn (20 wt.% Sn) coatings already presented in section 3.1.7.5. Also this group observed a reduction of the whisker growth with increase in deposition rate in the range of 3 to $48\,\mu\mathrm{m/h}$, while all further deposition parameters as substrate temperature (+160 °C) and oxygen content (0.15 %) were kept constant.

The dependence between whisker growth and deposition rate can be explained by the incorporation of impurities from the residual gases H_2O, CO_2, CO, O_2 and N_2 present in the vacuum system. The ratio

between the impingement rate of the deposition material and the impingement rate of the impurity gas molecules determines the impurity concentration C_i of the deposit which is given by [126]:

$$C_i = 5.82 \times 10^{-2} \frac{P}{\sqrt{M_g T}} \frac{M_a}{\rho \dot{d}} \tag{3.1}$$

where P [torr] indicates the residual vapour pressure, M_a, M_g [g/mol] refer to the molecular weights of the deposit and gas, T [K] is the absolute temperature, ρ [g/cm³] is the density of the deposit and $\dot{d}$ [cm/sec] refers to the deposition rate. The formula shows that the impurity concentration linearly decreases with increasing deposition rate of the desired material. Furthermore, impurities may desorb with increased deposition temperature as a result of the higher rate of energy deposition.

While the deposition experiments in oxygen doped atmospheres, made within this study, did not show a direct correlation between whisker growth on zinc coatings and oxygen impurities it has to be kept in mind that the forming probability of impurity layers is increased at lower deposition rates.

3.1.7.7 Whisker growth

Apart from vapour deposited films, spontaneous whisker growth at room temperature is often observed with electroplated coatings of low melting point materials like Sn, Zn, Cd and Bi [149, 175–177]. Successive observations of spontaneously growing whiskers showed that the material needed for the growth is delivered from the surrounding of the whisker base or root. For their growth, different models have been suggested. The first growth model, independently proposed by Eshelby [178], Frank [179] and Amelinckx [180], is based on dislocation motion. A second model proposed by Ellis et al. [181] and further developed by Furuta and Hamamura [182], Tu [183] and Kawanaka [184] is based on recrystallisation [175]. The experiments of Lindborg [176], who investigated the growth of whiskers on Zn, Cd and Sn-electroplates, showed that the whisker growth depends primarily on the internal macrostress, built into the plates during electrodeposition. A strong crystallographic texture $\{11\bar{2}0\}$ and a flat "lath" like microstructure in the plate are additional factors which favour whisker growth. Lindborg proposed a two stage growth model, where the expansion of a dislocation loop by climb, under emission of vacancies which diffuse far away from the whisker root, is followed by glide of the loop through a network of other dislocations towards the surface. A necessary condition for whisker growth at a certain growth rate is that diffusion is rapid enough to provide interstitial adatoms that recombine with the vacancies formed. Also the passing of obstacles by the gliding dislocations is a thermally activated process. As a result whisker growth at room temperature (25 °C) is only observed for low melting point materials. For zinc room temperature corresponds to $0.42\,T_m$, for cadmium $0.49\,T_m$ and for tin $0.458\,T_m$. The following Tab. 3.14, giving the activation energies for self diffusion for each of the investigated coatings materials, shows that the self diffusion energy of zinc is lower than all other metals used for alloying.

element		Q_D[kJ/mol]	for lowest measured temperature range [K]
Zn	⊥ c axis	101.7	513–83
	∥ c axis	91.3	513–83
Fe	α-Fe	281.5	970–1167
Ti	α-Ti	122.7	963–1123
Al		126.4	358–482
Cr		441.9	1073–1446
Mg	⊥ c axis	136.1	741–908
	∥ c axis	134.8	741–908

Table 3.14: Activation energy for self diffusion for the coating materials used [185]

As observed with electroplated coatings, intrinsic stress is also present with sputtered metal films. Due to the complexity of the plasma environment and the effect of the working gas, generalisations with

respect to the origin of intrinsic stress are difficult to make. According to Buckel [126, 186] the conditions and processes conducive to internal stress generation in films can be classified in the following categories:

- differences in the thermal expansion coefficients of film and substrate

- incorporation of atoms (e.g. residual gases) or chemical reactions

- differences in the lattice spacing of monocrystalline substrates and the film during epitaxial growth

- variation of the interatomic spacing with the crystal size

- recrystallisation processes

- microscopic voids and special arrangements of dislocations

- phase transformations

Especially the stress mentioned first, caused by thermal expansion, is often found in thin films. It is the result of a thermal mismatch between the coating and the substrate it is deposited on. In some cases heating to higher deposition temperatures and subsequent cooling to room temperature leads to a delamination or a complete failure of the thin films, especially in case of brittle coatings. At good adhesion and sufficient stiffness of the film a bending of the entire composite is observed. The thermal expansion stress $\sigma_{thermal}$ occurring with cooling or heating of a substrate-coating combination can be calculated according to formula 3.2 [175]:

$$\sigma_{thermal} = \left(\frac{E_{coat}}{1 - v_{coat}} \right) \int_{T_0}^{T_1} (\alpha_{substrate} - \alpha_{coat}) dT \tag{3.2}$$

where T_1 and T_0 are the deposition and final temperature, E_{coat} the Young's modulus of the coating, v_{coat} its Poisson ratio and $\alpha_{substrate}$, α_{coat} the respective thermal expansion coefficients of the substrate and coating. The formula shows that $\sigma_{thermal}$ is linearly dependent on the difference between the thermal expansion coefficients of the film and its substrate. The following Tab. 3.15 gives an overview of the thermal expansion coefficients of the coating and substrate materials used for the experiments made here. The Poisson ratio of zinc is 0.29, whereas its Young's modulus is given as 103 GPa [187]. The

material	use	α at 25℃ [10^{-6}/℃]
Zn	coating	35
Fe	coat./subs.	12
Ti	coating	8.5
Al	coating	25
Cr	coating	6
Mg	coating	25
Si	substrate	3

Table 3.15: Thermal expansion coefficients of the materials used [188]

given values show that there is a big difference in the thermal expansion coefficients between zinc and the substrate materials silicon and iron (steel). This difference, in combination with the low activation energy for diffusion, could be one of the reasons for the observed whisker growth in zinc coatings at high deposition temperatures.

Other observations made by Lee and Lee [175] showed that the growth of whiskers can be caused by biaxial compressive stress. They studied the spontaneous growth of tin whiskers from tin electroplates on phosphor bronze sheets. The stress is caused by the diffusion of copper atoms from the phosphor bronze substrate into the tin film along its grain boundaries and a subsequent formation of Cu_6Sn_5 phase. The biaxial compressive stress elongates the grains in a direction normal to the film plane. Due to the elastic anisotropy of tin the elongation of the grains is not uniform and depends on their orientation. This difference in elongation leads to a cracking of the tin oxide layer on top of the grains, whose orientation

is different from the major orientation of the tin film. To release the stress in the film, the grains, whose surface oxide is sheared, extrude tin in the form of whiskers. The whisker growth is controlled by the expansion of the prismatic dislocation loops by climb and their subsequent glide in the slip direction toward the surface of the film.

The influence of the target microstructure on the growth of whiskers was studied by Succo et al. [189]. This group investigated sputtered films of aluminium-copper-silicon alloys from targets whose microstructures were varied with regard to their contents of homogeneous solid solution, Al_2Cu and silicon second phase precipitates by different heat treatments. They showed that the propensity for whisker growth in sputter deposited films is linked to the presence of second phase precipitates in the target material. Hillocks and single crystal whiskers in aluminium or aluminium alloy films on silicon substrates appeared when the films were subjected to thermal expansion stresses at temperatures of $\sim 400\,°C$. The growing whiskers relieved the thermal expansion stress in the film. As mechanism for the influence of the presence of second phase precipitates in the target material and thus resulting whisker growth in the film, they proposed a dimer (Al_2Cu) or trimer emission from the target. The dimers condense on the substrate and promote the nucleation of second phase precipitates in the film. These second phase precipitates reduce the grain boundary mobility by pinning of grains and prevent the stress relief by hillocking. The film is forced to a different mode of stress relief: the evolution of single crystal whiskers.

3.1.7.8 Ion Assistance

The results of the ion bombarded zinc and low alloyed zinc iron coatings obtained in this study are similar to the results for magnetron sputtered zinc coatings obtained by Musil et al. [174]. Simultaneous ion bombardment smoothens the growing films. Even at higher substrate temperatures $T_s = +150\,°C$, where the non ion assisted coatings show a rough, whisker-like microstructure, smooth specular reflecting surfaces have been achieved. The smoothing of the film surfaces can be explained by two mechanisms. According to the first mechanism the smoothing of coatings by concurrent ion bombardment is explained by erosion of the peaks and filling of the interjacent "valleys" with material produced by "forward sputtering". The second mechanism attributes the smoothing to an incorporation of argon, stemming from the bombardment, into the film. The incorporated argon suppresses the grain growth, resulting in a decrease of grain size and smoothens the film surface in that way. [99, 190–192]

Whisker growth due to ion bombardment on seeded metal surfaces   A correlation between the ion energy of an ion bombardment on metal surfaces with metal impurities resulting in cone or whisker formation was found by Wehner et al. [148]. Wehner and his coworkers showed that intentionally or unintentionally formed seed cones are the result of an interplay between simultaneous growth and sputtering of seed atoms creating the nucleation centres of the cones. In particular these cones are observed on sputter targets of soft metals like Cu, Ag and Au. With these metals they can often be formed without any intentional seeding, even on 99.999 % pure copper targets. The embedded surface impurities originating from the fabrication of the "pure" target metal are responsible for the seeding. A clear sign that such cones arise from impurities is the fact that rows of cones appear in the rolling or drawing direction and on cut edges of the target metal. For the ion bombardment of the targets Wehner and his coworkers used a low gas pressure triode plasma of mercury and argon. The ion energies were varied from 500 eV down to energies lower than the sputtering threshold energies, which for Argon are roughly four times the heat of sublimation of the metal. As a seed source a thin wire of the seed metal was wrapped around the target. By bombardment of about 50 target metal/seed metal combinations with ions (energy < 1 keV) they found several combinations where cone forming seed metals had a higher sputtering yield, but not a single one had a lower melting point than the target metal. Seed cones formed

only at elevated target temperatures. The required temperatures, which were higher for high melting point target materials, were in the order of $^1/_3$ T_m. These temperatures seemed to be necessary, at least at low ion energies, to enhance the movement of seed and target atoms at the surface.

Apart from the seed cones they observed also "deposit cones" with a quite different shape. These cones appeared when large amounts of lower melting point metals agglomerated into islands on higher melting point surfaces and were converted into conelike protuberances by the ion bombardment. They found that for cone formation a critical density of foreign seed atoms is necessary. Below this threshold value the cone formation ceased. The critical density was of course a function of many parameters such as substrate species, seed atom species, substrate temperature, crystal orientation, substrate sputtering rate, surface roughness, etc.

By lowering the bombarding ion energies near to sputtering threshold values and maintaining the required elevated temperatures Wehner and his coworkers observed the genuine growth of shiny, straight single crystal whiskers. The whiskers seemed to grow from target atoms which were fed in at their base. Their growth direction was not related to the ion beam direction. They grew in all possible directions. This was proof that these whiskers were not the result of a left standing phenomenon but resulted from a true growth process. The growth of the whiskers required not only an elevated (melting point related) temperature but it required an oxygen and nitrogen free plasma. These gases retard surface migration of atoms which seems to be essential for whisker growth and cone formation. By subsequent bombarding with higher energetic ions the whiskers were gradually transformed into ion beam aligned cones. Only on carefully cleaned pure metals, avoiding any trace of seed atoms, no cone or whisker formation was observed.

Summarising section 3.1.7, the evolution of whisker like microstructures with sputtered zinc and low alloyed zinc coatings, observed with the depositions experiments made in this study, seems to be the result of an interplay of high deposition temperature, low melting point of the deposited zinc, residual gases present, low deposition rate and high kinetic energy of the sputtered adatoms. As already stated in the preceding section the low deposition rate increases the forming probability of impurity top layers from residual gases. These may block further take up of the adatoms in the grains, leading to a repeated nucleation. The high deposition temperature (high T_s/T_m) and high kinetic energy of the adatoms increase their diffusivity and surface mobility. These facts together with an additional thermal expansion stress may lead to a growth phenomenon similar to the ones observed by Grung and Wehner presented in sections 3.1.7.3 and 3.1.7.8.

The intentional growth of such cones or whiskers under controlled conditions, extended to further coating materials could find some potentially useful applications: applications in which an increased surface roughness allows better optical or electron absorption, increased catalytic activity, better interlocking with subsequently deposited coatings, improved interlocking of body implants or the production of field emitters.

3.2   Chemical Composition

Tab. 3.16 gives the chemical compositions of the magnetron and ion beam sputtered zinc alloy coatings measured by EDX and information of the film structures obtained by the XRD measurements, which will be presented in detail in the following section. The values for the phase compositions in Tab. 3.16 expected according to the equilibrium phase diagrams are calculated by means of the lever rule with data taken from [41, 42, 111].

Magnetron sputtered coatings

Sample	Number of alloying screws	Composition alloying element in the coating [at.%]		Structure and phases present	Composition expected according to the equilibrium phase diagram [~at.%]
		T_{float}	+8 °C		
ZFe 3	14	2.7	3.3	CSS	57 hex(Zn) + 43 ζ-FeZn$_{13}$
ZFe 7	36	6.8	6.5	CSS	5 hex(Zn) + 95 ζ-FeZn$_{13}$
ZFe 13	59	13.2	13.6	CSS	2 ζ-FeZn$_{13}$ + 98 δ-FeZn$_{10}$
ZTi 1	9	1.2	1.7	CSS	76 hex(Zn) + 24 Zn$_{15}$Ti
ZTi 5	22	5	5.5	CSS, ASS	16 hex(Zn) + 84 Zn$_{15}$Ti
ZTi 9	32	9.8	9.4	CSS, ASS	93 Zn$_{10}$Ti + 7 Zn$_5$Ti
ZTi 10	36	7.7	—	CSS	74 Zn$_{15}$Ti + 26 Zn$_{10}$Ti
	"	—	11.1	ASS	50 Zn$_{10}$Ti + 50 Zn$_5$Ti
ZAl 4	2.7 at.%Al	T_{iso}: 3.9	4.5	CSS	96 hex(Zn) + 4 fcc(Al)
ZAl 2	target	T_{float}: 2.2	2.6	CSS	98 hex(Zn) + 2 fcc(Al)
ZCr 3	6	2.9	3.1	CSS	46 hex(Zn) + 54 CrZn$_{17}$
ZCr 11	17	10.3	12.8	CSS	CrZn$_{13}$ + bcc(Cr) ?
ZMg 2	9	2.5	2.1	hex(Zn) +MgZn$_2$	85 hex(Zn) + 15 Mg$_2$Zn$_{11}$
ZMg 15	18	—	13.9	hex(Zn) +Mg$_2$Zn$_{11}$ +Mg$_4$Zn$_7$	10 hex(Zn) + 90 Mg$_2$Zn$_{11}$
	18	16	—	hex(Zn) +Mg$_2$Zn$_{11}$ +Mg$_4$Zn$_7$	97 Mg$_2$Zn$_{11}$ + 3 MgZn$_2$

Ion beam sputtered coatings

	Number of alloying screws	Composition alloying element in the coating [at.%]		Structure and phases present	Composition expected according to the equilibrium phase diagram [~at.%]
		$T_s = +150$ °C	$T_s = +25$ °C		
ZFeIB 1	6	2.6	—	CSS	63 hex(Zn) + 37 ζ-FeZn$_{13}$
ZFeIB 2	10	4.7	—	CSS	33 hex(Zn) + 67 ζ-FeZn$_{13}$
ZFeIB 3	13	7.8	—	CSS	88 ζ-FeZn$_{13}$ + 12 δ-FeZn$_{10}$
ZFeIB 4	15	11.5	—	CSS	31 ζ-FeZn$_{13}$ + 69 δ-FeZn$_{10}$
ZFeIB 5	17	14.5	14.5	CSS	93 δ-FeZn$_{10}$ + 7 Γ_1-Fe$_{11}$Zn$_{40}$

CSS = crystalline super saturated solid solution, ASS = amorphous super saturated solid solution

Table 3.16: Compositions and structures of sputtered zinc alloy coatings. The expected equilibrium phases are taken from [41, 42, 111]

Tab. 3.17 gives the respective zinc concentrations, structure data and Gibbs energies of formation $\Delta_f G^0$ for the various zinc alloy phases which should be obtained in the relevant concentration range according to their equilibrium phase diagrams.

Since the deposited zinc iron coatings range up to 14.5 at.% iron as can be seen in Fig. 3.112 one could
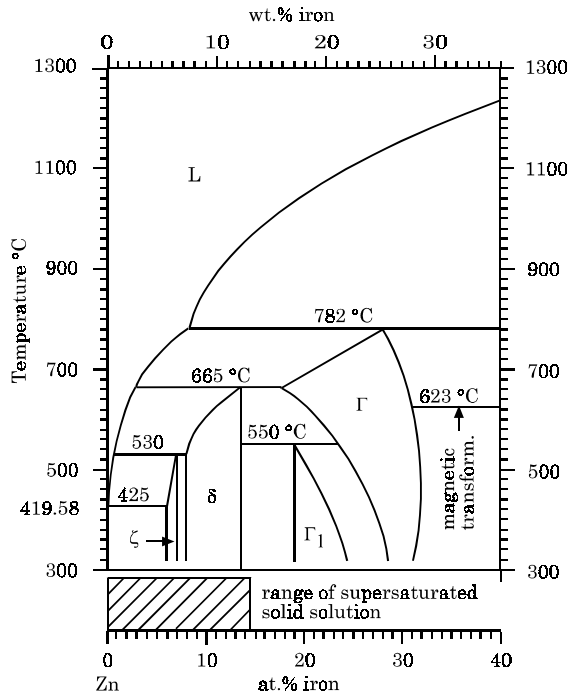
Figure 3.112: Zinc rich corner of the zinc–iron phase diagram [41]
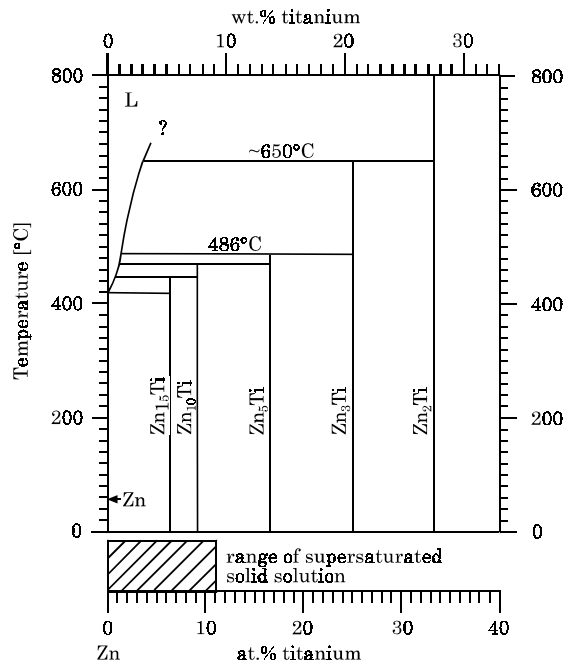
Figure 3.113: Zinc rich corner of the zinc–titanium phase diagram [42]
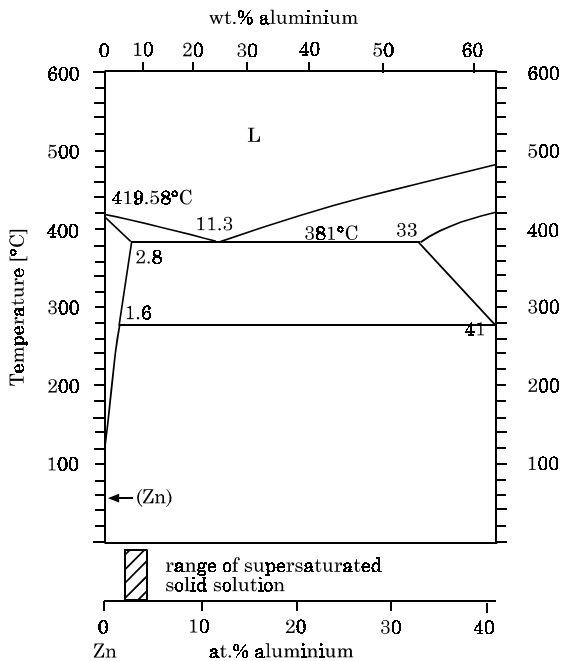
Figure 3.114: Zinc rich corner of the zinc–aluminium phase diagram [42]
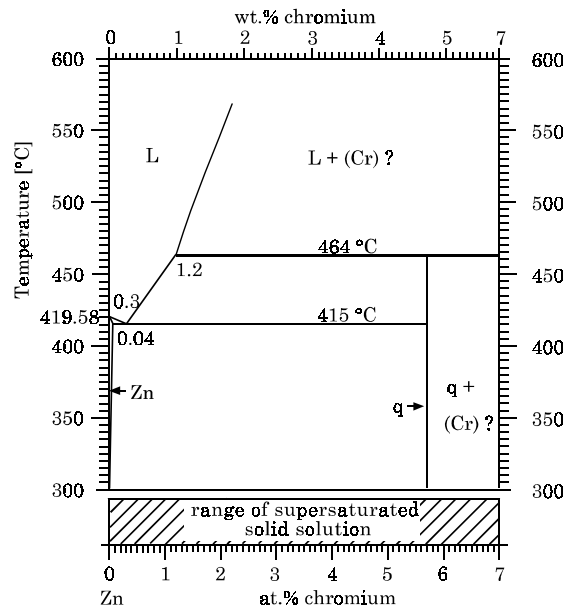
Figure 3.115: Zinc rich corner of the zinc–chromium phase diagram [42]

Alloy	Phase	x-[at.%] of Zn in alloy or compound	Structure	Prototype	$\Delta_f G^0$ at 298.15 K [J/mol]
Al-Zn	Zn	100	hex	Mg	—
	Al	0	fcc	Cu	—
Cr-Zn	$CrZn_{17}$	94.4	—	—	-579
	$CrZn_{13}$	93	—	—	-679
	Cr	0	bcc	W	0
Fe-Zn	ζ: $FeZn_{13}$	93		$CoZn_{13}$	-2268
	δ: $FeZn_{10}$	86.5		$FeZn_{10}$	-3110
	Γ_1: $Fe_{11}Zn_{40}$	72.0		$Fe_{11}Zn_{40}$	-5544
	Fe	0	fcc	Cu	0
Mg-Zn	Mg_2Zn_{11}	84.6		Mg_2Zn_{11}	-5255
	C14 Laves $MgZn_2$	66.7		$MgZn_2$	-10906
	Mg	0	hcp	Mg	0
Ti-Zn	$Zn_{15}Ti$	93.7	orth	$Zn_{15}Ti$	no data available
	$Zn_{10}Ti$	90.9		—	no data available
	Zn_5Ti	83.3		—	no data available
	Zn_3Ti	75	cub	$AuCu_3$	no data available

Table 3.17: Equilibrium phases, their structure and standard Gibbs energies of formation $\Delta_f G^0$ according to [9, 41, 42, 111, 193, 194]
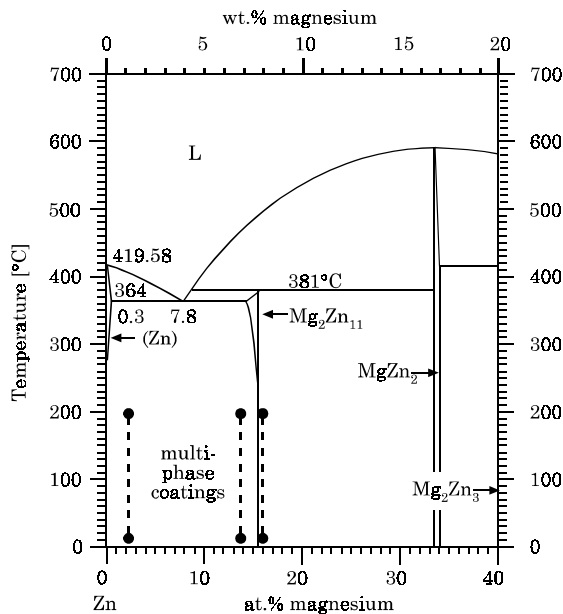
Figure 3.116: Zinc rich corner of the zinc–magnesium phase diagram [111]

expect the hexagonal zinc and the intermetallic ζ-$FeZn_{13}$, δ-$FeZn_{10}$ and Γ_1-phases to occur. Actually the sputtered coatings consist of several supersaturated solid solutions.

As shown in Fig. 3.113, at equilibrium state the deposited zinc titanium coatings with compositions of up to 11.1 at.% titanium could consist of hexagonal zinc and the intermetallic phases $Zn_{15}Ti$, $Zn_{10}Ti$ and Zn_5Ti. The obtained structures are crystalline or amorphous super saturated solid solutions. At room temperature the Zn–Al equilibrium phase diagram (Fig. 3.114) shows a miscibility gap between the hex Zn and fcc Al phases over the entire composition range. The sputter deposited Zn-Al coatings instead condense in a super saturated crystalline phase.

The Zn–Cr system (Fig. 3.115) shows the existence of the two intermetallic phases $Zn_{17}Cr$ and $Zn_{13}Cr$ at room temperature. The vapour quenched coatings show complete solubility over the entire concentration range.

As shown in Fig. 3.116 the zinc magnesium coatings deposited up to an alloy content of 16 at.% magnesium could consist of the intermetallic Mg_2Zn_{11}- and $MgZn_2$- phases. The sputtered coatings

however crystallise in the Mg_2Zn_{11}- and Mg_4Zn_7-phases.

3.2.1 Metastable, super saturated solid solutions obtained by sputtering

The data given in Tab. 3.16 show that the phase compositions of many zinc alloys coatings sputtered in this study deviate from those expected according to the equilibrium phase diagrams in Fig. 3.112 to 3.116. Many of them consist at given compositions of single phase supersaturated solid solutions (Zn-Fe, Zn-Ti), although the respective equilibrium phase diagram predicts a two phase system and/or the creation of compounds at this composition. The zinc titanium coatings condense additionally in a nanocrystalline/amorphous structure.

The deviation from equilibrium can be explained by the fact that sputter deposition takes place far from thermodynamic equilibrium. According to Turnbull [195] therefore all these structures are "metastable structures or, more accurately, configurationally frozen metastable structures".

The classical picture of forming a metastable phase is the crossing of an equilibrium phase boundary without configurational changes. The general procedure is to energise and then quench a material at high cooling rate. The energisation of the material can be obtained by evaporation, dissolution, irradiation, plastic deformation or simply heating the material into a state, solid or liquid, in which its volume is not much expanded.

A metastable material, e.g. an undercooled liquid, is in internal equilibrium, though its free energy is above that of the same body in the stable state. Within this metastable body, local atomic rearrangements can occur very rapidly so that it passes freely through the many microstates which constitute its macrostate. A more stable phase will be obtained if a nucleus of the stable phase is formed and the interface between the stable and metastable phase migrates through the body. Although the atomic mobility may be high enough to permit the migration of the interface the metastable phase can persist for long or even indefinite periods. The reason for this fact is that no nucleation of the stable takes place owing to the high activation barrier. No nucleation is the key criterion for metastable structure synthesis.

In addition to the classical synthesis routes, where the phase boundaries are crossed at high speed, there are other routes creating metastable structures more slowly. Table 3.18 gives an overview on methods delivering metastable structures and their maximal quench rates approached.

An arbitrary classification of metastable structures, the nature of metastability and their energy in excess, which describes the deviation from equilibrium, is given in Tab. 3.19.

Metastability is observed with metal alloys as well as pure metals. Many solids used in practice are in states which are, in some essential respect, configurationally frozen [195]. An obvious example is a homogeneous alloy with a composition in the spinodal range, which has been quenched to a temperature, where the frequency of the interatomic exchanges which affect compositional fluctuations is negligible. One example is the freezing of the compositional short range order in alloys with compositions well within the solubility limits. A striking example is the "glass transition" of an undercooled liquid.

3.2.1.1 Vapour Quenched Metastable Phases

As the metastable structures in this study are derived by sputtering which is a vapour quenching technique, the following section deals with this process in detail. An overview of various metastable metals and alloys obtained by vapour quenching techniques especially sputtering can be found in [198–236].

A good introduction to the field of vapour quenched metastable phases is given by Cantor and Cahn [208] who deposited Al-Ni-, Al-Cu- and Al-Fe-alloys by co-sputtering on liquid nitrogen cooled substrates. In almost all cases the vapour quenched alloys consisted of a variety of polycrystalline non-equilibrium phases. The equiaxed crystals had grain sizes in the range of 50–100 Å similar to that of other sputtered alloys and there was only occasionally evidence for columnar growth. The grainsize of ∼50–100 Å showed that there was continual repeated nucleation during deposition. The rate of re-nucleation and therefore

Method		"Quench rate" [K/s]
Melt or solid quench	Conventional	10^3
	"Splat"	10^5 to 10^8
	Laser pulse	to 10^{13}
Condensation	Vapour	"
	Sputter	10^{12}
	Electro	"
	Chemical	"
Irradiation	Particle Bombardment	"
	Ion implantation	10^{12}
	Ion beam mixing	"
Mechanical alloying	Cold working, co-deformation	—
	Ball milling	—
Hydrogen dissolution		—
High pressure process	Diamond formation	—
Reaction: thermal interdiffusion	Solid-state amorphisation	—

Table 3.18: Methods for metastable structure synthesis [195–197]

Nature of meta- (or "in") stabilities	Materials examples	Typical excess energy [RT$_m$]
Compositional	Supersaturated solutions	$\lesssim 1$
Structural	Intermetallic compounds	$\lesssim 0.5$
	Amorphous solids	"
Morphological	Microcrystalline	"
	Compositionally modulated films	$\lesssim 0.1$
	Interphase dispersions	"

Table 3.19: Classification of metastable structures and their energies in excess from Turnbull [195]. The energies in excess are given in units of RT$_m$ where T$_m$ denotes the average of the equilibrium melting temperatures of the elementary constituents.

the grain size, provides a measure of the degree of quenching and the deviation from equilibrium during film growth. In the extreme case of re-nucleation every 1-2 atoms of thickness, the resulting structure would be expected to be amorphous. With the alloys deposited by Cantor and Cahn re-nucleation occurred every 20-30 atoms of thickness and the structure was polycrystalline. For each alloy system the solubility limit of the vapour quenched alloys was greater than that obtained by liquid quenching (up to eutectic composition), and much greater than the equilibrium solubility limit. Vapour quenched Al-Ni and Al-Fe alloys prepared by sputtering showed a higher solubility limit than equal thermal evaporated alloys.

The extensive supersaturation of vapour quenched solid solutions, which is even higher than that of liquid quenched ones, can be explained by the nearly impossible short range ordering or clustering in the gas phase. According to Kumar et al. [237] in the liquid phase some pre freezing short range ordering or clustering seem to occur which act as nuclei for equilibrium phases during the subsequent quenching.

The fact of no ordering in the gas phase can be used even for the fabrication of "immiscible" alloy systems by non-equilibrium vapour quenching. Due to a positive heat of mixing ΔH_{mix} the two constituent elements of "immiscible" systems show little or no mutual solubility even in the liquid state up to very high temperatures. Examples for such systems are Ag-Fe, Ag-Ni, Cu-W and Ti-Mg. A comprehensive overview of such alloys, their synthesis by vapour quenching and their characterisation is given by Ma [238].

Non equilibrium processing leads to a variety of compositional and structural metastabilities as amorphous phases, supersaturated crystalline solid solutions and even some metastable intermediate compounds. With the vapour quenched Al-Ni and Al-Cu alloys of Cantor and Cahn [208] a wide variety

of complex equilibrium intermetallic compounds have been suppressed and replaced by a disordered bcc phase. The formation of this quenched bcc phase is not surprising because both alloy systems contain ordered bcc phases (Ni_2Al_3, NiAl in the Ni-Al system, CuAl, δ, Cu_9Al_4, Cu_3Al in the Cu-Al system) under equilibrium conditions. The fact that equilibrium phases formed by vapour quenching are often closely packed and disordered simple unit cells, has been reported by Anseau [206]. "An intermetallic compound with an ordered structure is in principle the same as an order/disorder alloy, except that the critical temperature for the onset of ordering is higher than the melting point. Solid-state quenching can inhibit ordering in an order/disorder alloy, therefore it is reasonable that the more severe technique of vapour quenching can inhibit ordering in an intermetallic compound." [208].

The observation that an alloy made of the constituents A and B can solidify in an amorphous state can be explained by the fact that its enthalpy is lower than the enthalpy of the corresponding crystalline solid solution. An example for such a system is the Ni-Zr system [239]. At approximately the same concentrations of nickel and zirconium the change in enthalpy ΔG_{mix} for the amorphous solid solution is $\approx -40 \, kJ/mol$, for a solid solution with hexagonal crystal structure $\Delta G_{mix} \approx -20 \, kJ/mol$, at bcc structure $\Delta G_{mix} \approx -25 \, kJ/mol$ and in fcc structure $\Delta G_{mix} \approx -30 \, kJ/mol$. That is to say the amorphous state is thermodynamically preferred compared to the crystalline one. The thermodynamically even more favourable intermetallic phase NiZr with $\Delta G_{mix} \approx -50 \, kJ/mol$ is experimentally first observed by longer annealing over $400 \, °C$. The formation of this intermetallic phase at lower temperatures is kinetically hindered. This is caused either by a smaller effective diffusion coefficient of Zr due to a lower mobility or due to bigger critical nuclei radii for the heterogeneous nucleus formation of the well ordered intermetallic phase.

Also the various Zn-alloys of this study seem to condense in simple unit cells as shown by the simulations of tentative unit cells based on the x-ray patterns given in the next section on x-ray diffraction. Instead of creating the Θ equilibrium phase with a hexagonal unit cell containing 287 atoms [240] the zinc-chromium coatings seem to form a more simple hexagonal unit cell. A guiding principle for synthesis of metastable structures given by Turnbull [195] states that "the paths most favoured kinetically in structural evolution are those requiring the lesser correlations of atomic positions and motions. These would also be the paths of lesser, but not necessary minimum, entropy change. Thus, short range order, whether compositional or topological, can develop more rapidly than long range order."

The phase formation during non equilibrium materials processing is an interplay between thermodynamics and transformation kinetics [234, 241, 242]. The dominant kinetics factors that control phase selection are nucleation, growth and interdiffusion. Whether an alloy can order during vapour quenching depends upon the relation between deposition rate and diffusion.

Cantor and Cahn suggested that ordering in alloy films was controlled by the root mean square distance $\bar{x}$, that deposited surface atoms could move on the surface. After being initially deposited as a random homogeneous mixture, they will be "buried" and therefore stopped by subsequent adatoms. The distance $\bar{x}$ an atom diffuses in a time t is given by the Einstein relation [208, 243]:

$$\bar{x} = (2D_S t)^{1/2} = (2vt)^{1/2} \ a \ \exp\left(\frac{-Q_{SD}}{2kT}\right) \tag{3.3}$$

where D_S is the surface diffusivity, v is the vibrational frequency of surface atoms, a is the individual jump distance, Q_{SD} is the activation energy for surface diffusion, k is Boltzmann's constant and T is the substrate temperature. According to Shao and Tsakiropoulos [244] the surface diffusivity D_S of metallic systems can be approximated as

$$D_S \approx 10^{-7} \exp\left(-10\frac{T_m}{T}\right) \tag{3.4}$$

where T_m is the melting point of the respective alloy. At a deposition rate r_d [Å thickness /sec], each

atom diffuses in the time t for $\sim a/r_d$ sec before being surrounded and restricted by adjacent atoms. The mean diffusion distance per deposition atom is therefore given as

$$\overline{x} = \left(2v\,\frac{a}{r_d}\right)^{1/2}\,a\,\exp\left(\frac{-Q_{SD}}{2kT}\right) \tag{3.5}$$

The exponential form of the relationship indicates that the diffusion distance $\bar{x}$ is largely determined by the activation energy for surface diffusion Q_{SD} and the substrate temperature T. Below a critical substrate temperature the mean diffusion distance is less than one interatomic spacing and atoms that are fully intermixed in the vapour will deposit as single-phase structures. The surface diffusion may be sufficiently rapid for ordering to occur during nucleation but not during subsequent growth.

Starting from the view of Cantor and Cahn and their experiments at low temperature, taking into account only surface diffusion, Saunders and Miodownik [225] extended their considerations also to bulk diffusion of atoms which will become significant at high temperatures. They expected that atoms that are initially "buried" by the depositing atoms will be able to move back to the surface and participate again in the diffusional breakdown of the initially homogeneous mixture. This can occur when the distance X, that a recently deposited atom can move due to bulk diffusion, is greater than the thickness of the film covering it. Saunders and Miodownik calculated X to be

$$X \sim \left[2v\left(\frac{a}{r_d}+\frac{D_B}{r_d^2}\right)\right]^{1/2}\,a\,\exp\left(\frac{-Q_{SD}}{2RT_S}\right)\left(\frac{G_T}{RT_S}\right)^{1/2} \tag{3.6}$$

where G_T is the integral free energy change on the formation of the equilibrium structure from the initial single phase mixture, and

$$D_B = D_0\exp\left(-Q_B/RT_S\right) \tag{3.7}$$

the bulk diffusion, where D_0 is a constant and Q_B the activation energy for bulk diffusion. Following, these authors proposed a hypothesis for predicting non-equilibrium phase formation in co-deposited alloy films, which can be summarised in the following way: "Depositing atoms lose their kinetic energy within a few atomic vibrations and any transformation involving an intermediate high temperature phase, whether it be a liquid or a solid phase must be considered highly unlikely. Nucleation and growth processes are controlled by the substrate temperature and, therefore, when X is less than a few atomic spacings, the structure of the film should reflect the most energetically stable single-phase structure available to it at the temperature of the substrate. This phase can be found directly from the free energy (G) against composition (x) diagrams of the alloy of interest." Analysing a number of systems e.g. (Ni-Fe and Cu-Sn), where both co-deposition and thermodynamic analysis have been reported the authors observed good correlations between the structures observed and the G-x diagrams. The major fact in multiphase formation in co-deposited alloy thin films is the diffusional breakdown of fully intermixed depositing atoms during deposition. By variation of the substrate temperature three kinetic regimes are observed:

1. At low temperature the surface mobility is insufficient for decomposition of the fully intermixed depositing atoms, and the films are constrained to be single-phases.

2. With increasing substrate temperature diffusion will become sufficiently large for small atomic movements to occur on the surface, and the atoms should be able to rearrange themselves sufficiently to form supersaturated two-phase structures.

3. At even higher temperatures diffusion should be large enough to allow full atomic arrangements necessary for equilibrium phase formation.

The important influence of diffusion on the structural evolution of the coatings, determined by the substrate temperature, can be seen also with the zinc and zinc alloy coatings of this study. With increasing substrate temperature a significant trend to crystallinity has been observed (see chapter 3.3).

Summarising the previous paragraphs have shown that the formation of metastable structures by sputtering is a complex interplay between thermodynamics and transformation kinetics. Several factors such as the activation energy for self diffusion, the deposition rate and deposition temperature determine the resulting structure.

3.2.2   Auger Spectroscopy on Zinc Coatings

Figure 3.117 shows the Auger spectra of the electro deposited EZ reference coating, the magnetron sputtered deposited zinc coating ZC_8 and their respective steel substrates. The spectra were obtained from ground and polished cross sections of the samples. The measured spots were $1\,\mu m$ distant from each other and separated by the coating-substrate interface. The spectra show that both coatings are quite pure without visible impurities. Only the expected peaks of zinc, iron and carbon are present. The carbon peaks could originate from impurities on the surface or small grains of diamond polishing paste, which have been pressed into the soft coating during the polishing procedure.

3.2.3   Argon Entrapment in Ion Beam Assisted Zinc Coatings

The EDX spectrum taken from the ion assisted coating ZIB A2 given in Fig. 3.118 shows that the bombardment of the growing zinc films with argon ions lead to the incorporation of argon in the film. The amount of the entrapped argon is ~0.4 at.% for the ZIB A1 coating and ~1.5 at.% for sample ZIB A2. The implantation of gas atoms in ion assisted depositions at implantation energies above 100 eV has been reported by various authors [87]. Apart from the "active" charging of thin films by concurrent ion bombarding "passive" working gas incorporation phenomena have been found also for solely sputtered thin films deposited in diode, triode, ion beam and magnetron sputtering systems [204, 212, 245]. The entrapped gases range from small helium atoms over argon up to large krypton atoms. Even if the gases are virtually insoluble in metals (e.g. He: ppm range) they are effectively trapped at open-volume defects such as vacancies, dislocations, and grain boundaries [246]. The gas trapping mechanism in metal thin films has been reported to be a result of energetic neutrals produced by gas ions scattered off the target in binary collisions [245, 246]. The ability to trap even up to 8–9 at.% of krypton in sputtered glassy metal alloys (Fe-Y, Zr-Fe and Ni-Y) lead even to the consideration to use sputter deposition as viable technique for the storage of radioactive gases from spent nuclear fuels [247, 248].

3.2.4   XPS on Zinc Iron Coating

Figure 3.119 shows the XPS–spectrum of a $0.5\,\mu m$ thick magnetron sputtered zinc iron coating ZFe 13_XPS with 13 at.% iron content. Apart from the compositional analysis made on this sample other samples of these deposition runs have been used for adhesion tests where the influence of interlayers on the coating adhesion have been studied. Due to this reason an titanium interlayer has been additionally deposited between the steel substrate and the zinc iron coating. This layer can be clearly detected in the spectrum. The spectrum shows that carbon- and oxygen impurities in the coating are very low. Only at the film surface the carbon and oxygen content increase.

3.3   Crystallographic Structure

To identify the phases created and to investigate their crystal structures, XRD analysis have been used on the deposited coatings. As references for the peak positions and intensities, data from the JCPDS databank have been used. The JCPDS card 4-831 for synthetic zinc gives a hexagonal structure, symmetry group P63/mmc (194) with lattice parameters a=0.2665 nm and c=0.4947 nm. The zinc unit cell consists of two atoms.
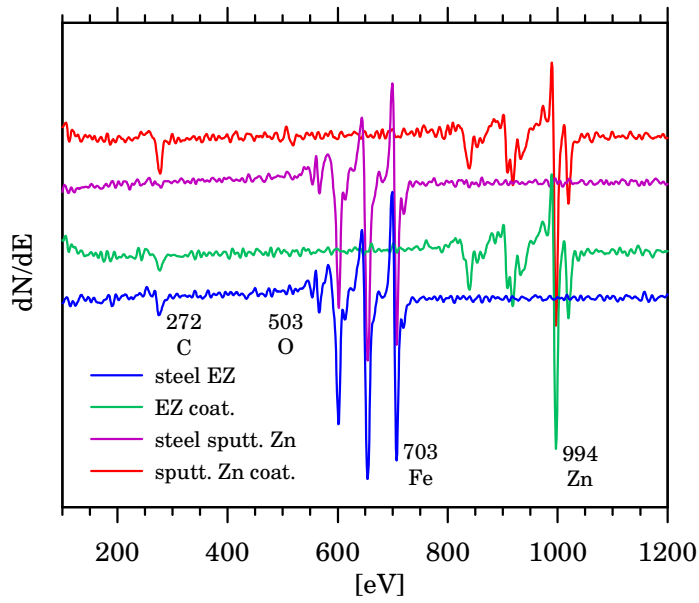
Figure 3.117:
Auger spectra of electro gal-
vanised and sputtered zinc
coatings and their respective
steel substrates
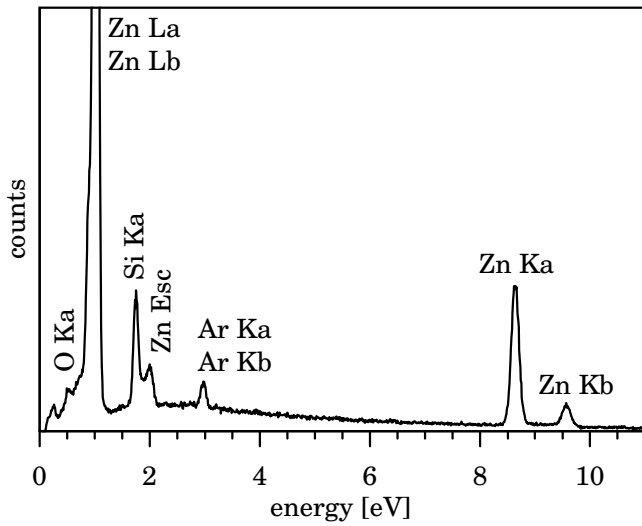
Figure 3.118:
EDX spectrum: Argon entrap-
ment in ion beam assisted zinc
film
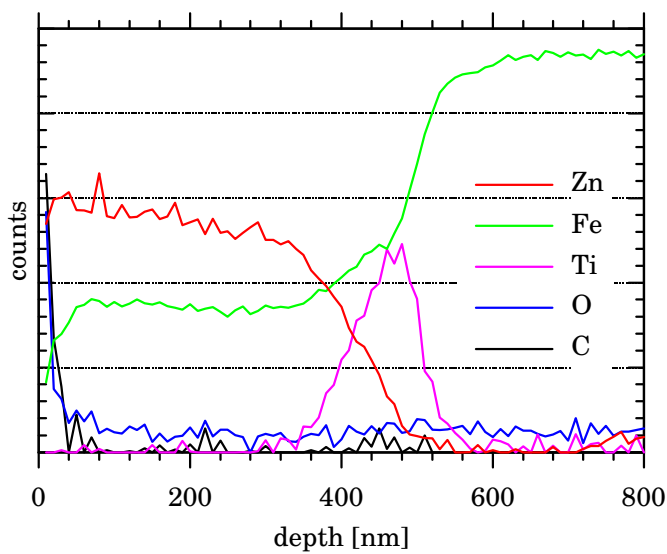
Figure 3.119:
XPS-depth profile of a zinc iron
coating deposited on steel

Due to the penetration depth of the x-rays the diffraction peaks of the substrate materials steel (iron) and silicon are also observed. The preferred orientations of the coatings are expressed in terms of a texture fraction (TF) which is defined as follows:

$$TF = \frac{I(hkl)/I_0(hkl)}{\Sigma\left[I(hkl)/I_0(hkl)\right]} \tag{3.8}$$

where $I(hkl)$ and $I_0(hkl)$ are the intensities of the diffracting planes (hkl) of the measured samples and the JCPDS reference powder sample respectively. When the TFs of all diffracting planes are equal, the distribution of the crystal orientations is random. If the TF of any plane (hkl) is larger than the mean value of the TFs a preferred orientation or texture in direction of the concerning plane exists. The larger the TF value, the greater is the degree of preferred orientation.

3.3.1 Zinc Coatings

3.3.1.1 Electro Plated Zinc Coating

Figure 3.120 shows the XRD patterns of the electrogalvanised coating EZ together with the magnetron sputtered zinc coatings ZC_8 and ZC_{float}. The electrogalvanised zinc coating EZ shows the hexagonal structure of the zinc reference powder from the JCPDS database. The intensities given in Tab. 3.20 indicate a slight, preferred orientation in [110], [101] and [112] directions, whereas the [001] and [100] directions are at a disadvantage.

3.3.1.2 Magnetron Sputtered Zinc Coatings

As the pattern of the electrogalvanised coating also the pattern of the magnetron sputtered coatings ZC_8 and ZC_{float} in Fig. 3.120 show the hexagonal structure of zinc. Additionally, a texture in [002] direction is observed. This texture, with an orientation of the basal plane of the hexagonal lattice parallel to the film surface, is even more pronounced with sample ZC_8. The TFs of these specimens are given in Tab. 3.20.

					Zinc			
	JCPDS 4-831		EZ		ZC_8		ZC_{float}	
hkl	2Θ	Int. %	Int. %	TF	Int. %	TF	Int. %	TF
002	36.33	53	4.8	0.02	**100**	**0.29**	**100**	**0.2**
100	39.02	40	21.3	0.09	1.3	0.01	10.2	0.03
101	43.27	**100**	**100**	0.17	8.7	0.01	53.4	0.06
102	54.38	28	12.7	0.08	4	0.02	19.3	0.07
103	70.12	25	11	0.08	7.5	0.05	18.4	0.08
110	70.73	21	32.9	**0.27**	-	-	20.4	0.1
004	77.1	2	1	0.08	6.7	**0.53**	5.2	**0.28**
112	82.18	23	17.4	0.13	1.9	0.01	7.6	0.04
200	83.85	5	1.2	0.04	-	-	0.9	0.02
201	86.64	17	4.1	0.04	0.4	-	2.8	0.02
104	90.01	3	1.1	0.06	1.5	0.08	3	0.11

Table 3.20: X-ray peak positions, intensities and texture fractions of the electrogalvanised EZ and magnetron sputtered zinc coatings

3.3.1.3 Ion Beam Sputtered Zinc Coatings

Influence of Substrate Temperature

The XRD patterns of the ion beam sputtered zinc coatings ZIB_{-60}, ZIB_{-20}, ZIB_{+20} and ZIB_{+160} are shown in Fig. 3.121. The peak positions and intensities of the XRD patterns of the coatings deposited
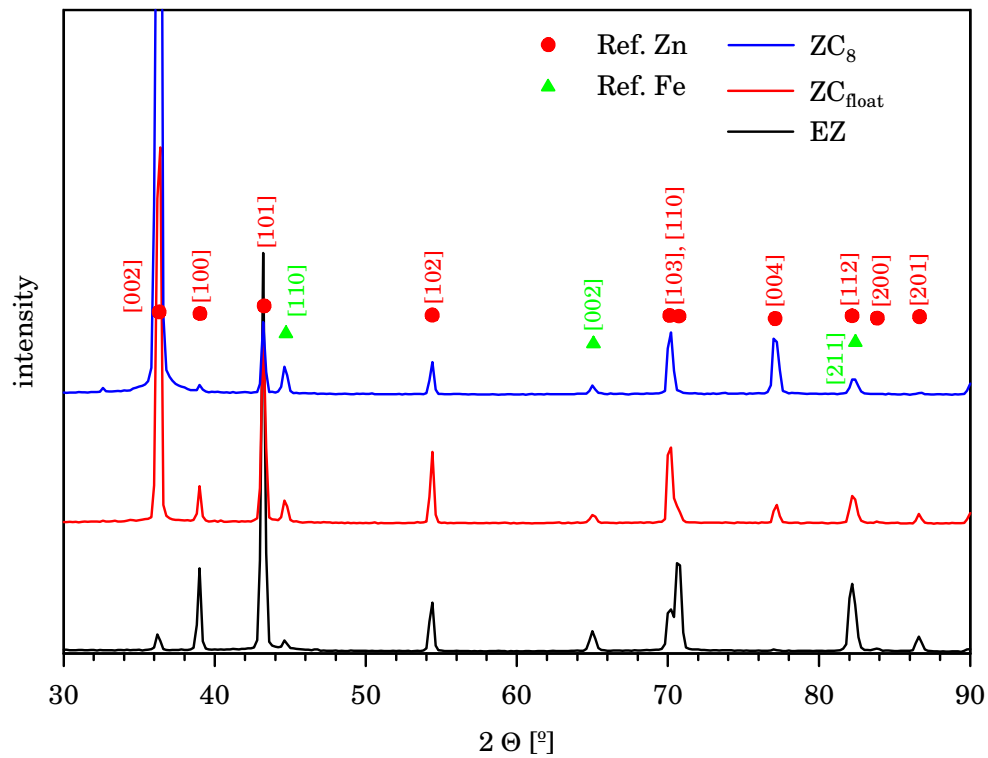
Figure 3.120: XRD patterns of the electrogalvanised EZ and the magnetron sputtered zinc coatings ZC_8 and ZC_{float}
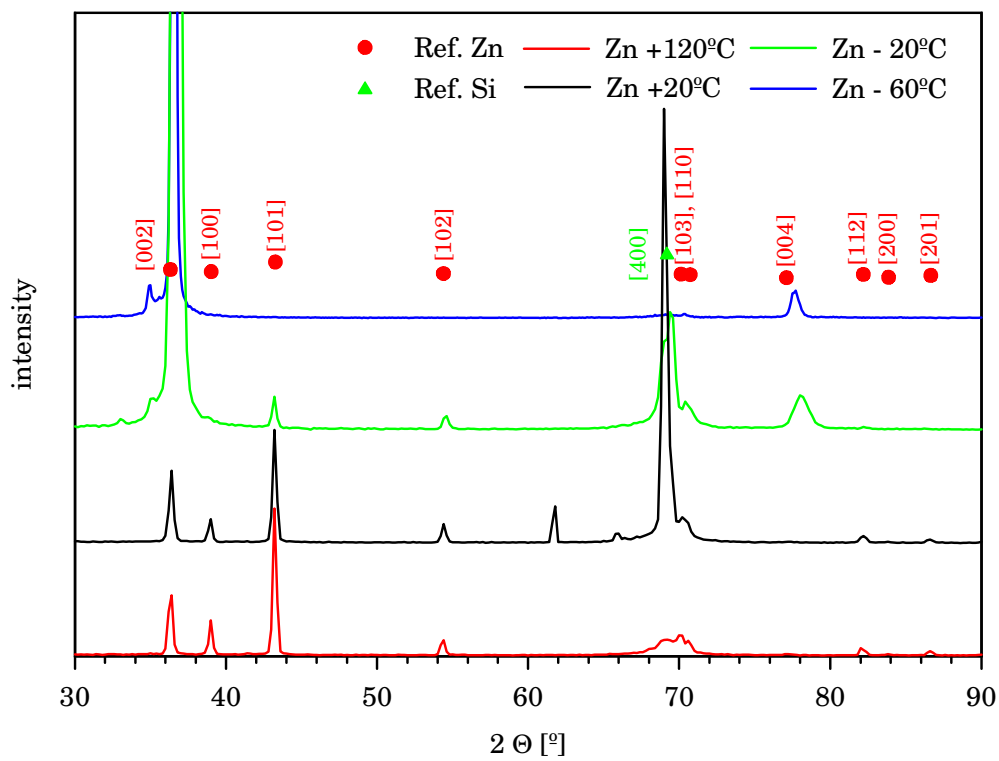
Figure 3.121: XRD patterns of ion beam sputtered zinc coatings deposited at substrate temperatures varying from -60 °C to +120 °C

between $+20\,°C$ and $+120\,°C$ correspond to the JCPDS reference data for zinc powder. The peaks show the same position and intensity distribution. In contrast to these films both coatings deposited at lower temperatures of -20 °C and -60 °C show a preferred texture in [002] direction. With coating ZIB_{-60} all further peaks disappeared. Only the (002) and (004) peak remained. In addition, a shoulder at about 35 ° can be seen. This type of a satellite peak has also been observed with other highly oriented hexagonal samples, e.g. CdTe coatings for solar cells [249]. With these specimens the normal ABCABC sequence of the hexagonal structure of the columnar growing grains is disturbed by stacking faults.

	Zinc													
	JCPDS 4-831		ZIB_{-60}			ZIB_{-20}			ZIB_{+20}			ZIB_{+160}		
hkl	2Θ	Int. %	2Θ	Int. %	TF	2Θ	Int. %	TF	2Θ	Int. %	TF	2Θ	Int. %	TF
002	36.33	53	36.5	**100**	**0.55**	36.6	**100**	**0.52**	36.4	63.9	0.21	36.2	35.8	0.14
100	39.02	40	-	-	-	-	-	-	39	21.5	0.09	39	27.5	0.14
101	43.27	**100**	-	-	-	43.2	2.9	0.01	43.2	**100**	0.17	43.2	**100**	0.21
102	54.38	28	-	-	-	54.6	1.3	0.01	54.4	17.3	0.11	54.4	10.4	0.08
103	70.12	25	70.4	0.5	0	70.4	2.5	0.03	70.2	23.2	0.16	-	-	-
110	70.73	21	-	-	-	-	-	-	-	-	-	70.6	12.1	0.12
004	77.1	2	77.7	3	**0.44**	78	3.1	**0.42**	77.2	1.6	0.13	77	1.6	0.16
112	82.18	23	-	-	-	82.2	0.4	0	82.2	6.5	0.05	82	6.1	0.06
200	83.85	5	-	-	-	-	-	-	83.8	1.4	0.05	83.8	1.3	0.05
201	86.64	17	-	-	-	86.2	0.2	0	86.6	3.7	0.04	86.6	3.4	0.04

Table 3.21: X-ray peak positions, intensities and texture fractions of ion beam sputtered zinc coatings deposited at various substrate temperatures

Influence of Assisting Ion Beam

The XRD patterns of ion beam sputtered sample ZIB_{+20} and the ion assisted samples ZIB A1 and ZIB A2, deposited at $T_s=+20\,°C$, are shown in Fig. 3.122. For sample ZIB A1, deposited under assistance of an ion beam of $18\,\mu A/cm^2$ current density and an ion energy of $300\,eV$, the onset of a texture in [002] direction can be noticed. By raising the beam current density to $36\,\mu A/cm^2$ (ZIB A2) this texture is increased and the peaks of the other crystallographic directions disappear. The shifting of the (002) and (004) peaks towards larger diffraction angles indicates a contraction of the c axis. The c spacing is reduced from $c = 4.9364\,nm$ for the non assisted coating to $c = 4.8846\,nm$ for the $18\,\mu A/cm^2$ assisted coating and to $c = 4.7358$ nm for the coating with the highest ion beam current density of $36\,\mu A/cm^2$. This observation could lead to the conclusion that the film is under tensile stress. Usually sputtered films are under compressive stress. Since the films were grown under argon bombardment argon atoms are embedded in interstitial sites of the hexagonal lattice and/or additionally segregated in the grain boundaries, see section 3.2.3. These effects cause the distortion of the crystal lattice, namely the change of the c/a ratio [212, 250]. The broadening of the (002) peaks could originate from a variation in the average crystallite size, and/or from compositional variations due to the incorporation of argon.

Influence of Oxygen in Sputter Atmosphere

Figure 3.123 shows the XRD patterns of a "pure" zinc coating ZIB_{+70} and the samples ZIB O1, ZIB O2, ZIB O3 and ZIB O4, which have been deposited in working gas atmospheres with different oxygen contents. Sample ZIB_{+70} deposited in a gas atmosphere without additional oxygen shows the XRD pattern of a non textured zinc coating with the main peaks of the (101), (002) and (100) planes. With all patterns a strong peak at 69.2 ° can be observed. This peak originates from the (004) planes of the silicon wafer which is used as substrate material. This peak is so strong that it also drowns out further Zn and ZnO
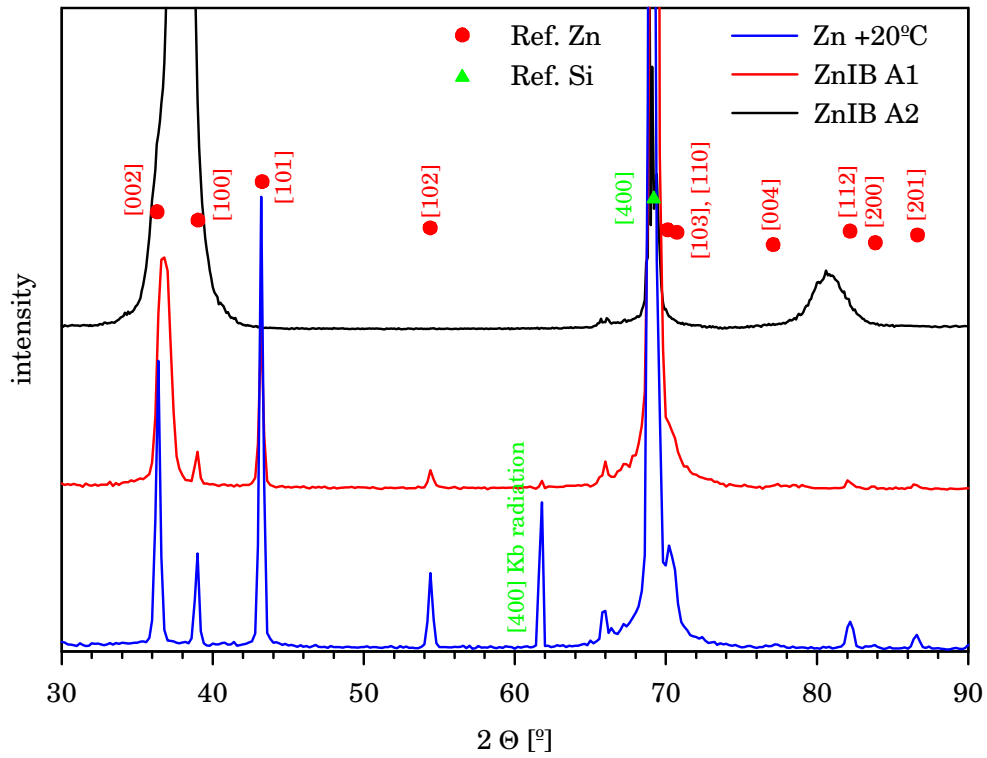
Figure 3.122: XRD patterns of ion beam sputtered and assisted zinc coatings
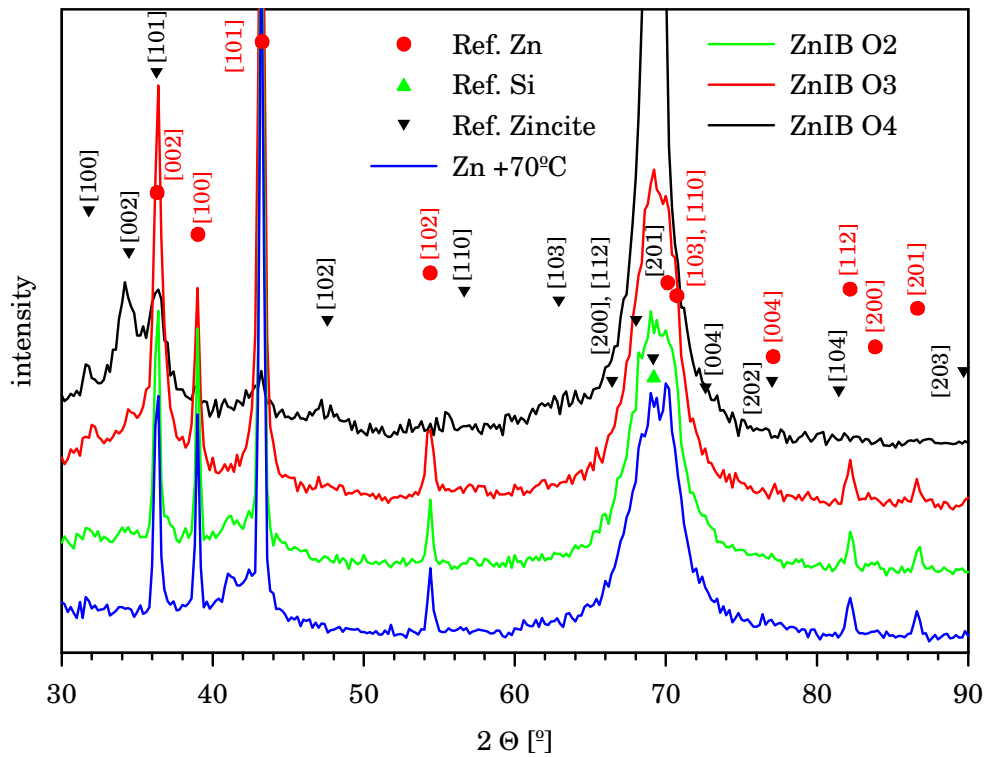
Figure 3.123: XRD patterns of zinc coating deposited in atmospheres with different oxygen content

	Zinc										
sample	JCPDS 4-831		ZIB$_{+20}$			ZIB A1			ZIB A2		
ion beam: 300 eV			no assistance			$18\,\mu\mathrm{A/cm^2}$			$36\,\mu\mathrm{A/cm^2}$		
hkl	2Θ	Int. %	2Θ	Int. %	TF	2Θ	Int. %	TF	2Θ	Int. %	TF
002	36.33	53	36.4	63.9	0.21	36.8	**100**	**0.55**	38	**100**	**0.6**
100	39.02	40	39	21.5	0.09	39	16.6	0.12	-	-	-
101	43.27	**100**	43.2	**100**	0.17	43.2	72.4	0.21	-	-	-
102	54.38	28	54.4	17.3	0.11	54.4	8.6	0.09	-	-	-
103	70.12	25	70.2	23.2	0.16	-	-	-	-	-	-
110	70.73	21	-	-	-	-	-	-	-	-	-
004	77.1	2	77.2	1.6	0.13	-	-	-	80.6	92	**0.4**
112	82.18	23	82.2	6.5	0.05	-	-	-	-	-	-
200	83.85	5	83.8	1.4	0.05	-	-	-	-	-	-
201	86.64	17	86.6	3.7	0.04	86.6	2.5	0.04	-	-	-

Table 3.22: X-ray peak positions, intensities and texture fractions of ion beam sputtered and assisted zinc coatings

peaks. It has been shown that the strong silicon peak can be reduced by tilting the sample by 1 or 2 degrees. In this configuration the diffracted peaks of the polycrystalline coating remain more or less unchanged, whereas the intensity of the silicon single crystal peak strongly diminishes. With increase of the oxygen content in the sputter gas the obtained coatings change their structure. They contain more and more zinc oxide. Already with the lowest oxygen doped coating ZIB O1 with 0.08 % oxygen content, weak zinc oxide peaks at 31.8 ° (100) and 34.4 ° (002) can be observed. At an oxygen content of 1.4 % (ZIB O2) this trend continues and additionally the ZnO peak at 36.3 ° (101), which overlaps with the Zn (002) peak, increases. Coating ZIB O4 sputtered with 7 % oxygen content finally consists mainly of zinc oxide. Apart from the strong (101) peak all other zinc peaks disappeared and only zinc oxide peaks are visible.

3.3.2 Zinc Iron Coatings

3.3.2.1 Galvanealed Coating

The XRD pattern of the Galvaneal coating is given in Fig. 3.124. With the Galvaneal coating the annealing step after galvanising leads to mutual diffusion of zinc (coating) and iron (steel sheet) resulting in intermetallic zinc-iron phases. Due to its practical use the commercially available Galvaneal coating is already well investigated. A variety of publications [45–48, 50, 51, 56, 61, 62, 251] report the compositions and crystalline structures of the occurring zinc-iron phases.

The Galvaneal coating characterised in this study consists mainly of a pure zinc phase, the zinc iron phase $Fe_{11}Zn_{40}$ (according Bastin $= \Gamma_1$, JCPDS card 32-478) [252] as well as the δ-$ZnFe_7$-phase, according to Gellings [57].

3.3.2.2 Magnetron Sputtered Zinc Iron Coatings

Figures 3.125 and 3.126 show the XRD patterns of the magnetron deposited zinc iron coatings ZFe 3, ZFe 7 and ZFe 13, with different Fe contents, which were deposited at $T_s = T_{float}$ and $T_s = +8$ ℃ respectively. These XRD patterns show clearly the influence of deposition temperature and alloying content on the crystalline structure evolution of the deposits. Since the obtained patterns do not fit any of the reported crystal structures for zinc iron phases in the JCPDS database or literature, computer simulations for the crystal structures and the resulting XRD patterns have been made with Carine®. It might be the case that metastable phases are present. Table 3.23 gives an overview of the cell parameters of the simulated,
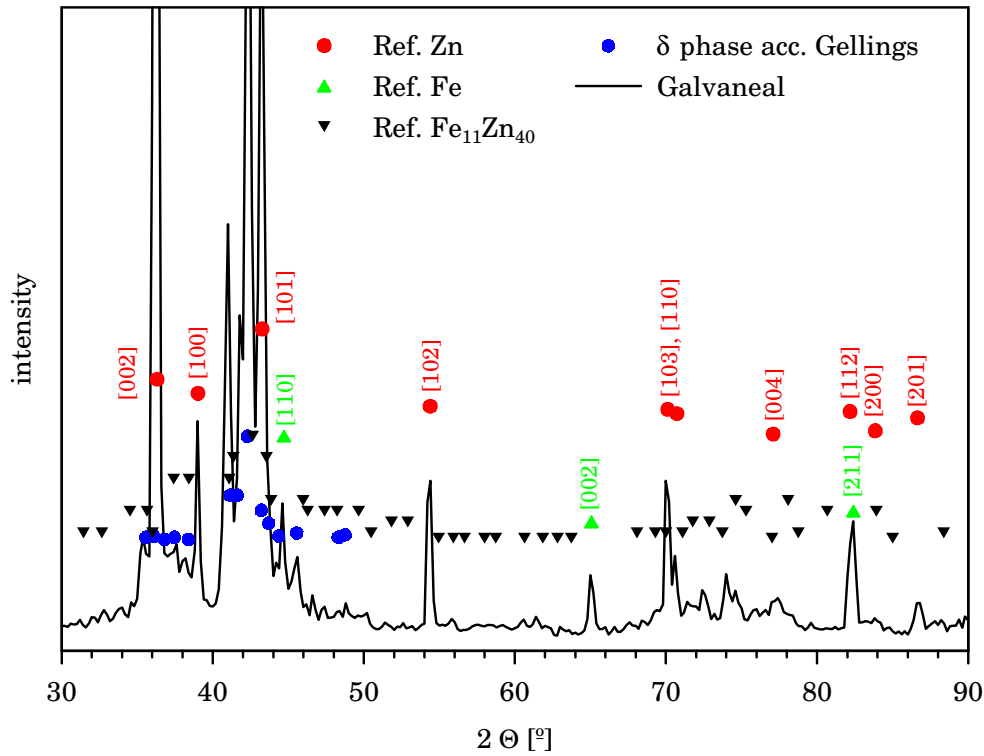
Figure 3.124: XRD patterns of Galvaneal (zinc iron) coating

Simulated lattice		SHex ZFe1	SHex ZFe2	SHex ZFe3	SHex ZFe4	SCub ZFe
Fe content at.%		∼3	∼6.5	∼13.6	∼15	∼13.3
hexagonal	a	2.72	2.75	2.737	2.64	-
	c	4.582	4.3916	4.3764	4.3764	-
cubic	a	-	-	-	-	3.71

Table 3.23: Cell parameters of simulated zinc iron phases occurring in sputtered zinc iron coatings

tentative zinc iron phases. The existence of actual crystalline structures with those exact parameters is not proven and could not be proven from the few peaks observed in the XRD patterns measured.

The patterns of sample ZFe 3_{float} shows all peaks of the hexagonal Zn phase as they occur with the pure zinc coatings. The intensity distribution is however changed now. The preferred orientation of the sputtered Zn coatings in [002] direction disappeared. Several small overlapping peaks at about 40°, 56° and 75° indicate the possible evolution of various distinct phases. Due to the peak width and overlap the phases can not be clearly identified or simulated. With increasing alloying content, ZFe 7_{float} the hexagonal Zn phase disappears more and more. It seems to be replaced by a phase with a simulated hexagonal unit cell (SHexZFe2 a=2.75 / c=4.3916) and strong texture in [002] direction. The highest alloyed coating ZFe 13_{float} can be simulated most likely by a cubic phase SHexCubZFe with lattice parameter a=3.71. This coating is highly oriented in [111] direction. The (100) peak occurs due to reduction, breaking the symmetry of the cubic structure.

The XRD pattern of ZFe 3_8 shows only a small fraction of pure zinc phase. It is dominated by phase whose hexagonal structure with strong texture in [002] can be simulated with an unit cell SHexZFe1 a= 2.72 / c=4.582. Also the higher alloyed zinc iron coatings ZFe 7_8 and ZFe 13_8 show hexagonal structures. They can be simulated best by hexagonal unit cells SHexZFe2 with a=2.75 / c=4.3916 respectively SHexZFe3 with a=2.737 / c=4.3764, whose lattice spacings decrease with increasing iron content. Additionally, the level of texture is increasing with increasing alloying content. The [102] and [103] directions, clearly present with ZFe 3_8, diminish steadily with increasing iron content in favour to the [002] oriented
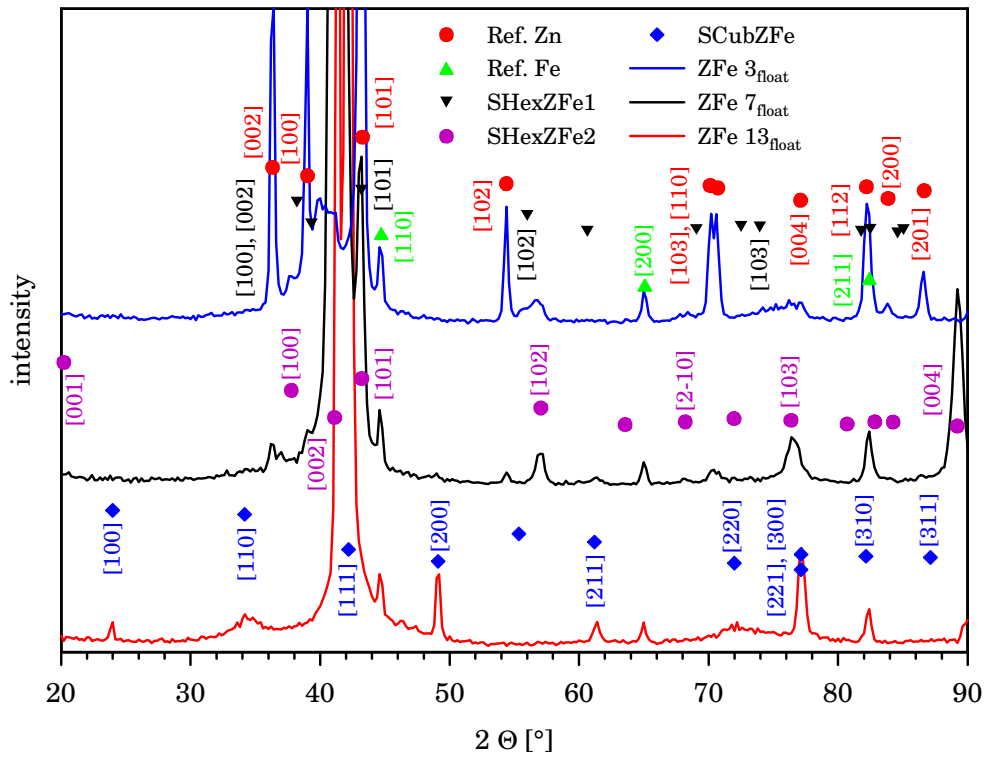
Figure 3.125: XRD patterns of magnetron sputtered zinc iron coatings ZFe 3, ZFe 7 and ZFe 13 with different Fe contents deposited at $T_s = T_{float}$
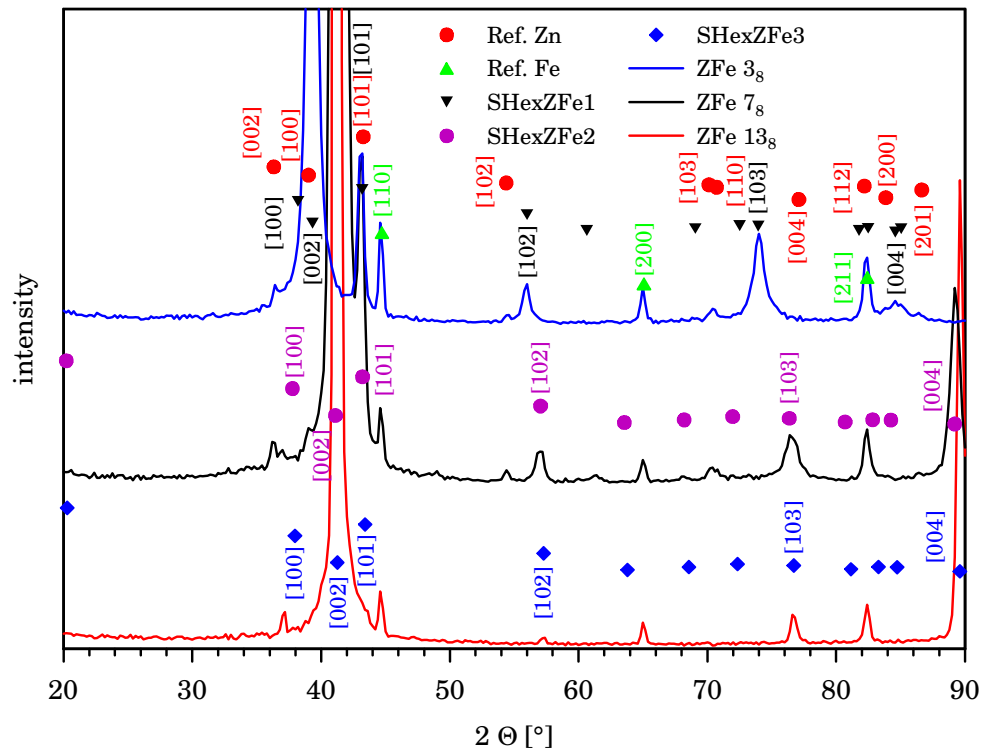
Figure 3.126: XRD patterns of magnetron sputtered zinc iron coatings ZFe 3, ZFe 7 and ZFe 13 with different Fe contents deposited at $T_s = +8$ °C
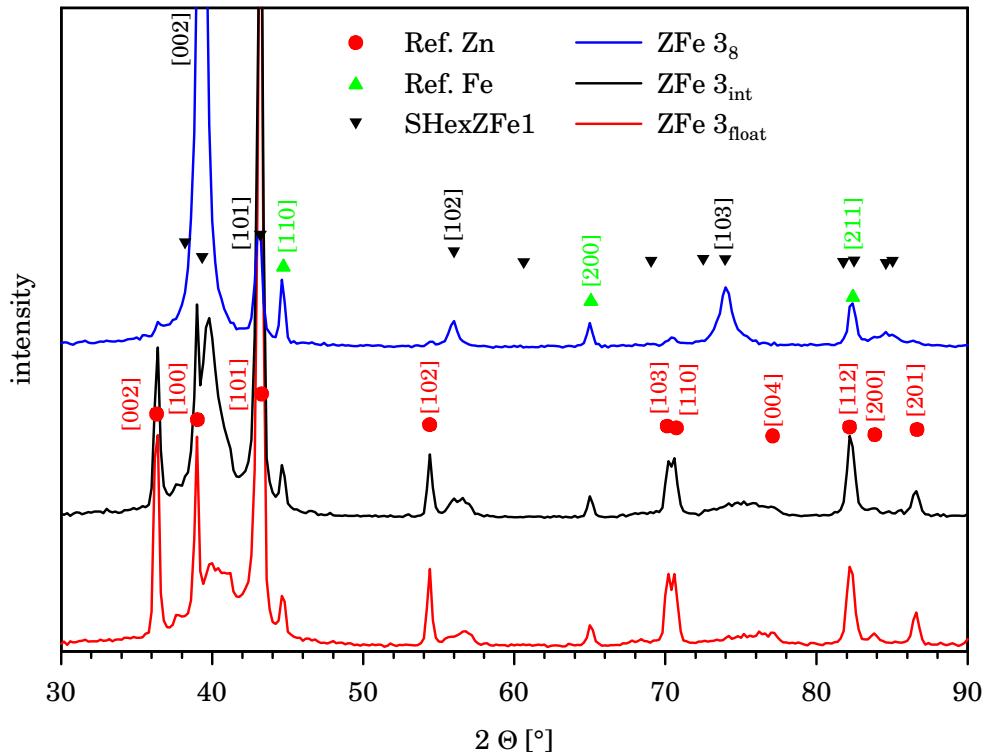
Figure 3.127: XRD patterns of magnetron sputtered zinc iron coatings with about 3 % Fe content deposited at different substrate temperatures

crystallites.

Figure 3.127 shows the influence of deposition temperature on the crystalline structure of magnetron sputtered zinc iron coatings. The figure compares the XRD patterns of the coatings $ZFe\,3_8$, $ZFe\,3_{float}$ and $ZFe\,3_{int}$; the latter one is deposited in an interval deposition. All coatings have an iron content of about 3% but they grew at different substrate temperatures. At high deposition temperature ($ZFe\,3_{float}$) and therefore sufficient diffusion, the resulting structure consists mainly of pure zinc phase with a very low fraction of a phase with the simulated hexagonal cell SHexZFe1. Lowering the deposition temperature ($ZFe\,3_8$) and resulting thereof also diffusion, the zinc phase disappears in favour of a phase with the hexagonal cell SHexZFe1. The interval deposited coating $ZFe\,3_{int}$ with its intermediate deposition temperature shows a pattern with both phases present.

3.3.2.3   Ion Beam Sputtered Zinc Iron Coatings

Figure 3.128 presents the XRD patterns of the ion beam sputtered zinc iron coatings $ZFeIB\,1_{150}$ to $ZFeIB\,5_{150}$ with different Fe contents deposited at $T_s=+150\,°C$. The crystallographic structure of the lowest alloyed coating $ZFeIB\,1$ (2.6 % Fe) is dominated by the hexagonal structure of pure zinc. The intensity distribution of the peaks indicates no preferred orientation. In addition to the zinc peaks, as a first indication of the beginning of a new phase, a small peak at $42.2\,°$ occurs. This phase can be simulated best with the cubic cell SimCubZnFe given in Tab. 3.23. With increase of the iron content to 7.8 % Fe ($ZFeIB\,3_{150}$) the new phase becomes more pronounced and the zinc phase is reduced. At an alloying content of 14.5 % Fe, coating $ZFeIB\,5_{150}$ finally consists mainly of the cubic phase SimCubZnFe.

Figure 3.129 shows the XRD patterns of the ion beam sputtered zinc iron coatings $ZFeIB\,5_{25}$ and $ZFeIB\,5_{150}$ with about 15 % Fe content, which were deposited at the substrate temperatures $T_s=+25\,°C$ and $T_s=+150\,°C$ respectively. As with the magnetron deposited coatings, the ion beam sputtered samples also reveal the role of the substrate temperature for the evolution of the crystalline structure. Even at approximately the same chemical composition the crystal structure of samples grown at different T_s is completely different. Sample $ZFeIB\,5_{+25}$ crystallises in a hexagonal structure, simulated best with

the SHexZFe4 structure given in Tab. 3.23, while coating ZFeIB 5_{+150} crystallises in the cubic structure SimCubZnFe.
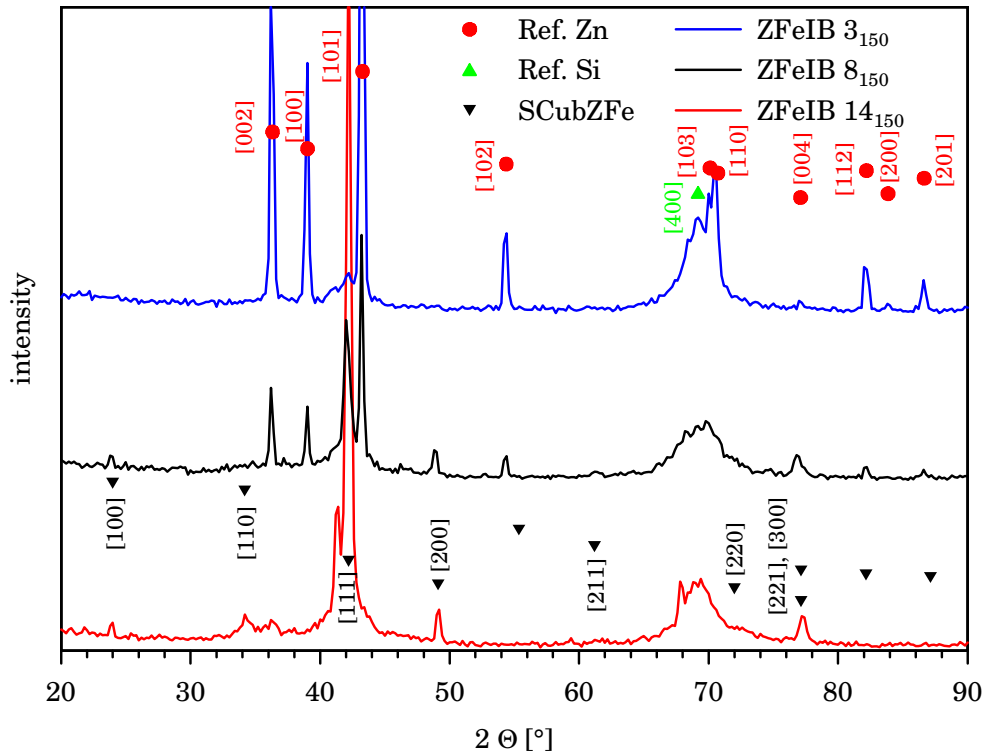
Figure 3.128: XRD patterns of ion beam sputtered zinc iron coatings with different iron contents deposited at T_s=+150 ℃

Annealed zinc iron coatings

To check the influence of an additional annealing step on the stability of the metastable phases and a possible conversion into stable phases the different magnetron sputtered zinc iron coatings have been annealed for 2 hours at 300 ℃ in argon atmosphere. Subsequently, the sample were cooled to room temperature over night. XRD patterns of the annealed specimens ZFe 3_{float}, ZFe 7_{float} and ZFe 13_{float} are shown in Fig. 3.130. All samples show a change in the crystalline structure due to annealing. The occurring phases are represented best by the zinc iron phases Fe_4Zn_9 (JCPDS card 33-697) and the δ-phase reported by Bastin [252].

3.3.3 Zinc Titanium Coatings

Figure 3.131 presents the XRD patterns of the magnetron sputtered zinc titanium coatings ZTi 1_8 to ZTi 10_8. The low alloyed sample ZTi 1_8 (1.7 % Ti) shows the randomly oriented hexagonal structure of zinc with indications of a second phase. With increasing titanium content two broad halos at 35–50 ° and 68–78 ° indicate the occurrence of a x-ray amorphous phase. At a titanium content of 11.1 %, ZTi 10_8, the zinc structure completely disappeared. None of the samples shows indications of zinc-titanium or titanium phases.

Figure 3.132 shows the XRD patterns of magnetron sputtered zinc titanium coatings ZTi 1_{float} to ZTi 10_{float}. These samples show the same behaviour as the samples deposited at T_s=+8 ℃ , but the amorphous phase is less developed. Even the highest alloyed coating still shows signs of crystalline zinc.

In contrast to the other zinc titanium coatings, samples ZTi 10 were deposited in RF mode. Of all zinc titanium depositions this deposition run had the highest target titanium content. Hence sample ZTi 10_8
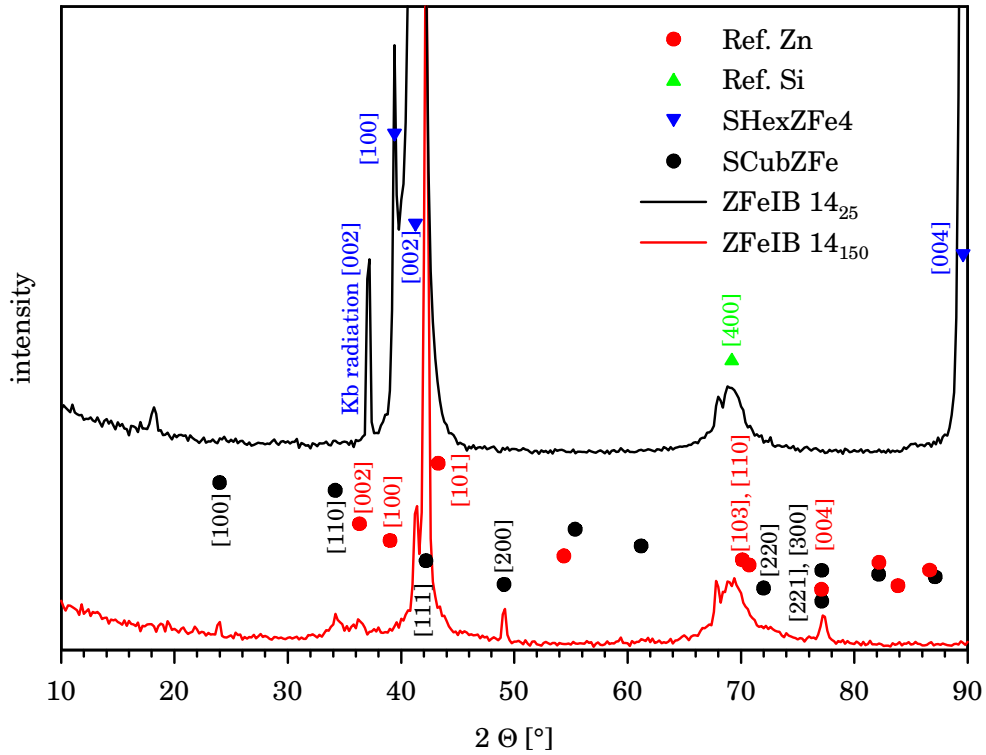
Figure 3.129: XRD patterns of ion beam sputtered zinc iron coatings with an iron content of about 15 % deposited at different substrate temperatures
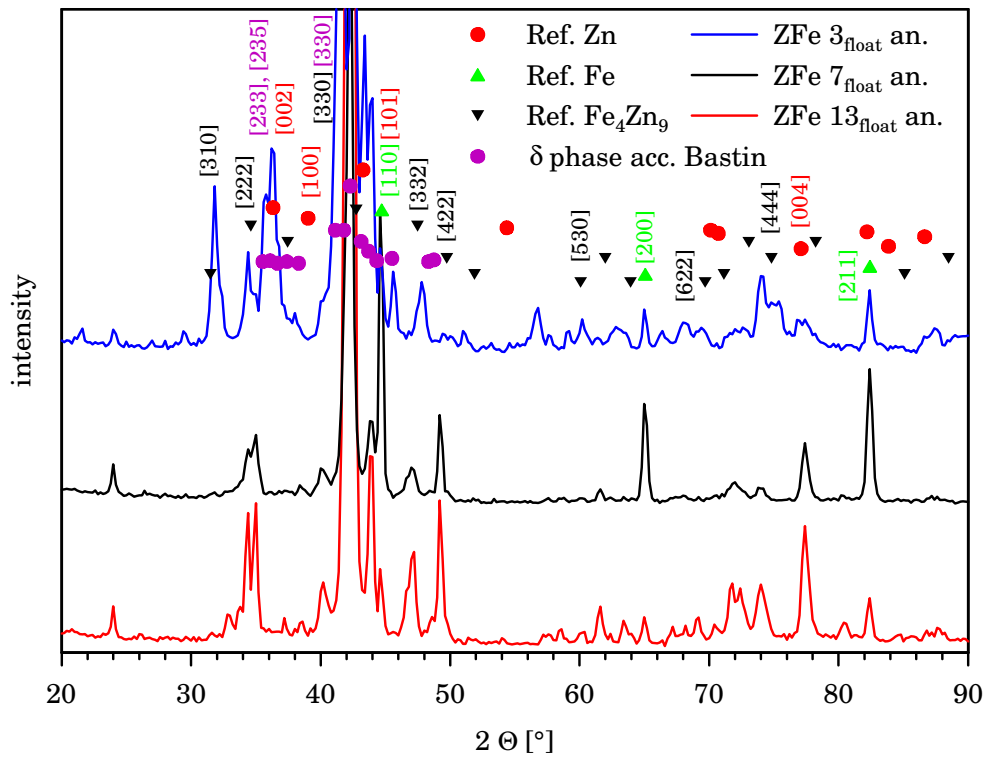
Figure 3.130: XRD patterns of magnetron sputtered and annealed zinc iron coatings
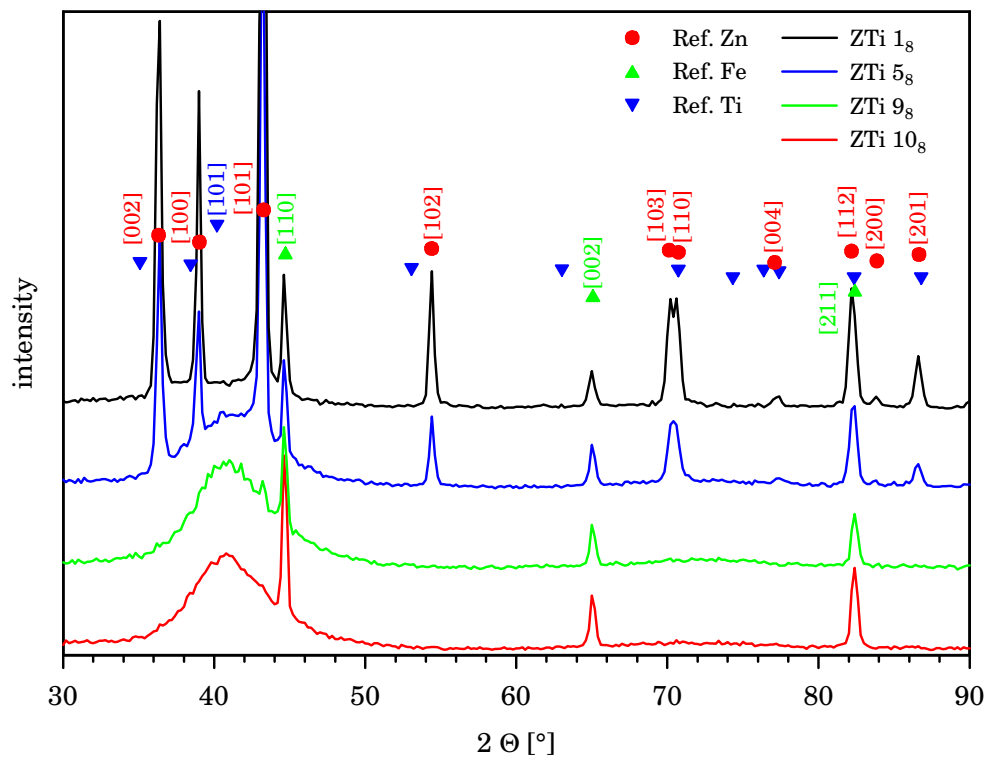
Figure 3.131: XRD patterns of magnetron sputtered zinc titanium coatings ZTi 1_8 to ZTi 10_8 with different titanium contents
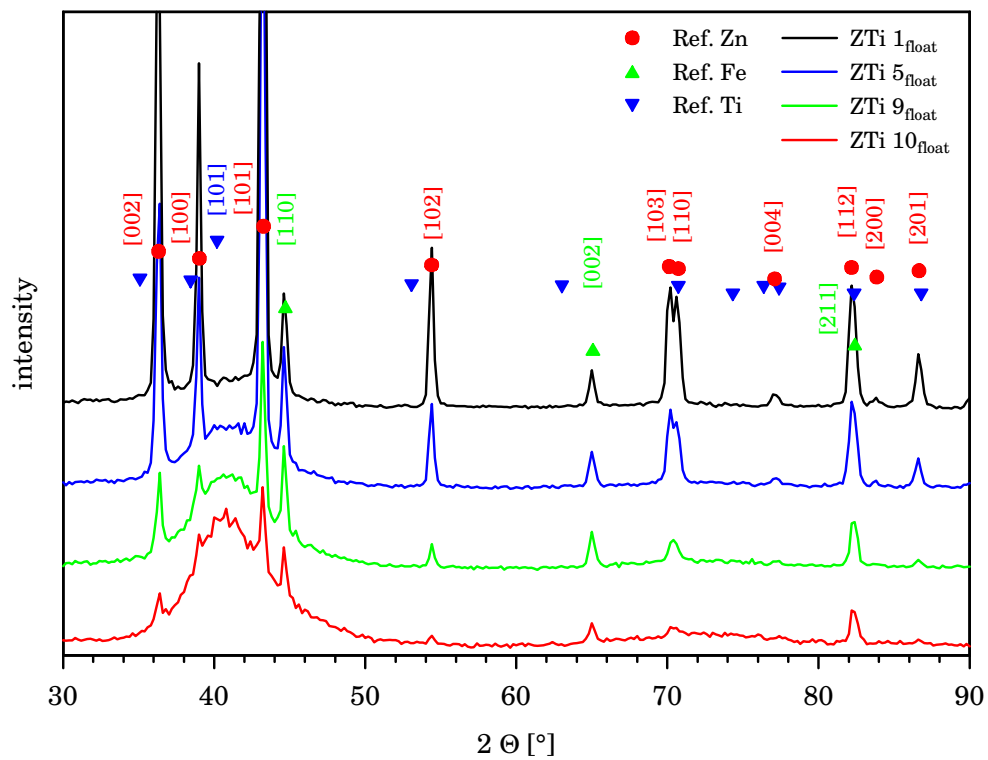
Figure 3.132: XRD patterns of magnetron sputtered zinc titanium coatings ZTi 1_{float} to ZTi 10_{float} with different titanium contents

is also the highest titanium alloyed film. In contrast coating ZTi 10_{float} has an alloy content which is lower than the one of ZTi 9_{float}. In comparison to sample ZTi 9_{float}, the more amorphous structure of ZTi 10_{float} shows that apart from the alloying content, other deposition parameters such as sputter mode and substrate temperature also influence the crystalline structure evolution.

Annealed zinc titanium coatings

To check the influence of an additional annealing step on the stability of the metastable phases and a possible conversion into stable phases the zinc titanium coatings ZTi 1_{float} and ZTi 9_{float} have been annealed for 2 hours at 300 °C in argon atmosphere. Subsequently, the samples were cooled to room temperature over night. The XRD patterns of these samples are shown in Fig. 3.133. As observed with
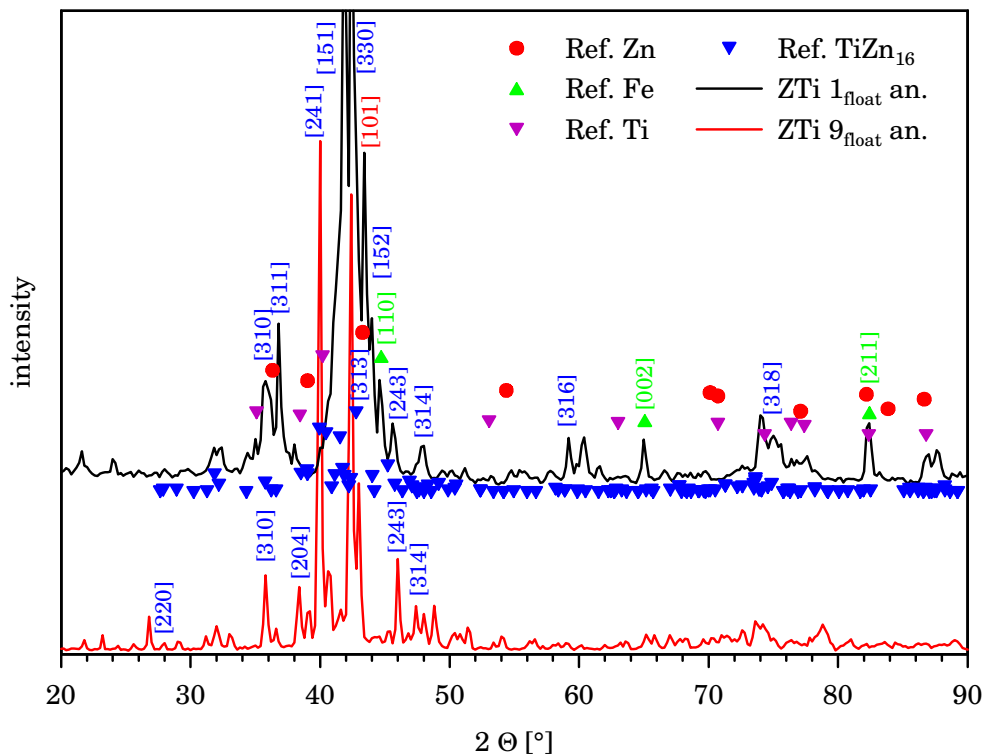
Figure 3.133: XRD patterns of magnetron sputtered and annealed zinc titanium coatings ZTi 1_{float} and ZTi 9_{float}

the zinc iron coatings, also here annealing leads to a change in the crystalline structure. Independent of their alloying content with annealing both metastable, amorphous coatings seem to crystallise in the zinc titanium phase TiZn$_{16}$ (JCPDS card 41-1283). Due to the complexity of the patterns and their overlapping peaks a clear determination of the present phases is not possible.

3.3.4 Zinc Aluminium Coatings

Figure 3.134 shows the XRD patterns of the zinc aluminium coatings ZAl 4. Both coatings show the hexagonal structure of pure zinc. As already observed with other coatings, also with these depositions the evolution of the crystalline structure is influenced by the deposition temperature. Sample ZAl 4_{iso} has a randomly oriented structure, while deposit ZAl 4_8 is strongly textured in the [002] direction. With ZAl 4_8 the (002) and (004) peaks are additionally shifted towards larger diffraction angles, caused by a decrease of the c lattice spacing.
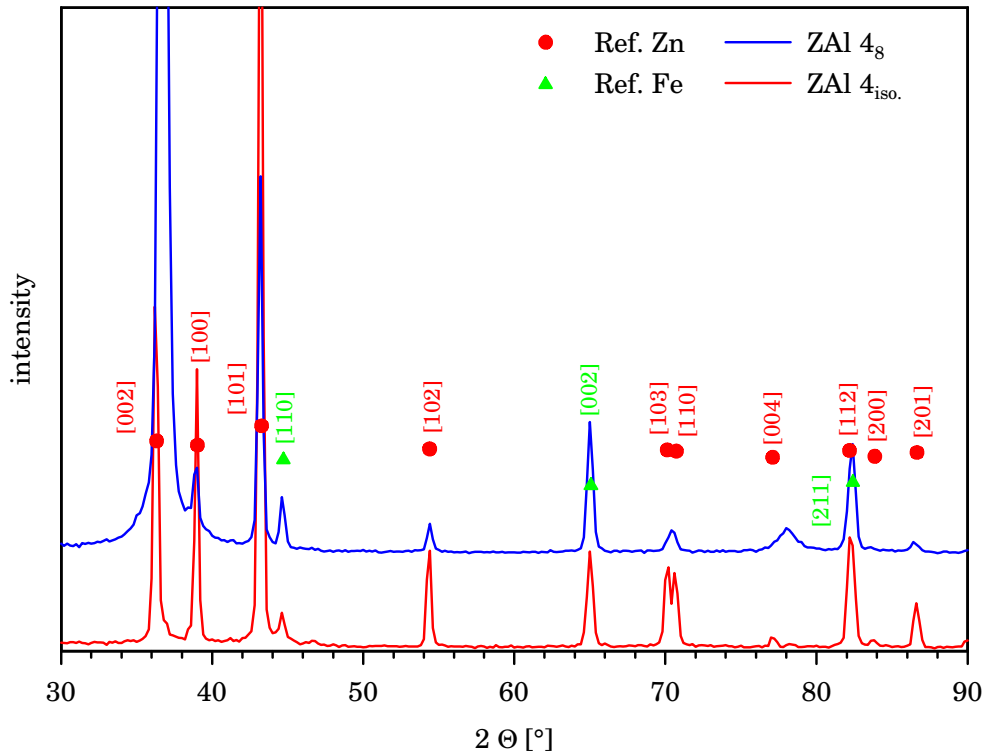
Figure 3.134: XRD patterns of magnetron sputtered zinc aluminium coatings ZAl 4 with an aluminium content of about 4 % deposited at different T_s

3.3.5 Zinc Chromium Coatings

Since no reference data for zinc chromium crystal structures are available in the JCPDS database and also the crystal structures as proposed by Alonso et al. [253] do not fit to the patterns obtained, computer simulations for the unit cells of the zinc chromium phases have been performed. The cell parameters of these tentative phases are given in Tab. 3.24. Figures 3.135 and 3.136 show the XRD patterns of

Simulated lattice		**SHex ZCr1**	**SHex ZCr2**
Cr content at.%		~ 3	$\sim 10.3 - 12.8$
hexagonal	a	2.71	2.74
	c	4.6908	4.4472

Table 3.24: Cell parameters of simulated zinc chromium phases occurring in sputtered zinc chromium coatings

magnetron sputtered zinc chromium coatings ZCr 3 and ZCr 11. Both low alloyed samples consist of a mixture of hexagonal zinc phase and an intermetallic phase with the simulated hexagonal structure SHexZCr1. The fraction of zinc phase is here much higher for ZCr 3_{float}. With ZCr 3_8 most of the zinc peaks disappeared and the structure is slightly oriented in the [102] direction. Samples ZCr 11 crystallise in the hexagonal structure SHexZCr2 with a very small fraction of hexagonal zinc. Sample ZCr 11_8 is strongly textured in [002] direction.

Annealed zinc chromium coatings

Like other zinc alloy coatings also the zinc chromium coatings have been annealed in argon atmosphere. The XRD patterns of these samples are given in Fig. 3.137. With sample ZCr 3_{float} annealing leads to a change from the SHexZCr1 structure to an unidentified structure with its main diffraction peak at 42°.

Also ZCr 11_{float} changes its crystalline structure with annealing. As main component the XRD pattern shows the hexagonal structure SHexZCr2, but additionally some other peaks from an unidentified phase.
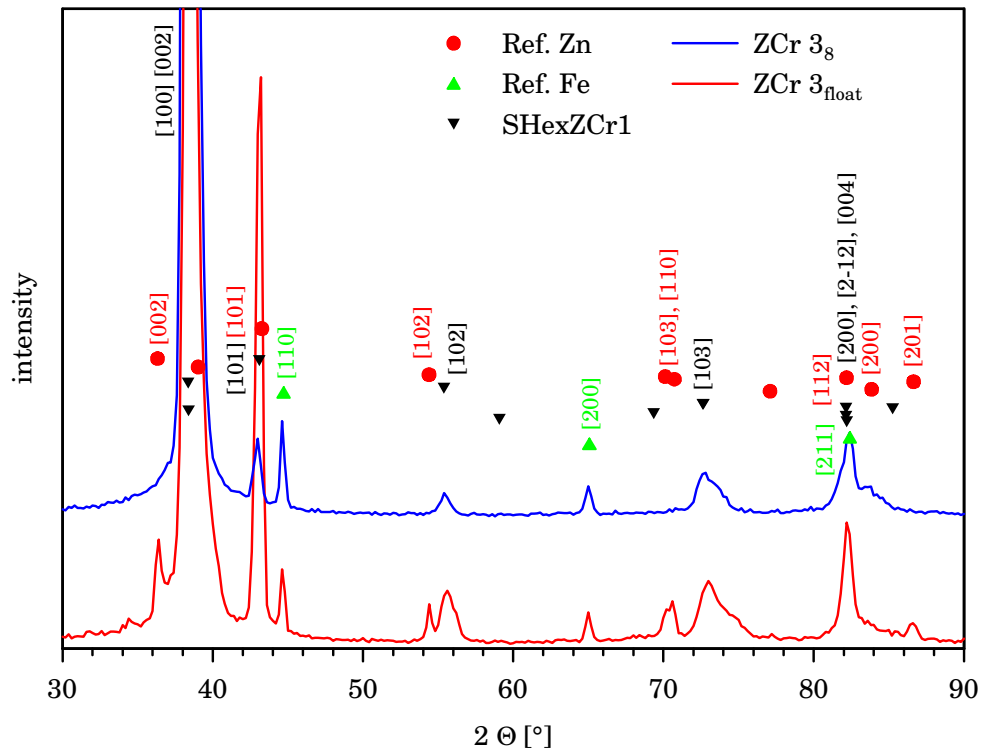
Figure 3.135: XRD patterns of magnetron sputtered zinc chromium coatings ZCr 3 with a chromium content of about 3 % deposited at different T_s
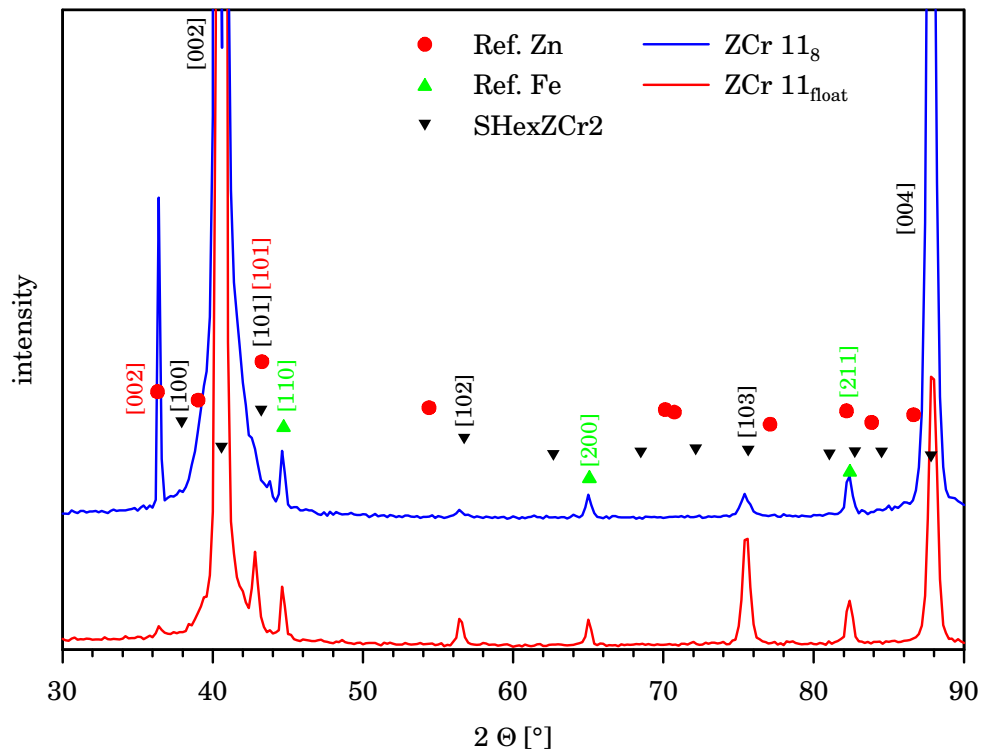
Figure 3.136: XRD patterns of magnetron sputtered zinc chromium coatings ZCr 11 with a chromium content of about 10–13 % deposited at different T_s
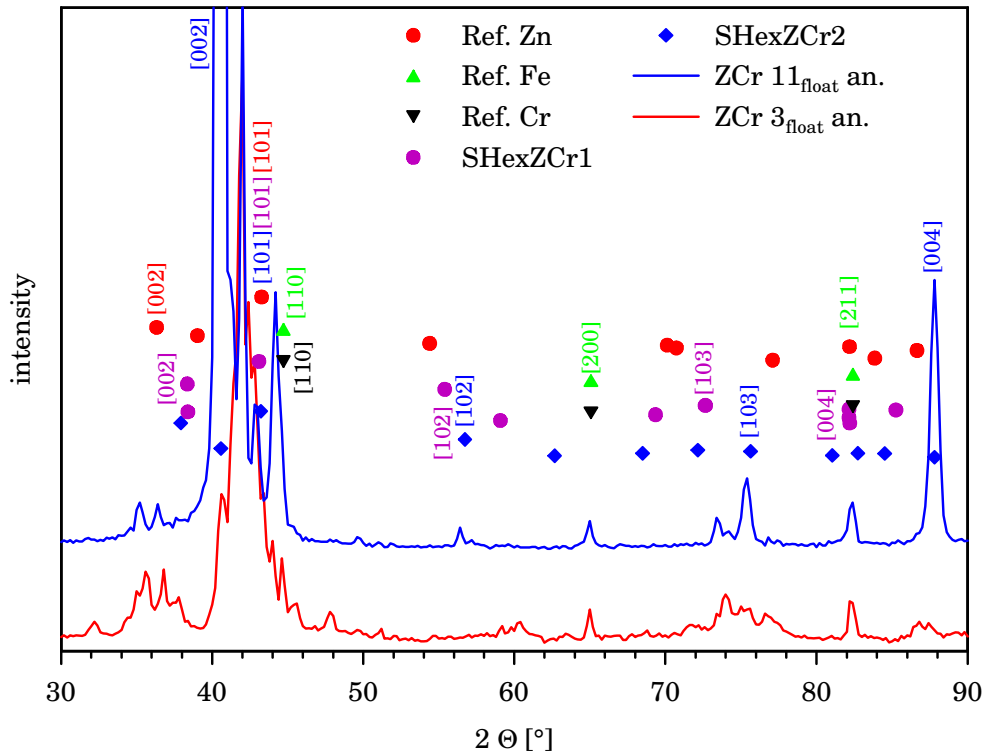
Figure 3.137: XRD patterns of magnetron sputtered and annealed zinc chromium coatings ZCr 1_{float} and ZCr 2_{float}

3.3.6 Zinc Magnesium Coatings

Figure 3.138 presents the XRD patterns of the magnetron sputtered zinc magnesium coatings ZMg 2_{float} and ZMg 2_8. Both samples consist of a mixture of pure hexagonal zinc phase and a small fraction of the hexagonal MgZn$_2$ phase (JCPDS card 34-457). The created crystal structures depend on the deposition temperatures. Sample ZMg 2_8 tends more to the development of the intermetallic MgZn$_2$ phase than ZMg 2_{float}. The zinc phase of ZMg 2_{float} is randomly oriented, whereas the one of ZMg 2_8 is strongly textured in [002] direction.

The XRD patterns of the higher alloyed coatings ZMg 15_{float} and ZMg 15_8 are presented in Fig. 3.139. These coatings consist of a mixture of the pure hexagonal zinc phase, the cubic phase Mg$_2$Zn$_{11}$ (JCPDS card 6-664) and the monoclinic phase Mg$_4$Zn$_7$ (JCPDS card 29-878). Also here the deposition temperature influences the crystallinity, which is better developed for ZMg 15_{float}. With this sample the zinc peaks and the intermetallic phase peaks are more pronounced. Their intensity distribution indicates a random orientation of the phases.

Annealed zinc magnesium coatings

Figure 3.140 shows the XRD patterns of the annealed zinc magnesium coatings ZMg 2_{float} and ZMg 15_{float}. With sample ZMg 2_{float} annealing changes the crystalline structure from a dual phase system Zn–MgZn$_2$ to the triple phase system zinc, MgZn$_2$ and the triclinic Mg$_2$Zn$_3$ phase (JCPDS card 8-196). The triple phase system of ZMg 15_{float} transforms completely to the dual phase system MgZn$_2$–Zn, with the main component being MgZn$_2$.

3.3.7 Discussion of XRD results

The presented XRD results show that the crystallographic structure and composition of the sputtered coatings depends on several deposition parameters: the deposition temperature, the target alloy content, the deposition rate and the sputter mode. According to the interplay of these parameters the
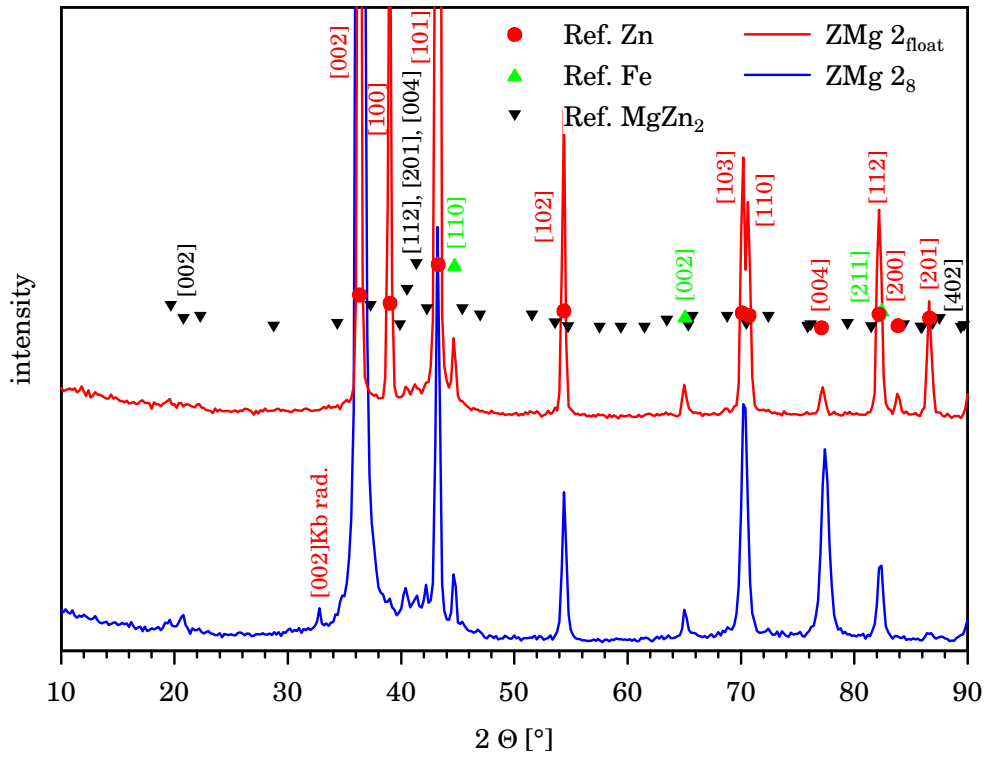
Figure 3.138: XRD patterns of magnetron sputtered zinc magnesium coatings ZMg 2_{float} and ZMg 2_8
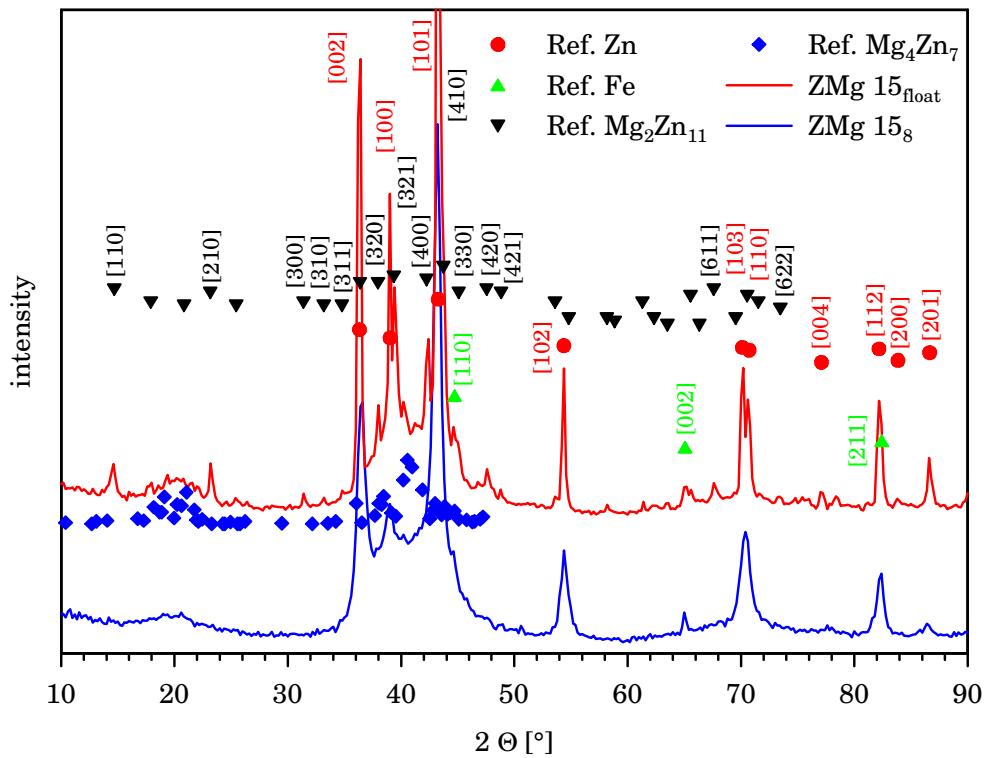
Figure 3.139: XRD patterns of magnetron sputtered zinc magnesium coatings ZMg 15_{float} and ZMg 15_8
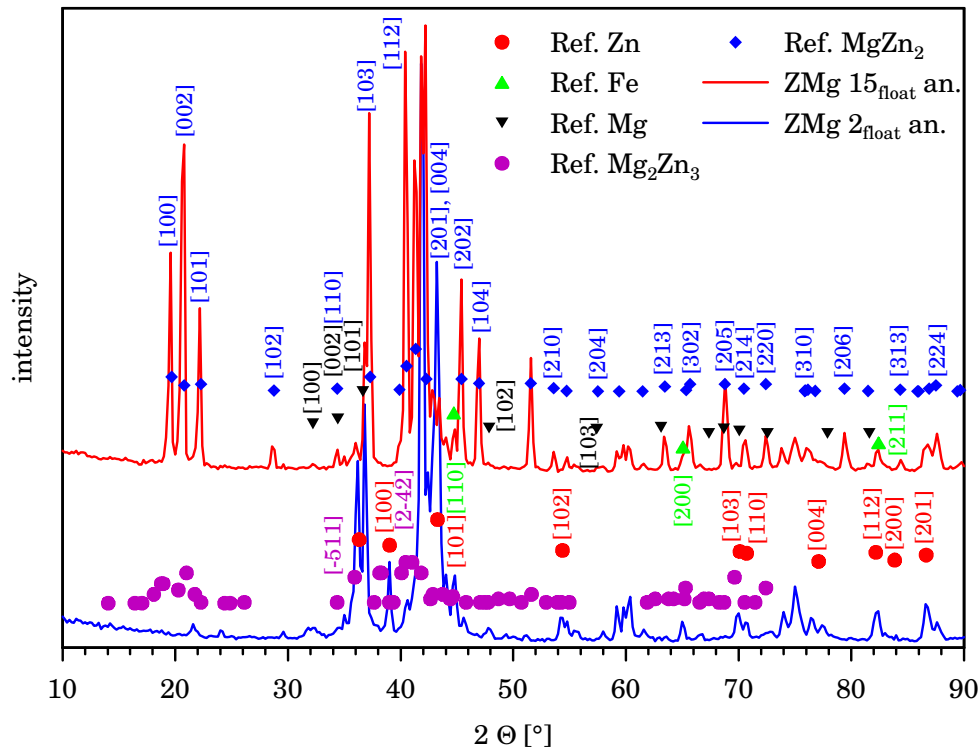
Figure 3.140: XRD patterns of magnetron sputtered and annealed zinc magnesium coatings $ZMg\,2_{float}$ and $ZMg\,15_{float}$

crystallographic structures and compositions range from crystalline, single phase systems (e.g. zinc), to crystalline, multiple phase systems (e.g. Zn–Mg), to x-ray amorphous systems (e.g. Zn–Ti) [110, 211].

The influence of deposition temperature and hence the diffusion can be clearly seen with all depositions. In most cases the samples deposited at higher substrate temperatures show a better developed crystallinity, pronounced evolution of stable phases and a reduction of preferred orientation.

According to Greene [254, 255] the 3–D nucleation and growth of films depend on the deposition rate R, the substrate surface site number density N_0 and the adatom surface diffusivity D_s. At sufficiently high deposition rates R or low deposition temperatures where $R > N_0 D_s$ the developed film is amorphous. The adatoms do not have enough time to diffuse across the surface and find low energy sites before they are buried by subsequentially deposited adatoms.

The fact that sputtering is a far from equilibrium process with high quench rates can be seen with almost all alloy depositions of this study, as they form metastable phases. See also The limited diffusion in the sputter process, especially for depositions carried out at low substrate temperature, lead to the evolution of metastable phases with simple unit cells. In vapour quenching processes the vapour species striking a cold substrate first form highly compact configurations which can be readily frozen in. The subsequent displacements necessary to form less compact and complex crystalline intermediate or equilibrium phases would require a higher activation energy. The simple unit cell structures obtained by vapour quenching also distinguish it from liquid quenching where in a variety of alloys systems phases with unit cells ranging form simple cubic with one atom per unit cell to complex fcc structures with 500 atoms per unit cell have been created [206]. For the liquid quenched structures, already in the liquid state atomic arrangements (nature of the bonds, co-ordination numbers, atom clusters) may prove sources for nucleation. As an illustration it is worth considering a few results obtained on Hume-Rothery γ brass structure phases as they are mainly found with noble metal alloys, as e.g. Ag–Zn. Under equilibrium conditions the system Ag–Zn forms a γ brass type phase, Ag_8Zn_8 around 61.5 at.% zinc. The co- evaporated samples of Michel [256] deposited at room temperature have not shown this structure. The electron diffraction on the evaporated films gave patterns of a β' -phase (CsCl type) and a δ-phase (close packed

hexagonal). After ageing the samples for three months at room temperature allowing diffusion, the seven first electron diffraction peaks of the γ brass structure appeared on the spectra.

Most of the sputtered coatings (pure zinc, zinc chromium, zinc magnesium films) exhibit a preferred orientation in [002] direction parallel to the film surface. Koll and Alsmann [257] showed that this texture has a positive influence on the forming properties of the coated steel sheets. With deep drawing tests (Erichsen tests) on electrogalvanised zinc coatings they observed a reduced wear of the basal plane oriented coatings in comparison to randomly oriented coatings at higher strip pull forces. Additionally, the basal plane oriented coatings showed no occurrence of microcracks as observed with the randomly oriented coatings.

Apart from the mechanical behaviour, the corrosion behaviour of metallic coatings also depends on their crystallographic structure. By exposition to a corrosive environment the corrosion rate of differently oriented grains is correlated to the planar packing density of their crystallographic planes [258,259]. With increase in packing density the binding energy of the surface atoms is raised. As a result the closely packed planes, i.e. the low index planes, are known to be more resistant to dissolution. For the hexagonal zinc the packing density ρ increases in the order $\rho(\text{h00}) < \rho(\text{hk0}) < \rho(001)$. This indicates that a basal texture (002), as observed with the sputtered zinc and zinc alloy coatings, has a positive influence on the corrosion resistance.

Further factors which influence the corrosion of a metal are the density and distortion of its crystalline lattice. Zinc crystallises in a distorted form of the perfect, closest packed hexagonal structure. Its axial c/a ratio is 1.85 instead of 1.63 for the ideal hexagonal lattice.

Examining the a and c lattice parameters in Tab. 3.25 it can be seen that for the zinc alloys a is higher and c lower than for pure zinc crystals. Hence, with the alloyed coatings a decrease of c/a with increasing alloying content occurs. A decrease in the c/a ratio implies a denser and less distorted lattice formation which might play an important role in the ionic transport processes [259]. This could be the reason why the alloyed zinc coatings are less active for oxygen reduction and metal ionisation processes thus offering an improved corrosion protection as shown in the following section 3.5.

Lattice	ideal hex. lattice	zinc	SHex ZFe1	SHex ZFe2	SHex ZFe3	SHex ZFe4	SHex ZCr1	SHex ZCr2	MgZn$_2$
a	-	2.665	2.72	2.75	2.737	2.64	2.71	2.74	5.2225
c	-	4.947	4.582	4.3916	4.3764	4.3764	4.6908	4.4472	8.5684
c/a	1.63	1.8563	1.6842	1.5969	1.5989	1.6577	1.7309	1.6230	1.6407

Table 3.25: c/a ratios of different zinc and zinc alloy crystal lattices

3.4 Mechanical Properties

3.4.1 Microhardness

Figure 3.141 shows the results of the microhardness measurements on the steel substrate, zinc bulk material, the reference coatings EZ and Galvaneal and the various sputter deposited zinc and zinc alloy coatings. The stated values are the averages of ten indentation experiments per sample and their corresponding standard deviations.

The 1.0338 grade steel sheet used as substrate material has a microhardness of 166 HV 0.245/15. The Vickers hardness of the electrogalvanised reference coating EZ is 59 HV. With 44 HV respectively 48 HV the hardnesses of the sputtered zinc coatings are slightly lower than that of the EZ reference. Even lower is the hardness of a zinc bulk material with a hardness of 34 HV, which can be explained by its much bigger grain size of about 500 μm.
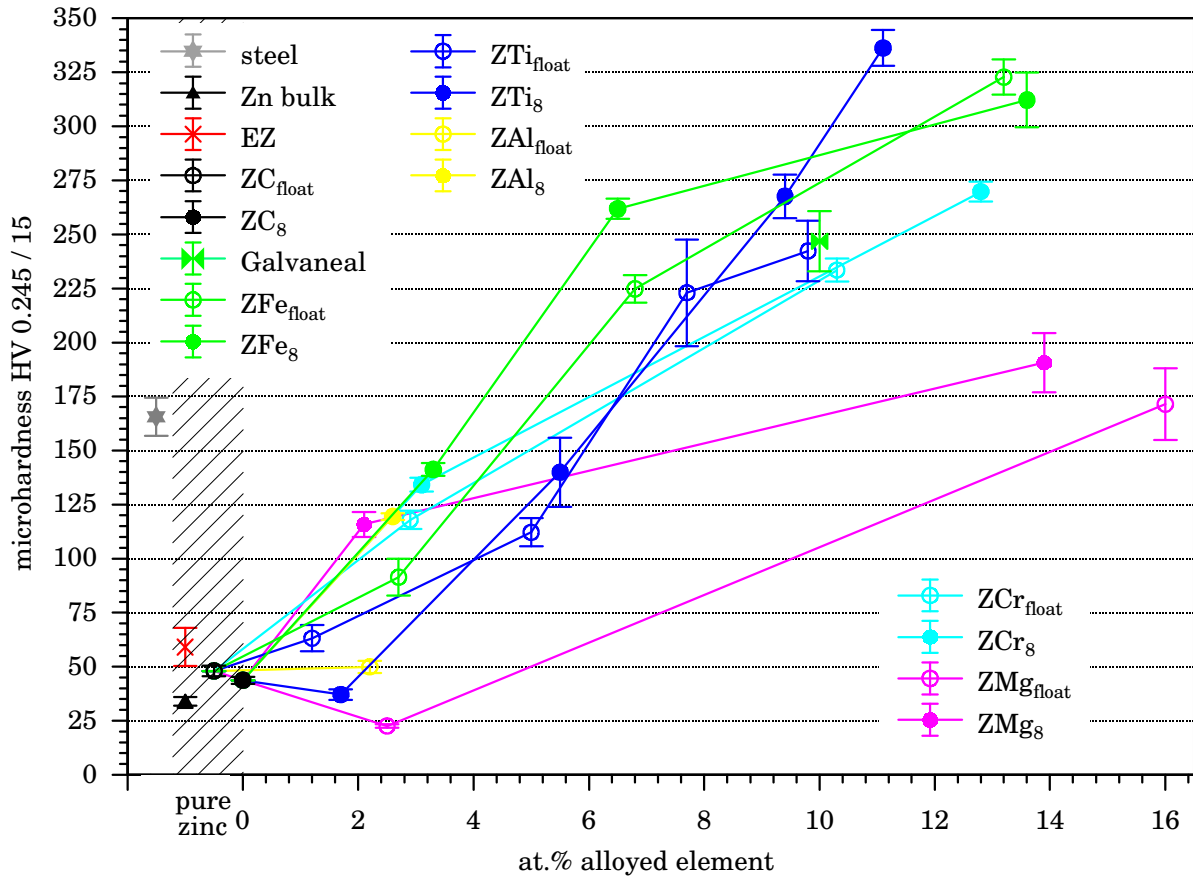
Figure 3.141: Microhardness of zinc and zinc alloy coatings

The first factor which influences the hardness of the coatings, is the effect of alloying. The Galvaneal coating alloyed with ~10 at.% iron has in contrast to the EZ coating a hardness of 247 HV, higher by a factor of four.

This alloying effect is also observed with all sputtered coatings. At low alloying contents especially with the zinc titanium, zinc aluminium and zinc magnesium coatings the hardnesses are almost in the same range of the pure zinc coatings or sometimes even lower. With increasing alloying contents the hardnesses rise. For the highest alloyed coatings (ZnFe, ZnTi, ZnCr) the hardnesses are about the six to eight fold of the hardnesses of the pure zinc coatings.

Apart from the lowest alloyed zinc titanium samples ZTi 1 a second hardness influencing parameter is observed for all sputtered coatings: It is the influence of the deposition temperature. With all coatings deposited at T_{float} the hardnesses are lower with respect to those deposited at $T_s = +8 °C$. This effect could be explained by two factors:

First, the coatings deposited at T_{float} are generally more porous than those deposited at $T_s = +8 °C$. Their grains are clearly separated by grain boundaries and voids. Second, the higher deposition temperatures ($\geq 0.5 \, T_m$ for pure zinc) lead to "annealed" coatings. This effect was also indirectly observed by Fountzoulas and Nowak [153]. By preparation of coating cross sections for the SEM they found that coatings which were deposited at $T_s/T_m \leq 0.3$ cleaved much better than those deposited at higher T_s/T_m. The films with low normalised substrate temperatures are harder and less ductile. According to Movchan-Demchishin and Thornton films from zone III of the SZM behave like fully annealed metals [110, 150].

3.4.2 Coating Adhesion

3.4.2.1 Pull-Off and Shear Test

For a coated steel sheet, which will be joined to a second part by adhesive bonding, the adhesion of the film to the substrate should be better than the cohesion- or adhesion strength of the adhesive bonding. Due to this reason the adhesion strength of a coating can be measured only up to a load where the adhesive bonding fails. Since the tested steel sheets were not perfectly flat (being un-rolled material) it was difficult to obtain perfect and totally equal adhesive bondings. Therefore, the measured values, displayed in Tab. 3.26, could reflect variation in adhesive bondings, rather than the different adhesion strengths of the coatings. The given values have to be regarded as minimum values of the coating adhesion strength. Figure 3.142 shows typical recorded force/traverse path curves (normal-, shear force) of the sputtered, zinc coating ZC_8. The curve of the normal force shows here a steady increase up to the failure
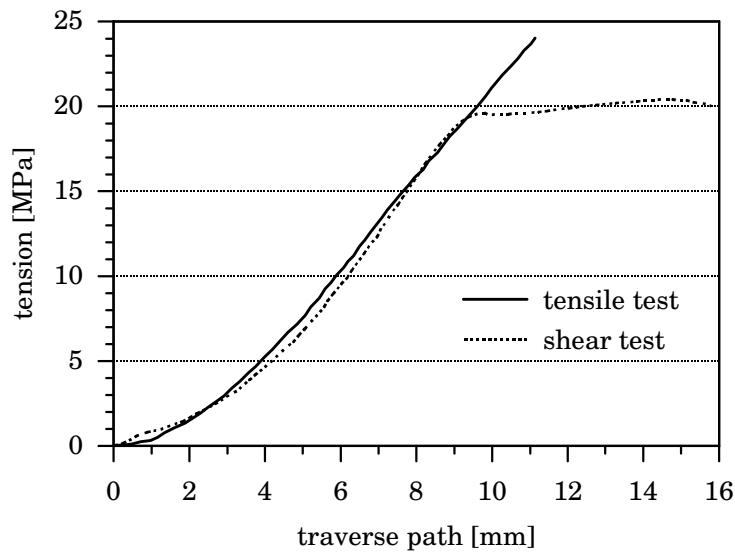
Figure 3.142: Load/traverse path curves recorded with adhesion tests of the sputtered zinc coatings ZC_8

Sample	Zn			Fe			Ti		
	ZB_8	ZC_8	ZE_8	$ZFe\,3_8$	$ZFe\,7_8$	$ZFe\,13_8$	$ZTi\,1_8$	$ZTi\,5_8$	$ZTi\,9_8$
Normal [MPa]	12.8	24.2	17.5	16	20	15.8	34.2	24	17.5
Shear [MPa]	16.5	17.6	16.3	16.3	17.9	16.5	18.6	20.1	15.7

Sample	Cr		Mg	
	$ZCr\,1_8$	$ZCr\,2_8$	$ZMg\,1_8$	$ZMg\,2_8$
Normal [MPa]	15.6	14	20.5	34.5
Shear [MPa]	15.8	17.3	16.7	18.9

Table 3.26: Adhesion strengths of adhesive bondings between coated steel sheets under normal- and shear force load

of the adhesive bonding at 24.2 MPa. The applied load is so big that the ductile steel sheet is deformed and pulled into the abutment of the tensile test machine. Thereby the occurring deformation partly peels the steel sheet from the glued stamp.

The curve of the shear test however shows a different curve shape. Up to loading of 19 MPa also this curve shows a steady increase of force with increasing traverse path. From this point on a constriction of the metal sheets and a peeling of the bond can be observed. The constriction occurs in the more ductile, non overlapping parts of the specimen, which are not clamped in the jaws of the tensile machine. The peeling of the bond occurs as result of a small normal force component. This force component is created due to the overlapping part of the specimen which is not in line with the jaws of the tensile test machine and thus slightly tilted. This process, combined with the constrictions of the sheets, is

visible as region of constant loading in graph 3.142. At constant force but decreasing bonding surface the adhesive bonding finally fails, and the sheets are separated. The values for the coating adhesion strengths were calculated from the maximum force at bonding failure and the initial bonding surface. Actually the bonding surfaces at adhesion failure were smaller than the initial ones due to the peeling effect. Therefore the actual coating adhesions should be higher than the values given here. However the obtained values already exceed the yield strength of the steel sheets and thus show the applicability of the coatings in adhesive joinings for car components.

3.4.2.2 Bending Test

Figure 3.143 shows an optical microscope image of the external part of a bent, $ZFe\,13_8$ coated steel sheet. The sample was bent around an outer diameter of $5\,mm$, embedded in epoxy resin and finally metallographically prepared. The upper dark part of the image shows the embedding epoxy resin, the middle, silver, grey part the zinc iron coating $ZFe\,13_8$ and the lower, white one the steel substrate. The microscope photograph shows that even after bending the coating adherence to the steel sheet is very good. The coating is very ductile and no delamination is visible. All bent samples showed the same performance and passed this test.
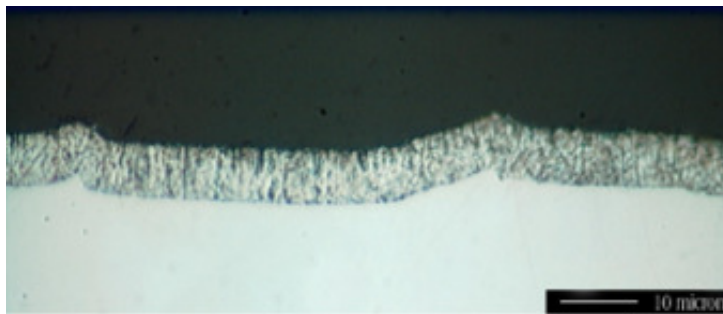
Figure 3.143: Bended zinc iron coating $ZFe\,13_8$

3.4.2.3 Clinching Test

Figures 3.144 to 3.149 show the fold lines of coated steel sheets, which are clinched by $180\,°$, viewed with a magnifying glass. The middle part of the photographs, which are well focused, shows the region of the fold with the highest curvature. At the left and right margins of the images the folded steel sheet is out of the focus. The first two figures display the EZ coating and the sputtered ZC_8 coating after clinching. Both samples show a coherent well adherent surface, without cracks. Only the surface roughness of the substrate is visible. The next two photographs show in contrast two coatings which have not passed this test. These are the zinc magnesium coating $ZMg\,15_{float}$ and the zinc aluminium coating $ZAl\,2_{float}$. Sample $ZMg\,15_{float}$ exhibits a lot of cracks parallel to the fold line, which expose the underlying steel substrate. The zinc aluminium coating even performs worse. Here already a big part of the folded coating is detached and the bare steel substrate is visible. Both last photographs show the fold line of the metallic, shiny zinc chromium and zinc titanium coatings, $ZCr\,11_8$ and $ZTi\,10_8$. Also here no cracking and delamination can be observed. Apart from coatings $ZMg\,15_{float}$ and $ZAl\,2_{float}$, all other samples passed this test.
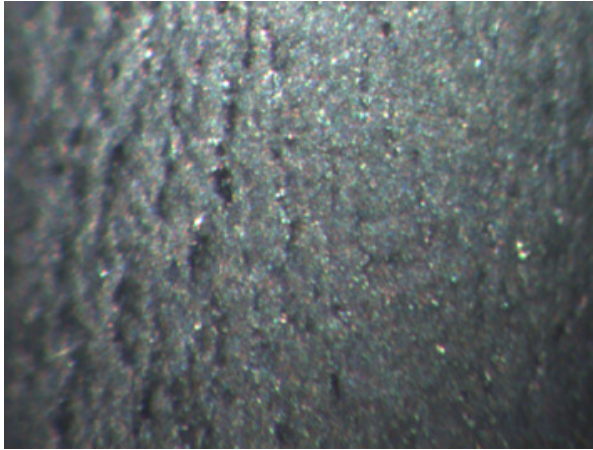
Figure 3.144: Clinched EZ coating
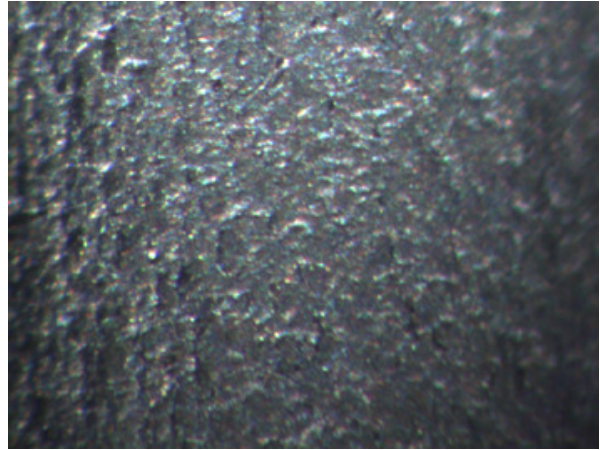
Figure 3.145: Clinched zinc coating ZC_8
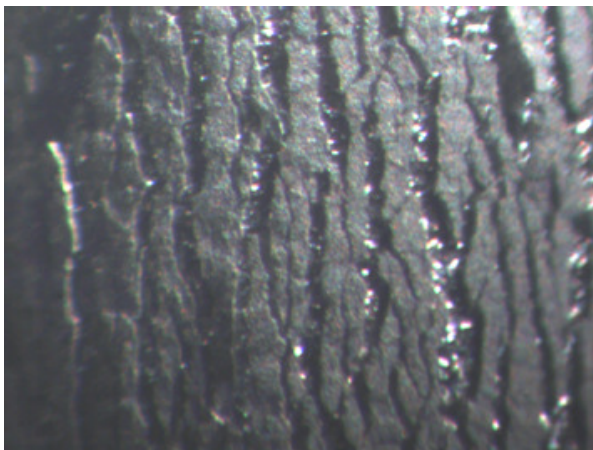
Figure 3.146: Clinched zinc magnesium coating $ZMg\,15_{float}$
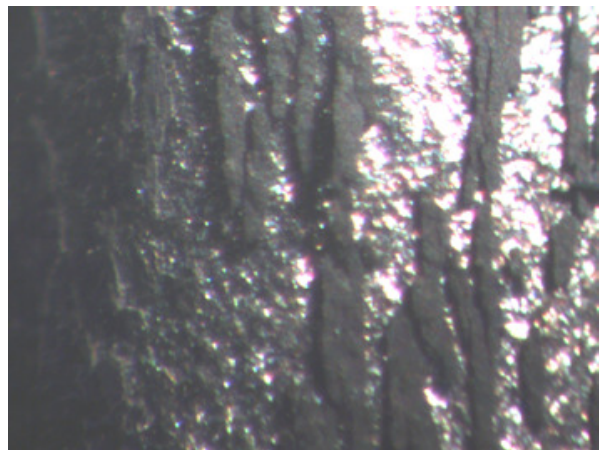
Figure 3.147: Clinched zinc aluminium coating $ZAl\,2_{float}$
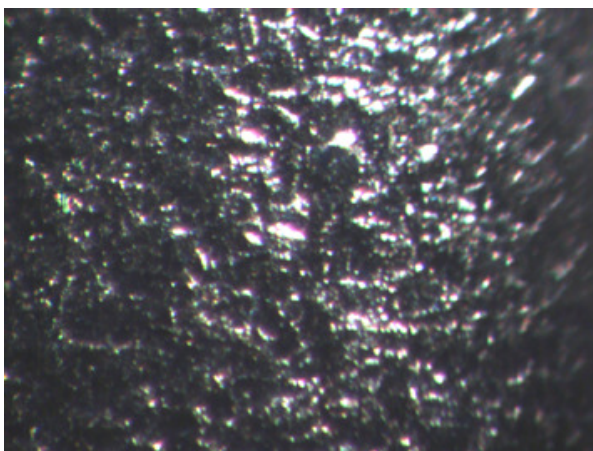
Figure 3.148: Clinched zinc chromium coating $ZCr\,11_8$
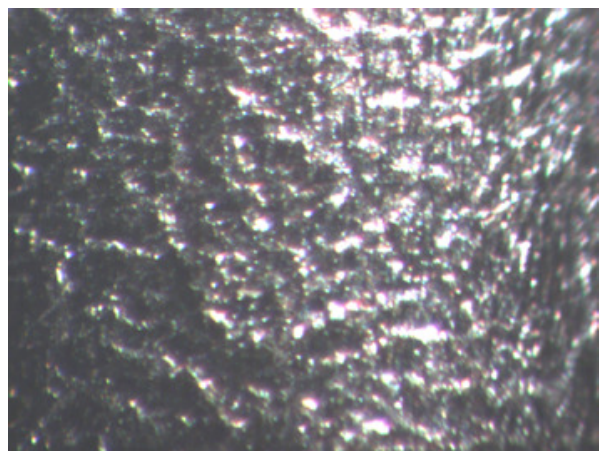
Figure 3.149: Clinched zinc titanium coating $ZTi\,10_8$

3.5 Corrosion

3.5.1 Electrochemical Corrosion

3.5.1.1 Open Circuit Potential vs. Time Measurement

The open circuit potential/time measurements have been carried out to determine the capabilities of the coatings to offer cathodic protection for the steel sheets during immersion in a saline solution. The following paragraphs 3.5.1.1.1 to 3.5.1.1.4 present the open circuit potential/time plots of the different zinc and zinc alloy coatings with their individual curve shapes, while paragraph 3.5.1.1.5 compares the coatings by calculating their normalised lifetimes in these environments.

3.5.1.1.1 Zinc Coatings   Figure 3.150 shows the open circuit potential (OCP)/time plots of different zinc coatings including the electro galvanised reference coating EZ. Apart from different lifetimes all zinc coatings show the same curve shape. Their start potential is between -1141 mV and -1100 mV. During the dissolution of zinc the potential remains stable at this low potential. The periods at low potential are directly related to the coating thicknesses. With continuous consumption of the coating the potential rises slightly, indicating an increase of the coating porosity. On reaching the pitting potential of zinc the potential rises dramatically up to about -720 mV, indicating the dissolution of the bare steel substrate. In contrast to the sputtered samples the EZ coating reaches a slightly higher final potential of -695 mV. In case of thin coated coatings (d < 20 μm) it was possible to finish the immersion experiments, as all these specimens reached the final potential, exposing the underlying steel. For the thick ZE_8 coating (d = 20 μm) the experiment could not be finished. The electrochemical cell with the clamped sample started to leak before the final potential was reached. After 490 h immersion time the sample/cell seal, a Teflon®O–ring, started to leak. The corrosion products, created at the coating-sealing interface, became porous and detached from the substrate so that a tight seal was not obtained anymore. In Fig. 3.154, which gives an overview of the normalised lifetimes of the different coatings, sample ZE_8 is marked as "stopped".
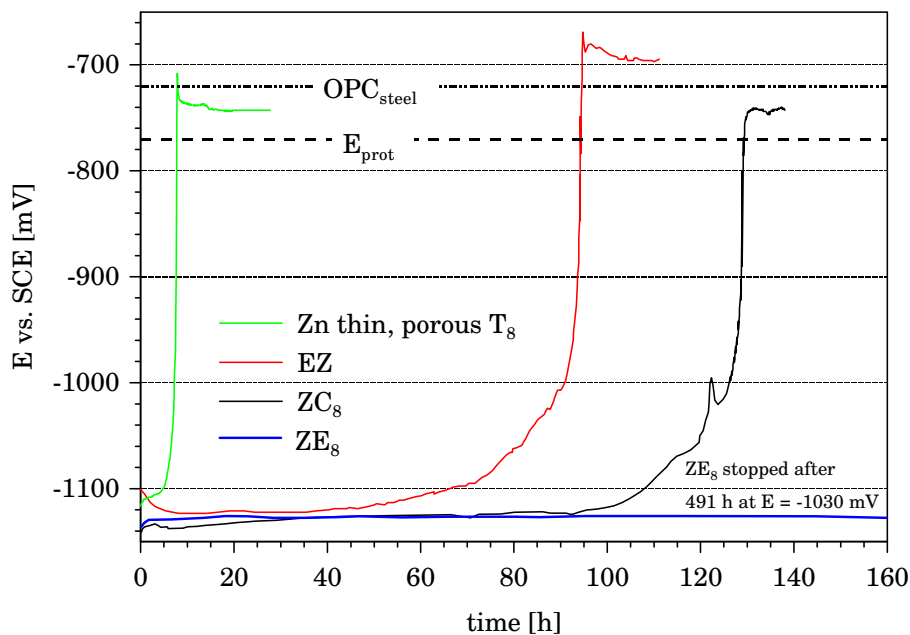
Figure 3.150: OCP/time curves of zinc coatings

3.5.1.1.2 Zinc Iron Coatings   Figure 3.151 displays the changes in the open circuit potentials of zinc iron coatings with immersion time. The first characteristic which can be noted in contrast to the

pure zinc coatings is the different start potential of these samples. According to their iron contents the start potentials indicate more noble material. The start potential of the lowest alloyed sample ZFe 3_8 (3.3 at.% Fe) at -1110 mV is in the range of the non alloyed zinc coatings. The highest alloyed coating ZFe 13_8 (13.6 at.% Fe) has a start potential of -1043 mV. The Galvaneal coating with an average iron content of about 10 at.% also starts at this higher potential. In contrast to the pure zinc coatings the iron alloyed coatings show a different curve shape. After a dwell time at the start the potentials rise in a stepwise fashion, with different plateaus up to the final potential of the bare steel. At about -820 mV a distinct plateau can be observed in all cases.

Similar potential curves have been obtained by Zhang et al. and Besseyrias et al. [269,270], who carried out electrochemical stripping experiments on galvanealed steels. Zhang et al. attributed the observed potential plateaus to different alloy layers ξ–phase, δ–phase, Γ_1–phase, Γ–phase in the galvanealed coating. They stated that the measured potentials are the combined results of dezincification, formation of iron particles, H_2 evolution as well as differences in the kinetics and changing surface areas of the various phases. The OCP/time curves of the sputtered zinc iron coatings of this study can not be explained in this way since the films consist of a single phase. They do not show the multilayered phase structure developing from mutual interdiffusion between the steel substrate and the zinc coating during annealing. The corrosion of the sputtered zinc iron coatings can better be explained by the corrosion mechanisms proposed by Besseyrias and his coauthors. This group attributed the potential changes during their dissolution experiments to a change in the corrosion mechanism of the electrode. They proposed a two phase dissolution mechanism for the dissolution of the ξ–phase and δ–phase: a selective zinc dissolution in the first period of immersion, followed by a uniform dissolution of the intermetallic phases increasing the electrode potential.
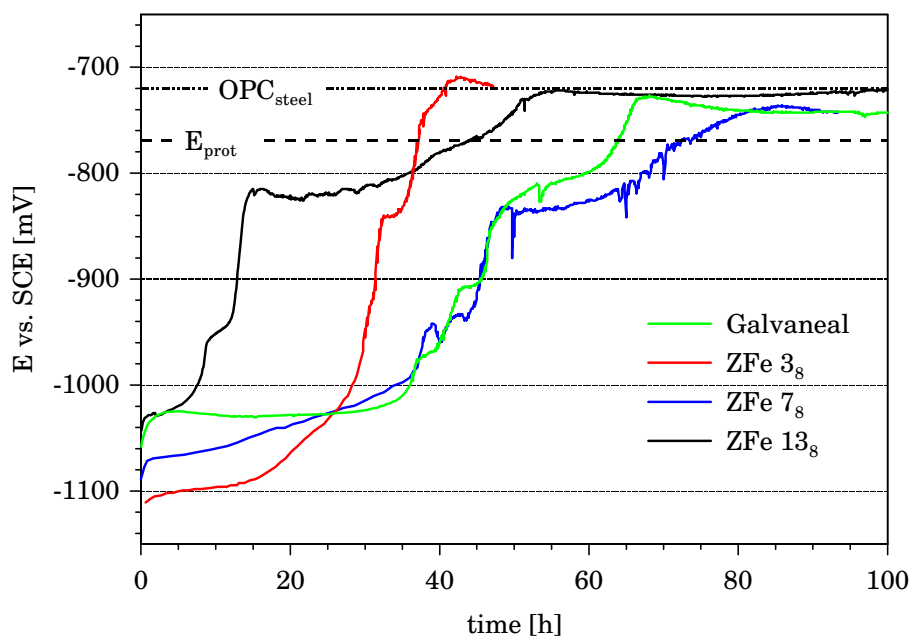
Figure 3.151: OCP/time curves of zinc iron coatings

3.5.1.1.3 Zinc Titanium Coatings Figure 3.152 presents the results of the OCP/time measurements for the different zinc titanium coatings. Both low alloyed zinc titanium coatings ZTi 1_8 and ZTi 5_8 exhibit approximately the curve shape of the pure zinc coatings with a start potential at about -1120 mV. After different periods at this potential, indicating the dissolution of zinc, the potentials rise rapidly to the final potentials of about -735 mV. Sample ZTi 9_8 with a titanium content of 9.4 at.% has a different curve shape. Starting at a potential of -1106 mV the curve rises quite early and reaches after 8 hours an

interim value of -825 mV. After an immediate drop, the potential rises again steadily, but now with a much lower slope. In the period between 40 and 90 hours the potential curve shows significant oscillations of about ± 20 mV. These oscillations are caused by the created corrosion products which cover and uncover the surface periodically. The high titanium content leads to the formation of corrosion products, passivating the surface thus leading to an increase of the OCP. In a second step the passivating layer cracks or dissolves, the underlying coating/substrate is exposed and the potential drops again. Notwithstanding this, the general trend of a potential increase is kept and after 110 hours of immersion the final potential of -725 mV is reached. For the even higher alloyed specimen $ZTi\,10_8$ the potential curve starts at -1080 mV. Within the first two hours it increases immediately to -775 mV and continues with the oscillating behaviour already described with $ZTi\,9_8$. The high, oscillating potentials measured with $ZTi\,9_8$ and $ZTi\,10_8$ do not indicate the entire consumption of the coatings. They show that the steel substrates are still covered by the coatings and the corrosion products created by them, but these films do not provide anymore cathodic protection since their potentials are close to the potential of bare steel. A similar behaviour can be observed with the highest alloyed zinc chromium coating $ZCr\,11_8$ in the next section.
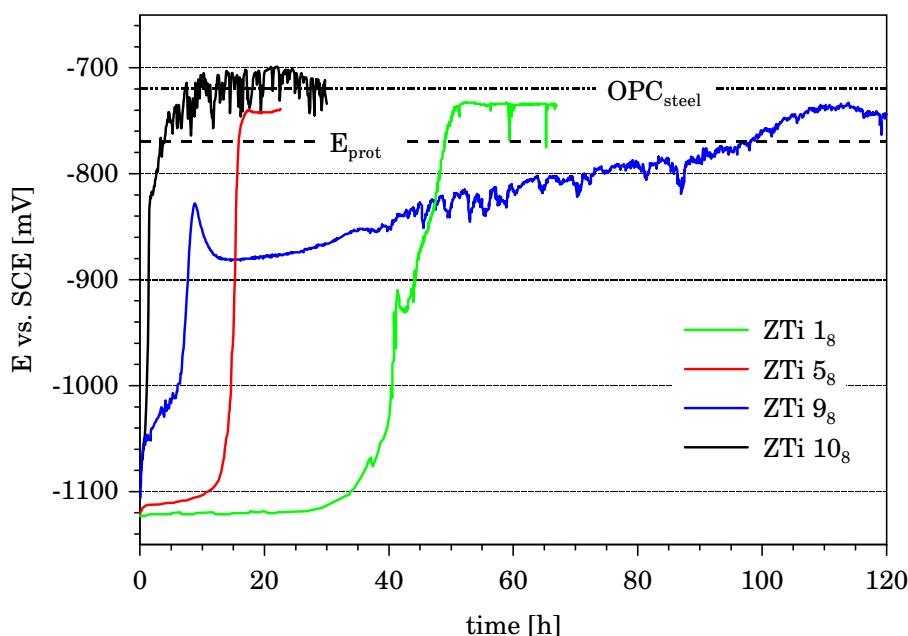
Figure 3.152: OCP/time curves of zinc titanium coatings

3.5.1.1.4 Zinc Chromium, Zinc Magnesium and Zinc Aluminium coatings The zinc magnesium coatings $ZMg\,2_8$, $ZMg\,15_8$ and the zinc aluminium coating $ZAl\,2_8$ in Fig. 3.153 show a curve shape similar to the one of the pure zinc coatings. The coatings differ only in their start potentials. Sample $ZAl\,2_8$ starts at -1136 mV whereas the zinc magnesium coatings have the lowest start potentials of all tested samples. These start due to the less noble alloyed magnesium at -1143 mV and -1156 mV.

The low alloyed zinc chromium coating $ZCr\,3_8$ with 3.1 at.% chromium shows approximately the same curve shape as the pure zinc coatings. Its start potential is at -1134 mV. After a hold time at low potential, the potential increases very rapidly to -750 mV. Following, the potential is not stabilised at this value. It increases, very slowly but constantly up to a value of -725 mV which is reached after 180 hours and where the experiment is stopped. The highest alloyed zinc chromium coating $ZCr\,11_8$ shows a curve shape comparable to the one of the highest alloyed zinc titanium coating $ZTi\,10_8$. The potential curve starts at -1109 mV, holds the low potential for 20 hours with slight instabilities and increases following

rapidly to a potential of -820 mV. With advancing time also here potential oscillations due to created corrosion products can be observed. Subsequently the potential increases very slowly but steadily and reaches after 300 hours a stable value of -680 mV.
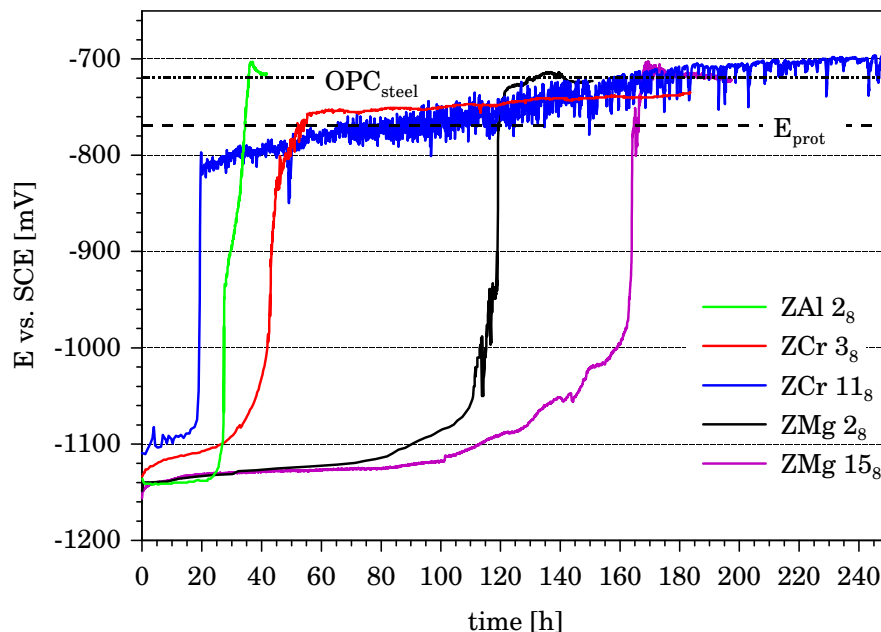
Figure 3.153: OCP/time curves of zinc magnesium, -chromium and -aluminium coatings

3.5.1.1.5 Normalised Lifetimes The lifetime of a sacrificial coating is defined as the period where the open circuit potential OCP of the coating is lower than the protection potential $E_{prot} = -770\,mV$. At this potential which is 50 mV lower than the corrosion potential (OCP) of the steel substrate a sacrificial coating provides sufficient cathodic protection to the substrate. Table 3.27 gives an overview of the coating thicknesses of the various samples, their lifetimes normalised to their coating thicknesses and the normalised lifetimes ratio with respect to the references. A graphical display of the normalised lifetimes is given in Fig. 3.154.

sample	thick-ness	normalised lifetimes	ratio to EZ	sample	thick-ness	normalised lifetimes	ratio to EZ	ratio to Galvaneal
EZ	9	10.4	1	$ZCr\,1_{float}$	7.7	4.4	0.42	-
ZD_8	2.4	2.9	0.28	$ZCr\,1_8$	7.2	7.4	0.71	-
ZC_{float}	6.3	16	1.54	$ZCr\,2_{float}$	6	5.3	0.51	-
ZC_8	4.9	26.3	2.53	$ZCr\,2_8$	6.2	11.5	1.11	-
ZE_8	20.1	24.5	2.36	$ZMg\,1_{float}$	15.3	10.2	0.98	-
$ZTi\,1_{float}$	5.6	2.5	0.24	$ZMg\,1_8$	7.9	15.1	1.45	-
$ZTi\,1_8$	8.5	5.8	0.56	$ZMg\,2_{float}$	9.9	10.6	1.02	-
$ZTi\,5_{float}$	5.4	3.7	0.36	$ZMg\,2_8$	9.2	18	1.73	-
$ZTi\,5_8$	4.9	3.3	0.32	**Galvaneal**	9.4	6.8	-	1
$ZTi\,9_{float}$	4.6	9.1	0.87	$ZFe\,3_{float}$	8.3	2.9	-	0.43
$ZTi\,9_8$	3.6	27.2	2.62	$ZFe\,3_8$	6.9	5.4	-	0.79
$ZTi\,10_8$	5.9	0.5	0.05	$ZFe\,7_{float}$	6.5	6.5	-	0.96
$ZAl\,2_{float}$	9.7	3.7	0.36	$ZFe\,7_8$	6.2	11.6	-	1.71
$ZAl\,2_8$	6.9	4.9	0.47	$ZFe\,13_8$	6	7.2	-	1.06

Table 3.27: Normalised lifetimes
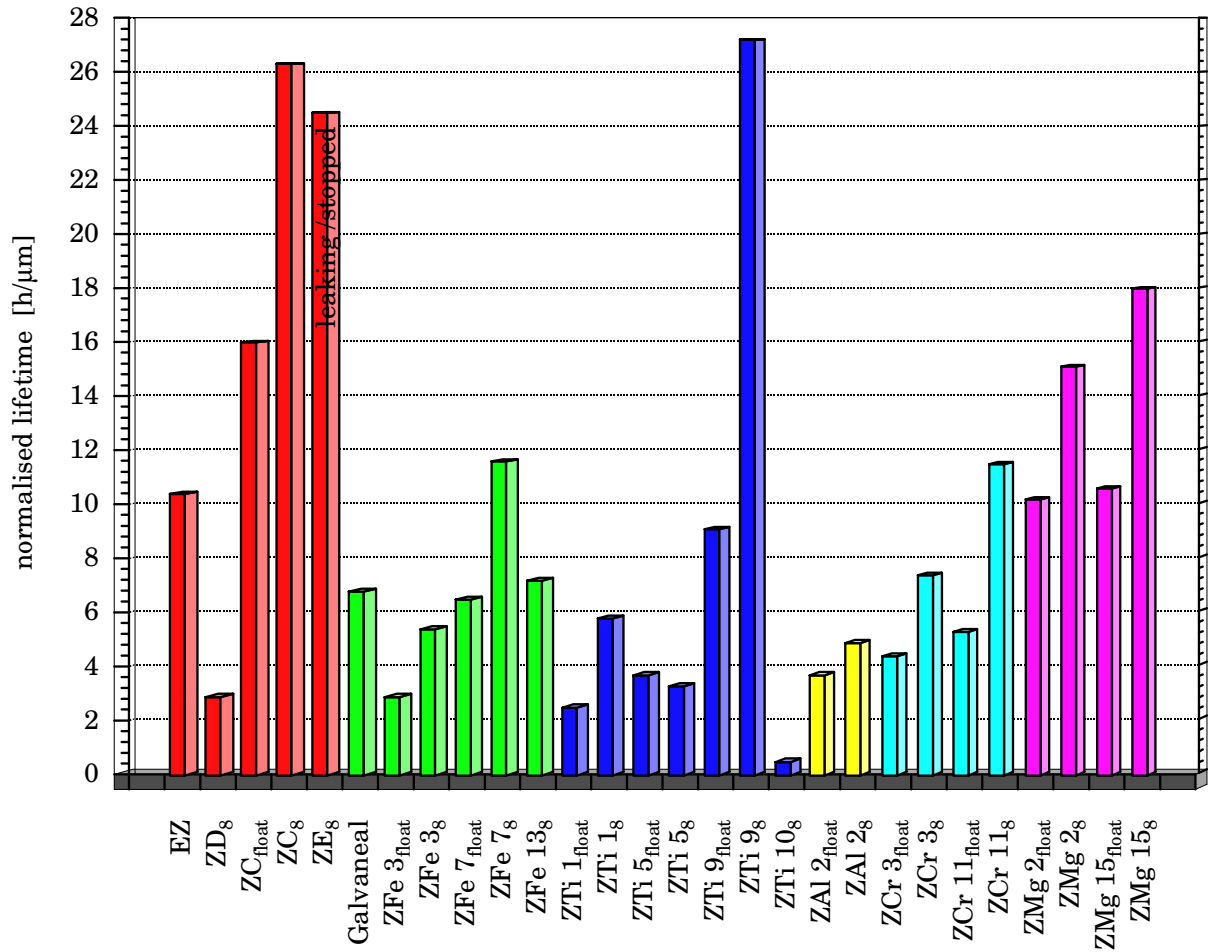
Figure 3.154: Normalised lifetime of different zinc and zinc alloy coatings with OCP/time measurements

The EZ reference coating with a thickness of $9\,\mu$m has a normalised lifetime of $10.4\,\mathrm{h}/\mu$m. This value is exceeded by all sputtered zinc coatings apart from the very thin $2.4\,\mu$m thick coating. The normalised lifetime of $26.3\,\mathrm{h}/\mu$m for deposit ZC_8 corresponds to an increase by a factor of 2.5 as compared to the reference EZ and is the second best result of all tested samples. The thick zinc coating ZE_8, whose immersion experiment was stopped due to leaking, reached a normalised lifetime of $24.5\,\mathrm{h}/\mu$m. Here certainly a much longer lifetime can be expected. It seems to be necessary that zinc coatings have a certain minimum thickness to reach a sufficient normalised lifetime.

With all sputtered coatings, independent of whether they are alloyed or unalloyed, the normalised lifetimes seem to depend on the film morphologies. The influence of the deposition temperature and the resulting morphology on the lifetimes can be observed with almost all coatings types, even with the zinc alloy coatings independent of the respective composition. All specimens deposited at a substrate temperature of $+8\,°$C have longer lifetimes than those samples deposited in the same batch at a floating substrate temperature T_{float}. This fact seems to show that the lifetimes of pure zinc and low alloyed zinc coatings are largely determined by the density of the coatings.

The Galvaneal reference with a thickness of $9.4\,\mu$m reaches a lifetime of $6.8\,\mathrm{h}/\mu$m. Apart from sample $ZFe\,1_{\mathrm{float}}$ the sputtered zinc iron films perform as well or slightly better than the Galvaneal reference. With a lifetime of $27.2\,\mathrm{h}/\mu$m the best performing film $ZTi\,3_8$ resists the immersion 2.6 times longer than the reference EZ. The highest alloyed zinc titanium and zinc chromium deposits (e.g. $ZTi\,4_8$, and $ZCr\,11_8$) however show very short "cathodic protection" lifetimes which are obviously shorter than their actual lifetimes. In these cases the coatings are still present but, as they are either enriched in more noble components such as titanium and chromium by dezincification or covered with corrosion products, they

reach corrosion potentials close to or higher than that of bare steel.

3.5.1.2 Potentiodynamic Polarisation Curves

The data obtained from the potentiodynamic polarisations were processed with the ParCalc and R_pCalc corrosion analysis softwares from EG&G. These softwares fit the obtained data, determine the Tafel slopes β_{anodic}, $\beta_{cathodic}$ of the electrochemical half reactions and extrapolate to obtain the corrosion potential E_{corr} and the corrosion current density i_{corr}. Based on the Stern-Geary equation (Eq. 3.9) given below the software routines calculate the polarisation resistance R_p from the Tafel slopes β_{anodic}, $\beta_{cathodic}$ and the corrosion current I_{corr}. [272, 273]

$$I_{corr} = \frac{\beta_a \cdot \beta_c}{2.3\, R_p(\beta_a + \beta_c)} \tag{3.9}$$

3.5.1.2.1 Zinc Coatings Figure 3.155 shows the potentiodynamic polarisation curves of the steel substrate, pure zinc (99.8 % bulk material) and the pure zinc coatings. The calculated electrochemical parameters are given in Tab. 3.28. The XP280 steel substrate used has a corrosion potential E_{corr} of

sample	d [μm]	E_{corr} [mV]	i_{corr} [μA/cm^2]	R_p [Ωcm^2]	E_{crit} [mV]	i_{crit} [mA/cm^2]	i_{pass} [mA/cm^2]
XP280	-	-721	38.4	991	-432	3.2	0.36
Zn bulk	-	-1140	45.3	442		no passivation	
EZ	9	-1097	3.9	1452	-960	9.9	turns cathodic
ZH$_8$ porous	7.5	-1132	28	333	-996	3.8	0.06
ZC$_8$	6.3	-1138	33.4	326	-997	8.3	turns cathodic
ZC$_{float}$	4.9	-1138	40.4	262	-999	8.5	0.04
ZE$_8$	20	-1134	19.6	496	-935	21.8	0.36
ZI$_8$	27.5	-1139	37.5	279	-856	22.4	1.62

Table 3.28: Electrochemical corrosion parameters of steel substrates, bulk zinc and zinc coatings

-721 mV. Above E_{corr} the steel substrate shows active dissolution ending at its primary passivation potential E_{pp} of -432 mV at a critical current density i_{crit} of 3.2 mA/cm². Here a passivity region begins which is due to the high chloride ion concentration. Its current density minimum i_{pass} of 0.36 mA/cm² is reached at -366 mV. The passivity is followed by pitting corrosion, accelerated by chloride anions, and resulting in a rising current density [274, 275].

The pure bulk zinc has a corrosion potential of -1140 mV. The anodic branch of the polarisation curve shows that the metal is continuously dissolved. Even at higher potentials no passivation and passivity is observed.

The sputtered zinc coatings have corrosion potentials E_{corr} in the range of -1139 mV to -1132 mV. These values correspond to the value of the pure zinc bulk material. The EZ coating instead, has due to unknown impurities (maybe iron), a slightly more noble E_{corr} of -1097 mV. With increase of the potential all zinc samples start to dissolve anodically. The slopes of the anodic curves correspond in this potential range to the slope of the zinc bulk material curve. After reaching their respective primary passivation potentials E_{pp} given in Tab. 3.28 all samples passivate. It can be observed that the potential range where active dissolution occurs is correlated to the thicknesses of the coatings. The thicker coatings ZE$_8$ and ZI$_8$ with higher zinc mass covering exhibit broader active dissolution regions. In the passivity region the EZ and ZC$_8$ samples even turn cathodic. Following this, the current densities rise again. The curve shapes and measured current densities indicate that nearly the entire coatings seem to be dissolved. From that point on mainly the polarisation curves of the corrosion products and/or substrates are measured.
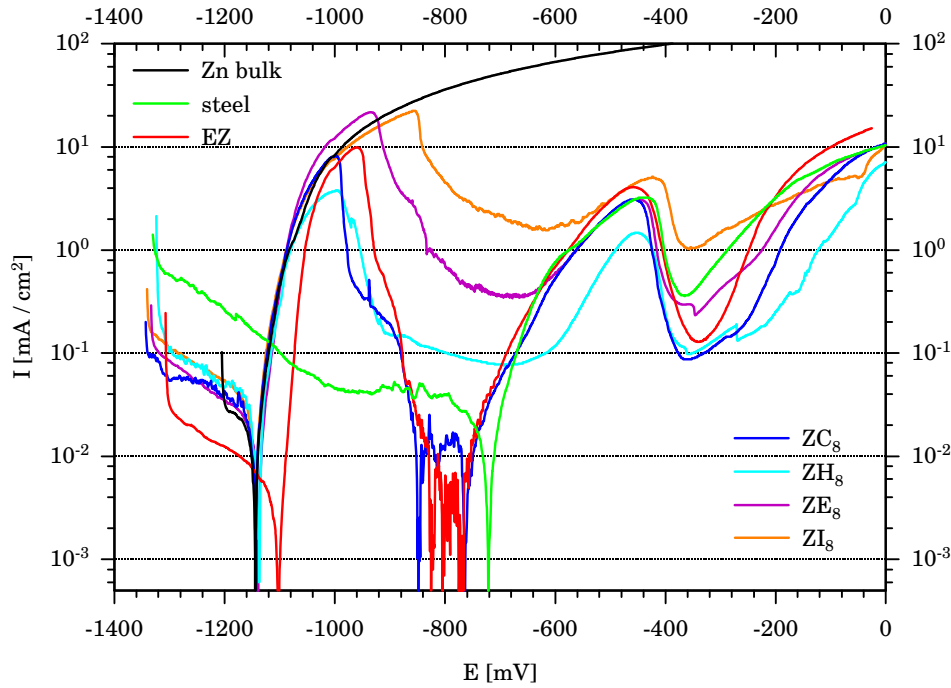
Figure 3.155: Current density/potential curves of zinc coatings

3.5.1.2.2 Zinc Iron Coatings The current density/potential curves of the different zinc iron coatings, which show in comparison to the pure zinc coatings a different curve shape, are given in Fig. 3.156 and 3.157. The obtained electrochemical parameters are given in Tab. 3.29. The first differences are

sample	E_{corr} [mV]	i_{corr} [$\mu A/cm^2$]	R_p [Ωcm^2]	E_{pp} [mV]	i_{crit} [mA/cm^2]	i_{pass} [mA/cm^2]
Galvaneal	-1033	106	446	-769	4.9	0.93
ZFe 3_{float}	-1128	75	179	-989	5.2	0.058
ZFe 3_8	-1115	41.7	266	-1000	4.4	0.06
ZFe 7_{float}	-1104	61.1	210	-932	2.5	0.24
ZFe 7_8	-1080	36.3	312	-932	1.6	0.09
ZFe 13_{float}	-1046	69.8	357	-867	3.2	0.29
ZFe 13_8	-1038	39.3	664	-871	2.3	0.39

Table 3.29: Electrochemical corrosion parameters of Galvaneal and zinc iron coatings

the shifted corrosion potentials, which are according to their alloying content more noble. Above the respective E_{corr} for all samples active dissolution starts. On reaching i_{crit}, which are lower than those of the pure zinc samples, all samples start to passivate. Apart from the Galvaneal coating all sputtered samples show a multi peak current density. Samples ZFe 7_{float}, ZFe 13_{float} and ZFe 13_8 show a second passivity region which spans over the active dissolution range of the steel substrate. This passivation, which suppresses the anodic dissolution of the steel substrate, leads on to expect an improved corrosion protection for these specimens.

3.5.1.2.3 Zinc Titanium Coatings Figure 3.158 presents the current density/potential curves of the zinc titanium samples whose electrochemical parameters can be found in Tab. 3.30. As with the zinc iron coatings, the zinc titanium coating alloying increases the corrosion potentials. The anodic branches of the low alloyed coatings are comparable to those of pure zinc coatings. All curves show a significant active dissolution which is followed by passivation. With $0.03\,mA/cm^2$ the critical current density of the higher alloyed coatings is two orders of magnitude lower than those measured for the pure zinc coatings and the low alloyed zinc titanium coatings. In the following passive region the current density of ZTi 10_8
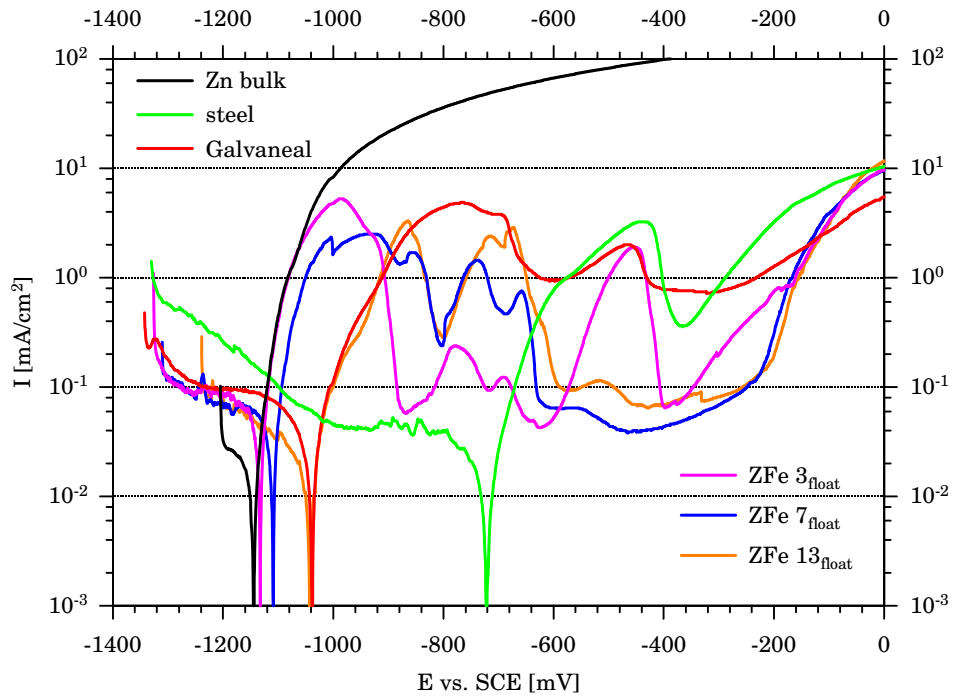
Figure 3.156: Current density/potential curves of zinc iron coatings deposited at $T_s = T_{float}$
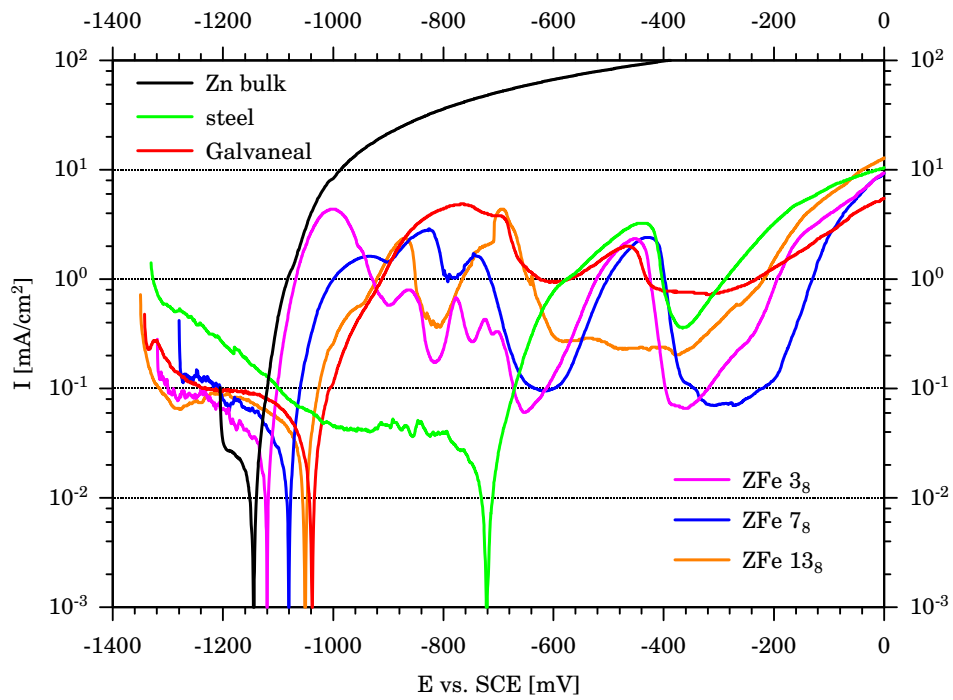
Figure 3.157: Current density/potential curves of zinc iron coatings deposited at $T_s = +8\,°C$
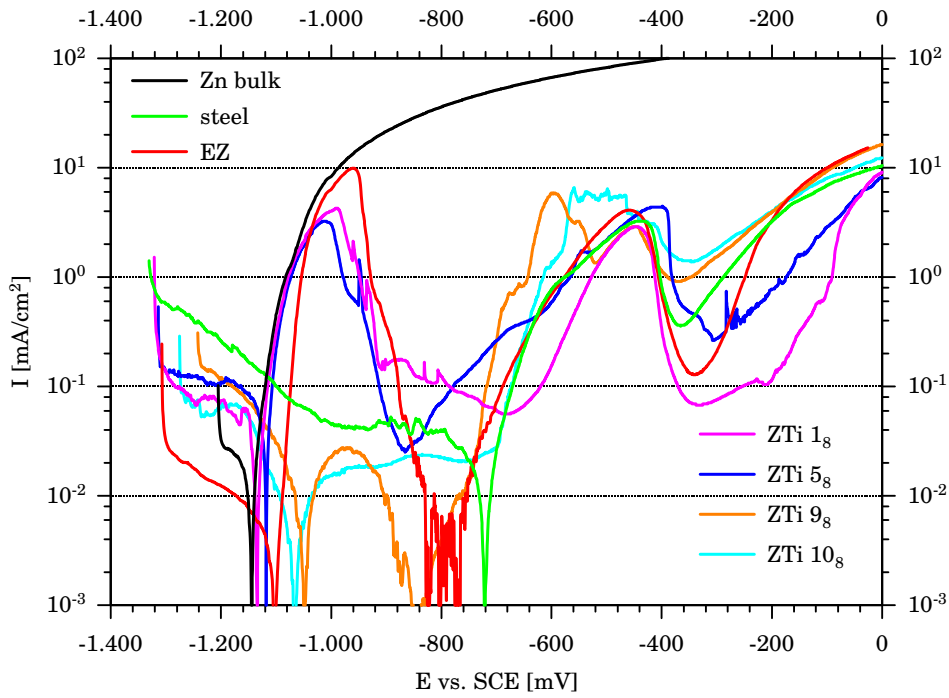
Figure 3.158: Current density/potential curves of zinc titanium coatings

sample	E_{corr} [mV]	i_{corr} [$\mu A/cm^2$]	R_p [Ωcm^2]	E_{pp} [mV]	i_{crit} [mA/cm^2]	i_{pass} [mA/cm^2]
ZTi 1_8	-1129	50.9	253	-988	4.26	0.056
ZTi 5_8	-1113	100	120	-1012	3.24	0.025
ZTi 9_8	-1044	31.8	1687	-969	0.03	0.00042
ZTi 10_8	-1061	23.9	2713	-1000	0.01	0.016

Table 3.30: Electrochemical corrosion parameters zinc titanium coatings

even turns to cathodic values. In the passivity region of the steel substrate (-400 mV to -200 mV), the higher alloyed samples exhibit a higher current density. Here the current density of the lowest alloyed coating ZTi 1_8 is $0.13\,mA/cm^2$, a factor of ten smaller than that of the highest alloyed coating ZTi 10_8 $(1.4\,mA/cm^2)$.

3.5.1.2.4 Zinc Chromium Coatings The current density/potential curves of zinc chromium coatings are displayed in Fig. 3.159. Also the zinc chromium coatings increase their corrosion potentials with

sample	E_{corr} [mV]	i_{corr} [$\mu A/cm^2$]	R_p [Ωcm^2]	E_{pp} [mV]	i_{crit} [mA/cm^2]	i_{pass} [mA/cm^2]
ZCr 3_8	-1123	36.9	337	-969	2.95	0.23
ZCr 11_8	-1105	35.2	512	-1077	0.095	turns cathodic

Table 3.31: Electrochemical corrosion parameters zinc chromium coatings

alloying of chromium. The low alloyed ZCr 3_8 exhibits a curve shape similar to that of the pure zinc coatings. The higher alloyed ZCr 11_8 behaves instead similar to the high alloyed zinc titanium coatings. Also ZCr 11_8 passivates quite early and twice turns cathodic in the passive region. Its second passivation potential E_{2p}, belonging to the passivation of the corrosion products and/or steel substrate, is shifted by about 100 mV to a more negative value.

3.5.1.2.5 Zinc Aluminium and Zinc Magnesium Coatings The potentiodynamic polarisation curves of the zinc aluminium coating ZAl 2_8 and the zinc magnesium coatings are given in Fig. 3.160.
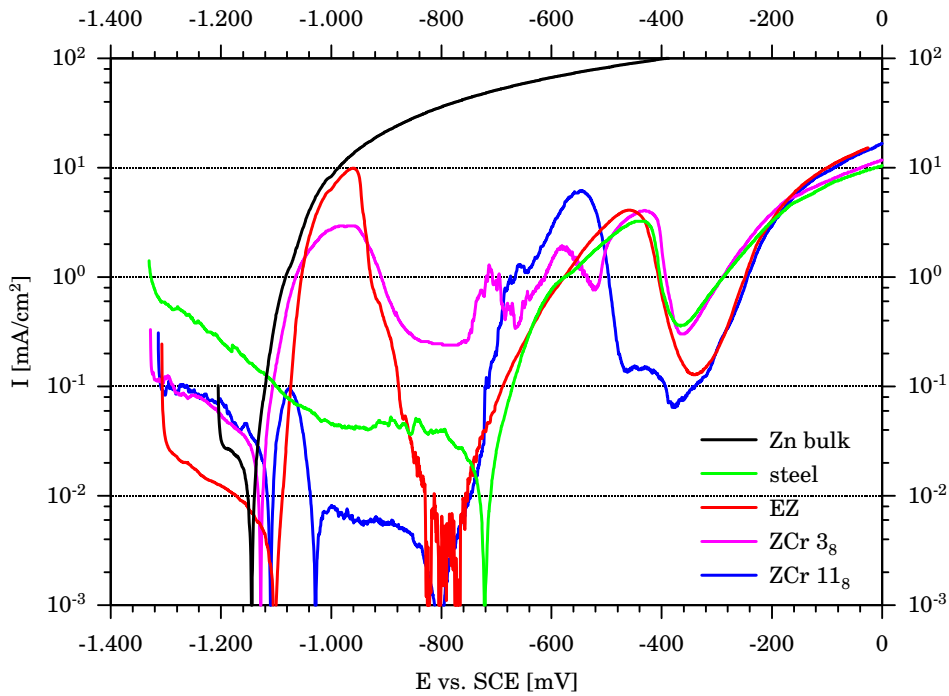
Figure 3.159: Current density/potential curves of zinc chromium coatings

The deduced electrochemical corrosion parameters are given in Tab. 3.32. The corrosion potential of -1148 mV for the low alloyed zinc aluminium coating is in the range of the pure zinc coatings. Also the polarisation curve shape is similar to those of pure zinc coatings.

sample	E_{corr} [mV]	i_{corr} [$\mu A/cm^2$]	R_p [Ωcm^2]	E_{pp} [mV]	i_{crit} [mA/cm^2]	i_{pass} [mA/cm^2]
$ZAl\,2_8$	-1133	38.1	306	-1051	3.1	0.11
$ZMg\,1_8$	-1141	23.5	380	-971	12	0.049
$ZMg\,2_8$	-1177	7.5	1977	-932	10	0.22

Table 3.32: Electrochemical corrosion parameters of zinc aluminium and zinc magnesium coatings

Due to the alloying with the less noble magnesium the zinc magnesium coatings have a more negative corrosion potential. The current density/potential curves of these films are comparable to those of the pure zinc coatings.

3.5.1.2.6   Discussion of Potentiodynamic Polarisation Curves   As shown in Fig. 3.161 the alloying of zinc with other elements changes the corrosion potentials of the alloyed coating towards the normal potential of the respective alloying element, see Tab. 2.3. Apart from the less noble magnesium and aluminium, which lower the corrosion potential, all more noble elements increase E_{corr} corresponding to their alloying content. Also the corrosion potential of the electro galvanised EZ coating differs from E_{corr} of the pure bulk material. Due to more noble impurities, which seem to be present, its corrosion potential is increased to -1097 mV.

Figure 3.162 shows the correlation between the alloying content and the resulting corrosion current density i_{corr}. For the zinc chromium and both types of zinc iron coatings no clear concentration dependence of i_{corr} can be observed. In contrast, a clear distinction between the morphologies of the zinc iron coatings concerning i_{corr} can be made. The more porous structures of the coatings deposited at $T_s = T_{float}$, having larger surface areas resulting in higher reactivities, approximately double the measured corrosion current densities. For the zinc magnesium coatings the corrosion current density is steadily lowered with increasing alloying content. This fact could be related to a possible passivation of the less
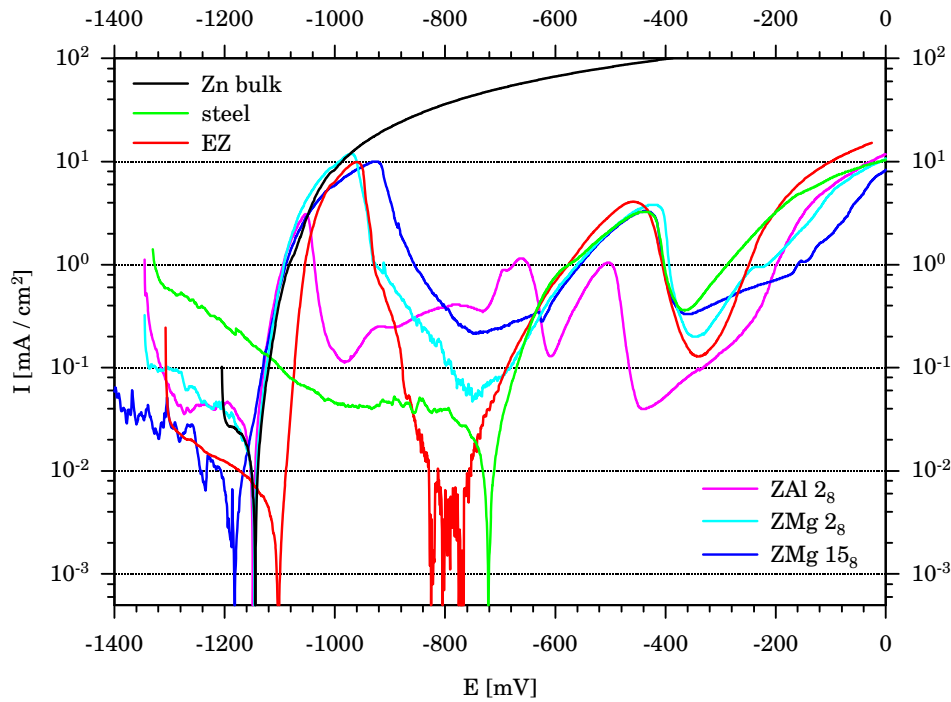
Figure 3.160: Current density/potential curves of zinc aluminium and zinc magnesium coatings

noble magnesium fraction at the adapted corrosion potential. With the zinc titanium coatings i_{corr} increases up to a maximum at 5.5 % Ti content and is subsequently lowered again. This behaviour could be explained by varying titanium distributions at different Ti concentrations within the x-ray amorphous films and a possible passivation of the titanium at higher titanium fractions.

The influence of alloying on the critical current density i_{crit} can be seen in Fig. 3.163. Apart from the zinc magnesium films which show no real concentration dependence of the critical current density, all other alloyed coatings lower their critical current density with increasing alloy concentration. With the zinc chromium- and zinc titanium films this effect is especially pronounced. At higher alloy concentrations (10-13 %) the critical current density is one or two orders of magnitude lower than those of the pure zinc coating.

Corrosion resistance is closely related to the alloy composition, the distribution of the alloying element and the microstructure of the coating [276]. The correlation between corrosion resistance of a coating, expressed as its polarisation resistance R_p, and the amount of alloying is displayed in Fig. 3.164. For all samples the same tendency can be observed: Initially the polarisation resistance is slightly reduced before it steadily increases with increasing alloying content (note the logarithmic scale of R_p). In particular the zinc magnesium and zinc titanium coatings show a strong increase of R_p. Additionally, the influence of the surface morphology of the zinc iron samples on the polarisation resistance can be observed. The smooth compact structures of the ZFe_8 samples give at all alloying concentrations a better corrosion resistance than the rougher, less compact ZFe_{float} samples.
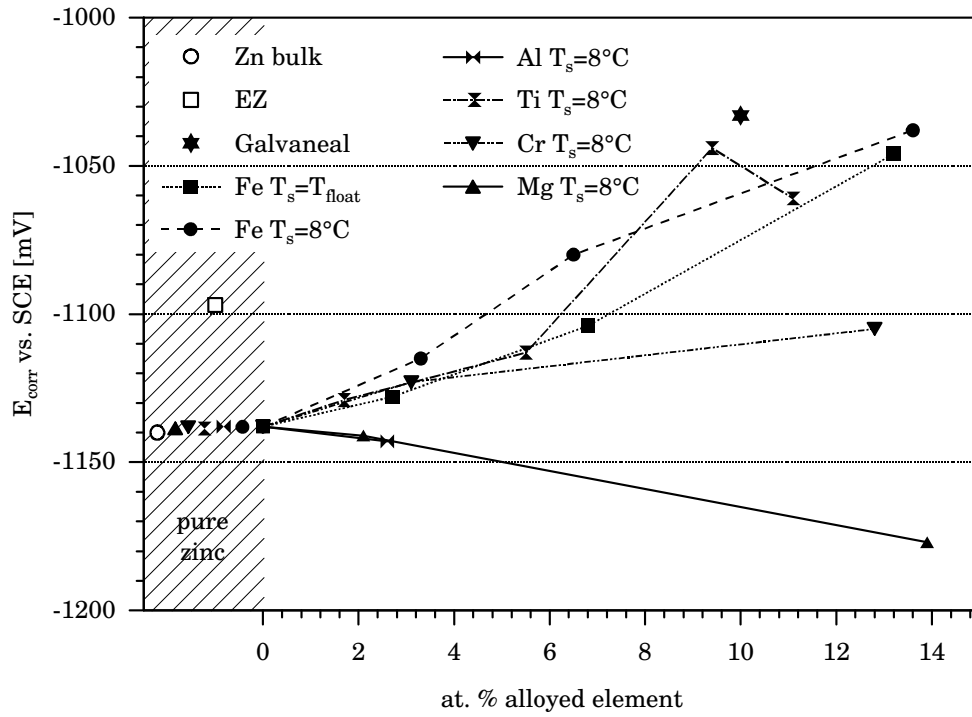
Figure 3.161: Corrosion potential E_{corr} versus alloying content
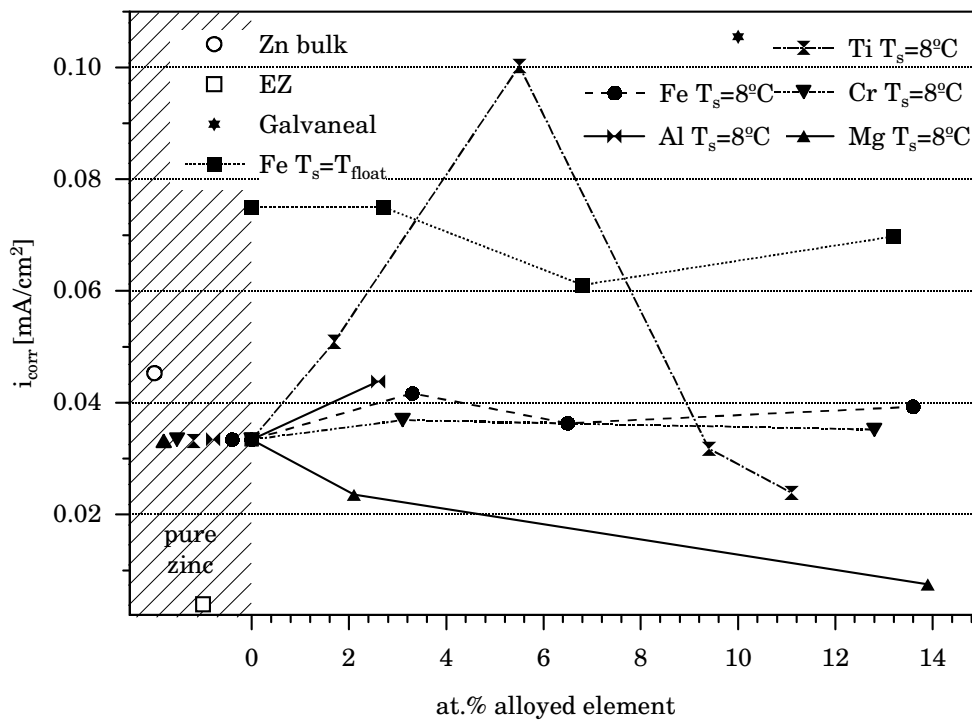
Figure 3.162: Corrosion current density i_{corr} versus alloying content
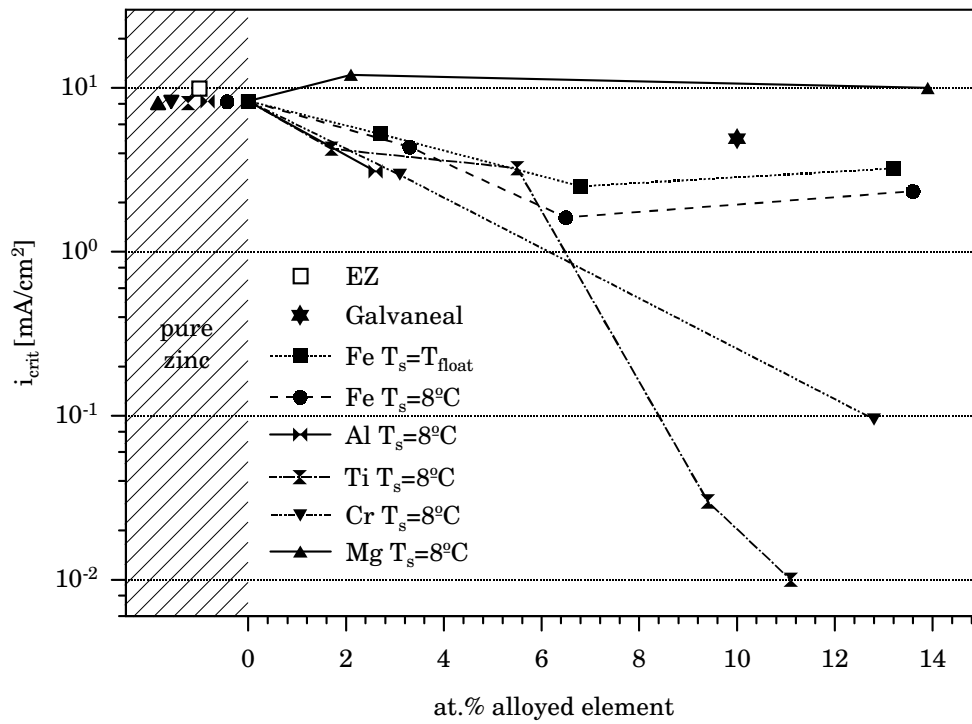
Figure 3.163: Critical current density i_{crit} versus alloying content
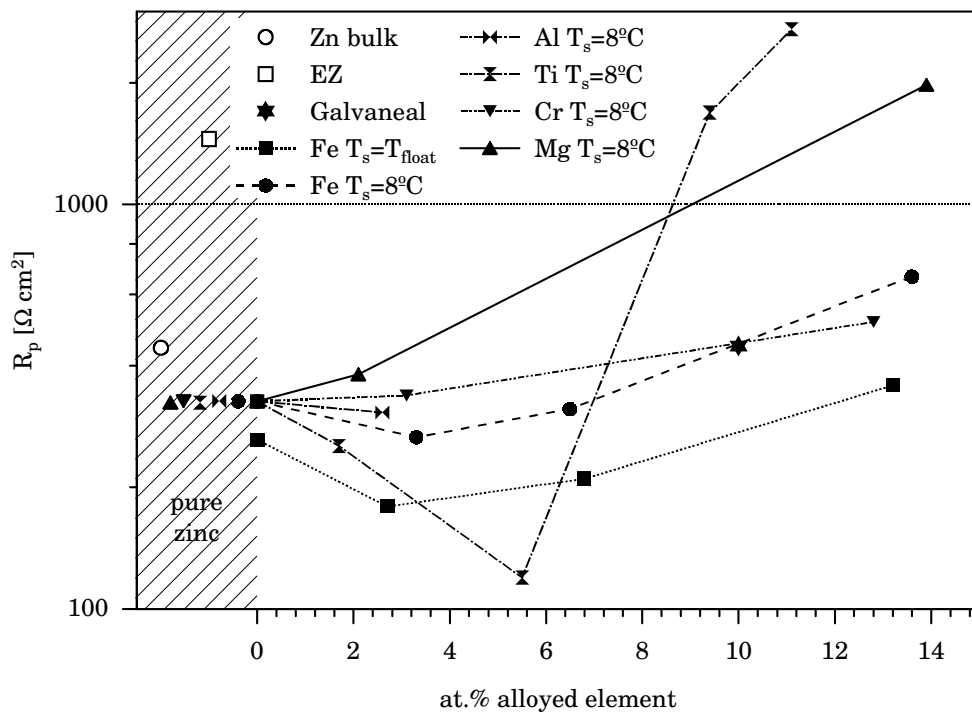
Figure 3.164: Polarisation resistance R_p versus alloying content

3.5.2 Corrosion in Accelerated Testing

3.5.2.1 Salt Spray Test DIN 50021

Having an average lifetime of conventional zinc coatings in mind, for the saltspray test (SST) at Zeuna Stärker a period of three weeks was planned. However after this period the failure criterion, the occurrence of red rust, and thus the test end was not reached for all samples. Due to the limited access to the salt spray cabinet for some specimens the test had to be stopped at the end of the foreseen test period (480 h) and before failure. In Fig. 3.165, which displays the results of the saltspray test, these samples are marked with a dot. The graph displays the performance of the coatings given as time to the occurrence of red rust normalised to their coating thickness. The blank steel sheets have a very limited lifetime in the salt spray test. After 23 hours these samples are completely covered by red rust, emerging the need for a protective coating. The tested coatings can be divided into three groups: coatings which last up to 20 h (group I), coatings with a lifetime of 20–60 h (group II) and coatings which last longer than 60 h (group III).

Both reference coatings EZ and Galvaneal as well as all the sputtered zinc and zinc iron coatings belong to group I. The electrodeposited coating EZ (d=9 μm) has a lifetime of 12 $^h/\mu m$ whereas the Galvaneal coating (d=9 μm) lasts 10 $^h/\mu m$. The lifetime obtained for the EZ coating is identical to those measured in tests carried out by Rover respectively Istituto Scientifico Breda S.p.A in the project [279]. Comparable lifetimes of 14.5–17.5 $^h/\mu m$ for electrodeposited pure zinc coatings obtained from alkaline cyanide free solutions have been measured by Pech-Canul et al. [280] and Ramanuaskas et al. [281]. The value for the Galvaneal coating is comparable to that of 8 $^h/\mu m$ obtained by Almeida and Morcillo [282] in salt spray testing. The sputtered zinc coatings range, depending on their morphology and thickness, from 7 $^h/\mu m$ for a thin porous ZB_8 coating to 16 $^h/\mu m$ for the thick, compact ZE_8 coating. In this case already the compact coating ZC_8 with a thickness of 5 μm reaches the performance of the reference EZ. The thicker ones perform even better.

With the sputtered zinc iron coatings the effect of alloying and the influence of morphology (deposition temperature) can be seen clearly. With increasing iron content the lifetime steadily increases. The lower alloyed samples last approximately as long as the Galvaneal reference whereas the higher alloyed coatings last slightly longer. Additionally, all coatings deposited at T_s=+8 °C perform better than those deposited at T_{float}.

The lowest alloyed zinc titanium coatings perform slightly better than EZ. The last coating which belongs to group I is the zinc aluminium sample $ZAl\,2_{float}$ which performs approximately as well as the zinc reference.

The next group looked at is group II. To this group belong, apart from sample $ZMg\,2_8$, all zinc magnesium samples. With times to red rust in the range of 30 $^h/\mu m$ to 53 $^h/\mu m$ the normalised lifetimes are increased by a factor of two to four in comparison to the reference.

The last group of coatings, i.e. group III, shows a further significant improvement in normalised times to red rust. In this group are all zinc titanium coatings, apart from the lowest alloyed one, all zinc chromium coatings as well as the zinc aluminium coating $ZAl\,2_8$. With a normalised lifetime of about 60 $^h/\mu m$ the coatings $ZTi\,10_{float}$, $ZAl\,2_8$, $ZCr\,3$ and $ZMg\,2_8$ reach five times the lifetime of the reference EZ. Sample $ZTi\,5_8$ which is the longest lasting sample reaching the failure criterion before test stop, has a normalised lifetime of 91 $^h/\mu m$. With this lifetime it lasts seven times longer than the reference EZ. The overall longest resisting sample is $ZTi\,9_8$ with 9.4 at.% titanium. This sample has a lifetime of 137 $^h/\mu m$, i.e. a 11 fold prolongation of lifetime in contrast to the electrodeposited reference coating. With the results presented one has always to keep in mind that for those samples for which the test was stopped, a further increase in lifetime is almost certain.

The appearance of the salt sprayed samples after test end can be seen in Fig. 3.166 to Fig. 3.181. After test end the samples have been washed with deionised water to remove excess sodium chloride solution
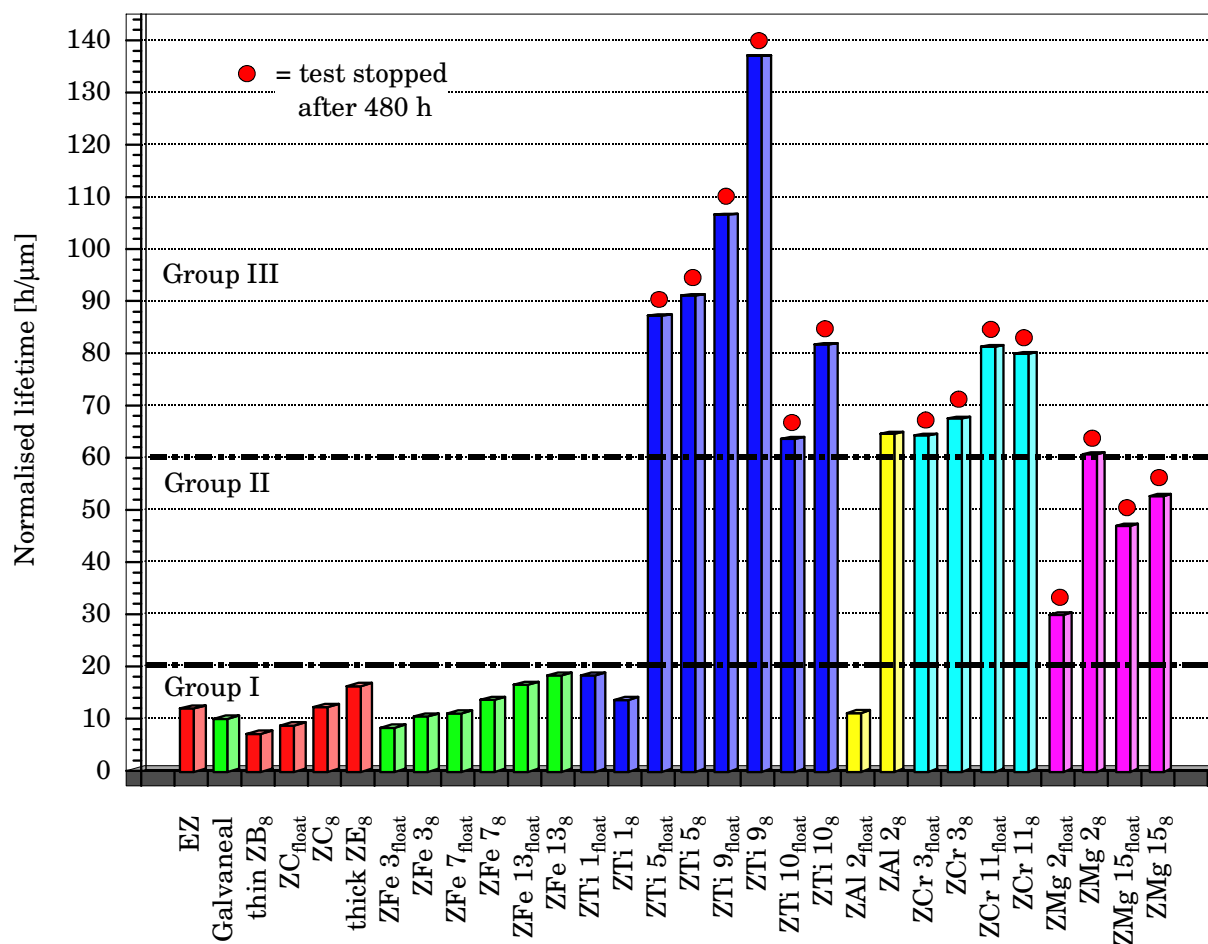
Figure 3.165: Normalised time to occurrence of red rust for different zinc and zinc alloy coatings with salt spray testing. Samples, for which the salt spray test has been stopped after 480 h, are marked with a dot •.

and rinsed with isopropanol to dry the samples. The photos of those samples, for which the salt spray test had been stopped, were taken two weeks after test stop. This might have resulted in further corrosion attack which occurred in the period between test stop and the moment of taking the photograph.

Figure 3.166 shows the electrodeposited reference sample EZ after 109 h of salt spray testing. The sample has a rough surface of white corrosion products agglomerating to fibrous structures. The sputtered sample ZC_8 in Fig. 3.167 looks similar. The thinner ZB_8 coating in Fig. 3.168 is similar in appearance to both. However, it has less agglomerates and due to its lower thickness more and wider spots of red rust appear.

The zinc aluminium coating $ZAl\,2_8$ in Fig. 3.169 is even after 446 h SST totally different in appearance. Much fewer and finely distributed corrosion products can be observed. The coating is dark grey and relatively smooth.

The photo of the Galvaneal reference sample is given in Fig. 3.170. In contrast to the pure zinc coatings, the surface covered by corrosion products is now orange–red. The different colouring is due to the iron contained in the zinc iron coating, which starts to corrode. The same behaviour can be noticed with the sputtered zinc iron coatings in Fig. 3.171 to Fig. 3.173. The lowest alloyed coating shows still more white corrosion products than the pure zinc coatings, but also the first signs of orange colouring. The 6,5 at.% Fe alloyed sample $ZFe\,7_8$ looks quite similar to the galvanealed one. The highest alloyed coating $ZFe\,13_8$ finally has a comparatively dark grey appearance. The white corrosion products disappeared completely and the surface is covered with a thin orange veil.

The zinc magnesium coatings $ZMg\,2_8$, $ZMg\,15_8$ in Fig. 3.174, 3.175 and the low alloyed zinc chromium coating $ZCr\,3_8$ in Fig. 3.176, which lasted 480 h in the saltspray cabinet, look quite similar. In general,

they are dark grey and more or less speckled with white corrosion products.

The high alloyed zinc chromium coating $ZCr\,11_8$ in Fig. 3.177 is completely different in appearance. Even after 480 h SST its surface is very smooth, marbled with a slight green–blue and in some areas even still displaying a metallic shine. It shows nearly no signs of outgrowing corrosion products.

The appearance of the low alloyed zinc titanium coating $ZTi\,1_8$ in Fig. 3.178 is similar to the one of $ZAl\,2_8$. Also here the dark, grey colour dominates, but it is speckled with white spots of corrosion products. The higher alloyed sample $ZTi\,5_8$ (5.5 at.% Ti) shown in Fig. 3.179 is still grey, but already much more covered by white corrosion products. In contrast, coating $ZTi\,9_8$ alloyed with 9.4 at.% titanium looks different. The centre of the sample is very smooth and only at very localised spots corrosion products appear. The outer areas of the samples instead show a strong attack of red rust, which occurred in the period between test stop and the moment of taking the photograph. The highest alloyed sample $ZTi\,10_8$ looks completely different. Its grey marbled surface is entirely smooth. Only very few spots of corrosion products are observed.

As a summary one can state that almost all sputtered coatings perform as well or much better than the reference coatings. The measurements showed that the normalised lifetime is influenced by the deposition temperature and the resulting morphology. All specimens deposited at a substrate temperature of $+8\,$°C have longer lifetimes than those samples deposited in the same batch at a floating substrate temperature T_{float}. Furthermore, a significant improvement of the corrosion performance is achieved upon alloying. In particular with the zinc chromium and zinc titanium films the time to red rust was prolongated by up to eleven times with reference to the EZ coating. In contrast to other coatings for these films the volume of occurring corrosion products was reduced and the samples maintained their metallic appearance. These results show that the zinc alloy coated steel sheets could also be used in applications where unpainted steel sheets are required.

3.5.2.2 Cyclic Corrosion Test VDA 621–415

The VDA 621–415 test is a widely accepted corrosion test in the automotive industry. The obtained paint creep values allow a comparison of the cathodic protection capabilities of coatings. Figures 3.182 and 3.183 show the painted and VDA tested samples EZ and a zinc iron coatings ZFe 13_VDA after two weeks of testing. Table 3.33 gives the values for the spread of blistering for the different coatings after two and ten weeks of testing.

Sample	titanium interlayer [nm]	thickness [µm]	rust type	spread after 2 weeks [mm]	spread after 10 weeks [mm]
EZ	-	8	WR	0.5–0.9	2
ZFe 13_VDA1	8	5.0	RR	0.5–0.9	3
ZFe 13_VDA2	8	6.5	RR	< 0.5	2
ZFe 13_VDA3	8	8.0	RR	< 0.5	1.5

Table 3.33: Spread of blistering by VDA 621–415 testing of painted, zinc or zinc iron coated steel sheets

It can be seen that the sputtered zinc iron coating ZFe 13_VDA1 with a coating thickness of $5\,\mu$m has an inferior corrosion protection than the $8\,\mu$m thick electrogalvanised reference coating. After ten weeks it shows 50 % more blistering than the reference EZ. However with a coating thickness of $6.5\,\mu$m the sputtered coating ZFe 13_VDA2 reaches the performance of EZ. At the same coating thickness sample ZFe 13_VDA3 is even superior as it shows 25 % less spread. The good protection of ZnFe alloy coatings against paint creep observed within this study was also reported by Amirudin et al. [283].

A fact which is disadvantageous with the zinc iron coatings is the occurrence of red rust within the scratches. The red rust stems from the iron content of the coating itself and not from the underlying steel
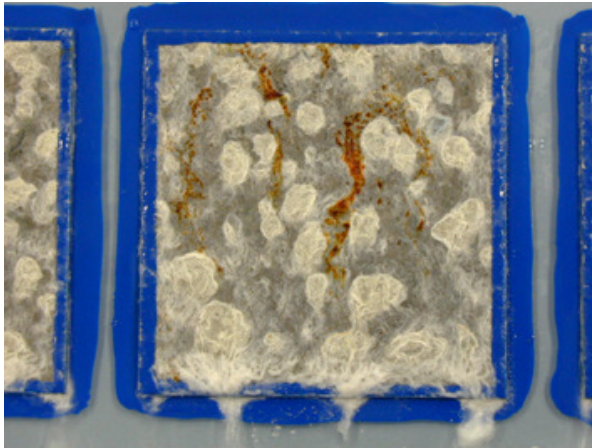
Figure 3.166: Electrodeposited EZ coating after 109 h SST

Figure 3.167: Sputtered zinc coating ZC_8 after 62 h SST

Figure 3.168: Thin sputtered ZB_8 zinc coating after 9 h SST

Figure 3.169: Sputtered zinc aluminium coating $ZAl2_8$ (+2.6 at.% Al) after 446.5 h SST
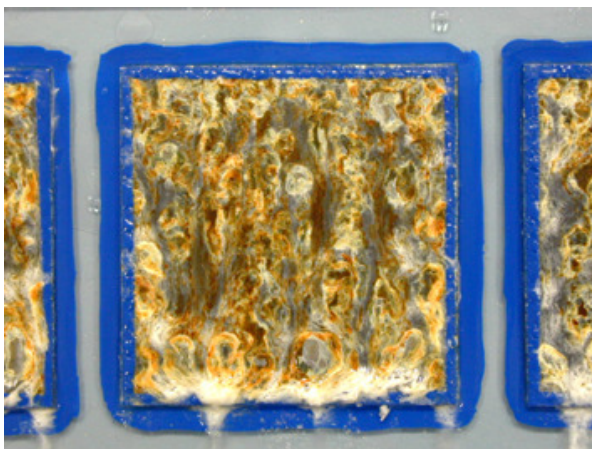
Figure 3.170: Galvaneal coating after 85.5 h SST
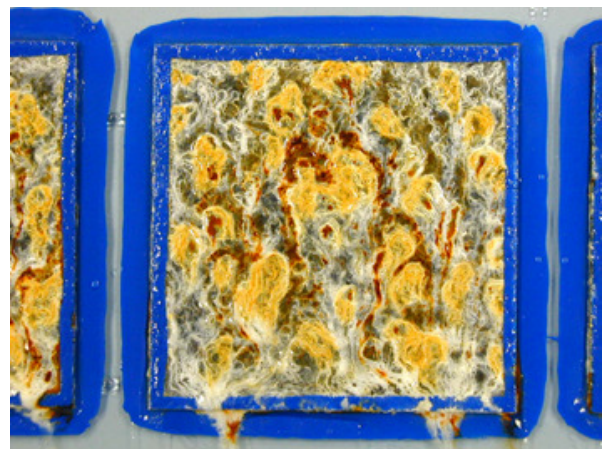
Figure 3.171: Sputtered zinc iron coating $ZFe3_8$ (+3.3 at.% Fe) after 72 h SST
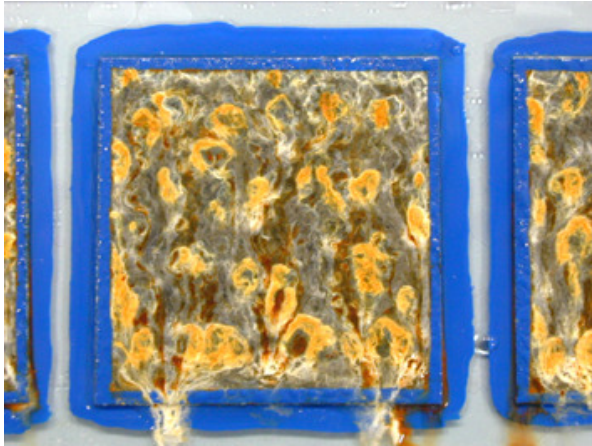
Figure 3.172: Sputtered zinc iron coating ZFe 7_8 (+6.5 at.% Fe) after 85. h SST
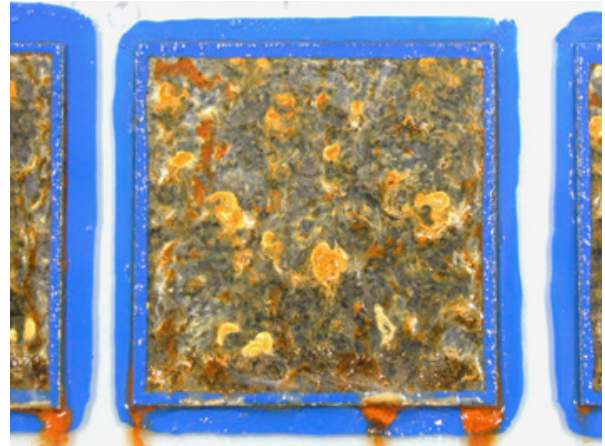
Figure 3.173: Sputtered zinc iron coating ZFe 13_8 (+13.6 at.% Fe) after 109 h SST
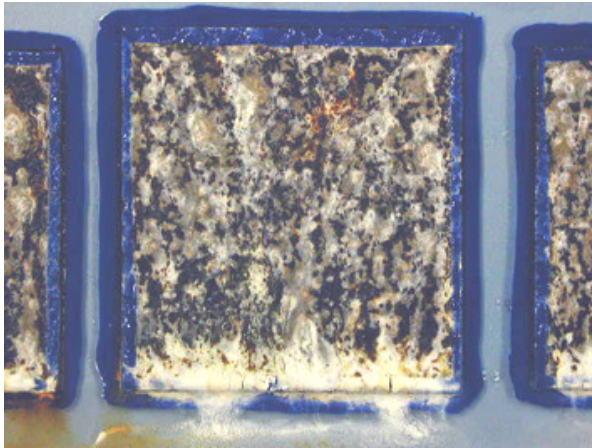
Figure 3.174: Sputtered zinc magnesium coating ZMg 2_8 (+2.1 at.% Mg) after 480 h SST
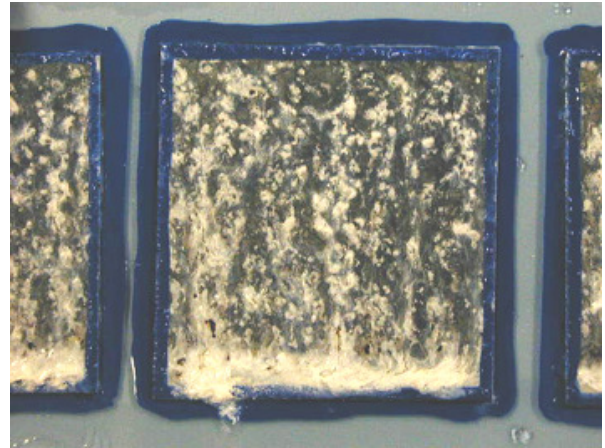
Figure 3.175: Sputtered zinc magnesium coating ZMg 15_8 (+13.9 at.% Mg) after 480 h SST

Figure 3.176: Sputtered zinc chromium coating ZCr 3_8 (+3.1 at.% Cr) after 480 h SST
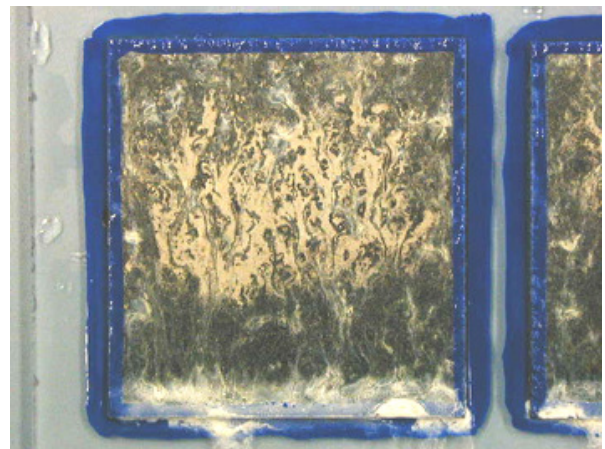
Figure 3.177: Sputtered zinc chromium coating ZCr 11_8 (+12.8 at.% Cr) after 480 h SST

Figure 3.178: Sputtered zinc titanium coating ZTi1_8 (+1.7 at.% Ti) after 119 h SST
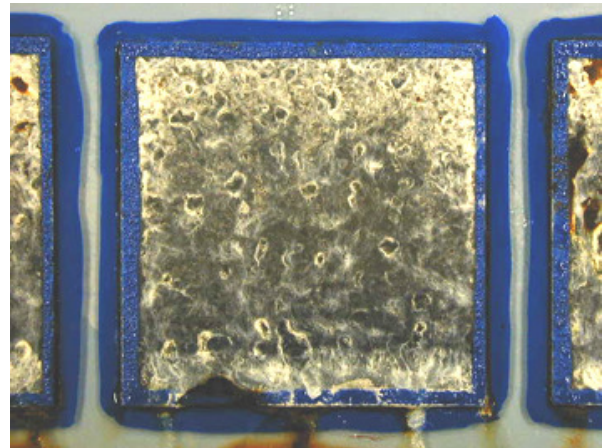
Figure 3.179: Sputtered zinc titanium coating ZTi5_8 (+5.5 at.% Ti) after 446 h SST

Figure 3.180: Sputtered zinc titanium coating ZTi9_8 (+9.4 at.% Ti) after 480 h SST
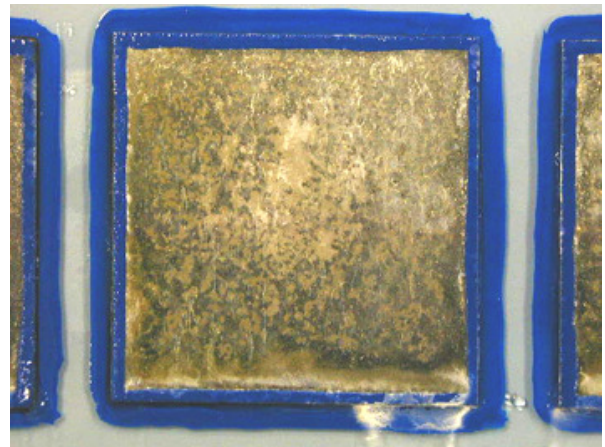
Figure 3.181: Sputtered zinc titanium coating ZTi10_8 (+11.1 at.% Ti) after 480 h SST
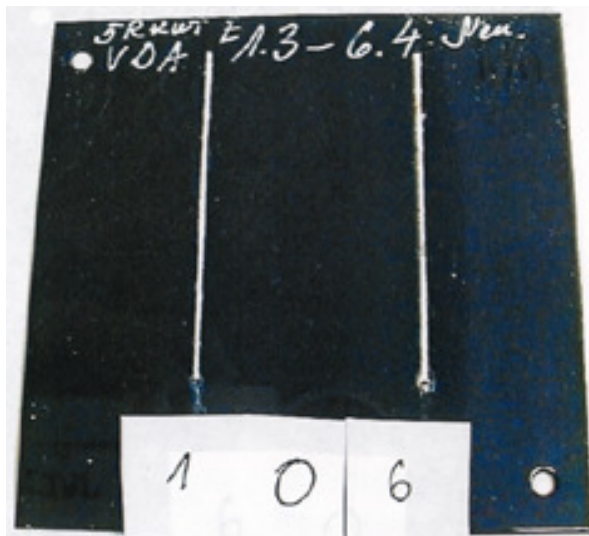
Figure 3.182: VDA tested EZ reference
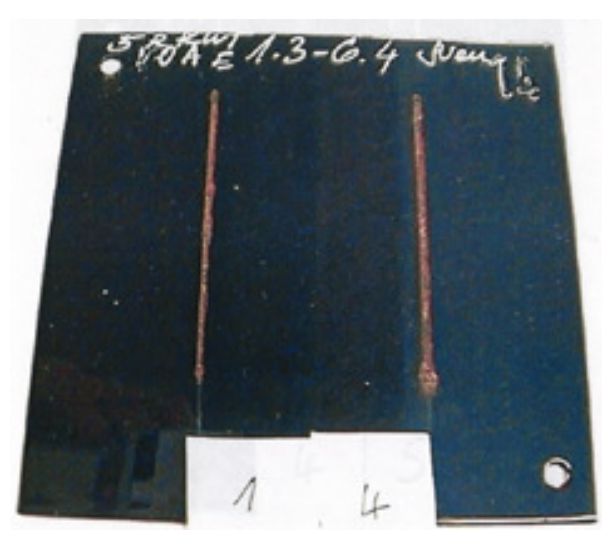
Figure 3.183: VDA tested ZFe 13_VDA3 coating

substrate. Since the automobile customer recognises red rust much easier than the white rust, that occurs with pure zinc coatings, this cosmetic effect might result in a lower acceptance of the iron containing coatings by the customers and therefore also by the car manufacturers.

3.5.2.3   Influence of the grain size and morphology on normalised lifetimes

The corrosion protection of steel by coating with zinc is based on the sacrificial anodic dissolution of the coating. As corrosion generally depends on the surface area exposed to the attacking solution and the porosity/morphology of the coatings, it is tried to verify whether the different corrosion performances can at least partly be explained by differences in grainsize and/or porosity/morphology.

Figure 3.184 which plots the normalised lifetimes of the coatings versus their grainsizes however indicates that no clear correlation between these parameters can be observed. The graph rather shows that the normalised lifetimes can be categorised by the various alloys.
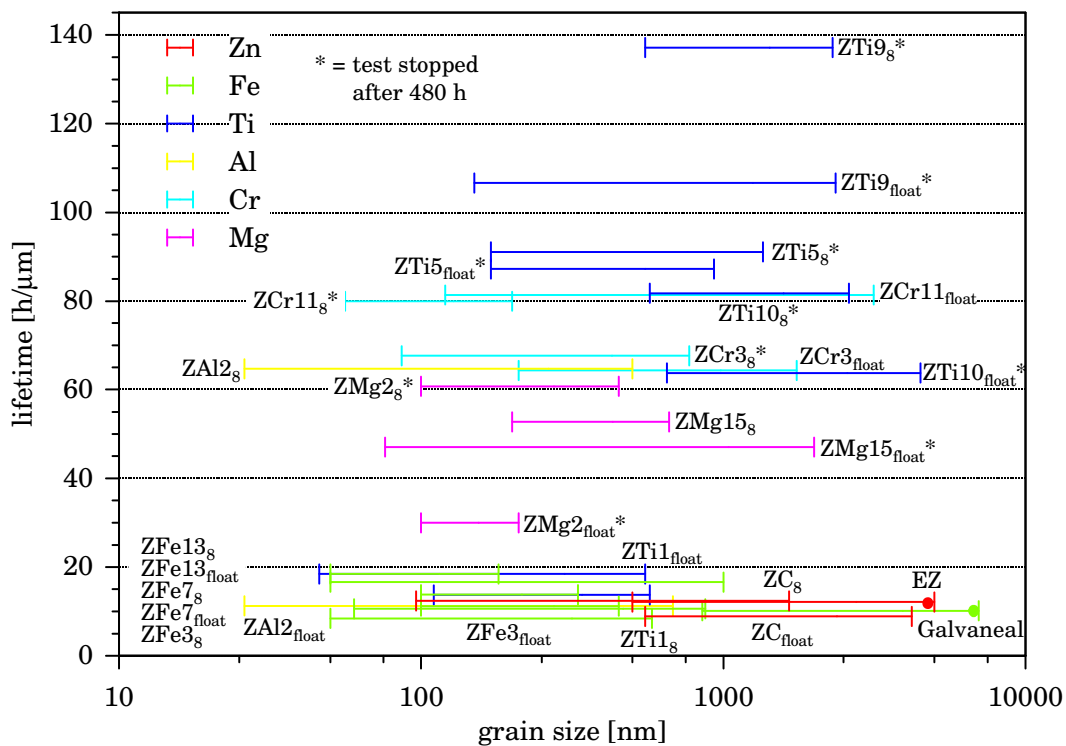
Figure 3.184: Lifetime of the coatings versus grainsize. Samples, for which the salt spray test has been stopped after 480 h, are marked with a star *.

Figure 3.185 instead plots the normalised lifetimes of the coatings versus their porosity/morphology classes. Since the porosities can not be measured quantitatively due to the lack of an appropriate measuring instrument, the majority of the coatings has been split according to their porosities/morphologies into six significant classes, each of them representing a specific type of porosity/morphology observed by SEM analysis. Coatings which could not be classified relatively clearly were omitted as the assumption should be proven in general in a first step. However, apart from classes three and four which themselves are rather consistent in lifetime all other classes show a strong scattering in lifetimes within the respective classes. Also this fact indicates that the normalised lifetime is rather influenced by the type of alloying than by the different porosities/morphologies of the coatings.

Summarising, the findings have shown that the by far most important factor influencing the corrosion performance is the alloy composition and the corrosion products created thereof. The effects of porosity and grain size on coating lifetimes can not be observed as clearly. However, when comparing them, it seems that porosity plays a more important role than grain size.

The following subsection therefore tries to find out whether the different corrosion protection properties can be attributed to the different corrosion products created.

porosity classes representing a specific type of porosity / morphology observed by SEM analysis	samples	example given
class 1	ZTi 1_8, ZMg 2_{float}	ZMg 2_{float}, Mag: 20k
class 2	ZC$_{float}$, ZTi 9_{float}, ZMg 15_{float}	ZTi 9_{float}, Mag: 10k
class 3	samples	example given
class 4	ZTi 5_{float}, ZTi 5_8	ZTi 5_{float}, Mag: 20k
class 5	ZFe 3_8, ZFe 7_8, ZCr 3_8, ZCr 11_8, ZMg 2_8	ZFe 7_8, Mag: 20k
class 6	ZTi 9_8, ZTi 10_{float}, ZTi 10_8	ZTi 10_{float} Mag 10k
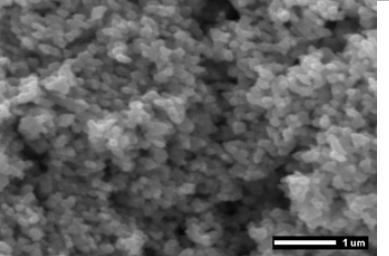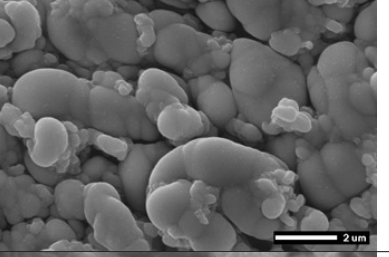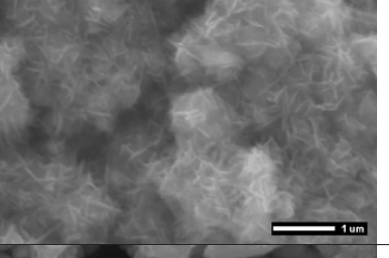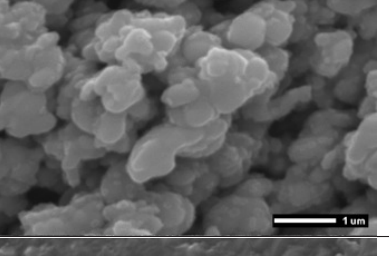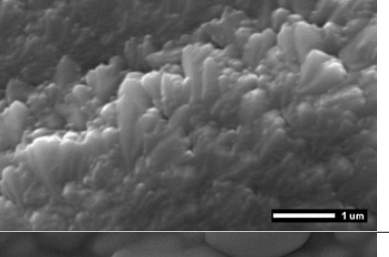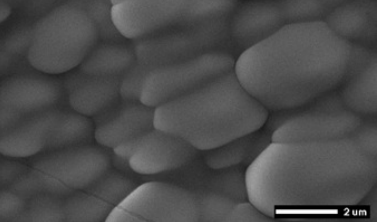
Table 3.34: Porosity classes of the coatings classified according to their appearance in the SEM
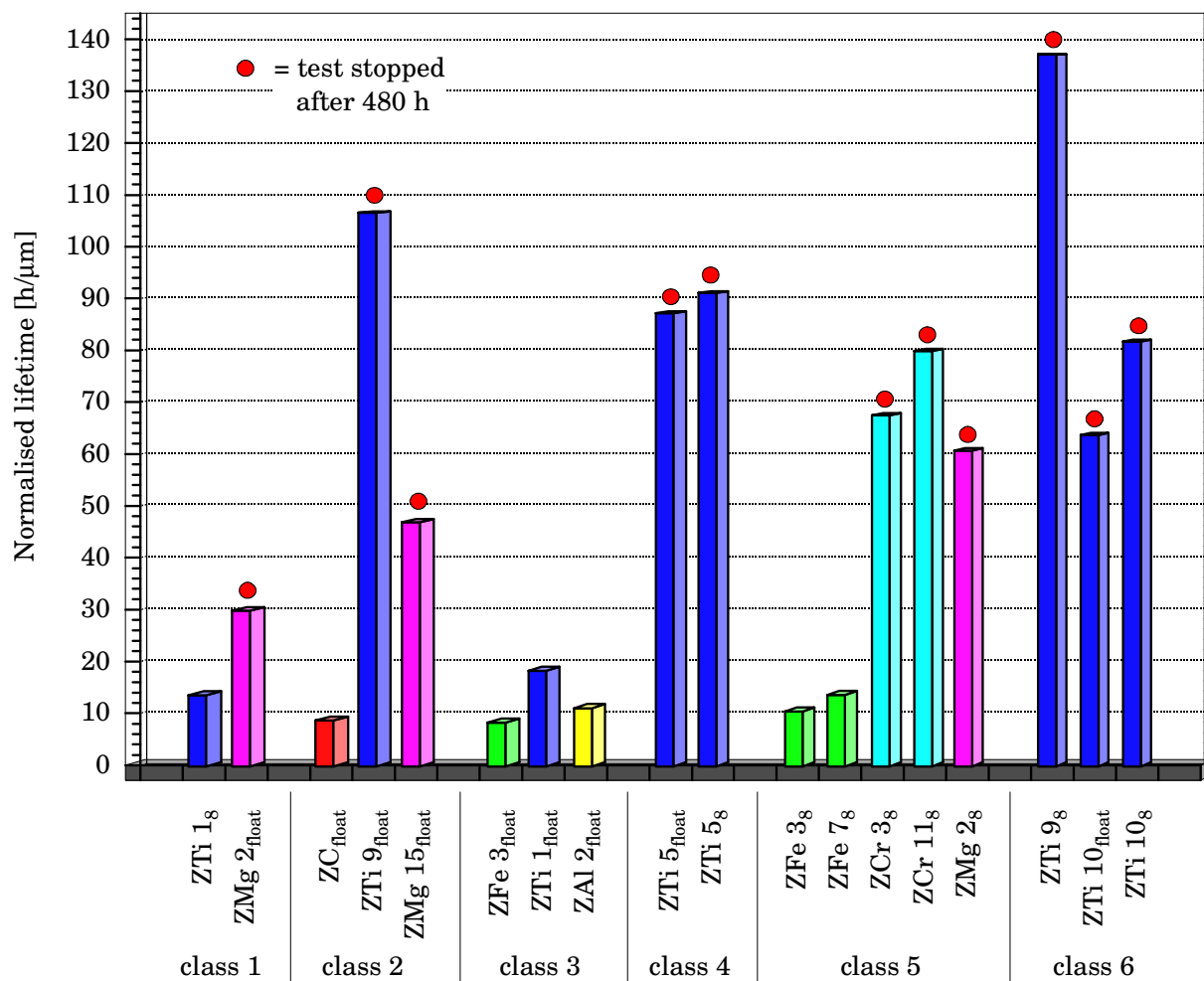
Figure 3.185: Lifetime of the coatings versus porosity. Samples, for which the salt spray test has been stopped after 480 h, are marked with a dot •.

3.5.2.4 Discussion of Corrosion Products Created by Accelerated Testing

The stability of a metal or alloy, exposed to specific, aggressive media, depends on the protective properties of the formed surface layer of corrosion products, separating the metal or alloy from the environment. The chemical composition, conductivity, adherence, solubility, hygroscopicity and morphological characteristics of the surface film determine its dissolution rate and its capacity to act as a controlling barrier [278, 284, 285]. The created corrosion products in turn depend on the attacking solution [17], its pH value, the temperature, the atmosphere (e.g. CO_2 content) [143] and the pattern of wet and dry exposure [14].

Section 3.5.2.1 has shown that the grown corrosion products exhibit macroscopically different types of surface morphologies. Figures 3.186 to 3.191 show now some microscopic views of the obtained surfaces.

To determine the composition of the created corrosion products the salt spray tested samples have been examined by x-ray diffraction. The corresponding XRD patterns are given in Fig. 3.192 to 3.198. According to the XRD patterns the corrosion products consist of the zinc compounds given in Tab. 3.35 which are reported also by [286–288]. The XRD patterns of the pure zinc coatings EZ and ZC_8 show that both coatings are consumed completely. No zinc phase is visible anymore. Also the Galvaneal coating is consumed completely whereas the simulated SHexZFe3 phase is still present with the $ZFe\,13_8$ coating. The "amorphous" halo of the zinc titanium coating $ZTi\,10_8$ disappeared, indicating the complete loss of this coating. In contrast, sample $ZCr\,11_8$ is only slightly consumed. Here even the [002] peak at 36°, originating from the Cu-K_b radiation, is still present. With the zinc magnesium sample $ZMg\,15_8$ the intermetallic zinc magnesium phases disappeared while the pure zinc phase still remains.
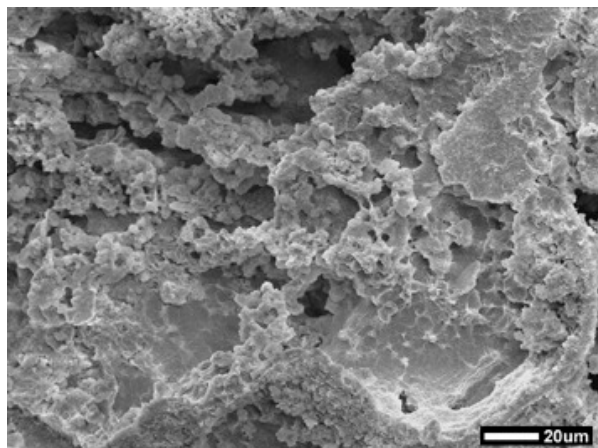
Figure 3.186: SEM image of the corroded EZ coating
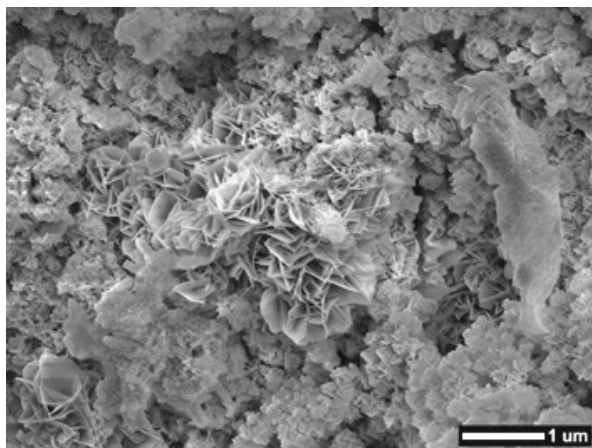
Figure 3.187: SEM image of the corroded Galvaneal coating with Simonkolleite crystals
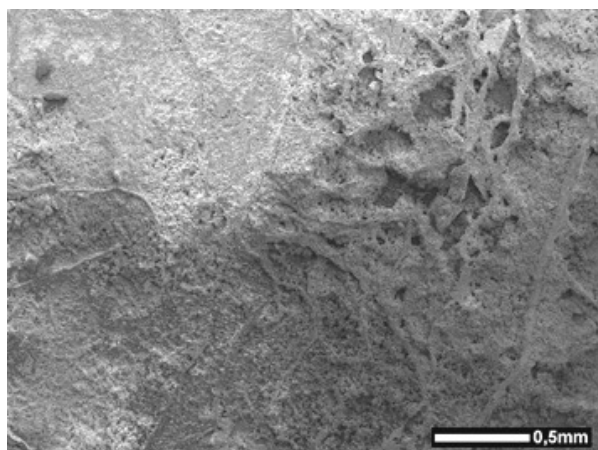
Figure 3.188: SEM image of the corroded zinc iron coating ZFe 13_8
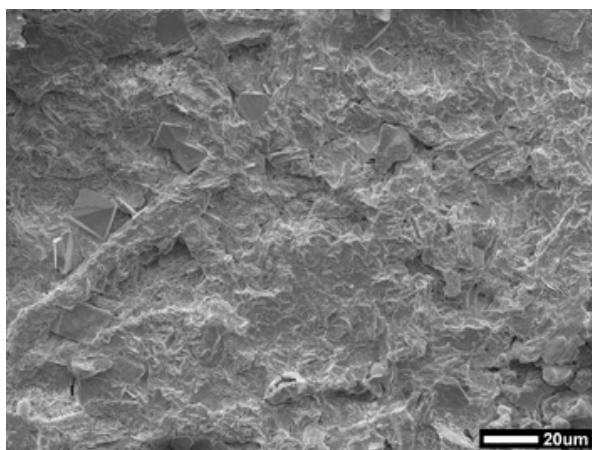
Figure 3.189: SEM image of the corroded zinc chromium coating ZCr 11_8
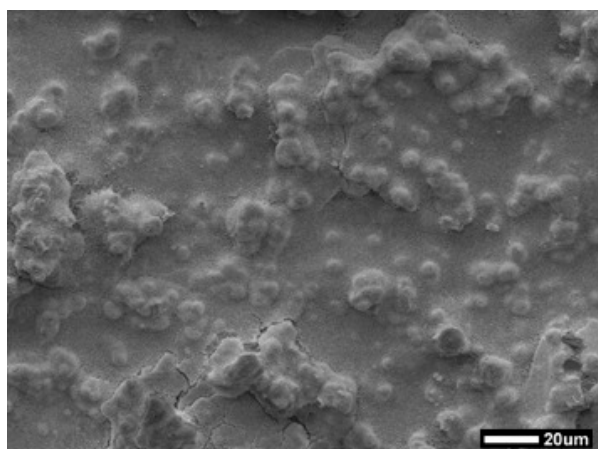
Figure 3.190: SEM image of the corroded zinc aluminium coating ZAl 2_8
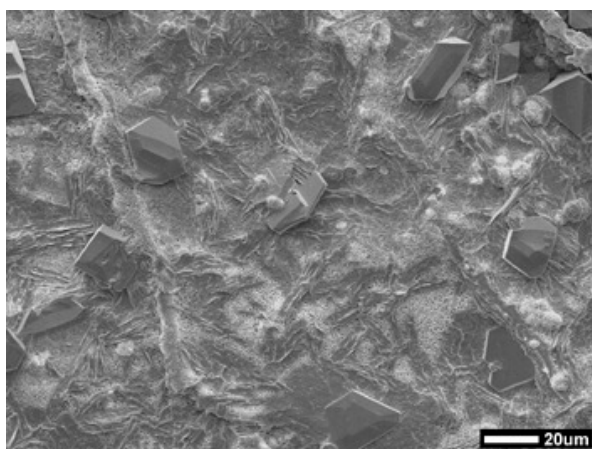
Figure 3.191: SEM image of the corroded zinc magnesium coating ZMg 15_8
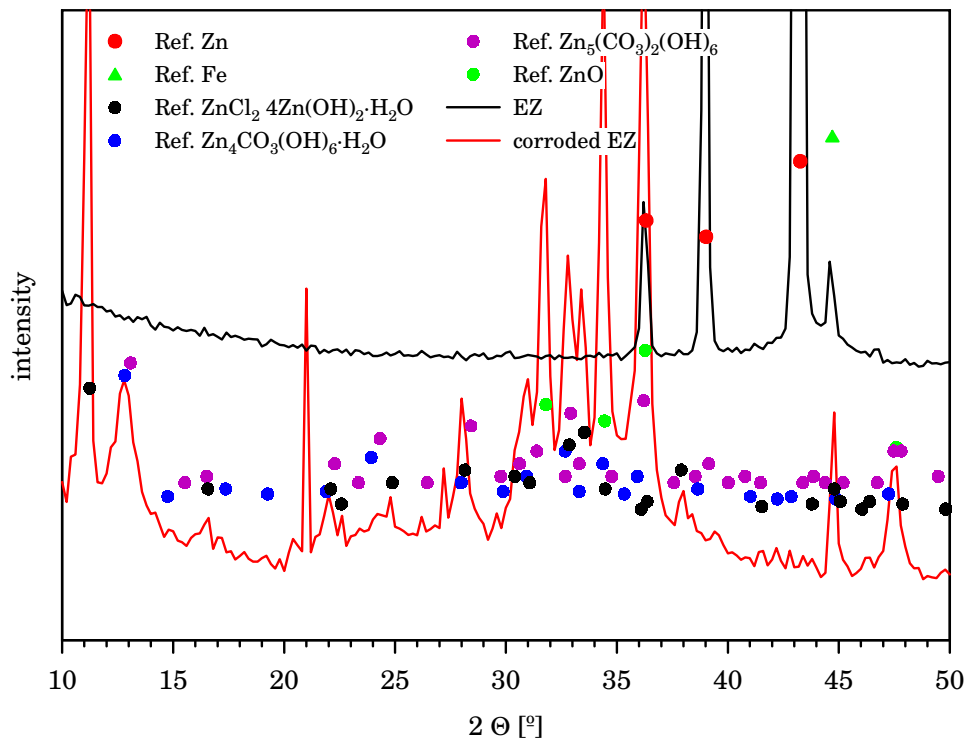
Figure 3.192: XRD pattern of electrogalvanised EZ coating after 62 h salt spray test
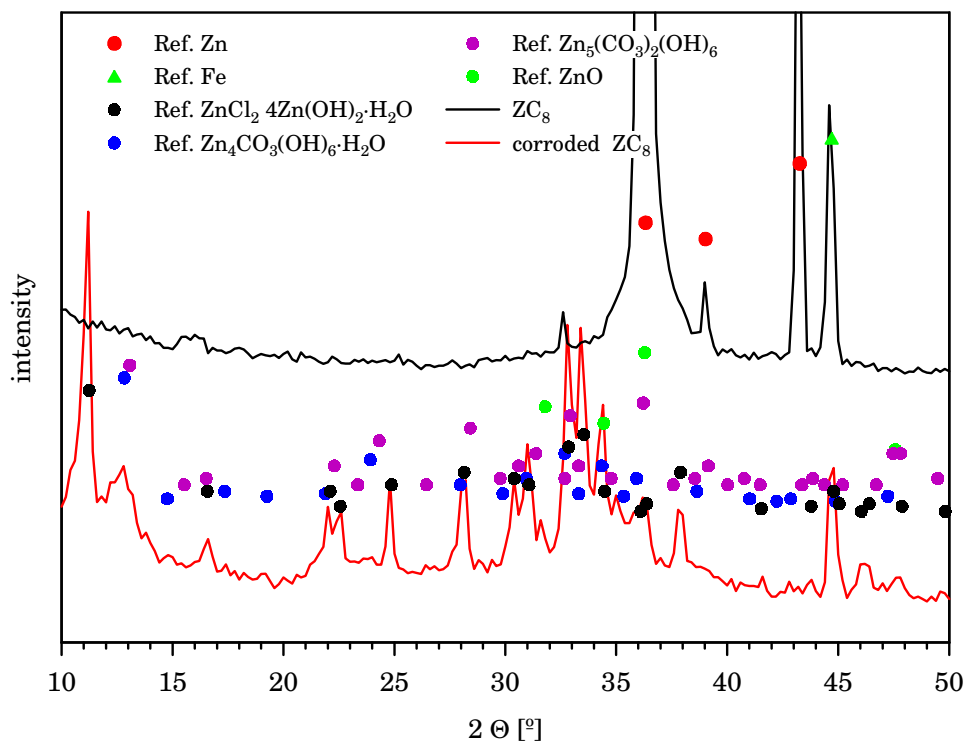
Figure 3.193: XRD pattern of coating ZC$_8$ after 62 h salt spray test
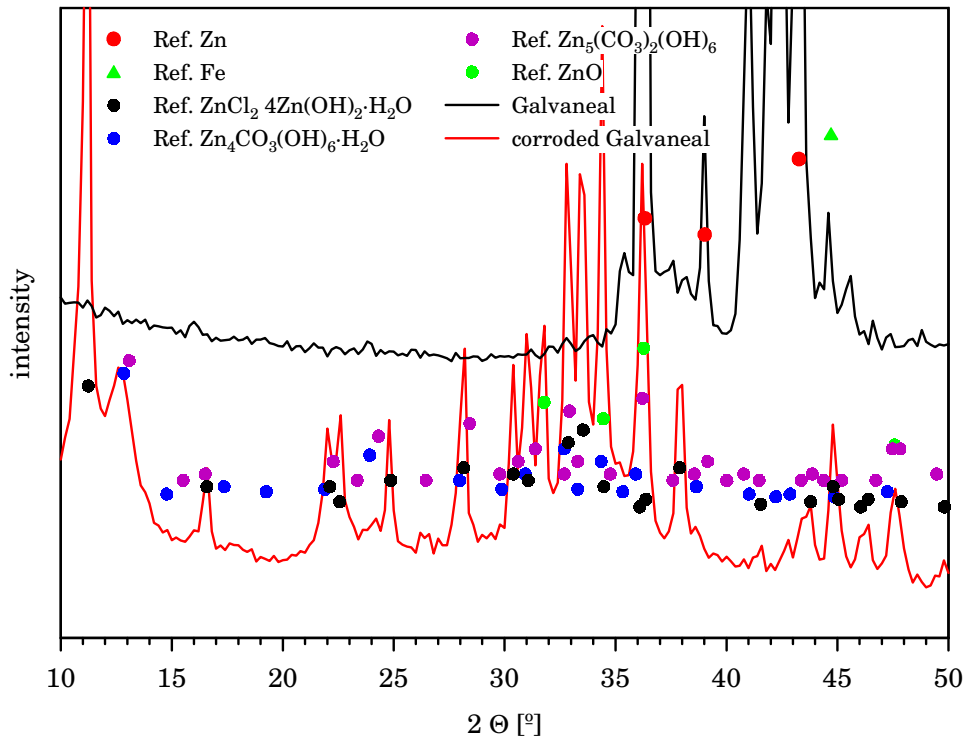
Figure 3.194: XRD pattern of Galvaneal coating after 85.5 h salt spray test
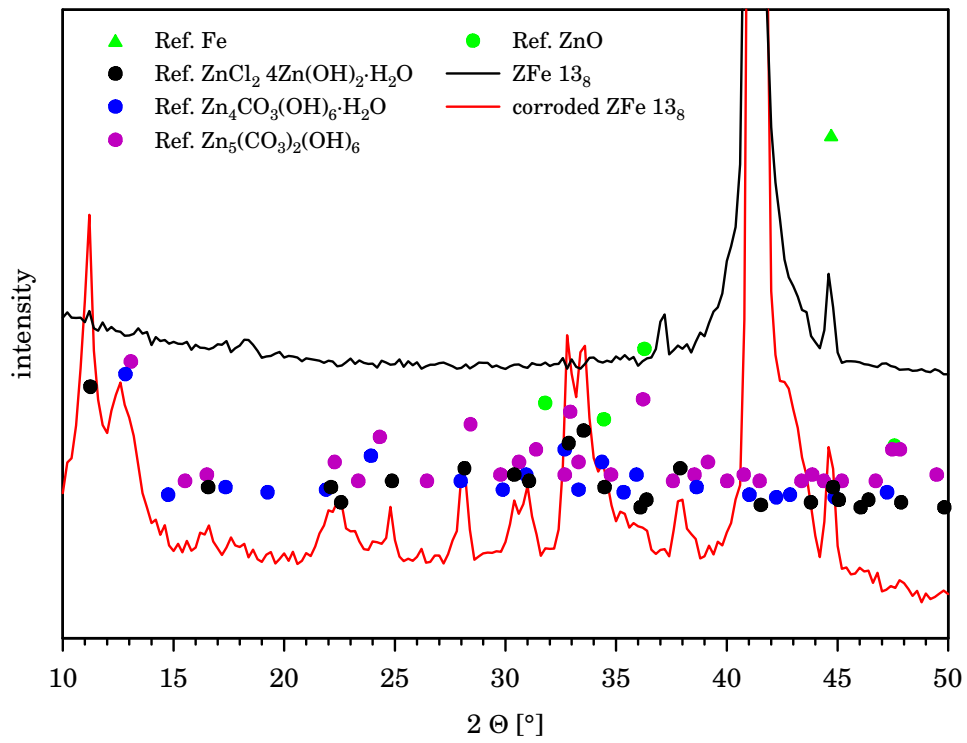
Figure 3.195: XRD pattern of coating ZFe 13$_8$ after 108 h salt spray test
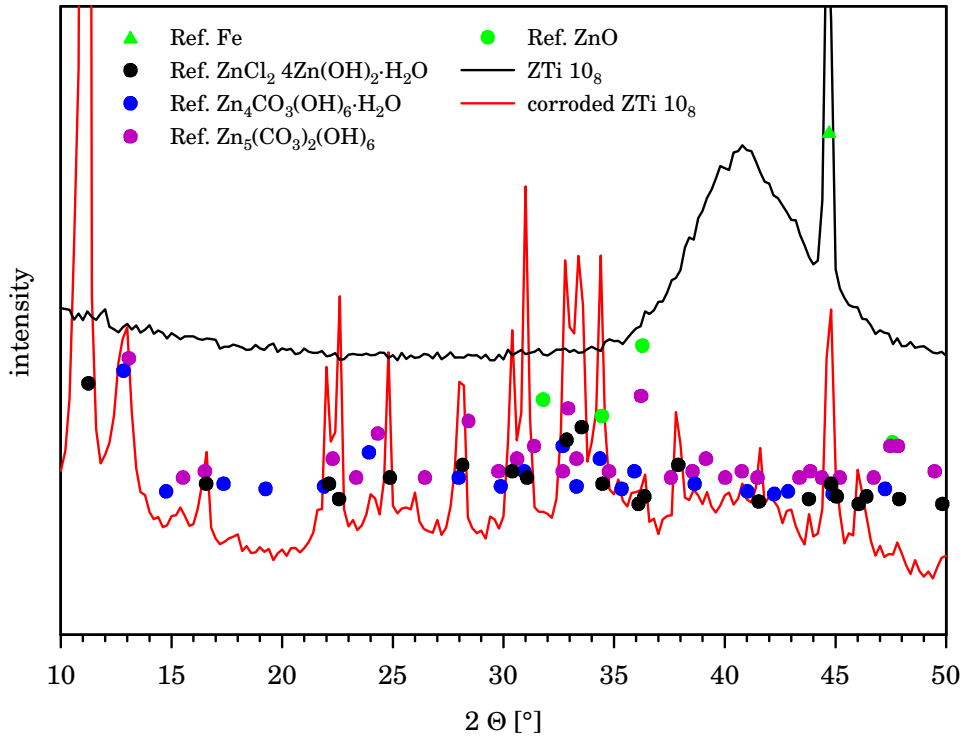
Figure 3.196: XRD pattern of coating ZTi 10_8 after 480 h salt spray test
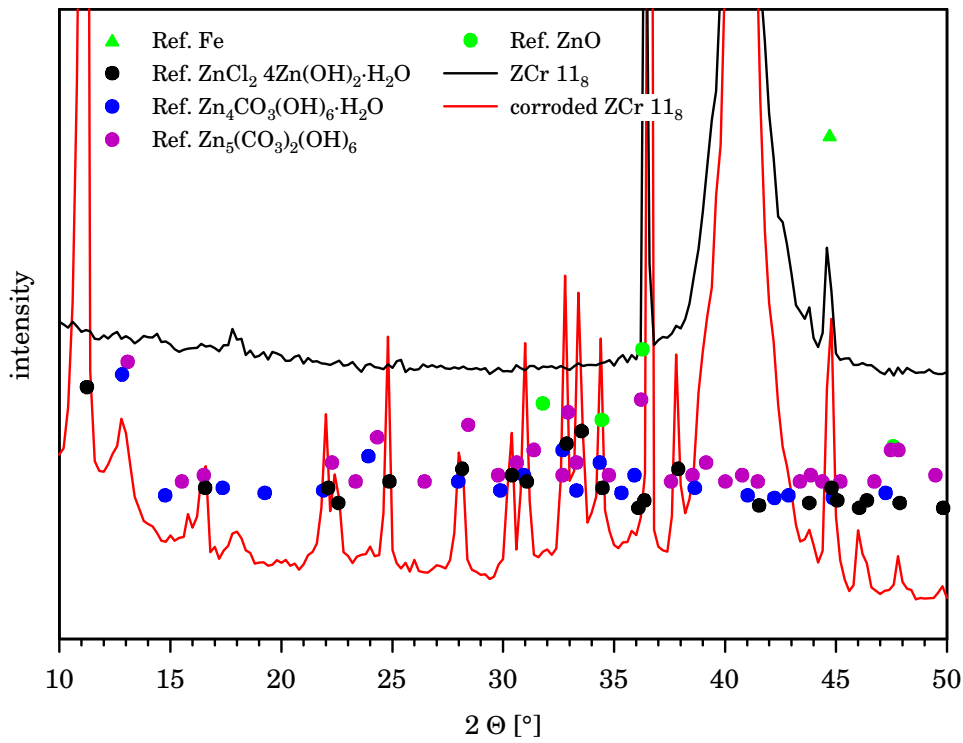
Figure 3.197: XRD pattern of coating ZCr 2_8 after 480 h salt spray test
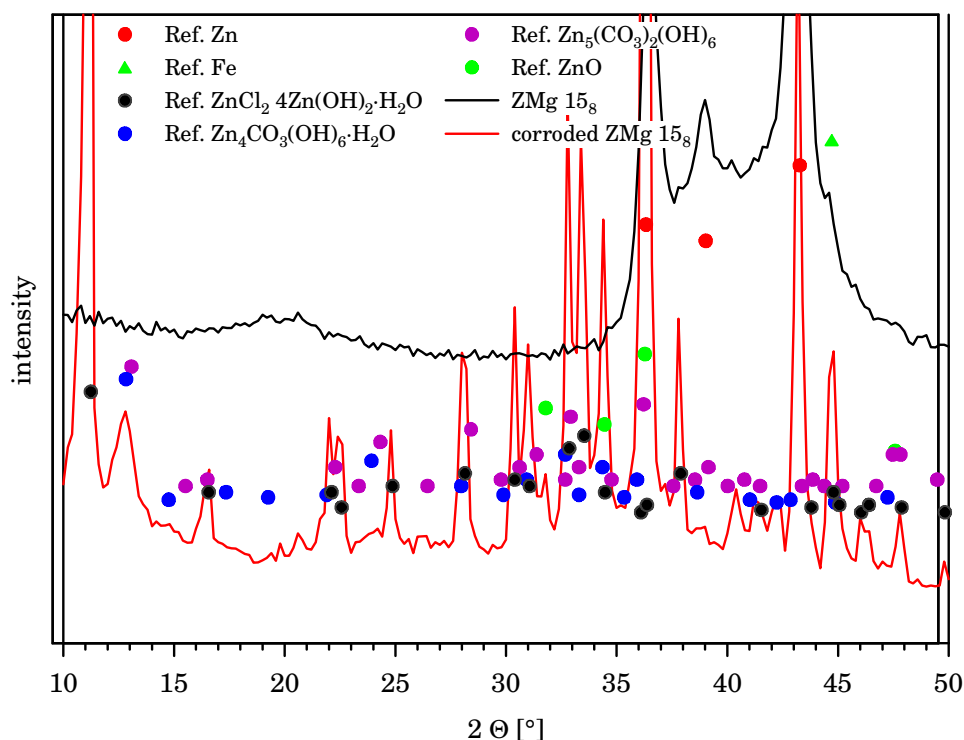
Figure 3.198: XRD pattern of coating $ZMg\,15_8$ after $480\,h$ salt spray test

name	chemical name	formula	identification peak
Simonkolleite	zinc chloride hydroxide hydrate	$ZnCl_2 \cdot 4Zn(OH)_2 \cdot H_2O$	11.2
-	zinc carbonate hydroxide hydrate	$Zn_4CO_3(OH)_6 \cdot H_2O$	12.8
Hydrozincite	zinc carbonate hydroxide	$Zn_5(CO_3)_2(OH)_6$	13.0
Zincite	zinc oxide	ZnO	31.8

Table 3.35: Corrosion products occurring with salt spray tested samples

The XRD patterns show that the different coating compositions seem to have no influence on the general composition of formed corrosion products. All samples show the occurrence of the same zinc compounds. Only the relative fractions of the various compounds in the overall corrosion layers are different.

To evaluate the fractions of the different compounds in the corrosion layers the XRD peak ratios of Simonkolleite/Zincite, basic zinc carbonate hydroxide/Zincite and Simonkolleite/basic zinc carbonate hydroxide have been calculated respectively and can be seen in Tab. 3.36. For the calculations the following XRD peaks have been used: Simonkolleite [003], 2Θ at $11.2\,°$, Zincite [100], 2Θ at $31.8\,°$, and basic zinc carbonate hydroxide, 2Θ at 12.8–$13.0\,°$. Table 3.36 shows that alloying of zinc with Fe,

Sample	EZ	ZC_8	Galvaneal	$ZFe\,13_8$	$ZTi\,10_8$	$ZCr\,2_8$	$ZMg\,15_8$
Simonkolleite / Zincite	1.7	4.2	3.2	2.6	23.7	18.3	8.7
basic zinc carbonate hydroxide / Zincite	0.6	1.7	0.8	1.6	2.5	2.5	1.4
Simonkolleite / basic zinc carbonate hydroxide	3.0	2.4	3.8	1.7	9.5	7.2	6.4

Table 3.36: XRD peak ratios of the different corrosion products

Ti, Cr and Mg increases the Simonkolleite/Zincite XRD peak ratio as well as the basic zinc carbonate hydroxide/Zincite XRD peak ratio, indicating an increase of the zinc hydroxide fraction in the corrosion

products. Similar results have been obtained by Kawafuku et al. [289] and Fukui et al. [290].

By plotting the Simonkolleite/Zincite and basic zinc carbonate hydroxide/Zincite XRD peak ratios versus the normalised lifetimes of the coatings a correlation between the created corrosion products, their corrosion protection and the resulting lifetime of the coatings can be found. Coatings with higher Simonkolleite and basic zinc carbonate hydroxide fractions afford better corrosion protection, thus resulting in longer lifetimes.
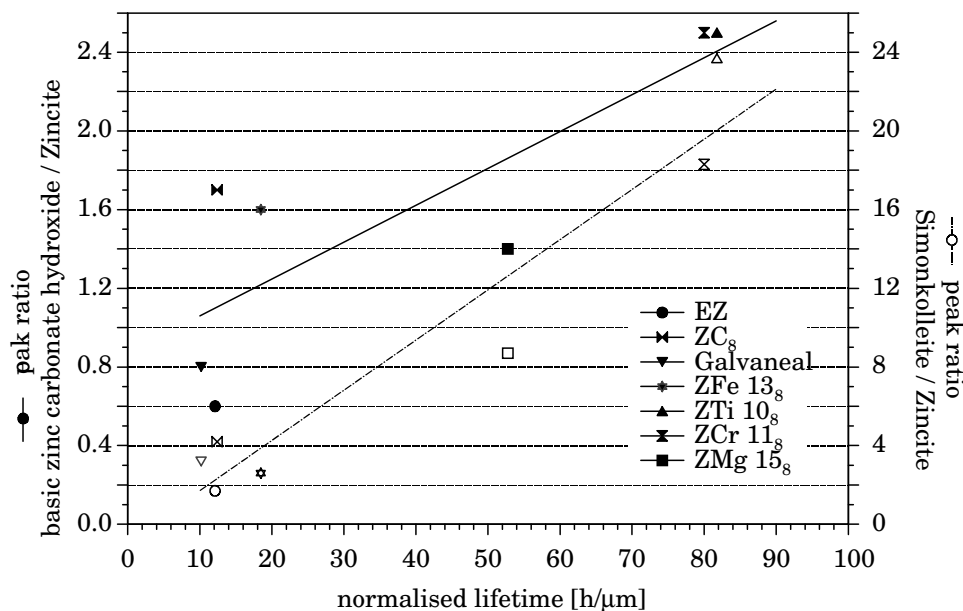
Figure 3.199: Relation between normalised lifetime and Simonkolleite/Zincite and basic zinc carbonate hydroxide/Zincite peak ratio respectively

An improved corrosion resistance of alloyed zinc coatings with $Zn(OH)_2$ rich corrosion products on the coating surface has been also reported by Okada et al., Maeda et al. and Wilcox et al. [76, 285, 291]. These authors attributed the improved corrosion resistance to the decreased electric conductivity of the hydroxides. In contrast to crystalline zinc oxide which is a n-type semiconductor with hexagonal Wurzite structure and a band gap of about 3.2 eV [292] the isolating zinc hydroxides retard oxygen reduction and lower the corrosion rate. The n-type conductivity of zinc oxide arises from the excess of Zn in the non-stoichiometric compound $Zn_{1+\delta}$ O with $\delta > 0$ [293]. Since zinc hydroxide dehydrates gradually to ZnO during outdoor exposure there is a need to retard this transformation in order to improve the corrosion protection. This can be achieved by alloying zinc with Al, Mg, Ni, Co and Cr as these elements stabilise zinc hydroxide and thus slow down the change [291].

Another explanation for the good corrosion protection of alloyed zinc coatings due to the growing zinc hydroxide rich corrosion products was given by Kautek et al. [294]. This group investigated the effects of transition metals on the corrosion protection of electroplated zinc alloy coatings. Their finding was that a partial coverage of the coatings with zinc hydroxide in neutral and weak alkaline environments limits the electrochemical dissolution. The alloyed d-metals added to this hydroxide film formation and obviously stabilised it, as they segregated into the hydroxide layers. To explain the corrosion inhibiting function of the d-metal components qualitatively, the authors proposed a dopant-vacancy interaction model. According to this model the corrosion current is reduced when the charge carriers, i.e. mobile, negatively charged Zn cation vacancies, are eliminated. This is achieved by the combination of vacancies with the segregated alloy elements, thereby forming immobile ion pairs. The model predicts good corrosion protection when the d-metals are strongly segregated, immobile and homogeneously distributed in the passive layer.

The most important factor improving the corrosion resistance of the alloyed zinc coatings within the salt spray test of this study seems to be the increased fraction of Simonkolleite within the corrosion products of these samples. Simonkolleite is generated by exposure of the corroding surface to atmospheric CO_2 and the subsequent conversion of soluble chloride (NaCl) to Simonkolleite.

The very first stage of Zn exposure in any humid environment results in the instant growth of an oxide and/or hydroxide film, which forms the basis of further growth of corrosion products. Equilibrium with carbon dioxide CO_2, with an atmospheric global average concentration of approximately 350 ppm [143], leads to the formation of hydrozincite $Zn_5(CO_3)_2(OH)_6$. If chloride or sulfate ions are present on the surface, it is possible to form zinc-hydrochlorides or -hydrosulfates with a different number of water molecules.

The corrosion of zinc in absence of atmospheric CO_2 but in presence of NaCl, the latter one increasing the conductivity of the electrolyte, leads to a heavy pitting of the metal. The localised nature of the corrosion strongly suggests that electrochemical corrosion elements with well separated anodic and cathodic areas are active on the surface. The anodic dissolution of zinc (Eq. 3.10) on a small fraction of the surface, results in the development of a small number of deep pits. This reaction is balanced by the oxygen reduction (Eq. 3.11) in the cathodic areas which are given by semiconducting ZnO [295].

$$Zn \quad \rightarrow \quad Zn^{2+}_{(aq)} + 2e^-_{(s)} \tag{3.10}$$

$$1/2\,O_2 + H_2O + 2e^- \quad \rightarrow \quad 2(OH)^-_{(aq)} \tag{3.11}$$
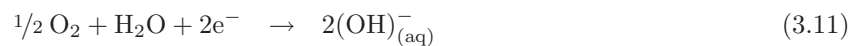
With the reaction going on, cations e.g. $Na^+_{(aq)}$, $Zn^{2+}_{(aq)}$ will migrate towards the cathodic areas while anions, e.g. $Cl^-_{(aq)}$ will move towards the zinc dissolution sites. The dissolution of $Zn^{2+}_{(aq)}$ ions give rise to a relatively low pH in the anodic region, whereas the accumulation of $Na^+_{(aq)}$ due to migration supports high pH in the cathodic areas. The corrosion cells established result in potential-, concentration- and notably pH gradients on the surface. According to Feitknecht [16], who also published the stability diagram given in Fig. 3.200, insoluble Simonkolleite, $ZnCl_2 \cdot 4Zn(0H)_2 \cdot H_2O$ precipitates when a solution containing zinc and chloride ions is neutralised according to Eq. 3.12. Other reactions of zincite and chloride resulting in simonkolleite with and without release of hydroxide are given in Eq. 3.13 and 3.14 [143, 296].

$$5Zn^{2+}_{(aq)} + 5H_2O + 8OH^-_{(aq)} + 2Cl^-_{(aq)} \quad \rightarrow \quad ZnCl_2 \cdot 4Zn(OH)_2 \cdot H_2O_{(s)} \tag{3.12}$$

$$5ZnO_{(s)} + 2Cl^-_{(aq)} + 6H_2O \quad \rightarrow \quad ZnCl_2 \cdot 4Zn(OH)_2 \cdot H_2O_{(s)} + OH^-_{(aq)} \tag{3.13}$$

$$4ZnO_{(s)} + Zn^{2+}_{(aq)} + 5H_2O + 2Cl^-_{(aq)} \quad \rightarrow \quad ZnCl_2 \cdot 4Zn(OH)_2 \cdot H_2O_{(s)} \tag{3.14}$$
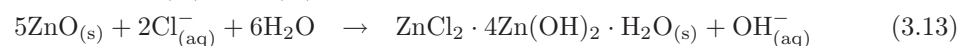
The stability diagram published by Feitknecht [16] shows that Simonkolleite is stable at intermediate
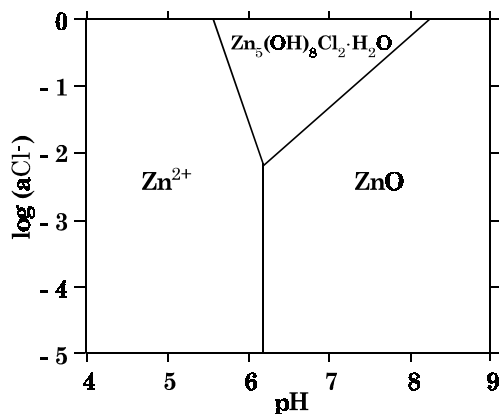
Figure 3.200: Stability diagram, $[Zn^{2+}] = 0.1\,M$ according to [16]

pH and relatively high chloride activities. In the cathodic areas where chloride activities are low and pH high, ZnO, tends to form. Simonkolleite is therefore expected to precipitate in the immediate vicinity to

the anodic sites. The higher the chloride activities, the more easily simonkolleite forms. Moving from the anode towards the cathode, the pH increases and Simonkolleite becomes thermodynamically unstable. This leads to the formation of Zincite according to the following reactions [295].

$$ZnCl_2 \cdot 4Zn(OH)_2 \cdot H_2O_{(s)} + 2OH^-_{(aq)} \rightarrow 5ZnO_{(s)} + 6H_2O + 2Cl^-_{(aq)} \tag{3.15}$$

$$Zn^{2+}_{(aq)} + 2OH^-_{(aq)} \rightarrow ZnO_{(s)} + H_2O \tag{3.16}$$
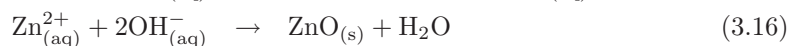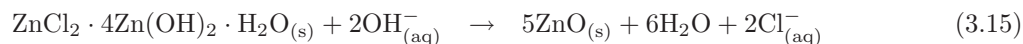
Since pH is expected to be high over much of the surface due to the formation of $OH^-_{(aq)}$ and the presence of $Na^+_{(aq)}$, Zincite is the predominant corrosion product and covers most of the surface.

The presence of approximately 350 ppm CO_2 [143], leads to the formation of hydrozincite $Zn_5(CO_3)_2$-$(OH)_6$. Carbon dioxide changes the effect of NaCl on the corrosion of zinc completely. Also in this environment the presence of NaCl leads to the localised corrosion of zinc, but the corrosion pits are more numerous and shallower, indicating that the corrosion cells are not as well developed as in the CO_2 free environment. As CO_2 dissolves in the surface electrolyte it tends to neutralise the later one by the following reactions [143, 295]:

$$CO_{2\,(aq)} + 2OH^-_{(aq)} \rightarrow CO^{2-}_{3\,(aq)} + H_2O \tag{3.17}$$

$$CO_{2\,(aq)} + CO^{2-}_{3\,(aq)} + H_2O \rightarrow 2HCO^-_{3\,(aq)} \tag{3.18}$$

$$CO_{2\,(aq)} + OH^-_{(aq)} \rightarrow HCO^-_{3\,(aq)} \tag{3.19}$$
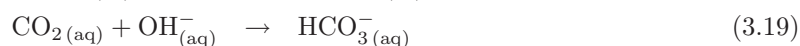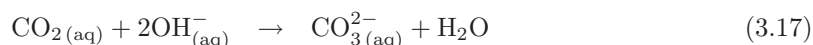
This has several effects [143, 295]:

1. As the pH decreases, the composition of the electrolyte in the cathodic areas changes. The charge of the sodium ions is balanced by carbonate and hydrogen carbonate rather than hydroxide.

2. As the pH decreases all over the surface, Zincite becomes thermodynamically unstable. This leads to the formation of Simonkolleite according to the reverse reactions of Eq. 3.15 and 3.13 and the formation of Hydrozincite according to, e.g.

$$4ZnO_{(s)} + CO_2 + 4H_2O \rightarrow Zn_4CO_3(OH)_6 \cdot H_2O_{(s)} \tag{3.20}$$
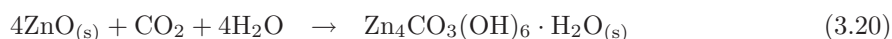
3. As a result of the precipitation of Simonkolleite, most of the chloride solved in the electrolyte is removed.

It may be noted that any acid compound depositing on the surface is expected to have similar effects as CO_2 [295].

The replacement of Zincite by Simonkolleite and Hydrozincite interferes with the cathodic reaction in two ways. First the insoluble products are more compact and therefore unfavourable to oxygen diffusion. Second Simonkolleite and Hydrozincite are excellent insulators. In contrast to the semiconducting Zincite they cannot act as an electrode. Additionally, effects 1 and 3 tend to decrease the conductivity of the surface electrolyte. Combining these effects the presence of carbon dioxide leads to a slow down of zinc corrosion in presence of NaCl by a factor of three to six [143].

The previous discussion on Simonkolleite-, and Hydrozincite formation in presence of carbon dioxide explains the partly different results obtained from the electrochemical corrosion tests and the salt spray tests of this study. The discrepancy that some coatings e.g. EZ perform "obviously" in a contradictory way in both tests can be explained by the different environments in which the corrosion tests have been carried out. The electrochemical tests have been carried out under immersion in saline solutions with limited CO_2 access whereas the accelerated tests have been performed in a salt fog environment in presence of CO_2. Additionally the electrolyte situation is different for both experiments. Local changes in the

composition or pH of the electrolyte as they occur in the small, limited volume of surface electrolyte on a salt sprayed sample, leading to the various corrosion products, do not occur in an immersion experiment. In the latter case these variations are levelled by the big volume of solution the sample is immersed in.

Similar differences between the corrosion rates obtained in salt spray tests and immersion tests in NaCl solutions have been observed by Baldwin et al. [297]. In the experiments of this group pure zinc was found to exhibit higher corrosion rates in the salt fog environment ($387.8 \, \mathrm{mg/dm^2 day}$) than in quiescent NaCl solution ($35.4 \, \mathrm{mg/dm^2 day}$). If the solution of the immersion test was additionally aerated the average corrosion rate of pure zinc obtained approached the value measured in the highly aspirated salt fog environment. In contrast the corrosion rate of the salt spray tested Zn-14 wt.% nickel alloys ($9.7 \, \mathrm{mg/dm^2 day}$) was found to be lower than that obtained under quiescent immersion conditions ($15.8 \, \mathrm{mg/dm^2 day}$). Additionally the corrosion current densities recorded in linear polarisation measurements under salt fog conditions for pure zinc were significantly higher than those observed for Zn-14 wt.% Ni alloy coatings.

This effect was thought to result mainly from the higher level of available oxygen in the salt spray environment and its effect of the corrosion products created. The corrosion products of the immersed pure zinc electrode were composed mainly of zinc oxide. For the zinc-nickel alloy the corrosion products were mainly Simonkolleite with traces of ZnO. However, it is supposed that also in the above mentioned case the influence of carbon dioxide present in ambient atmosphere, is the main influencing factor changing the type of corrosion.

Also the works of Zhu et al. [14, 298] on pure zinc and electrogalvanised steels showed the influences of the various exposure conditions (open or confined surfaces, wet/dry pattern, NaCl concentration, oxygen and carbon dioxide access) on the formation of different corrosion products. The main corrosion product that formed on confined surfaces changed from hydrozincite at low NaCl concentrations to Simonkolleite at high NaCl concentrations. When the drying time was longer and the atmospheric CO_2 access facilitated, Simonkolleite was the dominant compound formed on pure zinc and electrogalvanised steel. In contrast, zinc oxide was the dominant compound on confined surfaces of electrogalvanised steel exposed for shorter drying times, whereas similar proportions of zinc oxide, Simonkolleite and hydrozincite were formed on confined zinc surfaces. Differences between the results obtained from open and confined surfaces were explained as a result of differences in the corrosion rates and in the extent of localised corrosion as result of different drying rates for the open and confined surfaces.

Chapter 4

Summary and Outlook

The intensive use of de-icing salts and the need for weight reduction of cars by use of thinner, high strength steels call for an improved corrosion protection of car body parts. Therefore zinc precoated steel sheets are used in today's car manufacturing. The zinc coating affords cathodic protection to the steel sheet. Up to now the zinc precoats are either continuously electrogalvanised or hot dipped. This study examines sputtering as an alternative coating process as it allows the deposition of coatings which cannot be realised by hot dipping or electrodeposition. A further advantage is the higher environmental sustainability fulfilling even stricter environmental regulations, since the deposition occurs in closed chambers without generation of polluted waste waters.

In the presented study, magnetron sputtering and ion beam sputtering deposition experiments creating pure zinc and zinc alloy coatings have been carried out. The obtained coatings were examined with regard to their morphologies, chemical composition, crystallographic structures, mechanical properties and corrosion performance.

Morphologies and Chemical Composition The deposition experiments showed that the morphologies of sputtered zinc films depend very strongly on the sputter parameters. As main parameter the substrate holder temperature was identified. Since zinc is a low melting point material with high vapour pressure the obtained structures deviate from those predicted by the known structure zone models for sputtered films. Depending on further sputter parameters such as sputter power, sputter mode, deposition rate, rotating or static substrate holder, which directly influence the substrate temperature, the obtained morphologies range from highly dense, compact morphologies up to open, sponge like structures. With increasing substrate temperature an increase in grain size and porosity can be noticed. At higher deposition temperatures with normalised substrate temperatures of $T_s/T_m > 0.5$ even the growth of whisker like structures was observed. Due to the higher energy of the sputtered particles, the obtained zinc coatings also differ from those delivered by evaporation processes. The evolution of these whisker like microstructures with sputtered zinc and low alloyed zinc coatings, seems to be the result of an interplay between high deposition temperature, low melting point of the deposited zinc, residual gases, low deposition rate and the high kinetic energy of the sputtered adatoms.

Alloying with iron, titanium, chromium, aluminium and magnesium changes the structure evolution of the coatings. At higher alloying contents a densification with a tendency to smaller grain or column sizes can be observed. For high alloyed zinc iron samples even at elevated substrate temperatures no whiskers occur anymore.

The phase compositions of many zinc alloys coatings sputtered in this study deviate from those expected according to the equilibrium phase diagrams. Many of them are metastable structures and consist at given compositions of single phase supersaturated solid solutions (Zn-Fe, Zn-Ti), although the respective equilibrium phase diagram predicts a two phase system and/or the creation of compounds at

this composition. The zinc titanium coatings condense additionally in a nanocrystalline / amorphous structure. The deviation from equilibrium can be explained by the fact that sputter deposition is a vapour quenching technique that takes place far from thermodynamic equilibrium. The formation of metastable structures by sputtering is a complex interplay between thermodynamics and transformation kinetics. Several factors such as the activation energy for self diffusion, the deposition rate and deposition temperature determine the resulting structure.

The chemical analysis with XPS and Auger spectroscopy showed that the sputtered zinc and zinc alloy coatings are chemically pure. Only at the coating surfaces traces of carbon and oxygen were found.

Like alloying, ion bombardment also leads to a densification of zinc and low alloyed zinc coatings, even at high temperatures. Depending on the ion dose and the resulting ion to atom arrival ratios the deposition rate is reduced due to resputtering. Additionally, an entrapment of argon in the film can be observed. Ion bombardment also changes the crystallographic structure of these coatings as it causes a strong texture of the [002] direction and a reduction of the lattice c spacing.

The deposition experiments carried out in oxygen doped argon sputter gas atmospheres were intended to investigate the dependence of the occurrence of whisker like structures on the sputter gas composition, but no correlation was found. The admixture of oxygen did not result in an enhanced whisker growth. Only higher fractions of zinc oxides were found in these coatings.

Crystallographic Structure The XRD spectra showed that the crystallographic structure and composition of the sputtered coatings depend on several deposition parameters: the deposition temperature, the target alloy content, the deposition rate and the sputter mode. According to the interplay of these parameters the crystallographic structures and compositions range from crystalline, single phase systems (e.g. zinc) to crystalline, multiple phase systems (e.g. Zn–Mg), and to x-ray amorphous systems (e.g. Zn–Ti). In contrast to the electro galvanised reference sample with random, hexagonal structure the sputtered zinc coatings show a hexagonal structure with texture of the [002] direction. This texture is pronounced for samples deposited at low substrate temperatures.

The alloyed zinc coatings condensed in unknown, metastable phases, whose spectra did not fit to any of the reported crystal structures for zinc alloy phases in the JCPDS database or literature. Due to this reason these crystal structures, for which a decrease of the c/a spacing ratio is observed with increasing alloying content, have been tentatively simulated. Upon annealing, all of the metastable phases transformed into known, stable phases.

Mechanical Properties The microhardness measurements revealed that the Vickers hardnesses of the coatings are determined by the alloying contents and the substrate temperatures. For all zinc alloys coatings an increase in alloying element content lead to a rise in hardness. Furthermore, for samples deposited at low substrate temperatures higher hardnesses were measured than for those deposited at higher temperatures.

Almost all coatings showed very good adhesions to the steel substrates, which would allow their application in standard forming processes and car body assembly by adhesive bonding.

Corrosion The open circuit potential vs. time experiments showed that alloying with other elements shifts the start potential towards the rest potential of the alloying element, i.e the potential gets more negative for the less noble elements such as Al and Mg, while it is increased for the more noble elements such as Fe, Ti and Cr. With all sputtered coatings, whether they are alloyed or unalloyed, the normalised lifetimes seem to depend on the film morphologies. The influence of the deposition temperature and the resulting morphology on the lifetimes can be observed with almost all coatings types. All specimens deposited at a substrate temperature of $+8\,^{\circ}\mathrm{C}$ have longer lifetimes than those samples deposited in the same batch at a floating substrate temperature T_{float}. The highest alloyed zinc titanium and zinc chromium deposits reveal very short "cathodic protection" lifetimes which are obviously shorter than their actual lifetimes. In these cases the coatings are still existing but, as they are either enriched in more noble components such as titanium and chromium by dezincification or covered with corrosion products,

they reach corrosion potentials higher than that of bare steel quite early.

The potentiodynamic polarisation measurements also showed that alloying of zinc with other elements changes the corrosion potentials of the alloyed coatings towards the normal potential of the respective alloying element. The polarisation curves revealed that pure zinc bulk material shows no passivation, whereas thin films on steel substrates either hot dipped, electrogalvanised or sputtered, passivate. In comparison to the unalloyed zinc films the alloyed ones have a different passivation behaviour. The higher alloyed films have lower critical current densities and increased polarisation resistances, whereas the corrosion current densities do not vary significantly with alloying. The increased polarisation resistances indicate an improved corrosion protection of these deposits.

The salt spray test revealed that almost all sputtered coatings performed as well or much better than the reference coatings. Similar to the immersion test also here the influence of the deposition temperature and the morphology on the lifetimes was observed. All specimens deposited at a substrate temperature of $+8\,°C$ had longer lifetimes than those samples deposited in the same batch at a floating substrate temperature T_{float}. Furthermore, a significant improvement of the corrosion performance was achieved upon alloying. In particular with the zinc chromium and zinc titanium films the time to red rust was prolongated by up to eleven times with reference to the EZ coating. In contrast to other coatings for these films the volume of occurring corrosion products was reduced and the samples maintained their metallic appearance. These results show that the zinc alloy coated steel sheets could also be used in applications where unpainted steel sheets are required. The subsequent XRD measurements on the salt sprayed coatings explained the good corrosion performance of the alloyed coatings. They showed that there is a correlation between the created corrosion products, their corrosion protection and the resulting lifetime. Coatings delivering corrosion products with higher Simonkolleite and basic zinc carbonate hydroxide fractions afford better corrosion protection, thus resulting in longer lifetimes.

The cyclic corrosion tests VDA 621–415 on painted, zinc iron coated steel sheets showed that the zinc iron films have better cathodic protection capabilities than the pure zinc reference EZ. At the same coating thickness they showed 25 % less spread of blistering. A disadvantage of the zinc iron coatings is however the occurrence of red rust stemming from the coating, which could reduce their acceptance by the customer and therefore the car industry.

As a summary it can be stated that sputtering turns out to be an interesting alternative deposition method. The obtained coatings showed similar or better properties than conventionally deposited ones. In particular the alloyed zinc coatings showed promising perspectives due to their significantly better corrosion performances. However, the deposition rate needed for today's inline coating process and the linked condensation heat could cause a problem for the coating morphology: As zinc is a low melting point material with high vapour pressure and its growth upon sputtering is highly sensitive to the substrate temperature, an industrial coating process would require a satisfactory cooling for the steel sheets within the vacuum. Therefore further development in the plant construction is required. Additional investigations could also tackle the question whether the corrosion performance and other coating properties could be further improved by a subsequent heat treatment of the coatings. The results concerning the corrosion performances obtained in laboratory tests would also have to be confirmed in field experiments. This would allow to study various environmental influences and other corrosion determining factors occurring during the service of a car. Finally, in particular the use of zinc alloy coated steel sheets in the unpainted state could be envisaged for applications other than those in the automotive industry.

Bibliography

[1] European Committee for Standardization. EN ISO 8044:1999 Corrosion of metals and alloys - Basic Terms and definitions, 1999.

[2] J. Kruger. Corrosion of metals: Overview. In Buschow et al. [134]. 1701-1707.

[3] Gesellschaft für Korrosionsschutz e.V., 03 2004. Theodor-Heuss-Allee 25, D-60486 Frankfurt am Main, http://www.gfkorr.de/ last visit 24.09.2004.

[4] Corrosion doctors / Kingston Technical Software Co. http://www.corrosion-doctors.org/ last visit 24.09.2004.

[5] K. Mörbe, W. Morenz, H.W. Pohlmann, and H. Werner. *Praktischer Korrosionsschutz*. Springer Verlag, Wien, New York, 1987.

[6] H. Mc Arthur. *Corrosion prediction and prevention in motor vehicles*. Ellis Horwood Limited, Chichester, 1988.

[7] W.v. Baeckmann and W. Schwenk, editors. *Handbuch des kathodischen Korrosionsschutzes*. Wiley-VCH, Weinheim, New York, Chichester, Brisbane, Singapore, Toronto, 4 edition, 1999.

[8] P.J. Gellings, dt. Ausgabe K.H. Tostmann. *Korrosion und Korrosionsschutz von Metallen, Eine Einführung*. Carl Hanser Verlag, München, Wien, 1976.

[9] Scientific Group Thermodata Europe (SGTE). *Landolt-Börnstein: Numerical Data and Functional Relationships in Science and Technology - New Series Group 4: Physical Chemistry, Vol. 19: Thermodynamic Properties of Inorganic Materials, Subvolume B: Binary Systems, Part 3 Binary Systems from Cs-K to Mg-Zr*. Springer Verlag, 2005.

[10] M.B. Knaster and J.M. Parks. Mechanism of Corrosion and Delamination of Painted Phosphated Steel During Accelerated Corrosion Testing, Paper No. 860110, 1986.

[11] M. Pourbaix. *Atlas of electrochemical equilibria in aqueous solutions*. Pergamon Press, 1966.

[12] M.C. Bernard, A. Hugot-Le Goff, and N. Phillips. In situ Raman study of the corrosion of zinc-coated steel in the presence of chloride: I. Characterization and stability of zinc corrosion products. *J. Electrochem. Soc.*, 142(7):2162–2167, 1995.

[13] B. Beverskog and I. Puigdomenech. Revised pourbaix diagrams for zinc at 25-300°C. *Corrosion Science*, 39(1):107–114, 1997.

[14] F. Zhu, D. Persson, D. Thierry, and C. Taxen. Formation of corrosion products on open and confined zinc surfaces exposed to periodic wet/dry conditions. *Corrosion*, 56(12):1256–1265, 2000.

[15] V. Ligier, M. Wéry, J. Y. Hihn, J. Faucheu, and M. Tachez. Formation of the main atmospheric zinc end products: $NaZn_4Cl(OH)_6SO_4 \cdot 6H_2O$, $Zn_4SO_4(OH)_6 \cdot nH_2O$ and $Zn_4Cl_2(OH)_4SO_4 \cdot 5H_2O$ in $[CL^-][SO_4^{2-}][HCO_3^-][H_2O_2]$ electrolytes. *Corrosion Science*, 41:1139–1164, 1999.

[16] W. Feitknecht. Studies on the influence of chemical factors on the corrosion of metals. *Chem. Ind.*, pages 1102–1109, 1959.

[17] X.G. Zhang. *Corrosion and electrochemistry of zinc.* Plenum Press, 1996.

[18] X.G. Zhang. Galvanic corrosion of zinc and its alloys. *J. Electrochem. Soc.*, 143(4):1472–1484, April 1996.

[19] K. Kösters and M. Pimminger. Present state and future trends in surface coated steel sheets for automotive application. In *Proc. Int. Conf. 21st Century Steel Industry of Russia and CIS*, volume 5, pages 9–15, 1994.

[20] X.G. Zhang. Corrosion ratios of steel to zinc in natural corrosion environments. *Corrosion*, 55(8):787–794, Aug 1999.

[21] X.G. Zhang. Galvanic protection distance of zinc-coated steels under various environmental conditions. *Corrosion*, 56(2):139–143, 2000.

[22] G. Philip, B. Chamont, and M. Moustamsik. The anticorrosion strategy at PSA Peugeot Citroën. In *Galvatech 2001: 5th International Conference on Zinc and Zinc Alloy Coated Steel Sheet*, pages 45–48, Brussels, June 2001. Verlag Stahleisen.

[23] J.T. Johnson. Motor vehicles. CC Technologies, 6141 Avery Road, Dublin, Ohio, http://www.corrosioncost.com/transportation/motorvehicles/index.htm last visit 24.09.2004.

[24] H.E. Townsend. Extending the limits of growth through development of corrosion-resistant steel products. *Corrosion*, 55(6):547–553, June 1999.

[25] The Ultra Light Steel Auto Body Project. Car makers roll out ultra light steel technologies. *Sheet Metal Industries*, 55(5):37–38, May 1998.

[26] A. Matthews. The competition in the automotive industry to design "Reduced Emission Vehicles" (REVs). In *Fifth International Conference on Zinc Coated Steel Sheet, Birmingham, 97*, pages 1–6, Surrey, West Midlands, 1997. EGGA, Galvanizers Association and EZACSC.

[27] R.S. Charlton, J.A. Hanck, F.H. Meyer, and L.J. Korb. Corrosion in the automotive industry. In Korb et al. [28], pages 1011–1018.

[28] L.J. Korb, D.L. Olson, J.R. Davis, J.D. Destefani, H.J. Frissell, G.M. Crankovic, D.M Jenkins, R.L. Stedfeld, K.M. Mills, J.H. Johnson, R.T. Kiepura, and D.A. Humphries, editors. *Metals Handbook ® Ninth edition*, volume 13: Corrosion. American Society for Metals ASM International, Metals Park, Ohio 44073, 1988.

[29] D. Wolfhard and K.D. Ehlers. Korrosionsgeschütztes Stahlfeinblech für den Automobilbau. In *DVM–Tag 1995, Bauteil'95, Korrosion an Fahrzeugen*, pages 27–44, Unter den Eichen 87, D-12205 Berlin, 10.–12. Mai 1995. Deutscher Verband für Materialforschung u. -Prüfung.

[30] S.R. Taylor. Coatings for Corrosion Protection: An Overview. In Buschow et al. [134]. 1259-1263.

[31] S.R. Taylor. Coatings for Corrosion Protection: Inorganic. In Buschow et al. [134]. 1263-1269.

[32] S.R. Taylor. Coatings for Corrosion Protection: Metallic. In Buschow et al. [134]. 1269-1274.

[33] S.R. Taylor. Coatings for Corrosion Protection: Organic. In Buschow et al. [134]. 1274-1279.

[34] Y. de Abreu, A. Da Silva, A. Ruiz, R. Réquiz, N. Angulo, and R. Alanis. Study of zinc coatings on steel substrate attained by two different techniques. In *International Conference on Metallurgical Coatings and Thin Films, ICMCTF 99*, San Diego, California, USA, April 1999.

[35] A.R. Marder. The metallurgy of zinc-coated steel. *Progress in Materials Science*, 45:191–270, 2000.

[36] T. Kato, M.H. Hong, K. Nunome, K. Sasaki, K. Kuroda, and H. Saka. Cross-sectional TEM observation of multilayer structure of a galvanealed steel. *Thin Solid Films*, 319:132–139, 1998.

[37] H. Guttman and S. Belisle. Galfan - a new coating for automotive tubing, Paper No. 860274, 1986.

[38] K.L. Lin, C.F. Yang, and J.T. Lee. Correlation of Microstructure with Corrosion and Electrochemical Behavior of the Batch-Type Hot Dip Al-Zn Coatings: Part I. Zn and 5% Al-Zn Coatings. *Corrosion*, 47(1):9–17, 1991.

[39] J.H. Selverian, M.R. Notis, and A.R. Marder. The Microstructure of 55 w/o Al-Zn-Si (Galvalume) Hot Dip Coatings. *J. Materials Engineering*, 9(2):133–140, 1987.

[40] K.L. Lin, C.F. Yang, and J.T. Lee. Correlation of microstructure with corrosion and electrochemical behaviors of the batch-type Hot-Dip Al-Zn coatings: Part II. 55% Al-Zn Coating. *Corrosion*, 47(1):17–23, 1991.

[41] H. Okamoto, editor. *Phase Diagrams of Binary Iron Alloys*. American Society for Metals ASM International, Metals Park, Ohio 44073, 1993.

[42] T.B. Massalski, editor. *Binary Alloy Phase Diagrams, Second Edition*, volume 1. American Society for Metals ASM International, Metals Park, Ohio 44073, 1990.

[43] P. Karduck, T. Wirth, and H. Pries. Characterisation of intermediate layers in hot-dip zinc coated steels. *Fresenius J. Anal. Chem.*, 358:135–140, 1997.

[44] Z.T. Liu, M. Boisson, and O.N.C. Uwakweh. Kinetics of phase evolution of Zn-Fe intermetallics. *Metallurgical and Materials Transactions A*, 27A:2904–2910, oct. 1996.

[45] R.G. Grant and D.C. Cook. Iron-zinc phase identification in commercial galvanneal steel coatings. In I. Ortalli, editor, *Conference Proceedings ICAME-95*, volume 50, pages 929–932, Bologna, Italy, 1996.

[46] R.G. Grant, P.S. Cook, and D.C. Cook. Preparation and chemical analysis of high purity iron-zinc alloys. *J. Mater. Res.*, 10(10):2454–2462, 1995.

[47] R.G. Grant and D.C. Cook. Iron-zinc phase identification in commercial galvanneal steel coatings. In *Galvatech '95, The use and manufacture of zinc and zinc alloy coated sheet steel products into the 21st century*, pages 509–514, Chicago, Illinois, USA, 1995.

[48] R.G. Grant and D.C. Cook. Mößbauer effect and XRD studies of iron-zinc binary alloys. *Hyperfine Interactions*, 94:2309–2315, 1994.

[49] T. Gloriant, G. Reumont, and P. Perrot. The Fe–Zn–Ti system at 450 °C. *Zeitschrift für Metallkunde*, 88(7):539–544, 1997.

[50] D.C. Cook, R.S. Tuszynski, and H.E. Townsend. Zinc-iron phases formed on galvannealed steel. *Hyperfine Interactions*, 54:781–786, 1990.

[51] D.C. Cook and R.G. Grant. Identification of multiple iron sites in Fe–Zn binary alloys. In *Galvatech '95, The use and manufacture of zinc and zinc alloy coated sheet steel products into the 21st century*, pages 497–508, Chicago, Illinois, USA, 1995.

[52] M.H. Hong and H. Saka. X-ray and electron diffraction study on the partial disordering of the γ-phase in the Fe–Zn system. *Philosophical Magazine A*, 74(2):525–530, 1996.

[53] M.H. Hong and H. Saka. The mechanical properties and dislocation structure of the γ intermetallic phase in the Fe–Zn system. *Philosophical Magazine A*, 74(2):509–524, 1996.

[54] M.H. Hong and H. Saka. Plasticity and grain boundary structure of δ_{1k} and δ_{1p} intermetallic phases in the Fe-Zn system. *Acta Materialia.*, 45(10):4225–4230, 1997.

[55] P. Angermayer, M. Mayr, J. Angeli, and J. Faderl. Identification of Zn-Fe phases on galvanealed steel sheets by low incident angle X-ray diffraction in combination with electrochemical preparation. *Zeitschrift für Metallkunde*, 84(10):716–720, 1993.

[56] J.D. Culcasi, P.R. Seré, C.I. Elsner, and A.R. Sarli. Control of the growth of zinc-iron phases in the hot-dip galvanizing process. *Surface and Coatings Technology*, 122:21–23, 1999.

[57] P.J. Gellings, E.W. de Bree, and G. Gierman. Synthesis and characterisation of homogenous intermetallic Fe-Zn compounds, Part I: The δ_1 Phase. *Zeitschrift für Metallkunde*, 70(5):312–314, 1979.

[58] P.J. Gellings, E.W. de Bree, and G. Gierman. Synthesis and characterisation of homogenous intermetallic Fe-Zn compounds, Part II: The ζ Phase. *Zeitschrift für Metallkunde*, 70(5):315–317, 1979.

[59] P.J. Gellings, G. Gierman, D. Koster, and J. Kuit. Synthesis and characterisation of homogenous intermetallic Fe–Zn compounds, Part III: Phase Diagram. *Zeitschrift für Metallkunde*, 71(2):70–75, 1980.

[60] P.J. Gellings, D. Koster, J. Kuit, and T. Fransen. Synthesis and characterisation of homogenous intermetallic Fe-Zn compounds, Part IV: Thermodynamic properties. *Zeitschrift für Metallkunde*, 71(3):150–154, 1980.

[61] C.E. Jordan and A.R. Marder. Effect of substrate grain size on iron-zinc reaction kinetics during hot-dip galvanizing. *Metallurgical and Materials Transactions A*, 28A:2683–2694, December 1997.

[62] H.E. Townsend, G.L. Johnson, R.G. Grant, and D.C. Cook. Raman spectroscopy of the zeta phase zinc-iron intermetallic compound. *Scripta Metallurgica et Materialia*, 31(11):1445–1447, 1994.

[63] Z. Liu and O.N.C. Uwakweh. Mössbauer effect study of mechanically alloyed γ- and γ_1 Fe-Zn intermediate phases. *Metallurgical and Materials Transactions A*, 28A:743–747, mar. 1997.

[64] S.A. Kriner and K. Niederstein. Bandbeschichtungen mit Zweistofflegierungen. *Metalloberfläche*, 46:190–194, 1992.

[65] D.E. Tonini, S. Belisle, H.F. Graff, and D.C. Pearce. Hot dip galvanized coatings. In Wood et al. [66], pages 323–332.

[66] W.G. Wood, W.H. Cubberly, R.L. Stedfeld, K. Mills, L.G. Kruger, B. Sanders, and L. Borges Monroe, editors. *Metals Handbook $^{®}$ Ninth edition*, volume 5: Surface Cleaning, Finishing, and Coating. American Society for Metals ASM International, Metals Park, Ohio 44073, 1988.

[67] M. Simko. Coated sheet steel. In Buschow et al. [134].

[68] H.H. Geduld. Zinc plating. In Wood et al. [66], pages 244–255.

[69] H. Ashassi-Sorkhabi, A. Hagrah, N. Parvini-Ahmadi, and J. Manzoori. Zinc–nickel alloy coatings deposited from a chloride bath using direct and pulse current. *Surface and Coatings Technology*, 140:278–283, 2001.

[70] K.R. Baldwin, C.J.E. Smith, and M.J. Robinson. Cathodic protection of steel by electrodeposited zinc-nickel alloy coatings. *Corrosion*, 51(12):932–940, December 1995.

[71] K. Kondo, M. Yokoyama, and K. Shinohara. Morphology evolution of zinc-nickel binary alloys electrodeposited with pulse current. *J. Electrochem. Soc.*, 142(7):2256–2260, 1995.

[72] T. Adaniya, T. Hara, M. Sagiyama, T. Homa, and T. Watanabe. Zinc-Iron alloy electroplating on strip steel. *Plating and Surface Finishing*, pages 52–56, August 1995.

[73] K. Kondo, T. Murakami, and K. Shinohara. Morphology evolution of zinc-iron binary alloys electrodeposited with copper additive. *J. Electrochem. Soc.*, 143(4):L75–L77, 1996.

[74] M.R. El-Sharif, Y.J. Su, C.U. Chisholm, and A. Watson. Corrosion resistance of electrodeposited zinc-chromium alloy coatings. *Corrosion Science*, 35(5–8):1259–1265, 1993.

[75] M. Sagiyama, T. Urakawa, T. Adaniya, and T. Hara. Zinc-Manganese Alloy Electroplated Steel for Automotive Body, Paper No. 860268, 1986.

[76] G.D. Wilcox and D.R. Gabe. Electrodeposited zinc alloy coatings. *Corrosion Science*, 35(5–8):1251–1258, 1993.

[77] K.O. Legg, M. Graham, P. Chang, F. Rastagar, A. Gonzales, and B. Sartwell. The replacement of electroplating. *Surface and Coatings Technology*, 81:99–105, 1996.

[78] P. Carlsson, U. Bexell, and M. Olsson. Tribological behaviour of thin organic permanent coatings deposited on hot-dip coated steel sheet - a laboratory study. *Surface and Coatings Technology*, 132:169–180, 2000.

[79] T.F. Child and W.J. van Ooij. Application of silane technology to prevent corrosion of metals and improve paint adhesion. *Trans IMF*, 77(2):64–70, 1999.

[80] R. Kukla. Magnetron sputtering on large scale substrates: an overview on the state of the art. *Surface and Coatings Technology*, 93:1–6, 1997.

[81] S. Lucas, P. Vanden Brande, and A. Weymeersch. Plasma treatment of cold rolled steel: actual state, problems to overcome and future. *Surface and Coatings Technology*, 100–101:251–259, 1998.

[82] C. Metzner, B. Scheffel, and K. Goedicke. Plasma-activated electron beam deposition with diffuse cathodic vacuum arc discharge (SAD): a technique for coating strip steel. *Surface and Coatings Technology*, 86–87:769–775, 1996.

[83] S. Schiller, C. Metzner, and O. Zywitzki. New coatings on metal sheets and strips produced by EB PVD technologies. *Surface and Coatings Technology*, 125:240–245, 2000.

[84] R. Kukla, R. Ludwig, and J. Meinel. Overview on modern vacuum web coating technology. *Surface and Coatings Technology*, 86–87:753–761, 1996.

[85] T. Takahashi, Y. Oikawa, T. Komori, I. Ito, and M. Hashimoto. Surface modification of stainless steel in coil by an in-line dry coating process. *Surface and Coatings Technology*, 51:522–528, 1992.

[86] P.C. Zalm. Quantitative sputtering. In Cuomo et al. [87], pages 78–111.

[87] J.J. Cuomo, S.M. Rossnagel, and H.R. Kaufman, editors. *Handbook of ion beam processing technology*. Noyes Publications, Park Ridge, New Jersy, USA, 1989.

[88] J.A. Thornton and J.E. Greene. Sputter deposition processes. In Bunshah [89], pages 249–319.

[89] R.F. Bunshah, editor. *Deposition Technologies for Films and Coatings*. Noyes Publications, Park Ridge, New Jersey, USA, 1982.

[90] D.N. Ruzic. Fundamentals of sputtering and reflection. [91], pages 70–90.

[91] S.M. Rossnagel, J.J. Cuomo, and W.D. Westwood. *Handbook of Plasma Processing Technology*. Noyes, Park Ridge, N.J., 1990.

[92] P. Sigmund. Theory of sputtering. I. Sputtering yield of amorphous and polycrystalline targets. *Physical review*, 184:383–416, 1969.

[93] P. Sigmund. Theory of sputtering. I. Sputtering yield of amorphous and polycrystalline targets, Erratum. *Physical review*, 187:768, 1969.

[94] S.I. Shah. A.3.0 sputtering: Introduction and general discussion. In Glocker and Shah [96], pages 1–18.

[95] A.S. Penfold. A.3.1 glow discharge sputtering. In Glocker and Shah [96], pages 1–22.

[96] D.A. Glocker and S.I. Shah, editors. *Handbook of Thin Film Process Technology*. Institute of Physics Publishing Ltd., Bristol and Philadelphia, 1995.

[97] H.R. Kaufman, R.S. Robinson, and W.E. Hughes. Characteristics, capabilities and applications of broad-beam sources. Commonwealth Scientific Corporation, 1987.

[98] A.S. Penfold. A.3.2 magnetron sputtering. In Glocker and Shah [96], pages 1–27.

[99] F.A. Smidt. Use of ion beam assisted deposition to modify the microstructure and properties of thin films. *International Materials Reviews*, 35(2):61–128, 1990.

[100] E. Kay and S.M. Rossnagel. The modification of films by ion bombardment. In Cuomo et al. [87], pages 170–193.

[101] I. Takagi. Role of ions in ion-based film formation. *Thin Solid Films*, 1982.

[102] S.M. Rossnagel and J.J. Cuomo. Film modification by low energy ion bombardment during deposition. *Thin Solid Films*, 171:143–156, 1989.

[103] Balzers AG. *Partial pressure measurement in vacuum technology*. Balzers Instruments, FL-9496 Balzers, Liechtenstein.

[104] O. Knacke, O. Kubaschewski, and K. Hesselmann. *Thermo chemical properties of inorganic substances, Second edition*. Springer Verlag, 1991.

[105] J.R. Davis, editor. *Corrosion understanding the basics*. ASM International, Materials Park, Ohio, USA, 2000.

[106] J.C. Slater. *J. Chem. Phys.*, 39:3199, 1964.

[107] L.E. Sutton, editor. *Table of interatomic distances and configuration in molecules and ions, Supplement 1956-1959, Special publication No. 18*. Chemical Society, London, UK, 1965.

[108] A.F. Holleman and N. Wiberg. *Lehrbuch der Anorganischen Chemie*. Walter de Gruyter, Berlin, New York, 1985.

[109] C.B. Alcock, V.P. Itkin, and M.K. Horrigan. Vapour pressure equations for the metallic elements: 298–2500 K. *Canadian Metallurgical Quarterly*, 23(3):309–313, 1984.

[110] J.A. Thornton. High rate thick film growth. *Ann. Rev. Mater. Sci.*, 7:239–260, 1977.

[111] R. Agarwal, S.G. Fries, H.L. Lukas, G. Petzow, F. Sommer, T.G. Chart, and G. Effenberg. *Zeitschrift für Metallkunde*, 82(4):216–223, 1992.

[112] L. Guzman, M. Adami, and E. Voltolini. Zinc coatings on steel by advanced PVD techniques. In *Proceedings of The 4th International Conference on Zinc and Zinc Alloy Coated Steel Sheet (GALVATECH'98)*, pages 763–767, Chiba, Japan, 1998. The Iron and Steel Institute of Japan.

[113] J.A. Thornton. Substrate heating in cylindrical magnetron sputtering sources. *Thin Solid Films*, 54:23–31, 1978.

[114] K. Ellmer and R. Mientus. Calorimetric measurements with heat flux transducers of the total power influx onto a substrate during magnetron sputtering. *Surface and Coatings Technology*, 119–119:1102–1106, 1999.

[115] J.I. Goldstein, D.E. Newbury, P. Echlin, D.C. Joy, Jr. A.D. Romig, C.E. Lyman, C. Fiori, and E. Lifshin. *Scanning Electron Microscopy and X-ray analysis*. Plenum Press, New York, second edition, 1992.

[116] P. de Groot and L. Deck. Surface profiling by frequency-domain analysis of white light interferograms. *Proceedings Society of Photo-Optical Instrumentation Engineers*, pages 101–104, 1994.

[117] Europäisches Komitee für Normung. EN ISO 4287:1997 Geometrische Produktspezifikationen (GPS) Oberflächenbeschaffenheit: Tastschnittverfahren - Benennungen, Definitionen und Kenngrößen der Oberflächenbeschaffenheit, 1997.

[118] H. Hoischen. *Technisches Zeichnen: Grundlagen, Normen, Beispiele, Darstellende Geometrie*. Cornelsen, Girardet, 22 edition, 1988.

[119] M.E.R. Shanahan. Wetting phenomena: Their use and limitations in surface analysis. In Datta and Gray [120].

[120] P.K. Datta and J.S. Gray, editors. *Surface engineering*, volume III: Process Technology and Surface Analysis. Royal society of chemistry, Cambridge, 1993.

[121] W. Barthlott and C. Neinhuis. Purity of the sacred lotus, or escape from contamination in biological surfaces. *Planta*, 202:1–8, 1997.

[122] B. Meuthen, N. Petsch, G. Hartmann, P. Heidbüchel, and H. Beenken. Weiterverarbeitung von verzinktem und beschichtetem Stahlblech. Technical report, Stahl-Informations-Zentrum, 1997.

[123] DIN Deutsches Institut für Normung e.V. DIN EN 582 Ermittlung der Haft-Zugfestigkeit im Stirnzugversuch; Prüfung an thermisch gespritzten Schichten.

[124] American Society for Testing and Materials. ASTM D 1002-72 Standard test method for strength properties of adhesives in shear by tension loading (metal-to-metal), 1983.

[125] K. Meseure, C. Xhoffer, B.C. de Cooman, I. Hertveld, and J. Dilewijns. The shear strength of galvannealed coatings on IF steels. In *Fifth International Conference on Zinc Coated Steel Sheet, Birmingham, 97*, pages 1–8, Surrey, West Midlands, 1997. EGGA, Galvanizers Association and EZACSC.

[126] M. Ohring. *The materials science of thin films*. Academic Press Inc., 1992.

[127] R.W. Cahn and E. Lifshin, editors. *Concise Encyclopedia of Materials and Characterization*. Pergamon Press, 1 edition, 1993.

[128] J. Wernisch. Electron-probe microanalysis of thin films. In Eckertova and Ruzicka [166], pages 21–45. Proceedings of the International Summer School on Diagnostics and Applications of Thin Films 27th May - 5th June 1991, Chlum u Třeboně, Czechoslovakia.

[129] L.E. Davis, N.C. MacDonald, P.W. Palmberg, G.E. Riach, and R.E. Weber. *Handbook of Auger electron spectroscopy*. Physical Electronics Division Perkin-Elmer Corporation, 1976.

[130] A. Joshi. Auger electron spectroscopy. In Whan et al. [299], pages 549–567.

[131] J.B. Lumsden. X-ray photo electron spectroscopy. In Whan et al. [299], pages 568–580.

[132] N. Mårtensson. *Treatise on Materials Science and Technology*, volume 27: Analytical Techniques for Thin Films, chapter ESCA, pages 65–107. Academic Press, NY, 1988.

[133] P.N. Gibson. Thin films: Characterisation by x-rays. In Buschow et al. [134]. Article No. 73; Sect. No. 2.8.

[134] K.H.J Buschow, R.W. Cahn, M.C. Flemings, B. Ilschner, E.J. Kramer, and S. Mahajan, editors. *Encyclopedia of Materials: Science and Technology*. Pergamon, 2001.

[135] G. Lim, W. Parrish, C. Ortiz, M. Bellotto, and M. Hart. Grazing incidence synchrotron x-ray diffraction method for analyzing thin films. *J. Mater. Res.*, 2:471–477, 1987.

[136] R.C. Buschert, P.N. Gibson, W. Gissler, J. Haupt, and T.A. Crabb. Glancing incidence x-ray studies of titanium nitride thin films using a new multipurpose laboratory spectrometer. *Colloque de physique*, (supplement au n° 10, Tome 50):169–173, octobre 1989.

[137] T.A. Crabb. *Advanced surface sensitive X-ray techniques: Application to the study of the initial stages of high temperature corrosion of metals and alloys*. Phd thesis, University of Strathclyde, 1993.

[138] Joint Committee on Powder Diffraction Standards– International Center for Diffraction Data. Powder Diffraction File 2, Version 2.14, Sets 1–43, 1993.

[139] C. Boudias and D. Monceau, editors. *CaRIne Crystallography 3.1*. CaRIne Crystallography, 17, rue du Moulin du Roy, 60300 Senlis, France, 1998.

[140] DIN Deutsches Institut für Normung e.V. DIN 50918 Elektrochemische Korrosionsuntersuchungen, 1978.

[141] M. Stein, S.P. Owens, H.W. Pickering, and K.G. Weil. Dealloying studies with electrodeposited zinc-nickel alloy films. *Electrochimica Acta*, 43(1–2):223–226, 1998.

[142] DIN Deutsches Institut für Normung e.V. DIN 50021 Sprühnebelprüfungen mit verschiedenen Natriumchlorid-Lösungen, 1988.

[143] T. Falk, J.E. Svensson, and L.G. Johansson. The influence of CO_2 and NaCl on the atmospheric corrosion of zinc. *J. Electrochem. Soc.*, 145(9):2993–2999, 1998.

[144] T. Christmann, J.T. Stropki, and C.K. Schoff. Evaluation of accelerated corrosion test procedures, Paper No. 892583, 1989.

[145] Verband der Automobilindustrie e.V. (VDA). VDA 621–415 (2.82) Anstrichtechnische Prüfungen: Prüfung des Korrosionsschutzes von Kraftfahrzeuglackierungen bei zyklisch wechselnder Beanspruchung, 1982.

[146] J.A. Thornton. Influence of apparatus geometry and deposition conditions on the structure topography of thick sputtered coatings. *Journal of Vacuum Science and Technology*, 11(4):666–670, Jul./Aug. 1974.

[147] R. Messier, A.P. Giri, and R.A. Roy. Revised structure zone model for thin film physical structure. *Journal of Vacuum Science and Technology A*, 2(2):500–503, Apr./Jun. 1984.

[148] G.K. Wehner. Cone formation as a result of whisker growth on ion bombarded metal surfaces. *Journal of Vacuum Science and Technology A*, 3(4):1821–1835, Jul/Aug 1985.

[149] R.H Doremus, B.W. Roberts, and D. Turnbull, editors. *Growth and perfection of crystals.* J. Wiley & Sons, Inc.; Chapman & Hall, Limited, New York, London, 1958. Proceedings of an international conference on crystal growth held at Cooperstown, New York on August 27-29, 1958.

[150] B.A. Movchan and A.V. Demichishin. Study of the structure and properties of thick vacuum condensates of nickel, titanium, tungsten, aluminium oxide and zirconium dioxide. *Fiz. metal. metalloved.*, 28(4):653–660, 1969.

[151] S. Craig and G.L. Harding. Effects of argon pressure and substrate temperature on the structure and properties of sputtered copper films. *Journal of Vacuum Science and Technology*, 19(2):205–215, 1981.

[152] C.R.M. Grovenor, H.T.G. Hentzell, and D.A. Smith. The development of grain structure during growth of metallic films. *Acta metall.*, 32(5):773–781, 1984.

[153] C. Fountzoulas and W.B. Nowak. Influence of ion energy and substrate temperature on the structure of copper germanium, and zinc films produced by ion plating. *Journal of Vacuum Science and Technology A*, 9(4):2128–2137, 1991.

[154] P.B. Barna and M. Adamik. Growth mechanisms of polycrystalline thin films. In Matacotta and Ottaviani [155], pages 1–28.

[155] F.C. Matacotta and G. Ottaviani, editors. *Science and technology of thin films.* World Scientific, Singapore, New Jersey, London, Hong Kong, 1996.

[156] P.B. Barna and M. Adamik. Formation and characterisation of the structure of surface coatings. In Pauleau and Barna [157], pages 279–297.

[157] Y. Pauleau and P.B. Barna, editors. *Protective Coatings and Thin Films: Synthesis, Characterization and Applications.* Kluwer Academic Publishers, 1997.

[158] M. Lardon, R. Buhl, H. Signer, E. Moll, and H.K. Pulker. Influence of the substrate temperature and the discharge voltage on the structure of titanium films produced by ion-plating. *Vacuum*, 30(7):255–260, 1980.

[159] M. Neirynck, W. Samaey, and L. Van Poucke. Structure and properties of vacuum vapour deposited coatings on steel substrates. *Journal of Vacuum Science and Technology*, 11(4):647–652, Jul./Aug. 1974.

[160] L.J. Wan, B.Q. Chen, and K.H. Kuo. Morphology and microstructure of magnetron sputtering ion-plating Al films as a function of deposition time. *Journal of Vacuum Science and Technology A*, 6(6):3160–3163, 1988.

[161] O. Kubaschewski and E. LL. Evans, editors. *Metallurgical Thermochemistry*. Pergamon Press Ltd., London, 2 edition, 1956.

[162] J. Musil, J. Matouš, J. Vlček, L. Koydl, and K. Müller. Surface morphology of sputter deposited low melting point metallic thin films. *Czechoslovak Journal of Physics*, 44(6):565–574, 1994.

[163] J.F. Poòcza, A. Barna, P.B. Barna, I. Pozsgai, and G. Radnòczi. In situ electron microscopy of thin film growth. *Japan J. Appl. Phys.*, Suppl. 2 (Pt.1):525–532, 1974.

[164] B. Grung. Master thesis, University of Minnesota, 1972.

[165] P.B. Barna. Crystal growth and recrystallization during structure evolution of thin films. In Eckertova and Ruzicka [166], pages 295–310. Proceedings of the International Summer School on Diagnostics and Applications of Thin Films 27th May - 5th June 1991, Chlum u Třeboně, Czechoslovakia.

[166] L. Eckertova and T. Ruzicka, editors. *Diagnostics and applications of thin films*. Institute of Physics Publishing Ltd., Bristol and Philadelphia, 1992. Proceedings of the International Summer School on Diagnostics and Applications of Thin Films 27th May - 5th June 1991, Chlum u Třeboně, Czechoslovakia.

[167] P.B. Barna, G. Radnóczi, and F.M. Reicha. Surface growth topography of grain boundaries in Al thin films. *Vacuum*, 38(7):527–532, 1988.

[168] P.B. Barna, M. Adamik, G. Sáfrán, B. Pécz, A. Bergauer, and H. Bangert. Peculiar lamellar structure in Al single crystals grown in oxygen-doped Al and Al-Sn thin films. *Phys. Stat. Sol.*, 146:317–324, 1994.

[169] P. Schattschneider, H. Bangert, P. Pongratz, A. Bergauer, P.B. Barna, and F. Hofer. Structure and chemical composition of lamellae in sputtered AlSn20 films. *Materials Science Forum*, 217–222:1667–1672, 1996.

[170] P.B. Barna, M. Adamik, U. Kaiser, S. Laux, H. Bangert, M. Pulliainen, and K.A. Pischow. Structure related optical and mechanical properties of oxygen doped Al films. *Surface and Coatings Technology*, 100–101:72–75, 1998.

[171] E.O. Hall. The deformation and ageing of mild steel: III Discussion of results. *Proc. Phys. Soc., Ser. B*, 64:747–753, 1951.

[172] N.J. Petch. The cleavage strength of polycrystals. *J. Iron and Steel Institute*, pages 25–28, May 1953.

[173] A. Bergauer, H. Bangert, C. Eisenmenger-Sittner, and P.B. Barna. Whisker growth on sputtered AlSn (20 wt.% Sn) films. *Thin Solid Films*, 258:115–122, 1995.

[174] J. Musil, J. Matouš, and V. Valvoda. Effect of ion bombardment on the surface morphology of Zn-films sputtered in an unbalanced magnetron. *Vacuum*, 46(2):203–210, 1995.

[175] B.Z. Lee and D.N. Lee. Spontaneous growth mechanism of tin whiskers. *Acta Materialia.*, 46(10):3701–3714, 1998.

[176] U. Lindborg. Observations on the growth of whisker crystals from zinc electroplate. *Metallurgical Transactions A*, 6A:1581–1586, 1975.

[177] U. Lindborg. A model for the spontaneous growth of zinc, cadmium and tin whiskers. *Acta Metallurgica*, 24:181–186, 1976.

[178] J.D. Eshelby. A tentative theory of metallic whisker growth. *Physical review*, 91:755–756, 1953.

[179] F.C. Frank. On tin whiskers. *Philiosophical Magazine*, 44:854–860, 1953.

[180] S. Amelickx, W. Bontinck, W. Dekeyser, and F. Seitz. On the formation and properties of helical dislocations. *Philiosophical Magazine*, 2(15):355–378, 1957.

[181] W.C. Ellis, D.F. Gibbons, and R.C. Treuting. In Doremus et al. [149], page 102. Proceedings of an international conference on crystal growth held at Cooperstown, New York on August 27-29, 1958.

[182] N. Furuta and K. Hamamura. Growth mechanism of proper tin-whisker. *Japanese Journal of Applied Physics*, 8(12):1404–1410, 1969.

[183] K.N. Tu. Irreversible processes of spontaneous whisker growth in bimetallic Cu-Sn thin-film reactions. *Physical Review B*, 49(3):2030–2034, 1994.

[184] R. Kawanaka. *J. Jap. Ass. Cryst. Growth*, 8:145, 1981.

[185] H. Mehrer, editor. *Landolt-Börnstein, Zahlenwerte und Funktionen aus Naturwissenschaften und Technik, Gruppe III: Kristall- und Festkörperphysik, Band 26 Diffusion in festen Metallen und Legierungen.* Springer Verlag, 1990.

[186] W. Buckel. Internal stresses. *Journal of Vacuum Science & Technology*, 6(4):606, 1969.

[187] F. Vollertsen and S. Vogler. *Werkstoffeigenschaften und Mikrostruktur.* Carl Hanser Verlag, München, Wien, 1989.

[188] R.C. Weast and M.J. Astle, editors. *CRC Handbook of Chemistry and Physics*, volume 59. CRC Press, Inc., Boca Raton, Florida 33431, 1978.

[189] L. Succo, J. Esposito, M. Cleeves, S. Whitney, R.E. Lionetti, and Jr. C.E. Wickersham. Influence of target microstructure on the propensity for whisker growth in sputter-deposited aluminum alloy films. *Journal of Vacuum Science and Technology A*, 7(3):814–186, May/Jun 1989.

[190] P.J. Martin. Ion-assisted thin film deposition and applications. *Vacuum*, 36(10):585–590, 1986.

[191] D.M. Mattox. Deposition technologies for films and coatings. In Bunshah [255], chapter 6: Ion plating, pages 320–373.

[192] S. Mohan and M.G. Krishna. A review of ion beam assisted deposition of optical thin films. *Vacuum*, 46(7):645–659, 1995.

[193] Scientific Group Thermodata Europe (SGTE). *Landolt-Börnstein: Numerical Data and Functional Relationships in Science and Technology - New Series Group 4: Physical Chemistry, Vol. 19: Thermodynamic Properties of Inorganic Materials, Subvolume B: Binary Systems, Part 1 Elements and Binary Systems from Ag-Al to Au-Ti.* Springer Verlag, 2002.

[194] Scientific Group Thermodata Europe (SGTE). *Landolt-Börnstein: Numerical Data and Functional Relationships in Science and Technology - New Series Group 4: Physical Chemistry, Vol. 19: Thermodynamic Properties of Inorganic Materials, Subvolume B: Binary Systems, Part 2 Binary Systems from B-C to Cr-Zr*. Springer Verlag, 2004.

[195] D. Turnbull. Metastable structures in metallurgy. *Metallurgical Transactions A*, 12, 1981.

[196] W.L. Johnson. Thermodynamic and kinetic aspects of the crystal to glass transformation in metallic materials. *Progress in Materials Science*, 30:81–134, 1986.

[197] K.N. Tu, S.R. Herd, and U. Gösele. Metastablility in slow thin film reactions. *Physical Review B*, 43(1):1198–1201, 1991.

[198] W. Buckel. Elektronenbeugungs-Aufnahmen von dünnen Metallschichten bei tiefen Temperaturen. *Zeitschrift für Physik*, 136:136–150, 1954.

[199] J.P. Chu, J.W. Chang, P.Y. Lee, J.K. Wu, and J.Y. Wang. On the formation of nonequilibrium A15 crystal structure chromium thin films by sputter deposition. *Thin Solid Films*, 312:78–85, 1998.

[200] D. Akhtar, V.D. Vankar, T.C. Goel, and K.L. Chopra. Metastable structures of splat-cooled and vapour- depodited lead and antimony films. *Thin Solid Films*, 58(2):327–332, 1979.

[201] R. Stoering and H. Conrad. Metastable structures in liquid quenched and vapor quenched Ag-Cu alloys. *Acta Metallurgica*, 17(8):933–948, 1969.

[202] B. Cantor and R.W. Cahn. Vapour quenched Ag–Cu alloys. *Scripta Metallurgica*, 10:381–382, 1976.

[203] S. Mader, A.S. Nowick, and H. Widmer. Metastable evaporated thin films of Cu-Ag and Co-Au alloys - I. Occurence and morphology of phases. *Acta Metallurgica*, 15:203–214, 1967.

[204] J.J. Hauser. Amorphous ferromagnetic Ag-X (X=Ni, Co, Gd) alloys. *Physical Review B*, 12(11):5160–5165, 1975.

[205] J.H. He, H.W. Sheng, P.J. Schilling, C.L. Chien, and E. Ma. Amorphous Structures in the Immiscible Ag-Ni System. *Physical Review Letters*, 86(13), 2001.

[206] M.R. Anseau. Letters: A comparison of the limitations of vapour-quenching and liquid-quenching in the presentation of non-equilibrium alloys. *Journal of Materials Science*, 9:1189–1190, 1974.

[207] D. Nilsson and U. Wiklund. A flexible laboratory-scale approach to alloying and tailoring of thin films using single-magnetron co-sputtering. *Thin Solid Films*, 467:10–15, 2004.

[208] B. Cantor and R.W. Cahn. Metastable alloy phases by co-sputtering. *Acta Metallurgica*, 24(9):845–852, 1976.

[209] J. Creus, A. Billard, and F. Sanchette. Corrosion behaviour of amorphous Al-Cr and Al-Cr-(N) coatings deposited by dc magnetron sputtering on mild steel substrate. *Thin Solid Films*, 466:1–9, 2004.

[210] F. Sanchette, T.H. Loi, A. Billard, and C. Frantz. Structure-properties relationship of metastable al-cr and al-ti alloys deposited by r.f. magnetron sputtering: role of nitrogen. *Surface and Coatings Technology*, 74–75:903–909, 1995.

[211] R.D. Arnell and R.I. Bates. The deposition of highly supersaturated metastable aluminium-magnesium alloys by unbalanced magnetron sputtering from composite targets. *Vacuum*, 43(1/2):105–109, 1992.

[212] R.I. Bates and O.A. Abu-Zeid. Deposition of highly supersaturated metastable aluminium-molybdenum alloys by closed field unbalanced magnetron sputtering. *Vacuum*, 47(2):107–111, 1996.

[213] M. Naka, T. Shibayanagi, M. Maeda, S. Zhao, and H. Mori. Formation and physical properties of Al base alloys by sputtering. *Vacuum*, 59:252–259, 2000.

[214] R.C. Krutenat, J.K. Tien, and D.E. Fornwalt. Sputter deposition of a metastable phase in the Au–Si system. *Metallurgical Transactions*, 2:1479–1481, 1971.

[215] E. Kneller. Magnetic moment of Co–Cu solid solutions with 40 to 85% Cu. *Journal of Applied Physics*, 33(3):1355–1356, 1963.

[216] J.R. Childress and C.L. Chien. Reentrant magnetic behavior in fcc Co-Cu alloys. *Physical Review B*, 43(10):8089–8093, 1991.

[217] C. Michaelsen. On the structure and homogeneity of solid solutions: the limits of conventional X-ray diffraction. *Philosophical Magazine A*, 72(3):813–828, 1995.

[218] A.E. Berkowitz, J.R. Mitchell, M.J. Carey, A.P. Young, S. Zhang, F.E. Spada, F.T. Parker, A. Hutten, and G. Thomas. Giant magnetoresistance in heterogeneous Cu-Co alloys. *Physical Review Letters*, 68(25):3745–3749, 1992.

[219] J.A. Thornton and D.P. Ferriss. Structural and wear properties of sputter-deposited Laves intermetallic alloy. *Thin Solid Films*, 40:365–374, 1977.

[220] S.M. Shin, M.A. Ray, J.M. Rigsbee, and J.E. Greene. Growth of metastable $Cu_{1-x}Cr_x$ solid solutions by ion mixing during bias-sputter deposition. *Applied Physics Letters*, 43(3):249–251, 1983.

[221] D. McIntyre, J.E. Sundgren, and J.E. Greene. Summary abstract: Metastable face-centered-cubic $Cu_{1-x}Cr_x$ alloys ($0<x<0.23$) deposited by sputter deposition: Growth, structure, and physical properties. *Journal of Vacuum Science and Technology A*, 3(6):1708–1709, May/june 1988.

[222] A.G. Dirks and J.J van den Broek. Metastable solid solutions in vapor deposited Cu-Cr, Cu-Mo and Cu-W thin films. *Journal of Vacuum Science and Technology A*, 3(6):2618–2622, nov/dec 1985.

[223] L.-Chung Yang and A. Rockett. Cu–Mo contacts to $CuInSe_2$ for improved adhesion in photovoltaic devices. *Journal of Applied Physics*, 75(2):1185–1189, 1994.

[224] P. Djemia, F. Ganot, P. Moch, V. Branger, and P. Goudeau. Brioullin scattering investigation of elastic properties of Cu-Mo solid solution thin films. *Journal of Applied Physics*, 90(2):756–762, 2001.

[225] N. Saunders and A.P. Miodownik. Phase formation in co-deposited metallic alloy thin films. *Journal of Material Science*, 22:629–637, 1987.

[226] N. Kataoka, K. Sumiyama, and Y. Nakamura. Thermal stability of non equilibrium crystalline Fe–Ag alloys produced by vapour quenching. *Acta Metallurgica*, 37(4):1135–1142, 1989.

[227] S.D. Dahlgren and M.D. Merz. Solid Solutions in Sputter-Deposits of Iron with 0 to 5 wt. pct. C. *Metallurgical Transactions*, 2:1753–1760, 1971.

[228] C.L. Chien, S.H. Liou, D. Kofalt, Wu Yu, T. Egami, and T.R. McGuire. Magnetic properties of Fe_xCu_{100-x} solid solutions. *Physical Review B*, 33(5):3247–3250, 1986.

[229] E. Kneller. Magnetic and Structural Properties of Metastable Fe–Cu solid solutions. *Journal of Applied Physics*, 35(7):2210–2211, 1963.

[230] P. Nath, V. Dutta, and K.L. Chopra. Amorphous and polycrystalline ge-metal films prepared by physical vapour deposition. *Thin Solid Films*, 64(1), 1979.

[231] J.H. Hsieh, C. Li, C.M. Wang, and Z.Z. Tang. Boundary-free multi-element barrier films by reactive co-sputtering. *Surface and Coatings Technology*, 198(1-3):335–339, 2004.

[232] C. Michaelsen, C. Gente, and R. Bormann. The thermodynamics of amorphous phases in immiscible systems: The example of sputter-deposited Nb–Cu alloys. *J. Appl. Phys.*, 81:6024–6030, 1997.

[233] G.B. Thompson, R. Banerjee, X.D. Zhang, P.M. Anderson, and H.L. Fraser. Chemical ordering and texture in Ni-25 at% Al thin films. *Acta Materialia*, 50:643–651, 2002.

[234] Z.Z. Tang, J.H. Hsieh, S.Y. Zhang, C. Li, and Y.Q. Fu. Phase transition and microstructure change in Ta-Zr alloy films by co-sputtering. *Surface and Coatings Technology*, 2004.

[235] H. Hecht, G. Weigang, S. Eickert, and U. Geyer. Formation area of thin amorphous Zr-Mn and Zr-Ta films prepared by cocondensation. *Zeitschrift für Physik B*, 100:47–51, 1996.

[236] S.Z. Wang, G. Shao, P. Tsakiropoulos, and F. Wang. Phase selection in magnetron sputter-deposited TiAl alloy. *Materials Science and Engineering A*, 329–331:141–146, 2002.

[237] R. Kumar, M. Singh, and C.S. Sivaramakrishnan. Clustering in liquid aluminum–copper and lead–tin eutectic alloys. *Transactions of the Metallurgical Society of AIME*, 239:1219–1221, 1967.

[238] E. Ma. Alloys created by immiscible elements. *Progress in Materials Science*, 50:413–509, 2005.

[239] W.L. Johnson. Amorphization by interfacial reactions. In D. Wolf and S. Yip, editors, *Materials Interfaces, Atomic-Level Structure and Properties*, pages 517–549. Chapman & Hall, 1992.

[240] T. Heumann. Beitrag zur Kenntnis des Systems Zink-Chrom. *Zeitschrift für Metallkunde*, 39(2):45–52, 1948.

[241] G. Shao and P. Tsakiropoulos. The roles of thermodynamics and transformation kinetics on phase selection in the non-equilibrium processing of materials. *Materials Science and Engineering A*, 375-377:556–560, 2004.

[242] R.W. Bené. A kinetic model for solid-state silicide nucleation. *Journal of Applied Physics*, 61(5):1826—1833, 1987.

[243] J.P. Hirth and G.M. Pound. Condensation and evaporation: Nucleation and growth kinetics. *Progress in Materials Science*, 11, 1963.

[244] G. Shao and P. Tsakiropoulos. On the structural evolution of Fe–Al laminates obtained by physical vapour deposition. *Philosophical Magazine A*, 80:693–710, 2000.

[245] K. Kamoshida. Argon entrapment in magnetron-sputtered Al alloy films. *Thin Solid Films*, 283:57–60, 1996.

[246] L. Shi, C. Liu, S. Xu, and Z.Y. Zhou. Helium-charged titanium films deposited by direct current magnetron sputtering. *Thin Solid Films*, 479:52–58, 2005.

[247] M.A. Bayne, R.W. Moss, and E.D. McClanahan. Krypton entrapment in pulse-biased sputter-deposited metals. *Thin Solid Films*, 54:327–336, 1978.

[248] M.A. Bayne, R.W. Moss, and E.D. McClanahan. Krypton entrapment in continuous-biased sputter-deposited glassy metals. *Thin Solid Films*, 63:137–141, 1979.

[249] P.N. Gibson. personal communication, 2002.

[250] R. Kužel Jr., V. Valvoda, M. Chládek, J. Musil, and J. Matouš. XRD microstructural study of Zn films deposited by unbalanced magnetron sputtering. *Thin Solid Films*, 263:150–158, 1995.

[251] W. Maschek, S.P. Hayes, and A.R. Marder. Cross sectional studies of zinc iron phase growth in an environmental scanning electron microscope. In *Galvatech '95, The use and manufacture of zinc and zinc alloy coated sheet steel products into the 21st century*, pages 309–318, Chicago, Illinois, USA, 1995.

[252] G.F. Bastin, F.J.J. Van Loo, and G.D. Rieck. A new compound in the iron-zinc system. *Z.Metallkde.*, 65(H. 10):656–660, 3. Mai 1974.

[253] F. Alonso, V. Madina, J.L. Viviente, T. Mursell, and J.I. Oñate. Zn-Cr alloy coatings produced by ion beam assisted deposition. *Surface and Coatings Technology*, 103–104:87–92, 1998.

[254] J.E. Greene. Nucleation, film growth and microstructural evolution. In Bunshah [255], chapter 13, pages 681–739.

[255] R.F. Bunshah, editor. *Handbook of Deposition Technologies for Films and Coatings*. Noyes Publications, Park Ridge, New Jersey, USA, 1994.

[256] P. Michel. Préparation et étude par diffraction électroniques dalliages métalliques en couches minces. *Annales de Physique*, 1:719–744, 1956.

[257] T. Koll and M. Alsmann. Einfluß der Textur elektrolytisch verzinkter Feinblechoberflächen auf Gebrauchs- und Verarbeitungseigenschaften. In D. Dimigen and W. Paatsch, editors, *Werkstoffwoche 98*, volume Band IX, Symposium 11: Oberflächentechnik, pages 61–74, Weinheim, New York, Chichester, Brisbane, Singapore, Toronto, 1999. Wiley-VCH.

[258] H. Park and J.A. Szpunar. The role of texture and morphology in optimizing the corrosion resistance of zinc-based electrogalvanized coatings. *Corrosion Science*, 40(4/5):525–545, 1998.

[259] R. Ramanauskas, P. Quintana, L. Maldonado, P. Pomés, and M.A. Pech-Canul. Corrosion resistance and microstructure of electrodeposited Zn and Zn alloy coatings. *Surface and Coatings Technology*, 92:16–21, 1997.

[260] G. Reumont, J.B. Vogt, A. Iost, and J. Foct. The effects of an Fe-Zn intermetallic-containing coating on the stress corrosion cracking behavior of a hot-dip galvanized steel. *Surface and Coatings Technology*, 139:265–271, 2001.

[261] D.C. Cook. Study of the surface structure of tempered carbon steel. *Hyperfine Interactions*, 41:625–628, 1988.

[262] T.Q. Coddington and D.C. Cook. Study of the microstructure of Fe-Zn-Al ternary alloys. In *Galvatech '95, The use and manufacture of zinc and zinc alloy coated sheet steel products into the 21st century*, pages 515–517, Norfolk, USA, 1995.

[263] T.Q. Coddington and D.C. Cook. Intermetallic phase formation in galvannealed steel coatings with varying aluminum content. *Hyperfine Interactions*, C3:104–107, 1998.

[264] J. Battle, T. Clark, and B.J. Evans. Fe Mössbauer spectroscopy of zinc ferrite prepared by a variety of synthetic methods. *Journal de Physique IV*, 7(Colloque C1, Supplément au Journal de Physique III de mars 1997):257–258, 1997.

[265] I. Tomov, M. Adamik, P.B. Barna, and V. Yamakov. Texture and secondary extinction measurements in Al/Ti stratified films by X-ray diffraction. *Vacuum*, 50(3–4):497–502, 1998.

[266] N-Y. Tang. Discussion of 'kinetics and phase transformations evaluation of Fe-Zn-Al mechanically alloyed phases'. *Metallurgical and Materials Transactions A*, 28A:2433–2435, November 1997.

[267] M. Kurosaki, M. Imafuku, and K. Kawasaki. In-situ observation of zinc electrodeposition using synchrotron radiation x-ray diffraction. In *Proceedings of The 4th International Conference on Zinc and Zinc Alloy Coated Steel Sheet (GALVATECH'98)*, pages 521–525, Chiba, Japan, 1998. The Iron and Steel Institute of Japan.

[268] M. Ye, J.L. Delplancke, G. Berton, L. Segers, and R. Winand. Characterization and adhesion strength study of Zn coatings electrodeposited on steel substrates. *Surface and Coatings Technology*, 105:184–188, 1998.

[269] X.G. Zhang and I.C. Bravo. Electrochemical stripping of galvanealed coatings on steel. *Corrosion Science*, 50(4):308–317, April 1994.

[270] A. Besseyrias, F. Dalard, J.J. Rameau, and H. Baudin. Electrochemical behaviour of zinc-iron intermetallic compounds in an aqueous solution containing NaCl and $ZnSO_4$. *Corrosion Science*, 39(10–11):1883–1896, 1997.

[271] J.J. Duprat. Zink–Legierungsverfahren, Aktualisierte Entwicklung der Legierungverfahren zum Schutz von Stahl und Gusseisen. *Galvanotechnik*, 92(2):346–353, 2001.

[272] W.S. Tait. *An introduction to electrochemical corrosion testing for practicing engineers and scientists.* PairODocs Publications, St. Clair, Wisconsin, USA, 1994.

[273] K.I. Kanno, M. Suzuki, and Y. Sato. Tafel slope determination of corrosion reaction by coulostatic method. *Corrosion Science*, 20:1059–1066, 1980.

[274] Y. Pauleau, editor. *Materials and Processes for Surface and Interface Engineering.* NATO ASI Series, Series E: Applied Sciences, Volume: 290. Kluwer Academic Publishers, 1995.

[275] G.K. Wolf and R. Emmerich. Surface treatments for corrosion protection. In Pauleau [274], pages 565–594.

[276] K.Y. Kim and B.Y. Yang. An electrochemical study on Zn-Sn-alloy-coated steel sheets deposited by vacuum evaporation. Part I. *Surface and Coatings Technology*, 64:99–110, 1994.

[277] C. Bowden and A. Matthews. A study of the corrosion properties of PVD Zn-Ni coatings. *Surface and Coatings Technology*, 76–77:508–515, 1995.

[278] R. Ramanauskas, L.Gudavičiūte, L. Diaz-Ballote, P. Bartolo-Perez, and P. Quintana. Corrosion behaviour of chromated Zn and Zn alloy electrodeposits. *Surface and Coatings Technology*, 140:109–115, 2001.

[279] Brite Euram Project "PVD Alternatives To Conventional Zinc Coatings". T3/T4 Progress Report, 1998.

[280] M.A. Pech-Canul. An electrochemical investigation of passive layers formed on electrodeposited Zn and Zn-alloy coatings in alkaline solutions. *Electrochimica Acta*, 42(2):255–260, 1997.

[281] R. Ramanauskas, L. Muleshkova, L. Maldonado, and P. Dobrovolskis. Characterization of the corrosion behaviour of Zn and Zn alloy electrodeposits: Atmospheric and accelerated tests. *Corrosion Science*, 40(2/3):401–410, 1998.

[282] E. Almeida and M. Morcillo. Lap-joint corrosion of automotive coated materials in chloride media. Part 2 - Galvannealed steel. *Surface and Coatings Technology*, 124:180–189, 2000.

[283] A. Amirudin and D. Thierry. Corrosion mechanisms of phosphated zinc layers on steel as substrates for automotive coatings. *Progress in Organic Coatings*, 28:59–76, 1996.

[284] P.R. Seré, M. Zapponi, C.I. Elsner, and A.R. DiSarli. Comparative corrosion behaviour of 55aluminium-zinc alloy and zinc hot-dip coatings deposited on low carbon steel substrates. *Corrosion Science*, 40(10):1711–1723, 1998.

[285] S. Maeda. Surface chemistry of galvanized steel sheets relevant to adhesion performance. *Progress in Organic Coatings*, 28:227–238, 1996.

[286] W.J. van Ooij and A. Sabata. Under-vehicle corrosion testing of primed zinc and zinc alloy coated steels. *Corrosion Engineering*, 46(2):162–171, 1990.

[287] X. Zhang, S. Lo Russo, A. Miotello, L. Guzman, E. Cattaruzza, P.L. Bonora, and L. Benedetti. The corrosion behavior of Zn coatings on Al-3103 alloy. *Surface and Coatings Technology*, 141:187–193, 2001.

[288] Y. Li. Formation of nano-crystalline corrosion products on Zn-Al alloy coating exposed to seawater. *Corrosion Science*, 43:1793–1800, 2001.

[289] J. Kawafuku, J. Katoh, M. Toyama, H. Nishimoto, K. Ikeda, and H. Satoh. Structure and corrosion resistance of zinc alloy coated steel sheets obtained by continuous vapor deposition apparatus. *ISIJ*, 77(7):995–1002, 1991.

[290] Y. Fukui, H. Tanaka, M. Saito, and T. Deguchi. Corrosion resistance of vapor-deposited Zn-Mg plated steel sheet. In *Proceedings of The 4th International Conference on Zinc and Zinc Alloy Coated Steel Sheet (GALVATECH'98)*, pages 443–448, Chiba, Japan, 1998. The Iron and Steel Institute of Japan.

[291] H. Okada, K. Yamamoto, and I. Ito. A chemical method for searching new alloy plating. In *Proc. 5th Int. Cong. Metallic Corrosion*, Tokyo, Japan, 1972.

[292] A.E. Bohe, J.R. Vilche, K. Jüttner, W.J. Lorenz, and W. Paatsch. Investigations of the semiconductor properties of anodically formed passive layers on Zn and ZnO single crystals in different aqueous solutions by EIS. *Electrochimica Acta*, 34(10):1443–1448, 1989.

[293] P. Bonasewitz, W. Hirschwald, and G. Neumann. Influence of surface processes in electrical, photochemical, and thermodynamical properties of zinc-oxide films. *J. Electrochem. Soc.*, 133:2270–2278, 1986.

[294] W. Kautek, M. Sahre, and W. Paatsch. Transition metal effects in the corrosion protection of electroplated zinc alloy coatings. *Electrochimica Acta*, 39(8/9):1151–1157, 1994.

[295] R. Lindström, J.E. Svensson, and L.G. Johansson. The Atmospheric Corrosion of Zinc in the Presence of NaCl, The influence of Carbon Dioxide and Temperature. *J. Electrochem. Soc.*, 147(5):1751–1757, 2000.

[296] Q. Qu, C. Yan, Y. Wan, and C. Cao. Effects of NaCl and SO_2 on the initial atmospheric corrosion of zinc. *Corrosion Science*, 44:2789–2803, 2002.

[297] K.R. Baldwin, M.J. Robinsons, and C.J.E. Smith. Corrosion rate measurements of electrodeposited zinc-nickel alloy coatings. *Corrosion Science*, 36(7):1115–1131, 1994.

[298] F. Zhu, D. Persson, and D. Thierry. Formation of corrosion products on open and confined metal surfaces exposed to periodic wet/dry conditions – a comparison between zinc and electrogalvanised steel. *Corrosion*, 57(7):582–590, 2001.

[299] R.E. Whan, K. Mills, J.R. Davis, J.D. Destefani, D.A. Dieterich, G.M Crankovic, H.J. Frissell, D.M. Jenkins, W.H. Cubberly, R.L. Stedfeld, E. Coffman, R.T. Kiepura, and B.R. Sanders, editors. *Metals Handbook* $^{®}$ *Ninth edition*, volume 10: Materials Characterization. American Society for Metals ASM International, Metals Park, Ohio 44073, 1988.